



MONASH University

Hierarchical Porous Materials for Energy Conversion and Storage

Changlong Xiao

Master of Science

A thesis submitted for the degree of *Doctor of Philosophy* at

Monash University in 2018

School of Chemistry

Supervised by Professor Douglas R. MacFarlane

and Professor Xinyi Zhang

Copyright notice

© Changlong Xiao (2018).

I certify that I have made all reasonable efforts to secure copyright permissions for third-party content included in this thesis and have not knowingly added copyright content to my work without the owner's permission.

Abstract

The storage of renewable but intermittent solar energy is essential for economy and environmental security, which will change the way the world use energy in the future. The challenge of practical application of energy storage technologies lies in the low energy conversion efficiency. The development of active and efficient catalysts based on earth-abundant transition metals is critically important for improving the efficiency of solar or solar-electricity driven systems to produce hydrogen fuel and hydrogen-rich compounds (e.g. urea and ammonia). This project seeks to exploit hierarchical and mesoporous electrode materials and study their performance in energy conversion and storage including hydrogen production, ammonia synthesis and supercapacitors.

In chapter 2, a core-shell structured bifunctional electrocatalyst composed of a metallic Ni₃Fe alloy nanosheet-framework and a thin layer of Ni₃Fe(OH)₉ shell. The vertically-aligned Ni₃Fe alloy nanosheet provides large electroactive surface area and accelerates the electron transport, and the Ni₃Fe(OH)₉ nanoshell allows easy access for reagents and electrons and high catalytic activity. The electrochemical performance and catalytic activity for oxygen evolution and hydrogen evolution reactions in alkaline media were investigated

Furthermore, a three-dimensional MnO₂/MnCO₂O₄/Ni core-shell heterostructured electrode was fabricated through a facile hydrothermal method followed by electrodeposition. This electrode architecture consists of four levels of interconnected nanostructure: a primary macroporous Ni foam scaffold (≥ 500 μm), an intermediate MnCO₂O₄ core-nanoflake array (50–100 nm), topmost 2D MnO₂ nanosheets (~ 10 nm) and short-range ordered mesopores (~ 5 nm) on the MnO₂ nanosheets. This freestanding MnO₂/MnCO₂O₄/Ni exhibits excellent selectivity for the urea oxidation reaction and comparable hydrogen evolution reaction performance to Pt/C in alkaline solution. This noble-metal-free quadruple hierarchical electrode shows potential as a new strategy for energy-related applications.

Besides, Au-nanoparticle-modified $(\text{BiO})_2\text{CO}_3$ nanodisks have been fabricated through a facile hydrothermal method followed by chemical bath deposition. The photocatalytic activity of $\text{Au}/(\text{BiO})_2\text{CO}_3$ in the nitrogen reduction reaction for artificial photosynthesis of ammonia in a pure water system was examined at atmospheric pressure and room temperature. The introduction of Au nanoparticles can significantly enhance the light trapping and charge separation, leading to an $\text{Au}/(\text{BiO})_2\text{CO}_3$ hybrid catalyst which exhibited outstanding performance for ammonia production. However, further improvement in catalytic stability is required.

In Chapter 5, a highly ordered mesoporous MnCo_2O_4 with hierarchical porosity and high surface area of $133 \text{ m}^2/\text{g}$ was synthesized through a facile nanocasting method and applied in a hybrid supercapacitor. This study demonstrated that ordered ternary mesoporous materials with controllable porosity have great potential for high-energy-density electrochemical energy storage. In chapter 6, a binder-free, core-shell structured MnCo_2O_4 was further synthesised through a facile hydrothermal and electrodeposition method. The obtained dual- $\text{MnCo}_2\text{O}_4/\text{Ni}$ electrode possesses multiple hierarchy, and, when used in a hybrid capacitor, achieved an excellent capacity of 283 mAh g^{-1} and long-term performance stability over 2000 cycles.

Declaration

This thesis contains no material which has been accepted for the award of any other degree or diploma at any university or equivalent institution and that, to the best of my knowledge and belief, this thesis contains no material previously published or written by another person, except where due reference is made in the text of the thesis.

Signature: 

Print Name: Changlong Xiao

Date: 20/06/2018

1. Ali, M.; Zhou, F.; Chen, K.; Kotzur, C.; **Xiao, C.**; Bourgeois, L.; Zhang, X.; MacFarlane, D.R. Nanostructured Photoelectrochemical Solar Cell for Nitrogen Reduction Using Plasmon-Enhanced Black Silicon, *Nat. Commun.* **2016**, 7, 11335.
2. **Xiao, C.**; Hu, H.; Zhang, X.; MacFarlane D.R. "Nanostructured Gold/Bismutite Hybrid Heterocatalysts for Plasmon-Enhanced Photosynthesis of Ammonia," *ACS Sustain. Chem. Eng.*, **2017**, 5, 10858. (**Front Cover**)
3. **Xiao, C.**; Li, S.; Zhang, X.; MacFarlane, D.R. "MnO₂/MnCo₂O₄/Ni Heterostructured with Quadruple Hierarchy: A Bifunctional Electrode Architecture for Overall Urea Oxidation," *J. Mater. Chem. A* **2017**, 5, 7825 (**2017 Hot Paper, Front Cover**).
4. Mendes, T. **Xiao, C.**; Zhou, F.; Li, H. Knowles, G.; Hilder, M; Somers, A.; ... *ACS Appl. Mater. Interfaces* **2016**, 8, 35243.
5. **Xiao, C.**; Zhang, X.; Mendes, T.; Knowles, A.; Chaffee, A.; MacFarlane, D.R. "Highly Ordered Ordered Mesoporous MnCo₂O₄ with Cubic I α_{3d} Symmetry for Electrochemical Energy Storage," *J. Phys. Chem. C* **2016**, 120, 23976.
6. Ma, Z.; Kar, M.; **Xiao, C.**; Forsyth, M.; MacFarlane, D.R. Electrochemical Cycling of Mg[TFSI]₂/Tetraglyme Electrolytes, *Electrochem. Commun.* **2017**, 78, 29.
7. **Xiao, C.**; **Zhang, X.**; **Li, S.**; **Suryanto, B.**; **MacFarlane, D.** "In-Situ Synthesis of Core-shell Ni₃Fe(OH)₉/Ni₃Fe Hybrid Nanostructures as Highly Active and Stable Bifunctional Catalysts for Water Electrolysis" *ACS Applied Energy Mater.* **2018**, 1, 986.
8. Hong, H.; **Xiao, C.**; Lin, X.; Chen, K., Li, H.; Zhang, X. *J. Exp. Nanosci.* **2017**, 12, 33.
9. **Xiao, C.**; Zhang, X.; MacFarlane, D. "Dual-MnCo₂O₄/Ni Electrode with Three-level Hierarchy for High-performance Electrochemical Energy Storage" *Electrochim. Acta.* **2018**, 280, 55.
10. C.V. Manohar, T. Mendens, M. Kar, D. Bin **C. Xiao**, M. Forsyth, S, Mitra, D. MacFarlane "Ionic liquid electrolytes supporting high energy density in sodium-ion batteries based sodium vanadium phosphate composites" *Chem. Commun.* **2018**, 54, 3500.
11. B. Suryanto, C. Kang, D. Wang, **C. Xiao**, F. Zhou, L. Azofra, L. Cavallo, X. Zhang, D. MacFarlane "A Rational Electrode-Electrolyte Design for Efficient Ammonia Electrosynthesis under Ambient Conditions" *ACS Energy Lett.* **2018**, 3, 1219.

Thesis including published works declaration

I hereby declare that this thesis contains no material which has been accepted for the award of any other degree or diploma at any university or equivalent institution and that, to the best of my knowledge and belief, this thesis contains no material previously published or written by another person, except where due reference is made in the text of the thesis.

This thesis includes five original papers published in peer reviewed journals. The core theme of the thesis is hierarchical mesoporous materials for energy conversion and storage. The ideas, development and writing up of all the papers in the thesis were the principal responsibility of myself, the student, working within the School of Chemistry under the supervision of Professor Douglas R. MacFarlane and Doctorate Xinyi Zhang.

(The inclusion of co-authors reflects the fact that the work came from active collaboration between researchers and acknowledges input into team-based research.)

In the case of *Chapter 2, 3, 4, 5 and 6*, my contribution to the work involved the following:

Thesis Chapter	Publication Title	Publication Status	Nature and % of student contribution	Co-author name(s) Nature and % of Co-author's contribution*	Co-author(s), Monash student Y/N*
2	Highly Ordered Hierarchical Mesoporous MnCo ₂ O ₄ with Cubic <i>Ia3d</i> Symmetry for Electrochemical Energy Storage	<i>Published</i>	60% Designing and conducting experiments, analysing data and writing the draft	Dr. Gregory Knowles, 5% Dr. Tiago Mendes, 5% Dr. Xinyi Zhang, 10% Prof. Douglas R. MacFarlane, 20%	Yes
3	MnO ₂ /MnCo ₂ O ₄ /Ni Heterostructure with Quadruple Hierarchy: A Bifunctional Electrode Architecture for Overall Urea Oxidation	<i>Published</i>	70% Designing and conducting experiments, analysing data and writing the draft	Dr. Shuni Li, 5% Dr. Xinyi Zhang, 15% Prof. Douglas R. MacFarlane, 10%	No
4	In Situ Synthesis of Core-Shell-Ni ₃ Fe(OH) ₉ /Ni ₃ Fe Hybrid Nanostructures as Highly Active and Stable Bifunctional Catalysts for Water Electrolysis	<i>Published</i>	70% Designing and conducting experiments, analysing data and writing the draft	Dr. Shuni Li, 5% Dr. Bryan Suryanto, 5% Dr. Xinyi Zhang, 10% Prof. Douglas R. MacFarlane, 10%	Yes
5	Nanostructured Gold/Bismutite Hybrid	<i>Published</i>	50% Designing and	Dr. Hong Hu, 30% Dr. Xinyi Zhang, 10%	No

	Heterocatalysts for Plasmon-Enhanced Photosynthesis of Ammonia		<i>conducting experiments, analysing data and writing the draft</i>	<i>Prof. Douglas R. MacFarlane, 10%</i>	
6	Dual-MnCo ₂ O ₄ /Ni Electrode with Three-level Hierarchy for High-performance Electrochemical Energy Storage	<i>Published</i>	<i>80% Designing and conducting experiments, analysing data and writing the draft</i>	<i>Dr. Xinyi Zhang, 10% Prof. Douglas R. MacFarlane, 10%</i>	Yes

**If no co-authors, leave fields blank*

I have / have not renumbered sections of submitted or published papers in order to generate a consistent presentation within the thesis.

Student signature: 

Date: 20/06/2018

The undersigned hereby certify that the above declaration correctly reflects the nature and extent of the student's and co-authors' contributions to this work. In instances where I am not the responsible author I have consulted with the responsible author to agree on the respective contributions of the authors.

Main Supervisor signature: 

Date: 20/06/2018

Acknowledgement

My PhD student life at Monash University will finish once submitting this thesis. I would like to express my deepest gratitude to those who have provided guidance and support during the completion of this doctorate.

Firstly, I would like to give a heartfelt thanks to both my supervisors Prof. Douglas MacFarlane and Dr Xinyi Zhang for giving me this opportunity to study in their group. Particularly, their encouragements, patience and inspection help me overcome obstructs and difficulties during the research work and make me obtain great progress. During the study in the Monash ionic liquid group, my horizon has been extensively expanded, and my knowledge has also been considerably enriched. Please allow me to thank again for their limitless support and kind guidance through my entire PhD study.

Besides, I want to deliver my special gratefulness to Dr Fengling Zhou, Dr Tiago Mendes, Dr Peter Newman and Dr Gregory Knowles for sharing their excellent experimental skills and invaluable research experience, and assisting me complete my projects. My gratitude also goes to Dr Shuni Li, Dr Hong Hu, Dr Bryan Suryanto, Dr Ciaran McDonnell-Worth and Muataz Ali for their constructive suggestions to my projects.

Additionally, I would like to acknowledge Monash University School of Chemistry and ARC Centre of Excellence for Electromaterials Science (ACES) in the award of International Postgraduate Research Scholarship, which financially support my PhD study.

Last but not least, I warmly thank and appreciate my parents. I am grateful for the love you give me every minute, for the fact that you have always been there to support me during good as well as bad times. I could not complete this work without your encouragements. This work is dedicated to you.

Table of Contents

Abstract	i
Declaration	iii
Publication Record	iv
Acknowledgement	vi
1. Scientific Introduction	
1.1 Energy Matter and Storage Requirement.....	1
1.2 Hydrogen Production	2
1.2.1 Hydrogen Evolution Catalyst.....	5
1.2.2 Oxygen Evolution Catalysts.....	9
1.3 Nitrogen Cycle.....	12
1.3.1 Nitrogen Reduction Catalysts	13
1.3.2 Urea Oxidation Catalysts.....	16
1.4 Supercapacitors.....	16
1.5 Nanoporous Materials	18
1.5.1 Templating Method	18
1.5.2 Hydrothermal and Solvothermal Technologies	21
1.5.3 Electrodeposition Method	21
1.6 Aims of this project	22
2. In Situ Synthesis of Core–Shell-Ni₃Fe(OH)₉/Ni₃Fe Hybrid Nanostructures as Highly Active and Stable Bifunctional Catalysts for Water Electrolysis	
2.1 Chapter Overview	36
2.2 Article Main Text	38
2.3 Supplementary Information	45
3. MnO₂/MnCo₂O₄/Ni Heterostructure with Quadruple Hierarchy: A Bifunctional Electrode Architecture for Overall Urea Oxidation	
3.1 Chapter Overview	56
3.2 Article Main Text	58
3.2 Supplementary Information	66
4. Nanostructured Gold/Bismutite Hybrid Heterocatalysts for Plasmon-Enhanced Photosynthesis of Ammonia	
4.1 Chapter Overview	75
4.2 Article Main Text	77
4.3 Supplementary Information	83

5. Highly Ordered Hierarchical Mesoporous MnCo₂O₄ for Electrochemical Energy Storage

5.1 Chapter Overview	87
5.2 Article Main Text	89
5.3 Supplementary Information	97

6. Dual-MnCo₂O₄/Ni Electrode with Three-level Hierarchy for High-performance Electrochemical Energy Storage

6.1 Chapter Overview	105
6.2 Article Main Text	106
6.3 Supplementary Information	113

7. Conclusions and future work

7.1 Conclusions	117
7.2 Suggested future work.....	118

Chapter 1

Scientific Introduction

1.1 Energy Matter and Storage Requirement

Increased global energy demand and environmental issues have triggered the development of sustainable and renewable energy.¹ So far, electricity, as a secondary clean energy resource, is the dominant form of energy, and demand for electricity is increasing at a rapid pace.^{2, 3} Approximately 68% of current worldwide electrical energy is derived from fossil fuel combustion (coal (42%), natural gas (21%), oil (5%)), with other contributions from nuclear (14%) and only 3% is supplied from renewable energy techniques.⁴ The use of coal and natural gas for electricity generation is a primary cause of the significant rise in greenhouse gas and airborne dust, resulting in severe climate change and pollution.⁵⁻⁷ Meanwhile, fossil fuel production is predicted to peak over the next several decades.⁸ The development and use of renewable energy sources for electricity and other power generation becomes an effective solution to address these issues.

In terms of clean energy supply, solar energy dwarfs all other energy sources because it is inexhaustible, environmentally benign, and offers substantial storage. The energy from the sunlight striking the earth's surface ($\sim 1.74 \times 10^5$ terawatts, TW), is more than all other renewable energy sources (such as wind and hydropower) and two minutes sunlight striking is enough to meet worldwide energy requirement for an entire year (< 20 TW).⁹ Moreover, the global annual energy consumption from renewable sources has grown at an average rate of 2.2%, especially high for solar photovoltaic at 46.2% since 1990 (**Figure 1**).¹⁰ However, a key issue preventing large-scale application of solar power is its intermittency; the sunlight is only available in the daytime and in the absence of clouds. Thus, advanced technologies and

devices are needed to harvest solar energy economically and convert it into storable, transportable and useful chemical fuels.

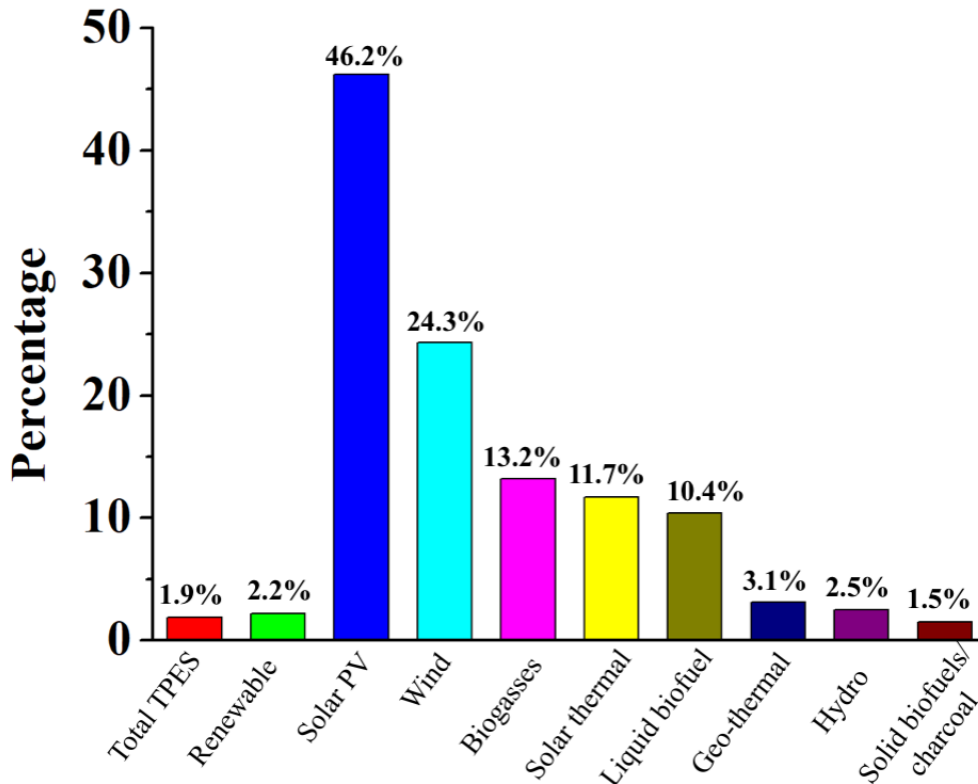


Figure 1. Annual growth rates of world renewable energy supply since 1990 (data adapted from International Energy Agency 2014).

1.2 Hydrogen Production

Electricity is difficult to store in large amounts, but hydrogen is easier with proper infrastructure. Hydrogen fuel is one of the most promising renewable candidates to replace conventional fossil fuels. Although hydrogen fuel is a zero-emission source of energy, it is locked up in vast amounts in water, hydrocarbons and other organic compounds.^{11, 12} Owing to its environmental friendliness and high energy density, hydrogen fuel has significant potential in a variety of applications, both in industrial manufacturing and daily life (**Figure 2**): *i*) Hydrogen fuel cells can serve as a green household energy supply to replace the conventional power grid, avoiding the huge energy losses during transport. *ii*) Benefiting

from its high energy density, hydrogen is an ideal liquid fuel for modern industry. *iii)* Hydrogen fuel engines exhibit zero carbon dioxide emission, and have the potential to replace traditional internal combustion engines to power vehicles.¹³⁻¹⁵

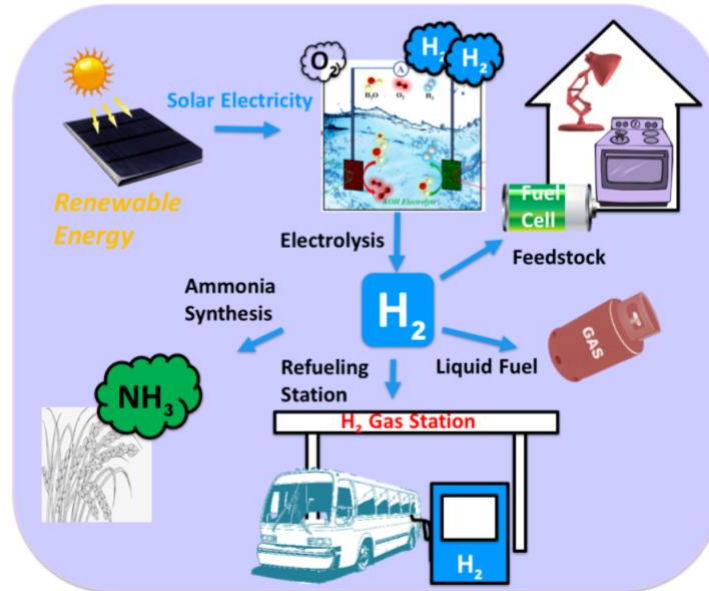
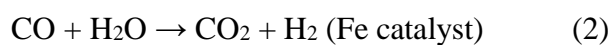


Figure 2. Schematic view of renewable hydrogen fuel cycles and applications.

Hydrogen is the simplest element, which consists of one proton and one electron. As a fuel, hydrogen is storable, transportable and usable energy, but is rarely found naturally on earth. Currently, the most commonly used technology to produce hydrogen is steam reforming from natural gas, oil or coal, accounting for 48%, 30% and 18% of hydrogen production, respectively.¹⁶ This process consists of two major steps: endothermic reactions to yield syngas, and a water gas shift reaction. In the first stage, the methane reacts with water to form carbon monoxide and hydrogen at high temperature (1). In the second stage, the obtained carbon monoxide further reacts with water to generate more hydrogen as well as carbon dioxide (2).



So far, hydrogen derived from non-renewable natural gas is the cheapest and dominant source for industrial supply. However, the generation of hydrogen fuel from hydrogen-

containing hydrocarbons would inevitably cause continued carbon dioxide emission, leading to further exacerbation of the global warming issues.¹⁷ In addition, this kind of hydrogen often contains large amounts of impurities which requires further purification.¹⁸

Apart from hydrocarbons, hydrogen can also be obtained from separating water into oxygen and hydrogen using an electric current. The utilization of renewable and sustainable energy sources to split water for hydrogen production is the key technological component of a hydrogen economy.^{19,20} Besides, immense reserves of hydrogen are stored in water, which covers more than 70% of the earth surface. As a long-term technology pathway, the use of solar or solar electricity to directly dissociate water to oxygen and hydrogen is regarded as the key source of renewable hydrogen fuel. So far, renewable hydrogen only accounts for 2–4% of global hydrogen fuel production, to increase this requires reducing costs via improved technology.^{21,22}

Water electrolysis consists of the anodic oxygen evolution reaction (OER) and cathodic hydrogen evolution reaction (HER), both involving multistep proton-coupled electron transport processes (**Figure 3**). Hence, it usually requires more input energy than the thermodynamic potential of 1.23 V to drive both uphill reactions to occur at appropriate rates. For industrial alkaline water electrolysis systems, the cell voltage efficiency range is 52–69%, corresponding to at least 31% energy lost.²³ Obviously, the cost of the hydrogen fuel is determined by the cost of the overall energy input; reducing this is the key for large-scale application of renewable hydrogen fuel. Therefore, it is critical to increase the overall energy conversion efficiency to make the renewable hydrogen price comparable to the cost of fossil fuel. A variety of catalytic materials have been investigated for electrolytic water splitting to produce hydrogen fuel. However, efficient and low-cost catalysts which can be expanded to industrial applications are still lacking.

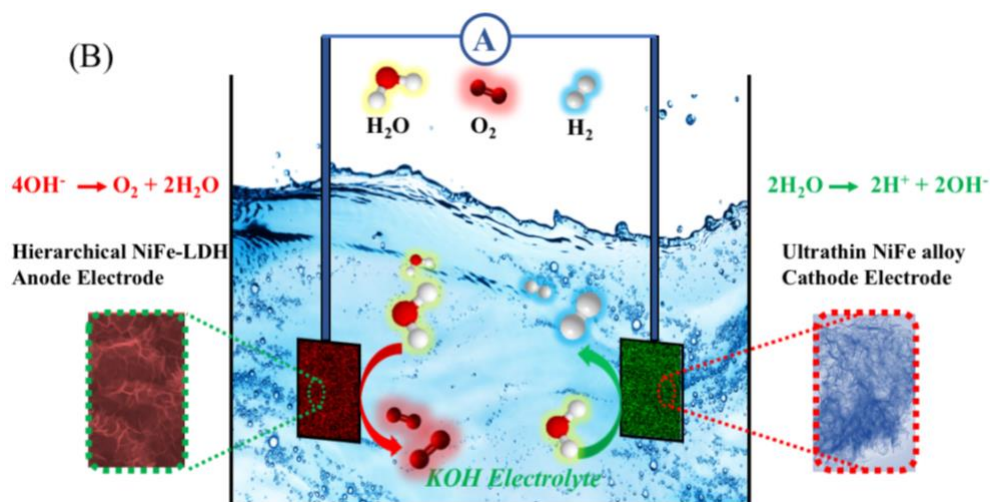


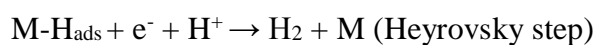
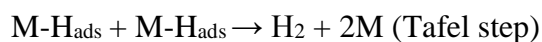
Figure 3. Schematic diagram of water electrolysis to produce hydrogen and oxygen.

1.2.1 Hydrogen Evolution Catalyst

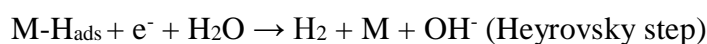
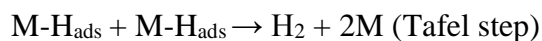
Hydrogen evolution is the cathodic reduction reaction in an electrochemical water splitting cell, which involves a two-electron transfer process to form one hydrogen molecule. The balanced HER half reactions, are: $2\text{H}^+ + 2\text{e}^- \rightarrow \text{H}_2$ (acid media) and $2\text{H}_2\text{O} + 2\text{e}^- \rightarrow \text{H}_2 + 2\text{OH}^-$ (alkaline media). In pursuit of high energetic efficiency for water splitting, cathodic catalysts are required to minimize the overpotential of the HER process. Hydrogen evolution catalysts (HECs) can basically be divided into three categories: *i*) pristine metals, *ii*) alloys or mixtures of metals and *iii*) metal compounds containing both metallic and non-metallic elements. In this section, several representative HECs, including their preparation methods and catalysis mechanisms for each category, are discussed.²⁴⁻²⁷

The HER catalysed on metal catalysts is generally considered to be a two-step process. To initiate the reaction, a proton must first be reduced and adsorbed onto the surface of the HEC (the Volmer step). Subsequently, two adsorbed hydrogen (H_{ads}) atoms combined together to release a hydrogen gas molecule (the Tafel step). The second H_{ads} can also be obtained by reducing another solution proton species (the Heyrovsky step). These processes in both acidic and basic solution are listed below, where M represents a metal HEC.^{28, 29}

Acidic solution:



Alkaline solution:



Platinum is the best performing HEC discovered to date, giving very small overpotentials even at high reaction rates in acidic conditions.³⁰ **Figure 4** depicts the HER volcano plot demonstrating the relationship between the M-H bond and the exchange current. Pt is presented at the top of the volcano plot, showing that the Pt-H bond strength is optimal for the combination of adsorption/reduction of H^+ and release of hydrogen gas. However, the scarcity and high cost of Pt restrict its widespread technological application for large-scale hydrogen production.

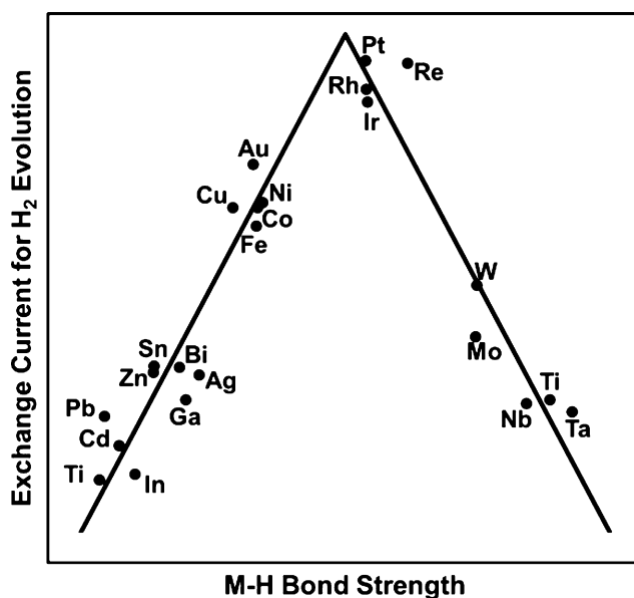


Figure 4. Volcano plot showing the relationship between the exchange current and the M-H bond strength. Reprinted with permission from Ref. 30, Copyright 2009 Elsevier.

Although other metals below Pt on the volcano plot have decreased HER catalytic activity, many of them are non-noble metals (Ni, Co, Cu et al.) and much cheaper than Pt.³¹⁻³⁴ Modifying the morphology of these metal HECs for optimum performance is one approach that may enable a viable efficiency-to-cost ratio to be achieved. For instance, in studies of nickel, the number of effective active sites for HER and the electrode surface area have been increased. Nevertheless, most of these non-noble metals are not stable in acidic media, and the HER test has to be carried out in alkaline environments.^{31-33, 35-37} They usually require a high overpotential ($\eta_{10 \text{ mA}} > 200 \text{ mV}$) to achieve a current density of 10 mA cm^{-2} (the overpotential to deliver a current density of 10 mA is often used as a benchmark to evaluate HER activity). This implies that the HER activity of pristine metal catalysts is unlikely to surpass that of Pt, which typically shows $\eta_{10 \text{ mA}} < 50 \text{ mV}$. One strategy to further promote the HER activity and stability of metal-based HECs is to develop metal alloys and mixtures.

Binary and ternary metal alloys usually exhibit improved HER performance compared to that of their corresponding single metal counterparts. The improved activity and stability is generally related to the following three aspects. Doping with one or two other metals may significantly alter the surface morphology, leading to a rougher electrode surface. As a result, higher current density can be achieved due to the enlarged surface area.³⁴ Doping can also change the electronic properties. Different transition metals exhibit different d-orbital characteristics, which may affect the strength of the M-H bond for proton adsorption and reduction. In addition, metal alloys usually have increased charge transfer capability, benefiting the overall HER process.³⁸ Finally, the improvement may also be ascribed to synergistic effects. As the HER is a two-step reaction, the rate-limiting step can change for different metals. Each component in the metal alloy may show optimum activity for different steps, thus resulting in an overall catalytic performance that is superior to those of the corresponding single-metal counterparts. For example, Ni and Mo have different roles in the

NiMo catalyst system for the HER. The Ni sites are favourable for proton reduction and adsorption, while the Mo sites show fast kinetics for further reducing the adsorbed hydrogen to hydrogen molecules.³⁹ Although these mixed-metal HECs still require alkaline catalytic conditions, their HER performances are superior to those of their components, and are sometimes even comparable to that of Pt at high reaction rates.^{35-37, 40}

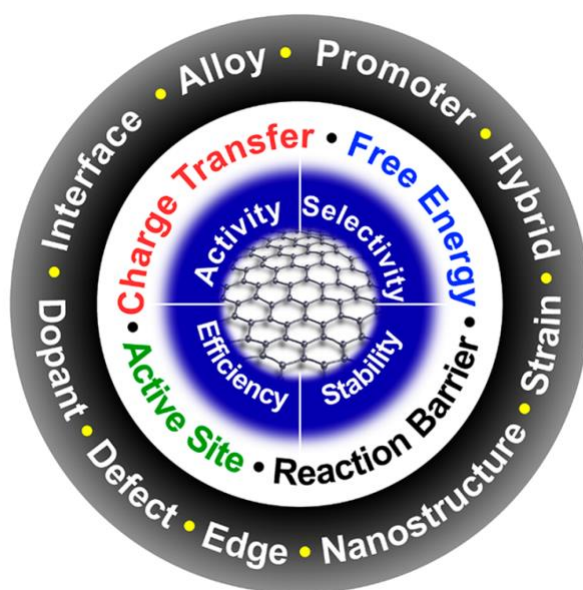


Figure 5 Typical strategies for designing hybrid materials for enhanced electrocatalytic performance. Reprinted with permission from Ref. 56, Copyright 2018, American Chemical Society.

In addition to metallic materials, compounds containing both metallic and non-metallic elements have also been extensively investigated in search of cost-effective and highly active HECs (**Figure 5**). Among them, some transition metal oxides/hydroxides have been extensively studied for HER under cathodic conditions, and exhibit very high activity and stability in both acidic and basic media. Examples include RuO_2 ,⁴¹ and NiFe layered double hydroxide;⁴² the latter showed HER performance comparable with that of Pt at high current density under basic conditions. Moreover, chalcogenides — metal sulfides and selenides, such as MoS_2 and CoSe_2 — have also attracted a great deal of attention for HER.^{43, 44} Metal-phosphides are another category of compounds which show promising HER activity.

Recently, iron phosphide (FeP) has been reported as an excellent HER catalyst in both acidic and neutral media.⁴⁵⁻⁵⁰

1.2.2 Oxygen Evolution Catalysts

The oxygen evolution reaction (OER) is the complementary anodic half reaction in a water electrolysis system with a thermodynamic potential of 1.23V. It requires four electron-and-proton transfers to release one oxygen molecule, and is consequently the major challenge for the overall efficiency of electrolysers. Therefore, efficient oxygen evolution catalysts (OECs) are needed to reduce the anodic overpotential and increase the reaction rate. The most intensively studied OECs can be divided into three major categories: *i*) binary oxides of noble metals, such as RuO₂ and IrO₂, *ii*) oxides and oxyhydroxides of earth-abundant transition metals including Mn, Fe, Co and Ni and *iii*) ternary oxides with specific crystalline structure, such as perovskite or spinel.

Figure 6 depicts the OER volcano plot of a variety of transition metal oxides showing the relationship between the OER activity on the metal oxide surface against the transition enthalpy in either acidic or basic conditions. Noticeably, IrO₂ and RuO₂ are at the top of this plot, revealing their superior catalytic activity over most other materials for OER to date.^{51, 52} As a result, both IrO₂ and RuO₂ are often used as benchmark OECs for OER performance comparison. However, the high price and low abundance of IrO₂ and RuO₂ make them not feasible for large-scale commercial application. Therefore, intensive research interest has been focused on improving the OER performance of cost-effective materials such as Co, Ni and Fe.

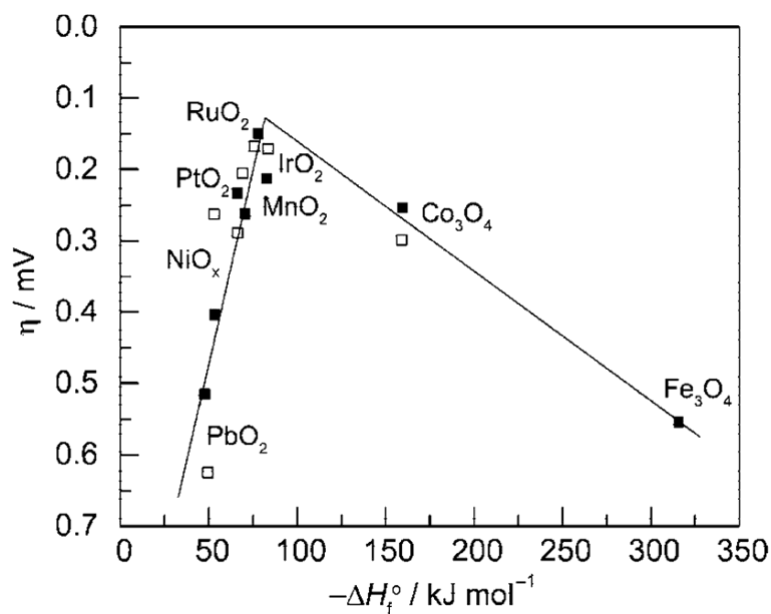
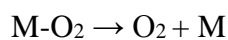
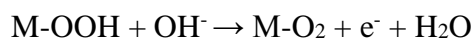
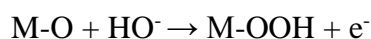
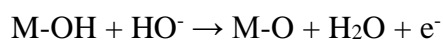
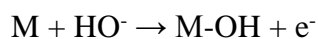


Figure 6 Volcano plot showing overpotential for O₂ production on metal oxide surfaces versus the enthalpy of formation of the oxide in acidic (□) and basic (■) solutions. Reprinted with permission from Ref. 52, Copyright 2016, Elsevier.

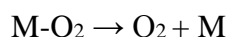
It is generally considered that the oxygen is evolved from the metal oxide surface rather than the bare metal, and the mechanism and pathways are more complex than those of the HER. OER mechanisms vary with surface structure. Catalysts with the same composition but different morphology, thickness or preparation method can show different mechanisms.⁵³⁻⁵⁶ Despite all this, a general OER mechanism and catalytic pathway on metal oxide surfaces has been proposed as below:

Alkaline media:



Acidic media:





First row transition metal oxides (TMOs) such as CoO_x , NiO_x and FeO_x have been extensively investigated as anode catalysts for OER.^{50, 57-61} It is recognised that their catalytic activity ($\text{NiO}_x > \text{CoO}_x > \text{FeO}_x$) is opposite to the bond strength of $\text{OH-M}^{2+\delta}$ ($0 < \delta < 1.5$, $\text{Ni} < \text{Co} < \text{Fe}$).^{62, 63} However, the OER activity of TMOs can be improved by fabricating them with desired dimension and nanostructures. For example, the control of morphologies can be easily realised by duplicating the mesoporous block copolymers and silica templates. By varying the copolymer compositions (i.e. molecular weight and PEO weight fractions) and inorganic contents, different mesostructures can be achieved as illustrated in Figure 7.

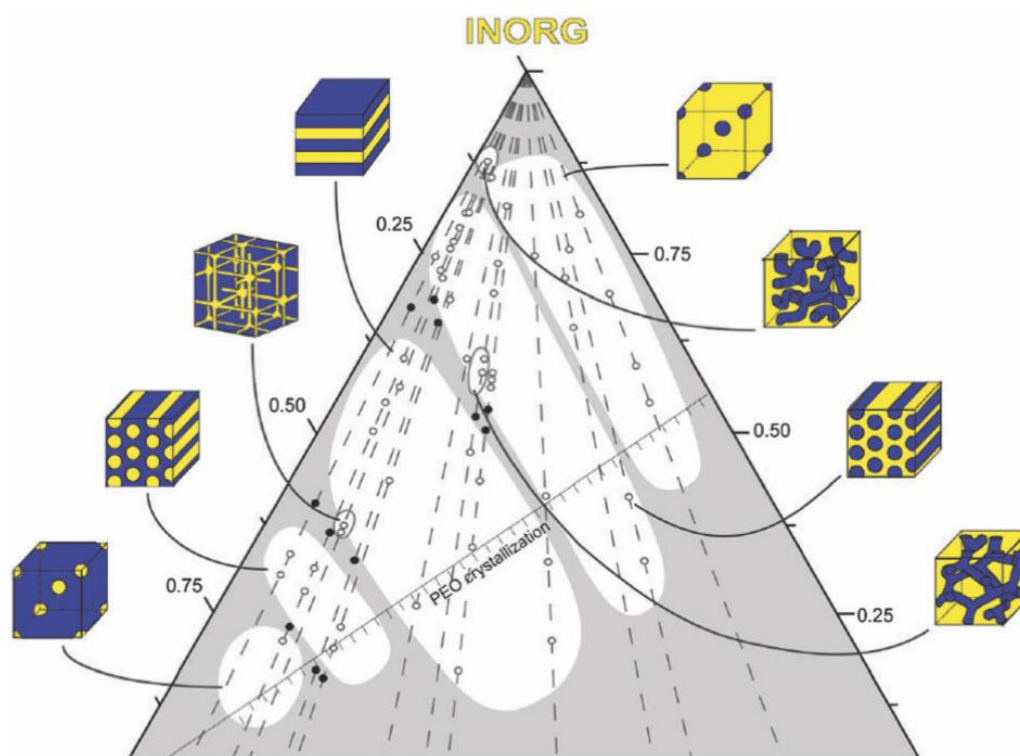


Figure 7 Ternary diagram mapping out morphologies directed by various templates.

Reprinted with permission from Ref. 63, Copyright 2013, The Royal Society of Chemistry.

Layered transition metal hydroxides and double hydroxides are another branch of non-noble metal OECs which can be synthesized via a variety of approaches including hydrothermal, electrodeposition, and chemical vapour deposition methods. These layered hydroxide catalysts exhibit varied activities, which are related to their inter-slab spacing, thickness and porosity.⁶⁴ Among them, NiFe layered double hydroxides (LDH) are the most widely studied material, which shows an extremely low OER onset potential of 1.47 V vs. RHE, high turnover frequency of 0.05 s^{-1} and excellent catalytic current delivery ability.⁶⁵ All these outstanding OER properties are superior to those of the benchmark IrO_2 and RuO_2 electrocatalysts. Furthermore, research interest was further extended to improve the poor electrical conductivity of NiFe-LDH by coupling them with conducting carbon materials such as graphene.⁶⁶⁻⁷⁰ More importantly, the combination of NiFe-LDH with nanostructured carbon can further induce synergistic effects, leading to greatly enhanced OER performance. Although the actual active sites/centres are not yet clear, the NiFe-LDH based materials are the most promising OECs for future commercial application. Other transition-metal based materials including perovskites, nitrides, carbonate hydroxides, phosphides, and chalcogenides have also attracted tremendous attention for OER owing to their unique physicochemical properties.^{50, 71-79}

1.3 Nitrogen Cycle

Like the “carbon cycle” and “water cycle”, the “nitrogen cycle” is another significant energy-related cycle.^{80, 81} In the natural nitrogen cycle, atmospheric nitrogen can be converted into various inorganic, organic and bio-available compounds. Among them, ammonia and urea are the most important nitrogen-containing compounds to human society for fertilizer and energy storage. In this section, two important energy-related reaction processes in the nitrogen cycle: the nitrogen reduction reaction (NRR) and urea oxidation reaction (UOR), have been summarized.

1.3.1 Nitrogen Reduction Catalysts

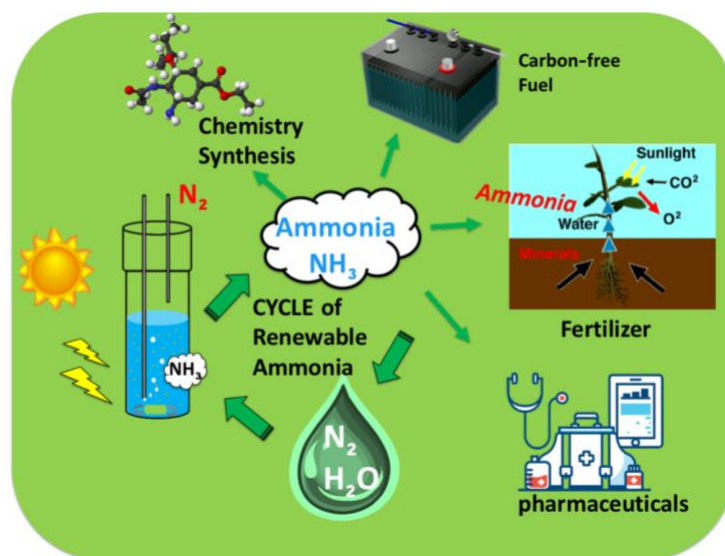


Figure 8 Schematic view of energy-saving ammonia production and applications.

Ammonia has a number of favourable attributes, the primary one being its high capacity for hydrogen storage, 17.6 wt.%, based on its molecular structure. Ammonia is also considered as a potential carbon-free and eco-friendly energy storage intermediate, and is widely used in various fields (**Figure 8**).⁸²⁻⁸⁶ In nature, ammonia can be produced through enzymatic reactions and geochemical fixation. However, these natural ammonia-production processes suffer from relatively low reaction rates and poor control, and are not capable of keeping up with the rising demand for ammonia.⁸⁷ Currently, the industrial-scale production of ammonia relies on the classic Haber-Bosch process, which uses Fe- and Ru- based catalysts to synthesise ammonia at high temperature and pressure (e.g. ~ 500 °C, 300 bar).⁸⁸ This process consumes 1–3 % of the global annual energy supply and 3–5% of world’s annual natural gas production, meanwhile emitting large quantities of carbon dioxide into the atmosphere.⁸⁰ Due to the strong covalent bonds of nitrogen, the fixation of nitrogen with high efficiency at ambient conditions is a significant scientific challenge.

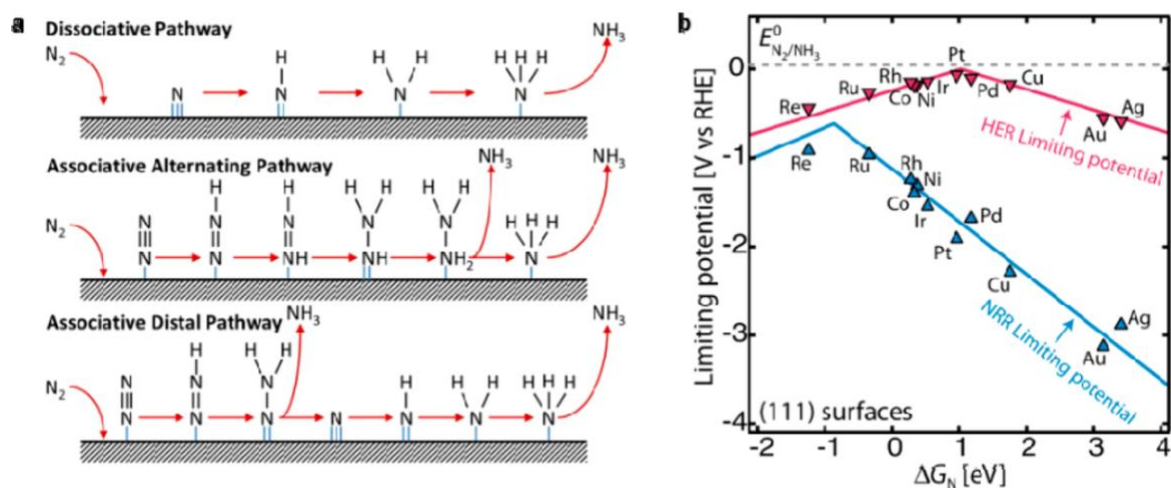


Figure 9 (a) Schemes of the NRR via different pathways and (b) Volcano plot for the NRR on a range of metals with the HER volcano plot overlapped for comparison. Reprinted with permission from Ref. 89, Copyright 2011, Wiley.

Recently, the concept of a proton-assisted NRR system integrated with renewable solar energy for ammonia production in a sustainable and environment friendly process has attracted intensive research interest.⁹⁰⁻⁹³ However, the NRR is a kinetically sluggish reaction requiring high energy input to break the strong triple bond of molecular nitrogen (940.95 kJ/mol) into nitrogen atoms.⁹⁴ The mechanisms of NRR are classed as either dissociative or associative mechanisms, as shown in **Figure 9a**.⁹⁵ In the dissociative mechanism, the triple bond of the nitrogen molecule should be broken and two active nitrogens are then adsorbed onto the surface of the catalyst. Afterwards, the hydrogen atoms are added to the active N-atoms, one by one, to form the ammonia molecules. In contrast, in the associative pathway, the nitrogen molecule is adsorbed onto the catalyst surface with the two N-atoms remaining bound to each other. The triple bond is cleaved as part of the hydrogenation process for each N-atom. Similar to the HER and OER, a volcano plot of NRR on a range of transition metal surfaces has also been constructed through density functional theory (DFT) calculations (**Figure 9b**). As the HER is a competitive cathodic reaction, the design principles for NRR

catalysts need to consider the adsorption energy of N_2 , protonation energy of NH^* to NH_2^* and the catalytic selectivity.⁹⁶

Recently, nanostructured Au/b-Si, Au/Bi₂O₃, and TiO₂ with oxygen vacancies have been reported as excellent nitrogen reduction catalysts (NRCs) for photosynthesis of ammonia.⁹⁷⁻⁹⁹ The experimental setup is shown in **Figure 10**. However, the energy conversion efficiency and ammonia yield are far below those required for practical application. According to the DFT results, the criteria for NRCs can be summarized as follows: *i*) the nitrogen molecule can be easily adsorbed onto the NRC surface for sufficient activation of the inert triple bond of the nitrogen molecule, *ii*) the NRCs should have suitable stabilization for the N_2H^* species and *iii*) appropriate destabilization of N_2H^* is needed to reduce the required overpotential during the hydrogenation process.⁹⁶ It is worth noting that most NRC design is based on theoretical calculations. The study of efficient NRCs is still a new research field and more exploration is needed.

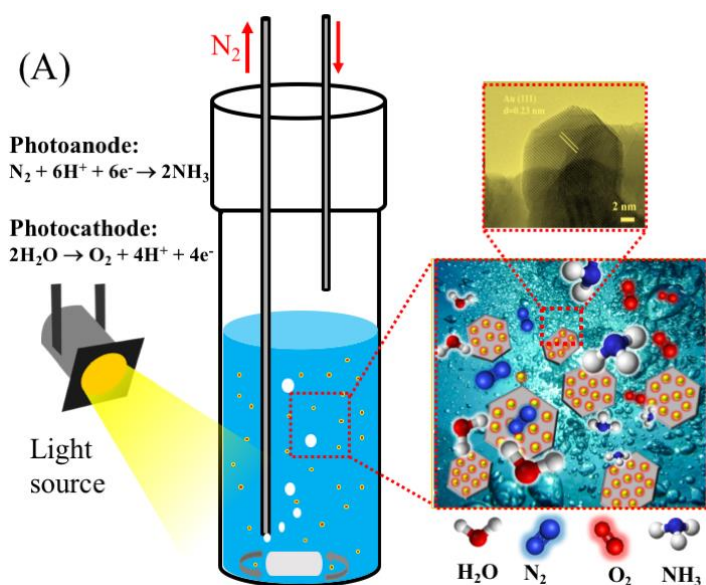


Figure 10 Schematic diagram demonstrating the photosynthesis of ammonia in aqueous solution under ambient conditions. Adapted with permission from Ref. 98, Copyright 2017, American Chemical Society.

1.3.2 Urea Oxidation Catalysts

Urea is another important hydrogen storage material which offers high energy density, low cost, low toxicity, and simple storage and transport. Besides, the electrolysis of urea-containing water is also a promising approach to produce hydrogen fuel. In a urea electrolyser cell, the urea oxidation reaction (UOR) ($\text{CO}(\text{NH}_2)_2 + 6\text{OH}^- \rightarrow \text{N}_2 + 5\text{H}_2\text{O} + \text{CO}_2 + 6\text{e}^-$) occurs at the anode, while hydrogen gas was generated at the cathode via the HER. The thermodynamic onset potential of UOR is 0.37 V vs. RHE, which is much lower than potential required for the OER (1.23 V vs. RHE).¹⁰⁰⁻¹⁰² Hence, the UOR is, in principle, a more efficient process than the OER for hydrogen generation. Nonetheless, the UOR involves a complicated gas-evolution process and is also kinetically sluggish. Usually, noble-metal based electrocatalysts such as Pt, Rh and Pd, are required to drive this uphill reaction at adequate reaction rates. However, the high price of these noble-metal based materials hinders their widespread application, thus cost-effective and efficient catalysts are critical.

To date, a variety of non-noble transition-metal based catalysts with different nanostructures, lateral sizes and active site oxidation states have been reported. Examples include small MnO_2 nanosheets with sub-nanometer thickness, S-doped $\text{Ni}(\text{OH})_2$ nanosheets and Ni-based metal-organic-framework (MOF).^{101, 103, 104} The material size, electronic conductivity and available surface area are crucial factors for designing excellent UOR electrocatalysts.¹⁰⁵⁻¹⁰⁸ Despite extensive research into the UOR, understanding of the mechanism and its practical application are still lacking.

1.4 Supercapacitors

Electrochemical capacitors (also called supercapacitors) are one of the most efficient energy storage devices. They store the energy by means of charge separation. Supercapacitors bridge the gap between electrolytic capacitors and rechargeable batteries as they typically show

capacity 10 – 100 times greater than that of electrolytic capacitors, meanwhile, realizing much faster charge/discharge cycles than those of batteries. Moreover, supercapacitors also have the advantages of long life stability (e.g., specific capacitances without obvious decays after thousands of charging/discharging cycles) and high Coulombic efficiencies.¹⁰⁹⁻¹¹³ Based on the differences in the mechanism of electrical energy storage, supercapacitors can be classified into two categories: electrochemical double layer capacitor (EDLC) and pseudocapacitor (Figure 11). In the EDLCs, the charge-separation process occurs at both negative and positive electrodes to form two electrical double layers. In comparison, the pseudocapacitor behaviour is similar to that of a rechargeable battery, where reversible Faradaic charge transfer takes place and a chemical redox reaction occurs between the electrode materials surface and the electrolyte ions. Recently, a new type of battery-supercapacitor hybrid system, which combines EDLC materials with battery-type materials, has attracted great research interest.¹¹⁴⁻¹¹⁸ These combined hybrid capacitors exhibit both the high energy density of pseudocapacitors and high-power density of EDLCs. For practical application, technological progress in terms of active material design and device manufacture is still required.

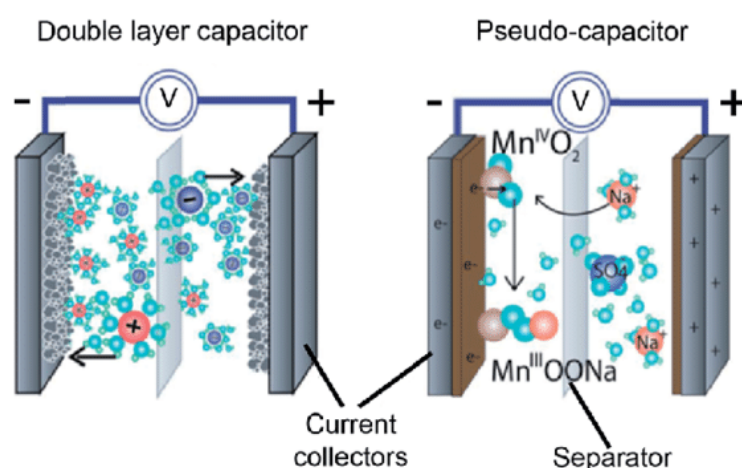


Figure 11 Comparison the working mechanisms between double layer capacitor and pseudo-capacitor. Adapted with permission from Ref. 113, Copyright 2016, Royal Society of Chemistry.

1.5 Hierarchical Nanoporous Materials

Nanoporous materials contain well-defined pores within an organic or inorganic framework. According to the pore size, nanoporous materials can be classified into three categories: microporous materials (0.2 – 2 nm), mesoporous materials (2 – 50 nm) and macroporous (50-1000 nm). By taking advantage of the regular porous matrix, nanoporous materials offer massive surface areas and the pores can be tailored so that particular reagents and products are favoured.¹¹⁹⁻¹²¹ Broadly speaking, hierarchical materials can be recognised as another type of porosity. The hierarchical order of a materials can be defined as numbers of levels of scale with recognised structures, which range from molecular level over mesoscopic length (nm) to macroscopic dimensions (μm).¹²²⁻¹²⁴ Although each level of hierarchy is different in size scales and morphologies, all structures should be interconnected forming an integrated entirety. In addition to the benefit arising from the high porosity, hierarchical structures also offer advantages of high utilisation rate of space to build more sophisticated nanostructures. The combination of ideas of hierarchical and nanoporous architecture in building electromaterials can further improve the exposure of electroactive sites and electrolyte/ion accessibility. Over the past decade, hierarchical porous materials have been intensively studied for a variety of applications, such as catalysis, energy storage, and sorption/desorption. In pursuit of high surface area, hierarchy and porosity, a large variety of synthesis methods have been developed, including templating, hydrothermal/solvothermal methods and electrodeposition.

1.5.1 Templating Method

Templating can be further subdivided into hard and soft templating, depending on the structure-directing agents used. The soft-template method is a sol-gel process which uses surfactants such as Pluronic P123, Pluronic F127, and Fuji 56 to control the pore size and internal structure. The synthetic pathways are generally divided into direct co-

condensation with opposite charged surfactants and indirect co-condensation of similarly charged species mediated by the addition of counter ions (K^+ and Na^+) at the interface between surfactant and inorganic.^{125, 126}

Another widely used soft templating method is polymeric micelle self-assembly technology, especially useful in the synthesis of ordered semicrystalline porous metallic and metal oxide materials (e.g. Pt, SnO_2 , TiO_2 , Al_2O_3 , ZrO_2) using commercial poly(alkylene oxide) block copolymers as surfactant/templates.¹²⁷⁻¹³³ The mechanism of the polymeric micelle assembly process has also been investigated via the *in-situ* small angle X-ray scattering (SAXS), wide angle X-ray scattering (WAXS) and Fourier transform infrared (FTIR) spectroscopy in the past several decades, and can be categorised into three steps: *i*) preparation of stable solution containing copolymer and metal precursor with appropriate stoichiometry; *ii*) evaporation associated with self-assembly process. The complete evaporation of solvent may induce the progressive concentration of the metal precursors into a homogeneous, flexible and condensed network surrounding the copolymer mesophase. *iii*) a treatment step including consolidation, template removal and crystallisation under different atmospheric conditions to obtain complex metallic or metal oxide nano-crystalline films.¹³²⁻¹³⁵ Advantages of soft templating method include low fabrication cost and mild synthetic conditions. Because the polymerisation of the transition metal precursors and the hydrolysis during the sol-gel process are difficult to control, the disadvantage lies in the low crystallinity of the final products.¹³⁶⁻¹³⁹

The hard-template method is advantageous for synthesising rigid mesostructures with high surface area via a nanocasting, exotemplating or repeated templating process. For example, anodic alumina membranes (AAO) were initially utilised as a mold for the synthesis of porous carbons and metals through electrodeposition,¹⁴⁰ chemical vapour

deposition¹⁴¹⁻¹⁴³ and atomic layer deposition.¹⁴⁴ The resultant pore sizes typically range from 15 nm up to approximately 150 nm. On the basis of this methodology, a variety of 3D mesoporous carbon (e.g. CMK-1),¹⁴⁵ mesoporous Pt networks¹⁴⁶ and metal oxides (e.g. Co_3O_4)¹⁴⁷ were prepared by duplicating silica template with various pore architectures (e.g. MCM-48, SBA-15 and KIT-6). Figure 12 presents a schematic diagram, in which KIT-6 is used as an example to demonstrate a hard-templating process. Similarly, the nanocasting method can be summarised into three steps: *i*) filtration of silica mesochannels with target precursor solution; *ii*) consolidation of precursor inside the pores by reduction or decomposition, and *iii*) removal of mesoporous silica template by washing the resulted precursor/silica mixtures with NaOH or HF solution.

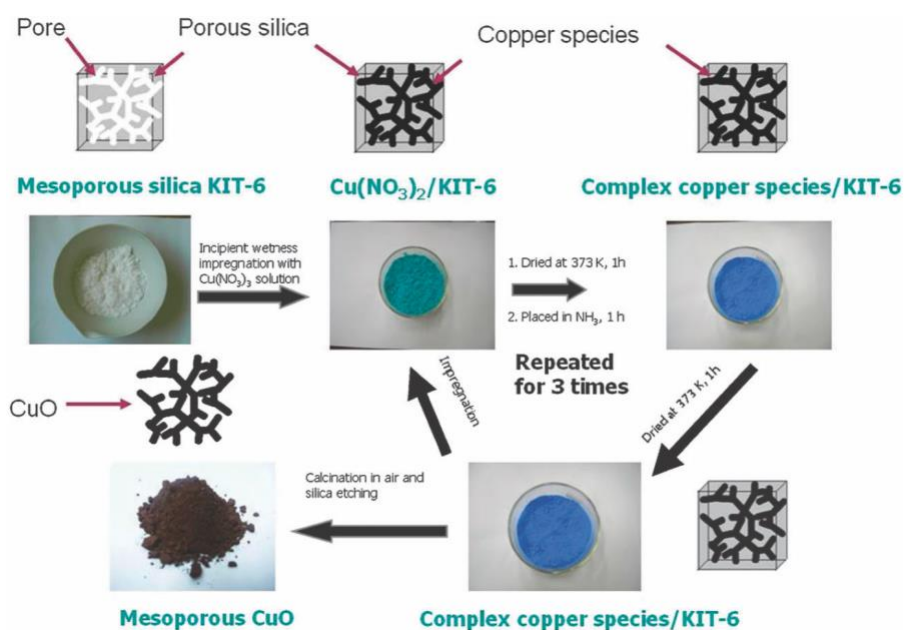


Figure 12 a schematic diagram of hard templating synthesis using KIT-6. Adapted with permission from Ref. 148, Copyright 2012, Royal Society of Chemistry.

According to the synthetic process, it can be further classified into two-solvent method,^{148,149} solvent-free solid-liquid method,¹⁵⁰ impregnation-precipitation-calcination method^{151,152} and solvent evaporation method.¹⁵³ In comparison to the soft-template method, the hard-template method has some unique advantages. Firstly, the structures of

the target metal oxides are controllable by replicating different silica templates with well-designed porous structures. Secondly, the silica templates are able to resist high temperature during calcination. Therefore, highly crystallised metal oxide materials can be obtained. Thirdly, the facile synthetic process makes it suitable for the synthesis of multi-metallic materials. Moreover, the obtained highly crystallised mesoporous metal oxides can be further reduced to low-valence metal materials, which significantly enrich the catalytic activity of the materials and their applications.

1.5.2 Hydrothermal and Solvothermal Technologies

Hydrothermal and solvothermal methods are easy and template-less solution-based techniques for fabricating highly crystalline nanowires, nanoparticles and other nanostructures.¹⁵⁴⁻¹⁶⁰ Both methods usually take place in a closed system, such as a Teflon-lined stainless steel autoclave. The hydrothermal processes involve completed heterogeneous reactions from high-temperature aqueous solution at high vapor pressures. It often used as a method of synthesis of single crystals, depending on the solubility of the products in aqueous media under high temperature and pressure. The solvothermal technique is similar to hydrothermal synthesis, except that it uses non-aqueous solvent. By altering the solvent type, precursor type and surfactant type, solvothermal processes allow for precise control over the size, shape distribution and crystallinity of metal oxide materials.

1.5.3 Electrodeposition Method

Electrodeposition is a practical method for fabricating nanostructured materials.¹⁶¹⁻¹⁷⁰ Especially with assistance of structure-directing agents (e.g. P123 and F127), thin films, multi-layered nanoparticles or nanocrystals, as well as nanowires and nanorods modified with nanopores can be achieved.¹⁷¹⁻¹⁷⁵ Typically, electrodeposition is carried out in a two- or three electrode electrochemical system by controlling either the electrode potential or

current density. In the electrochemical system, the electrolyte serves as both the source of the precursor and the conducting medium. The applied voltage/current can be varied to control the structure of the electrodeposited material, meanwhile ordered mesopores can be created after removal the structure-directing agents. The most commonly used electrodeposition techniques include chronoamperometry, cyclic voltammetry, potential step approach, potential pulse approach, chronopotentiometry, and current pulse deposition.

On account of its intrinsic advantages, electrochemical synthesis shows superiority in producing individual components and integrated system for electrocatalysis.¹⁷⁶⁻¹⁸⁰ First, it is a solution-based approach and compatible with ambient conditions, which makes it cost-effective and practical for industrial application. Second, as a traditional technique, various of materials including almost all semiconductors (e.g. metals, alloys, oxides and chalcogenides) can be produced through electrodeposition methods. Third, the solution-based nature of electrodeposition allows for easy manipulation of a variety of synthetic variables including current, potential, pH, additives, solvent types as well as temperatures to control the nucleation, crystal growth of desired materials. In addition, the thickness of the deposited materials can be monitored by controlling the charge transfer and/or deposition time. More importantly, binder-free electrodes can be obtained as the materials are grown directly on the substrate (working electrode) during the electrochemical synthesis.

1.6 Aims of this Project

The aim of this project is to develop hierarchical and mesoporous materials based on earth-abundant transition metals via a variety of technologies including templating, hydrothermal approaches, electrodeposition and solution-based methods. The project seeks to exploit the high surface area of the materials, synergistic effects and morphology control to produce

catalysts with excellent performance in chemical reactions that are relevant for energy conversion and storage. Specifically, this thesis is divided into 6 chapters, as follows:

- *Chapter 1:* General introduction
- *Chapter 2:* This chapter focuses on the fabrication of a core-shell structured bifunctional electrocatalyst composed of a metallic Ni₃Fe alloy nanosheet-framework and a thin layer of Ni₃Fe(OH)₉ shell. The vertically-aligned Ni₃Fe alloy nanosheet provides large electroactive surface area and accelerates the electron transport, and the Ni₃Fe(OH)₉ nanoshell allows easy access for reagents and electrons and high catalytic activity. The electrochemical performance and catalytic activity for oxygen evolution and hydrogen evolution reactions in alkaline media were investigated (This work was published in ACS Applied Energy Materials).
- *Chapter 3:* In this chapter, a three-dimensional MnO₂/MnCo₂O₄/Ni core-shell heterostructured electrode was fabricated through a facile hydrothermal method followed by electrodeposition. This electrode architecture consists of four levels of interconnected nanostructure: a primary macroporous Ni foam scaffold (≥ 500 μm), an intermediate MnCo₂O₄ core-nanoflake array (50–100 nm), topmost 2D MnO₂ nanosheets (~ 10 nm) and short-range ordered mesopores (~ 5 nm) on the MnO₂ nanosheets. This freestanding MnO₂/MnCo₂O₄/Ni exhibits excellent selectivity for the urea oxidation reaction and comparable hydrogen evolution reaction performance to Pt/C in alkaline solution. This noble-metal-free quadruple hierarchical electrode shows potential as a new strategy for energy-related applications. (This work was published in Journal of Materials Chemistry A)
- *Chapter 4:* In this chapter, Au-nanoparticle-modified (BiO)₂CO₃ nanodisks have been fabricated through a facile hydrothermal method followed by chemical bath deposition. The photocatalytic activity of Au/(BiO)₂CO₃ in the nitrogen reduction reaction for artificial photosynthesis of ammonia in a pure water system was examined at atmospheric pressure and

room temperature. The introduction of Au nanoparticles can significantly enhance the light trapping and charge separation, leading to an Au/(BiO)₂CO₃ hybrid catalyst which exhibited outstanding performance for ammonia production. However, further improvement in catalytic stability is required. (This work was published in ACS Sustainable Chemistry and Engineering)

- *Chapter 5:* In this chapter, a highly ordered mesoporous structure with crystalline framework has been studied for electrochemical energy storage. MnCo₂O₄ with hierarchical porosity and high surface area of 133 m²/g was synthesized through a facile nanocasting method and applied in a hybrid supercapacitor. This study demonstrated that ordered ternary mesoporous materials with controllable porosity have great potential for high-energy-density electrochemical energy storage. (This work was published in Journal of Physical Chemistry C)
- *Chapter 6:* This chapter is an extension work to chapter 5. A binder-free, core-shell structured MnCo₂O₄ was synthesised through a facile hydrothermal and electrodeposition method. The obtained dual-MnCo₂O₄/Ni electrode possesses multiple hierarchy, and, when used in a hybrid capacitor, achieved an excellent capacity of 283 mAh g⁻¹ and long-term performance stability over 2000 cycles (This work was published in Electrochimica Acta).
- *Chapter 7:* General conclusion for chapters 2-6 and future research proposal.

References

1. M. Steinberg, *Int. J. Hydrogen Energy* 1999, **24**, 771-777.
2. M. Dale and S. M. Benson, *Environ. Sci. Technol.* 2013, **47**, 3482-3489.
3. N. Ma, K. Zhang and Y. Yang, *Adv. Mater.* 2017, **29**, 1700144.
4. K. Nguyen and B. D. Bruce, *Biochim. Biophys. Acta* 2014, **1837**, 1553-1566.
5. M. F. Kuehnel, C. D. Sahm, G. Neri, J. R. Lee, K. L. Orchard, A. J. Cowan, E. Reisner, *Chem. Sci.* 2018, **9**, 2501-2509.
6. C. Brahic, *Science* 2006, **312**, 1123.

7. P. Williamson, *Nature* 2016, **530**, 153-155.
8. J. Tollefson, *Nature* 2018, **556**, 422-425.
9. Z. Niu, W. Zhou, X. Feng, T. Feng, S. Wu, P. Cheng, X. Lu, H. Du, X. Xiong, Y. Fu, *Environ. Sci. Pollut. Res. Int.* 2018, **11**, 1-9
10. I. Hanif, *Environ Sci. Pollut. Res. Int.* 2018, **15**, 15057-15067.
11. R. C. Prince, H. S. Kheshgi, *Crit. Rev. Microbiol.* 2005, **31**, 19-31.
12. P. Cai, Y. Li, G. Wang, Z. Wen, *Angew. Chem.* 2018, **57**, 3910-3915.
13. R. F. Service, *Science* 2008, **321**, 620.
14. M. Z. Jacobson, W. G. Colella, D. M. Golden, *Science*, 2005, **308**, 1901-1905.
15. J. Tollefson, *Nature* 2010, **464**, 1262-1264.
16. U. Schroder, *ChemSusChem* 2008, **1**, 281-282.
17. K. Caldeira, A. K. Jain, M. I. Hoffert, *Science* 2003, **299**, 2052-2054.
18. A. M. Ribeiro, C. A. Grande, F. V. Lopes, J. M. Loureiro, A. E. Rodrigues, *Chem. Eng. Sci.* 2008, **63**, 5258-5273.
19. Z. Zou, J. Ye, K. Sayama, H. Arakawa, *Nature* 2001, **414**, 625.
20. A. J. Bard, M. A. Fox, *Acc. Chem. Res.* 1995, **28**, 141-145.
21. T. L. Gibson, N. A. Kelly, *Int. J. Hydrogen Energy* 2010, **35**, 900-911.
22. J. Turner, G. Sverdrup, M. K. Mann, P. C. Maness, B. Kroposki, M. Ghirardi, R. J. Evans, D. Blake, *Int. J. Energy Res.* 2008, **32**, 379-407.
23. M. Carmo, D. L. Fritz, J. Mergel, D. Stolten, *Int. J. Hydrogen Energy* 2013, **38**, 4901-4934.
24. M. G. Walter, E. L. Warren, J. R. McKone, S. W. Boettcher, Q. Mi, E. A. Santori, N. S. Lewis, *Chem. Rev.* 2010, **110**, 6446-6473.
25. M. Zeng, Y. Li, *J. Mater. Chem. A*, 2015, **3**, 14942-14962.
26. X. Zou, Y. Zhang, *Chem. Soc. Rev.* 2015, **44**, 5148-5180.

27. D. Kang, T. W. Kim, S. R. Kubota, A. C. Cardiel, H. G. Cha, K.-S. Choi, *Chem. Rev.* 2015, **115**, 12839-12887.
28. B. Conway, M. Salomon, *Electrochim. Acta*, 1964, **9**, 1599-1615.
29. J. M. Bockris, E. Potter, *J. Electrochem. Soc.* 1952, **99**, 169-186.
30. S. Trasatti, *J. Electroanal. Chem. Interfacial Electrochem.* 1972, **39**, 163-184.
31. C. Lupi, A. Dell'Era, M. Pasquali, *Int. J. Hydrogen Energy* 2009, **34**, 2101-2106.
32. A. N. Correia, S. A. Machado, L. A. Avaca, *Electrochem. Commun.* 1999, **1**, 600-604.
33. R. Solmaz, G. Kardaş, *Electrochim. Acta*, 2009, **54**, 3726-3734.
34. E. Navarro-Flores, Z. Chong, S. Omanovic, *J. Molecular Catal. A: Chem.* 2005, **226**, 179-197.
35. N. Krstajić, V. Jović, L. Gajić-Krstajić, B. Jović, A. Antozzi, G. Martelli *Int. J. Hydrogen Energy* 2008, **33**, 3676-3687.
36. S. H. Hong, S. H. Ahn, J. Choi, J. Y. Kim, H. Y. Kim, H.-J. Kim, J. H. Jang, H. Kim, S.-K. Kim *Appl. Surface Sci.* 2015, **349**, 629-635.
37. L. S. Sanches, S. H. Domingues, C. E. Marino, L. H. Mascaro *Electrochem. Commun.* 2004, **6**, 543-548.
38. M. M. Jaksic, *Int. J. Hydrogen Energy* 2001, **26**, 559-578.
39. J. Highfield, E. Claude, K. Oguro, *Electrochim. Acta* 1999, **44**, 2805-2814.
40. Y. Wang, G. Zhang, W. Xu, P. Wan, Z. Lu, Y. Li, X. Sun, *ChemElectroChem* 2014, **1**, 1138-1144.
41. L. Vázquez-Gómez, S. Cattarin, P. Guerriero, M. Musiani, *Electrochim. Acta*, 2007, **52**, 8055-8063.
42. C. Xiao, Y. Li, X. Lu, C. Zhao, *Ad. Funct. Mater.* 2016, **26**, 3515-3523.
43. A. B. Laursen, S. Kegnæs, S. Dahl, I. Chorkendorff, *Energy Environ. Sci.* 2012, **5**, 5577-5591.

44. A. I. Carim, F. H. Saadi, M. P. Soriaga, N. S. Lewis, *J. Mater. Chem. A* 2014, **2**, 13835-13839.
45. I. Paseka, J. Velicka, *Electrochim. Acta* 1997, **42**, 237-242.
46. F. H. Saadi, A. I. Carim, E. Verlage, J. C. Hemminger, N. S. Lewis, M. P. Soriaga, *J. Phys. Chem. C* 2014, **118**, 29294-29300.
47. B. Daly, F. Barry, *Int. Mater. Rev.* 2003, **48**, 326-338.
48. C. Sequeira, D. Santos, P. Brito, *Energy* 2011, **36**, 847-853.
49. T. Morikawa, T. Nakade, M. Yokoi, Y. Fukumoto, C. Iwakura, *Electrochim. Acta* 1997, **42**, 115-118.
50. N. Jiang, B. You, M. Sheng, Y. Sun, *Angew. Chem.* 2015, **127**, 6349-6352.
51. X. Long, Z. Wang, S. Xiao, Y. An, S. Yang, *Mater. Today* 2016, **19**, 213-226.
52. S. Trasatti, *Electrochim. Acta* 1984, **29**, 1503.
53. C. G. Morales-Guio, L. Liardet, X. Hu, *J. Am. Chem. Soc.* 2016, **138**, 8946-8957.
54. L. Trotochaud, S. L. Young, J. K. Ranney, S. W. Boettcher, *J. Am. Chem. Soc.* 2014, **136**, 6744-6753.
55. Z. Lu, H. Wang, D. Kong, K. Yan, P. C. Hsu, G. Zheng, H. Yao, Z. Liang, X. Sun, Y. Cui, *Nat. Commun.* 2014, **5**, 4345.
56. H. Jin, C. Guo, X. Liu, J. Liu, A. Vasileff, Y. Jiao, Y. Zheng, S. Z. Qiao, *Chem. Rev.* 2018, **118**, 6337-6408.
57. R. Subbaraman, D. Tripkovic, D. Strmcnik, K. C. Chang, M. Uchimura, A. P. Paulikas, V. Stamenkovic, N. M. Markovic, *Science* 2011, **334**, 1256-1260.
58. L. Trotochaud, J. K. Ranney, K. N. Williams, S. W. Boettcher, *J. Am. Chem. Soc.* 2012, **134**, 17253-17261.
59. Y. Sun, S. Gao, F. Lei, J. Liu, L. Liang, Y. Xie, *Chem. Sci.* 2014, **5**, 3976-3982.

60. Y. Zhao, X. Jia, G. Chen, L. Shang, G. I. Waterhouse, L. Z. Wu, C. H. Tung, D. O'Hare, T. Zhang, *J. Am. Chem. Soc.* 2016, **138**, 6517-6524.
61. X. Long, Z. Ma, H. Yu, X. Gao, X. Pan, X. Chen, S. Yang, Z. Yi, *J. Mater. Chem. A*, 2016, **4**, 14939-14943.
62. X. Yan, L. S. Li, *J. Mater. Chem.* 2011, **21**, 3295-3300.
63. Y. Deng, J. Wei, Z. Sun, D. Zhao, *Chem. Soc. Rev.* 2013, **42**, 4054.
64. J. Huang, J. Chen, T. Yao, J. He, S. Jiang, Z. Sun, Q. Liu, W. Cheng, F. Hu, Y. Jiang, *Angew. Chem. Int. Ed.* 2015, **54**, 8722-8727.
65. F. Song, X. Hu, *J. Am. Chem. Soc.* 2014, **136**, 16481-16484.
66. C. Tang, H. F. Wang, X. L. Zhu, B. Q. Li, Q. Zhang, *Part. Part. Syst. Char.* 2016, **33**, 473-486.
67. J. A. Yan, M. Chou, *Phys. Rev. B*, 2010, **82**, 125403.
68. X. Long, J. Li, S. Xiao, K. Yan, Z. Wang, H. Chen, S. Yang, *Angew. Chem.* 2014, **126**, 7714-7718.
69. C. Tang, H. S. Wang, H. F. Wang, Q. Zhang, G. L. Tian, J. Q. Nie, F. Wei, *Adv. Mater.* 2015, **27**, 4516-4522.
70. Y. Li, M. Zhao, Y. Zhao, L. Song, Z. Zhang, *Part. Part. Syst. Char.* 2016, **33**, 158-166.
71. S. Jin, *ACS Energy Lett.* 2017, **2**, 1937-1938.
72. J. Wang, X. Ma, F. Qu, A. M. Asiri, X. Sun, *Inorg. Chem.* 2017, **56**, 1041-1044.
73. P. Chen, K. Xu, Z. Fang, Y. Tong, J. Wu, X. Lu, X. Peng, H. Ding, C. Wu, Y. Xie, *Angew. Chem.* 2015, **127**, 14923-14927.
74. F. Yu, H. Zhou, Z. Zhu, J. Sun, R. He, J. Bao, S. Chen, Z. Ren, *ACS Catal.* 2017, **7**, 2052-2057.

75. B. Zhang, C. Xiao, S. Xie, J. Liang, X. Chen, Y. Tang, *Chem. Mater.* 2016, **28**, 6934-6941.
76. A. Dutta, N. Pradhan, *J. Phys. Chem. Lett.* 2016, **8**, 144-152.
77. J. Wu, M. Liu, K. Chatterjee, K. P. Hackenberg, J. Shen, X. Zou, Y. Yan, J. Gu, Y. Yang, J. Lou, *Adv. Mater. Interfaces*, 2016, **3**, 1500669.
78. L. Liang, H. Cheng, F. Lei, J. Han, S. Gao, C. Wang, Y. Sun, S. Qamar, S. Wie, Y. Xie, *Angew. Chem. Int. Ed.* 2015, **54**, 12004-12008.
79. Y. Sun, S. Gao, F. Lei, C. Xiao, Y. Xie, *Acc. Chem. Res.*, 2014, **48**, 3-12.
80. C. J. van der Ham, M. T. Koper, D. G. Hetterscheid, *Chem. Soc. Rev.* 2014, **43**, 5183-5191.
81. Z. W. Seh, J. Kibsgaard, C. F. Dickens, I. Chorkendorff, J. K. Nørskov, T. F. Jaramillo, *Science* 2017, **355**, 4998.
82. V. Rosca, M. Duca, M. T. de Groot, M. T. Koper, *Chem. Rev.* 2009, **109**, 2209-2244.
83. D. E. Canfield, A. N. Glazer, P. G. Falkowski, *Science* 2010, **330**, 192-196.
84. H. P. Jia, E. A. Quadrelli, *Chem. Soc. Rev.* 2014, **43**, 547-564.
85. C. J. Pickett, J. Talarmin, *Nature* 1985, **317**, 652.
86. K. A. Brown, D. F. Harris, M. B. Wilker, A. Rasmussen, N. Khadka, H. Hamby, S. Keable, G. Dukovic, J. W. Peters, L. C. Seefeldt, *Science*, 2016, **352**, 448-450.
87. G. Marnellos, M. Stoukides, *Science* 1998, **282**, 98-100.
88. M. Kitano, Y. Inoue, Y. Yamazaki, F. Hayashi, S. Kanbara, S. Matsuishi, T. Yokoyama, S. W. Kim, M. Hara, H. Hosono, *Nat. Chem.* 2012, **4**, 934.
89. R. Lv, T. Cui, M. S. Jun, Q. Zhang, A. Cao, D. S. Su, Z. Zhang, S. H. Yoon, J. Miyawaki, I. Mochida, *Adv. Funct. Mater.* 2011, **21**, 999-1006.
90. G. F. Chen, X. Cao, S. Wu, X. Zeng, L.-X. Ding, M. Zhu, H. Wang, *J. Am. Chem. Soc.* 2017, **139**, 9771-9774.

91. D. Bao, Q. Zhang, F. L. Meng, H. X. Zhong, M. M. Shi, Y. Zhang, J. M. Yan, Q. Jiang, X. B. Zhang, *Adv. Mater.* 2017, **29**, 1604799.
92. J. Zhao, Z. Chen, *J. Am. Chem. Soc.* 2017, **139**, 12480-12487.
93. J. M. McEnaney, A. R. Singh, J. A. Schwalbe, J. Kibsgaard, J. C. Lin, M. Cargnello, T. F. Jaramillo, J. K. Nørskov, *Energy Environ. Sci.* 2017, **10**, 1621-1630.
94. M.-J. Cheng, Y. Kwon, M. Head-Gordon, A. T. Bell, *J. Phys. Chem. C*, 2015, **119**, 21345-21352.
95. M. A. Shipman, M. D. Symes, *Catal. Today*, 2017, **286**, 57-68.
96. E. Skulason, T. Bligaard, S. Gudmundsdóttir, F. Studt, J. Rossmeisl, F. Abild-Pedersen, T. Vegge, H. Jónsson, J. K. Nørskov, *Phys. Chem. Chem. Phys.* 2012, **14**, 1235-1245.
97. M. Ali, F. Zhou, K. Chen, C. Kotzur, C. Xiao, L. Bourgeois, X. Zhang, D. R. MacFarlane, *Nat. Commun.* 2016, **7**, 11335.
98. C. Xiao, H. Hu, X. Zhang, D. R. MacFarlane, *ACS Sustain. Chem. Eng.* 2017, **5**, 10858-10863.
99. H. Li, J. Shang, Z. Ai, L. Zhang, *J. Am. Chem. Soc.* 2015, **137**, 6393-6399.
100. R. Lan, S. Tao, J. T. Irvine, *Energy Environ. Sci.* 2010, **3**, 438-441.
101. R. P. Forslund, J. T. Mefford, W. G. Hardin, C. T. Alexander, K. P. Johnston, K. J. Stevenson, *ACS Catal.* 2016, **6**, 5044-5051.
102. R. Ding, L. Qi, M. Jia, H. Wang, *Nanoscale* 2014, **6**, 1369-1376.
103. D. Zhu, C. Guo, J. Liu, L. Wang, Y. Du, S. Z. Qiao, *Chem. Commun.* 2017, **53**, 10906-10909.
104. S. Chen, J. Duan, A. Vasileff, S. Z. Qiao, *Angew. Chem. Int. Ed.* 2016, **55**, 3804-3808.
105. D. Wang, W. Yan, S. H. Vijapu, G. G. Botte, *J. Power Sources* 2012, **217**, 498-502.

106. D. Wang, W. Yan, G. G. Botte, *Electrochem. Commun.* 2011, **13**, 1135-1138.
107. X. Zhu, X. Dou, J. Dai, X. An, Y. Guo, L. Zhang, S. Tao, J. Zhao, W. Chu, X. C. Zeng, *Angew. Chem. Int. Ed.* 2016, **55**, 12465-12469.
108. C. Xiao, S. Li, X. Zhang, D. R. MacFarlane, *J. Mater. Chem. A*, 2017, **5**, 7825-7832.
109. G. Wang, L. Zhang, J. Zhang, *Chem. Soc. Rev.* 2012, **41**, 797-828.
110. M. Zhi, C. Xiang, J. Li, M. Li, N. Wu, *Nanoscale* 2013, **5**, 72-88.
111. C. Zhong, Y. Deng, W. Hu, J. Qiao, L. Zhang, J. Zhang, *Chem. Soc. Rev.* 2015, **44**, 7484-7539.
112. A. González, E. Goikolea, J. A. Barrena, R. Mysyk, *Renewable Sust. Energy Rev.* 2016, **58**, 1189-1206.
113. U. Gulzar, S. Goriparti, E. Miele, T. Li, G. Maidecchi, A. Toma, F. De Angelis, C. Capiglia, R. P. Zaccaria, 2016. *J. Mater. Chem. A* 2016, **4**, 16771-16800.
114. D. Li, C. Ye, X. Chen, S. Wang, H. Wang, *J. Power Sources* 2018, **382**, 116-121.
115. R. Thangavel, K. Kaliyappan, D. U. Kim, X. Sun, Y. S. Lee, *Chem. Mater.* 2017, **29**, 7122-7130.
116. B. Babu, M. Shaijumon, *J. Power Sources*, 2017, **353**, 85-94.
117. C. Xiao, X. Zhang, T. Mendes, G. P. Knowles, A. Chaffee, D. R. MacFarlane, *J. Phys. Chem. C*, 2016, **120**, 23976-23983.
118. R. Li, Y. Wang, C. Zhou, C. Wang, X. Ba, Y. Li, X. Huang, J. Liu, *Adv. Funct. Mater.* 2015, **25**, 5384-5394.
119. G. A. Tompsett, W. C. Conner, K. S. Yngvesson, *ChemPhysChem* 2006, **7**, 296-319.
120. R. Vaidhyanathan, D. Bradshaw, J. N. Rebilly, J. P. Barrio, J. A. Gould, N. G. Berry, M. J. Rosseinsky, *Angew. Chem.* 2006, **118**, 6645-6649.
121. M. A. Hillmyer, in *Block Copolymers II*, Springer, 2005, 137-181.
122. R. Lakes, *Nature*, 1993, **361**, 511-515.

123. G. J. D. A. Soler-Illia, C. Sanchez, B. Lebeau, J. Patarin, *Chem. Rev.* 2002, **102**, 4093-4138.
124. C. M. Parlett, K. Wilson, A. F. Lee, *Chem. Soc. Rev.* 2013, **42**, 3876-3893.
125. D. M. Antonelli, A. Nakahira, J. Y. Ying, *Inorg. Chem.* 1996, **35**, 3126-3136.
126. M. S. Wong, D. M. Antonelli, J. Y. Ying, *Nanostruct. Mater.*, 1997, **9**, 165-168.
127. Y. Li, B. P. Bastakoti, V. Malgras, C. Li, J. Tang, J. H. Kim, Y. Yamauchi, *Angew. Chem. Int. Ed.* 2015, **54**, 11073-11077.
128. Y. Li, B. P. Bastakoti, M. Imura, S. M. Hwang, Z. Sun, J. H. Kim, S. X. Dou, Y. Yamauchi, *Chem. Eur. J.* 2014, **20**, 6027-6032.
129. B. P. Bastakoti, S. Ishihara, S. Y. Leo, K. Ariga, K. C. W. Wu, Y. Yamauchi, *Langmuir*, 2014, **30**, 651-659.
130. S. P. Nunes, A. R. Behzad, B. Hooghan, R. Sougrat, M. Karunakaran, N. Pradeep, U. Vainio, K. V. Peinemann, *ACS Nano*, 2011, **5**, 3516-3522.
131. B. P. Bastakoti, Y. Li, M. Imura, N. Miyamoto, T. Nakato, T. Sasaki, Y. Yamauchi, *Angew. Chem. Int. Ed.* 2015, **54**, 4222-4225.
132. H. Cui, Z. Chen, S. Zhong, K. L. Wooley, D. J. Pochan, *Science*, 2007, **317**, 647-650.
133. Y. Wan, D. Zhao, *Chem. Rev.* 2007, **107**, 2821-2860.
134. S. C. Owen, D. P. Chan, M. S. Shoichet, *Nano Today* 2012, **7**, 53-65.
135. B. P. Bastakoti, Y. Li, N. Miyamoto, N. M. Sanchez-Ballester, H. Abe, J. Ye, P. Srinivasu Y. Yamauchi, *Chem. Commun.* 2014, **50**, 9101-9104.
136. C. J. Brinker, Y. Lu, A. Sellinger, H. Fan, *Adv. Mater.* 1999, **11**, 579-585.
137. P. Liu, I. L. Moudrakovski, J. Liu, A. Sayari, *Chem. Mater.* 1997, **9**, 2513-2520.
138. D. M. Antonelli, *Adv. Mater.* 1999, **11**, 487-492.
139. F. Jiao, J. C. Jumas, M. Womes, A. V. Chadwick, A. Harrison, P. G. Bruce, *J. Am. Chem. Soc.* 2006, **128**, 12905-12909.

140. W. C. Yoo, J. K. Lee, *Adv. Mater.* 2004, **16**, 1097-1101.
141. C. M. Zelenski, P. K. Dorhout, *J. Am. Chem. Soc.* 1998, **120**, 734-742.
142. D. N. Davydov, P. A. Sattari, D. AlMawlawi, A. Osika, T. L. Haslett, M. Moskovits, *J. Appl. Phys.* 1999, **86**, 3983-3987.
143. J. Lee, J. Kim, T. Hyeon, *Adv. Mater.* 2006, **18**, 2073-2094.
144. P. Banerjee, I. Perez, L. Henn-Lecordier, S. B. Lee, G. W. Rubloff, *Nat. Nanotechnol.* 2009, **4**, 292-296.
145. R. Ryoo, S. H. Joo, S. Jun, *J. Phys. Chem. B* 1999, **103**, 7743-7746.
146. H. J. Shin, R. Ryoo, Z. Liu, O. Terasaki, *J. Am. Chem. Soc.*, 2001, **123**, 1246-1247.
147. R. L. Bao, K. Jiao, H. Y. He, J. H. Zhuang, B. Yue, *Stud. Surf. Sci. Catal.*, 2006, **165**, 267-270.
148. Y. Ren, Z. Ma, P. G. Bruce, *Chem. Soc. Rev.* 2012, **41**, 4909-4927.
149. M. Imperor-Clerc, D. Bazin, M. D. Appay, P. Beaunier, A. Davidson, *Chem. Mater.* 2004, **16**, 1813-1821.
150. T. A. Crowley, K. J. Ziegler, D. M. Lyons, D. Ertz, H. Olin, M. A. Morris, J. D. Holmes, *Chem. Mater.* 2003, **15**, 3518-3522.
151. F. Jiao, K. M. Shaju, P. G. Bruce, *Angew. Chem. Int. Ed.* 2005, **44**, 6550-6553.
152. W. Yue, W. Zhou, *Chem. Mater.*, 2007, **19**, 2359-2363.
153. Y. M. Wang, Z. Y. Wu, L. Y. Shi, J. H. Zhu, *Adv. Mater.* 2005, **17**, 323-327.
154. A. Chen, P. Holt-Hindle, *Chem. Rev.* 2010, **110**, 3767-3804.
155. P. Holt-Hindle, S. Nigro, M. Asmussen, A. Chen, *Electrochem. Commun.* 2008, **10**, 1438-1441.
156. J. Wang, D. F. Thomas, A. Chen, *Chem. Commun.* 2008, 5010-5012.
157. J. Wang, D. F. Thomas, A. Chen, *Anal. Chem.* 2008, **80**, 997-1004.
158. H. Chen, Y. Wang, S. Dong, *Inorg. Chem.* 2007, **46**, 10587-10593.

159. Z. Zhang, D. A. Blom, Z. Gai, J. R. Thompson, J. Shen, S. Dai, *J. Am. Chem. Soc.* 2003, **125**, 7528-7529.
160. Y. Hou, H. Kondoh, R. Che, M. Takeguchi, T. Ohta, *Small*, 2006, **2**, 235-238.
161. J. N. Tiwari, F. M. Pan and K. L. Lin, *New J. Chem.* 2009, **33**, 1482-1485.
162. J. Zhang, H. Ma, D. Zhang, P. Liu, F. Tian, Y. Ding, *Phys. Chem. Chem. Phys.* 2008, **10**, 3250-3255.
163. S. Kim and S. J. Park, *Electrochim. Acta*, 2008, **53**, 4082-4088.
164. F. Montilla, E. Morallon, I. Duo, C. Comninellis, J. Vazquez, *Electrochim. Acta*, 2003, **48**, 3891-3897.
143. S. M. Ayyadurai, Y. S. Choi, P. Ganesan, S. P. Kumaraguru, B. N. Popov, *J Electrochem. Soc.* 2007, **154**, B1063-B1073.
165. X. Chen, N. Li, K. Eckhard, L. Stoica, W. Xia, J. Assmann, M. Muhler, W. Schuhmann, *Electrochem. Commun.* 2007, **9**, 1348-1354.
166. Y. Zhao, L. Fan, H. Zhong, Y. Li, S. Yang, *Adv. Funct. Mater.* 2007, **17**, 1537-1541.
167. P. Yu, J. Yan, J. Zhang, L. Mao, *Electrochem. Commun.* 2007, **9**, 1139-1144.
168. M.-C. Tsai, T. K. Yeh and C. H. Tsai, *Electrochem. Commun.* 2006, **8**, 1445-1452.
169. N. Tian, Z. Y. Zhou, S. G. Sun, Y. Ding, Z. L. Wang, *Science* 2007, **316**, 732-735.
170. L. C. Nagle, J. F. Rohan, *J. Power Sources*, 2008, **185**, 411-418.
171. T. Xue, C. L. Xu, D. D. Zhao, X. H. Li, H. L. Li, *J. Power Sources* 2007 **164**, 953-958.
172. T. Pauporte, J. Rathouský, *J. Phys. Chem. C* 2007, **111**, 7639-7644.
173. J. J. Feng, J. J. Xu, H. Y. Chen, *Electrochem. Commun.* 2006, **8**, 77-82.
174. W. J. Zhou, J. Zhang, T. Xue, D. D. Zhao, H. L. Li, *J. Mater. Chem.* 2008, **18**, 905-910.
175. D. Wang, W. L. Zhou, B. F. McCaughy, J. E. Hampsey, X. Ji, Y. B. Jiang, H. Xu, J. Tang, R. H. Schmehl, C. O'Connor, C. J. Brinker, *Adv. Mater.* 2003, **15**, 130-133.

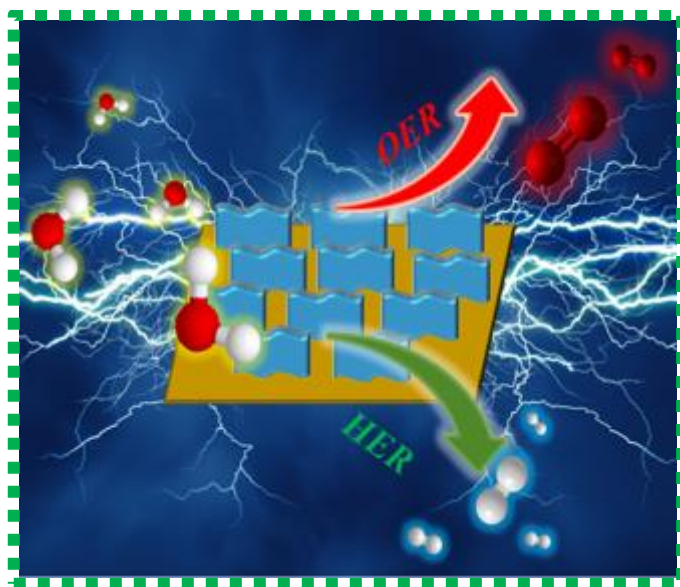
176. A. Walcarius, E. Sibottier, M. Etienne, J. Ghanbaja, *Nat. Mater.* 2007, **6**, 602.
177. K. S. Choi, E. W. McFarland, G. D. Stucky, *Adv. Mater.* 2003, **15**, 2018-2021.
178. V. Malgras, H. Ataee-Esfahani, H. Wang, B. Jiang, C. Li, K. C. W. Wu, J. H. Kim, Y. Yamauchi, *Adv. Mater.* 2016, **28**, 993-1010.
179. A. Keilbach, J. Moses, R. Köhn, M. Döblinger, T. Bein, *Chem. Mater.* 2010, **22**, 5430-5436.
180. C. Zhu, D. Du, A. Eychmüller, Y. Lin, *Chem. Rev.* 2015, **115**, 8896-8943.

Chapter 2

In Situ Synthesis of Core–Shell- $\text{Ni}_3\text{Fe}(\text{OH})_9/\text{Ni}_3\text{Fe}$ Hybrid Nanostructures as Highly Active and Stable Bifunctional Catalysts for Water Electrolysis

2.1 Overview

This chapter is a paper titled “In Situ Synthesis of Core–Shell- $\text{Ni}_3\text{Fe}(\text{OH})_9/\text{Ni}_3\text{Fe}$ Hybrid Nanostructures as Highly Active and Stable Bifunctional Catalysts for Water Electrolysis” which was published in ACS Applied Energy Materials in 2018.



This diagram illustrates a robust core-shell structured $\text{Ni}_3\text{Fe}(\text{OH})_9$ LDH/ Ni_3Fe alloy bifunctional electrocatalyst for overall water splitting in alkaline media.

Developing cost-effective, earth-abundant and high-performance bifunctional electrocatalysts for water splitting is the key technological requirement for the hydrogen economy.¹⁻³ In this work, we designed a facile approach for the fabrication of core-shell structured $\text{Ni}_3\text{Fe}(\text{OH})_9/\text{Ni}_3\text{Fe}$ bifunctional electrocatalyst constructed from an electroreductive deposited Ni_3Fe alloy nanosheets and an in-situ transformed $\text{Ni}_3\text{Fe}(\text{OH})_9$ layered double

hydroxide (LDH). This Ni₃Fe(OH)₉/Ni₃Fe hybrid exhibits excellent performance for OER in alkaline electrolytes, in terms of small onset potential (1.46 V vs. RHE), high current densities, low Tafel slope (28 mV/dec) and excellent durability. A low onset potential and high mass anodic peak current density, over 1000 mA cm⁻² mg⁻¹ at 1.57 V vs. RHE, have been achieved for water oxidation on this hybrid electrocatalyst. More importantly, the Ni₃Fe(OH)₉/Ni₃Fe hybrid electrode possesses bifunctional catalytic activity for both water oxidation and hydrogen generation. The Ni₃Fe(OH)₉/Ni₃Fe hybrid exhibits excellent HER performance (comparable to or even surpassing the performance of the state-of-the-art non-precious catalysts) in the same alkaline condition.

Consequently, this freestanding metallic Ni₃Fe nanosheet-framework based NiFe LDH hybrid electrocatalyst can lead to several significant innovations in a water electrolysis system: i) Significantly enhanced sites with greater activity and fast electron transfer ability. ii) Excellent mechanical stability under vigorous gas evolution conditions and electrode integrity.

References

1. C. Xiao, Y. Li, X. Lu and C. Zhao, *Adv. Funct. Mater.* 2016, **26**, 3515-3523.
2. C. Xiao, X. Lu and C. Zhao, *Chem. Commun.* 2014, **50**, 10122-10125.
3. C. Xiao, X. Zhang, S. Li, B. H. Suryanto and D. R. MacFarlane, *ACS Appl. Energy Mater.* 2018, **1**, 986-992.

In Situ Synthesis of Core–Shell-Ni₃Fe(OH)₉/Ni₃Fe Hybrid Nanostructures as Highly Active and Stable Bifunctional Catalysts for Water Electrolysis

Changlong Xiao,[†] Xinyi Zhang,^{*,†} Shuni Li,[‡] Bryan H. R. Suryanto,[†] and Douglas R. MacFarlane^{*,†}

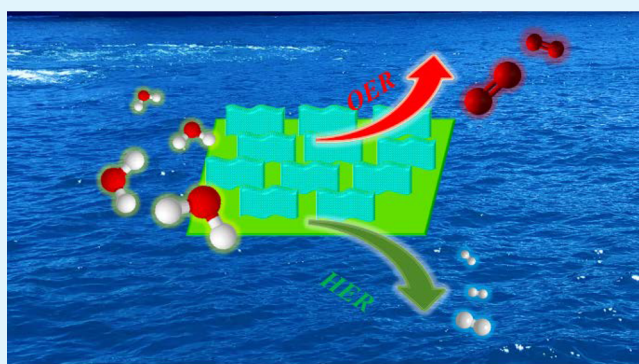
[†]Australian Centre for Electromaterials Science, School of Chemistry, Monash University, Melbourne, Victoria 3800, Australia

[‡]School of Chemistry and Chemical Engineering, Shaanxi Normal University, Xi'an, Shaanxi 710062, China

Supporting Information

ABSTRACT: Development of cost-effective, high-performance electrocatalysts for water splitting is the key technological requirement for the hydrogen economy. Here, we report an in situ transformation approach for the preparation of a core–shell structured bifunctional electrocatalyst composed of a metallic Ni₃Fe nanosheet-framework and a thin layer of Ni₃Fe(OH)₉ shell on various substrates. The Ni₃Fe alloy nanostructured framework provides large electroactive surface area and accelerates the charge transport, while the Ni₃Fe(OH)₉ nanoshell allows an excellent electrochemical accessibility and high catalytic activity. When acting as an anode for the oxygen evolution reaction (OER), the hybrid catalyst is characterized by a low onset potential ($\eta_{\text{onset}} = 230$ mV), small Tafel slope (28 mV/dec), and stable catalytic activity (over 24 h). More importantly, the hybrid can act as an excellent bifunctional catalyst and deliver a current density of 10 mA cm⁻² at a cell voltage of 1.63 V with long stability in a symmetric alkaline electrolyzer for overall water electrolysis.

KEYWORDS: water electrolysis, core–shell structure, NiFe layered double hydroxide, bifunctional electrocatalyst, in situ synthesis



Water splitting represents an environmentally friendly and sustainable solution for large-scale storage of energy from renewable but intermittent sources such as sun and wind.^{1–4} The water-splitting process is composed of the oxygen evolution reaction (OER) and the hydrogen evolution reaction (HER), both involving a multistep proton-coupled electron transfer process.^{5,6} In pursuit of a highly efficient water-splitting system, electrode materials with outstanding catalytic performance are highly desirable for both the anodic OER and cathodic HER. So far, IrO₂/RuO₂ based materials and Pt group metals are the state-of-the-art electrocatalysts for OER and HER, respectively.^{7–9} However, the low abundance and high prices of these precious metals restrict their large-scale application. Earth abundant transition metal based catalysts, including metallic and oxide/hydroxide materials, have been considered as potential candidates to replace expensive metals in water-splitting technology. Particularly, iron group metal (Fe, Co, and Ni) based catalysts have been regarded as plausible alternatives to the precious-metal based materials, owing to their superior activity toward both OER and HER.^{10–15} Among these, NiFe (oxy)hydroxide based alkaline electrocatalysts exhibit extraordinary activity for OER and comparable catalytic behavior for HER, although the actual active center (Ni or Fe) has not been fully explained yet.^{16–19} It has been confirmed that the use of high-surface-area conductive supports and dispersion of active

sites can significantly enhance the electrochemical addressability and accessibility, thus improving the catalytic activity.^{20–27} So far, a variety of techniques and catalyst supports have been found to show superior catalytic activity. Examples include solvothermally prepared NiFe layered double hydroxide on carbon nanotubes,²⁸ Ni₃Fe(OH)₉ electrodeposited on nickel foam,²⁹ Ni–Fe nanosheets on reduced graphene oxide,³⁰ and small NiFe double hydroxide nanoparticles on Vulcan carbon.³¹ In consideration of the good intrinsic conductivity of zerovalent metals, one approach to electrode fabrication is to hybridize an oxide/hydroxide with a metallic phase. It has been demonstrated that the presence of metal in metal oxide materials can dramatically enhance the electrocatalytic activity as well as the stability.^{12,19,33} Nonetheless, there is no facile method to achieve a robust electrocatalyst, which retains its conductivity and delicate nanostructure. The exploration of metallic Fe- and/or Ni-incorporated NiFe(oxy)-hydroxide hybrid materials is a promising strategy.

In this study, we report a core–shell structured Ni₃Fe(OH)₉/Ni₃Fe hybrid material with electroactive NiFe layered double hydroxides (LDHs) on the outer surface and a

Received: February 5, 2018

Accepted: March 5, 2018

Published: March 5, 2018

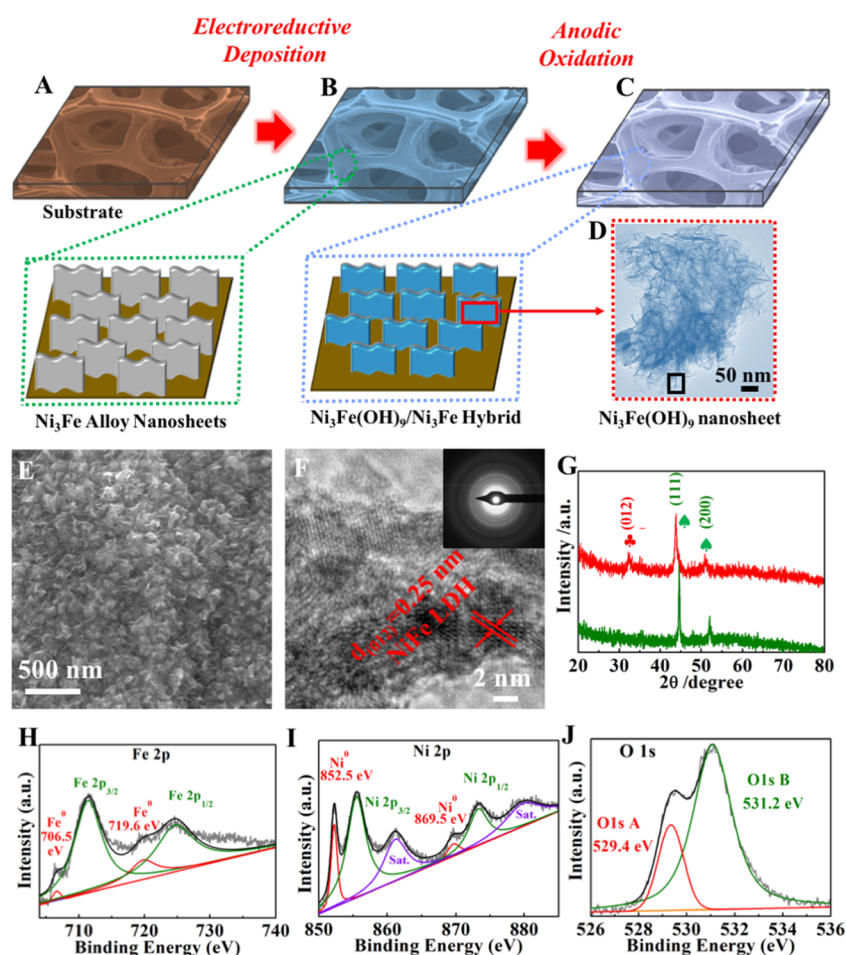


Figure 1. (A–C) Schematic illustration of the fabrication of the core–shell structured $\text{Ni}_3\text{Fe}(\text{OH})_9/\text{Ni}_3\text{Fe}$ hybrid, (D) TEM, (E) SEM, (F) HRTEM images of $\text{Ni}_3\text{Fe}(\text{OH})_9/\text{Ni}_3\text{Fe}$ hybrid, and (G) X-ray diffraction patterns of Ni_3Fe alloy (green) and $\text{Ni}_3\text{Fe}(\text{OH})_9/\text{Ni}_3\text{Fe}$ hybrid (red). XPS spectra of $\text{Ni}_3\text{Fe}(\text{OH})_9/\text{Ni}_3\text{Fe}$ hybrid: (H) high-resolution Fe 2p, (I) high-resolution Ni 2p, and (J) O 1s spectra.

conductive Ni_3Fe nanosheet alloy as the conductive skeleton. The fabrication process is shown in Figure 1A–C, and the details of the procedure are shown in Supporting Information. The doping with 25% Fe is well-known to induce a series of synergistic effects between Fe and Ni.^{28,33} Simultaneously, the coexistence of metallic Ni and Fe can dramatically improve the electrical conductivity and fast charge transfer between the hydroxide layers. Moreover, the shell- $\text{Ni}_3\text{Fe}(\text{OH})_9$ film and core- Ni_3Fe alloy are strongly coupled with each other and tightly attached onto the substrate. As a result, the obtained $\text{Ni}_3\text{Fe}/\text{Ni}_3\text{Fe}(\text{OH})_9$ hybrids exhibit outstanding OER charge delivery capability, low onset potential, and long-term catalytic stability, outperforming many recently reported NiFe LDHs as well as the benchmark $\text{IrO}_2/\text{RuO}_2$ catalysts. In addition, the obtained $\text{Ni}_3\text{Fe}(\text{OH})_9/\text{Ni}_3\text{Fe}$ hybrid is also an excellent cathodic catalyst and shows HER activity comparable to that of the benchmark Pt/C in alkaline media.

The SEM images in Figure S1 reveal that the deposited NiFe alloy consists of relatively uniform crumpled nanosheets with longitudinal orientation and larger functionalized electrode surface area, while single Fe or Ni crystals are usually cracked chunks or irregular particles (Figure S2).^{17,34} After anodic oxidation in alkaline media, the entire NiFe alloy material appears covered with a thin layer of NiFe double hydroxide without altering the original NiFe alloy nanosheet-framework (Figure 1E). Furthermore, TEM images (Figure 1D) illustrate

that an individual nanosheet is very thin and/or transparent with a lateral size around 300 nm. All of the obtained microscopic information indicates that each nanosheet is grown in situ on the support as an intact unit and the adjacent nanosheets are interconnected forming the entire porous NiFe alloy with high surface area. The energy-dispersive X-ray (EDX) spectrum was employed to investigate the elemental distribution of the deposition obtained NiFe alloy. To minimize the background signal from nickel foam, carbon fiber paper (CFP) was used as a substitute substrate. According to the EDX spectrum in Figure S3, both Ni and Fe are homogeneously distributed and cover the entire carbon fiber. Meanwhile, an atomic ratio between Ni and Fe of approximately 3:1 was further quantified by a multipoint EDX spectrum (Figure S4).

The phase and chemical composition were verified by X-ray diffraction (XRD) and X-ray photoelectron spectroscopy (XPS). In Figure 1G, two distinct diffraction peaks can be observed from the as-deposited Ni_3Fe alloy nanosheets, which are assigned to the (111) and (200) facets of the Ni_3Fe alloy, confirming its face-centered cubic (space group $Pm\bar{3}m$) structure. Furthermore, the survey XPS spectrum (Figure S5) also shows the presence of Ni and Fe on the surface of the obtained NiFe alloy nanosheets. Significantly, an atomic Ni/Fe ratio of 3:1 was also identified by the XPS analysis, which is consistent with the XRD and EDX measurements. Figure 1H,I

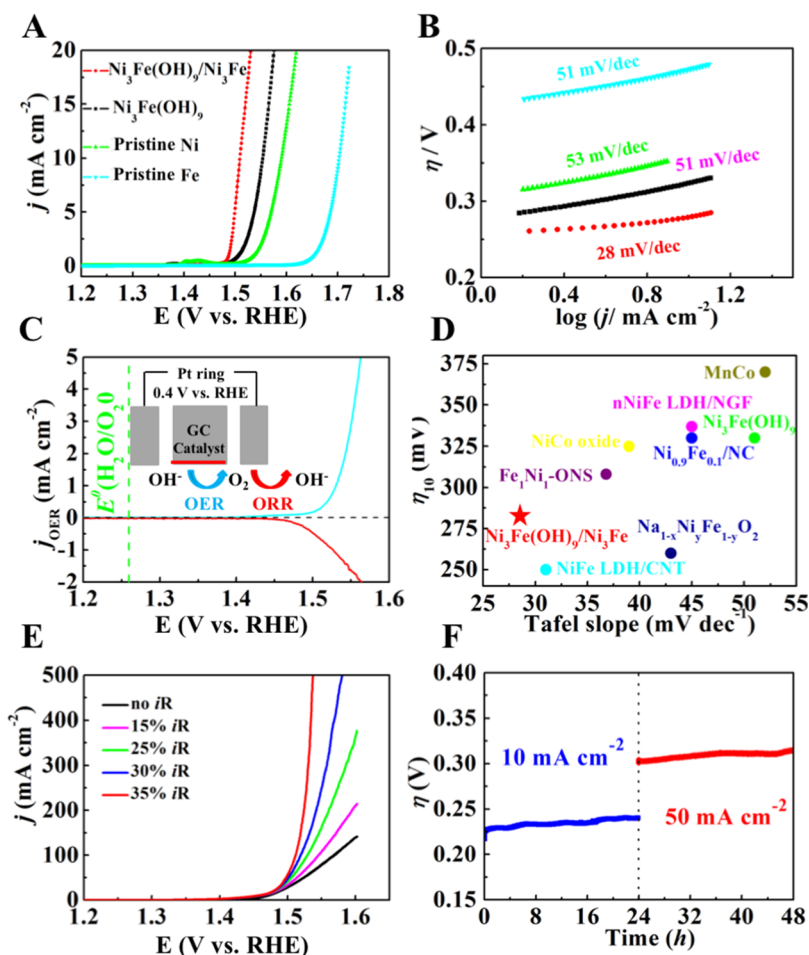


Figure 2. (A) OER polarization curves; (B) corresponding Tafel plots of $\text{Ni}_3\text{Fe}(\text{OH})_9/\text{Ni}_3\text{Fe}/\text{GC}$, $\text{Ni}_3\text{Fe}(\text{OH})_9/\text{GC}$, Ni/GC , and Fe/GC ; (C) RRDE voltammogram obtained from $\text{Ni}_3\text{Fe}(\text{OH})_9/\text{Ni}_3\text{Fe}$ hybrid; (D) comparison of overpotential required at 10 mA cm^{-2} and Tafel slope of $\text{Ni}_3\text{Fe}(\text{OH})_9/\text{Ni}_3\text{Fe}$ with reported high-performance OER electrocatalysts; (E) OER polarization curves with different iR -correction levels; and (F) chronopotentiometric curves at 10 and 50 mA cm^{-2} of $\text{Ni}_3\text{Fe}(\text{OH})_9/\text{Ni}_3\text{Fe}$ /nickel foam.

displays the high-resolution Fe 2p and Ni 2p XPS spectra, which were further deconvoluted into four subpeaks by a Gaussian fitting method. In the Fe 2p XPS spectrum, the binding energy peaks located at 706.5 and 719.6 eV can be indexed to zerovalent Fe (Fe^0). Similarly, the binding energy peaks which appeared at 852.5 and 869.5 eV in the Ni 2p XPS spectrum are ascribed to zerovalent Ni (Ni^0). The XPS results further confirm the metallic chemical nature of the electroreductive deposited Ni_3Fe alloy nanosheets. The energy peaks corresponding to higher valences of Ni and Fe (oxides and/or hydroxides) can also be detected, which may be caused by exposure to air during the synthesis and characterization processes causing surface oxidation.

After anodic oxidation in alkaline media, the original Ni_3Fe alloy nanosheets show decreased peak intensity along with the appearance of a new diffraction peak at a lower angle on the XRD pattern, in good agreement with the (012) crystal-plane of NiFe LDH.³³ This suggests the transformation of the top layer of the Ni_3Fe alloy to $\text{Ni}_3\text{Fe}(\text{OH})_9$, forming a core-shell structured $\text{Ni}_3\text{Fe}/\text{Ni}_3\text{Fe}(\text{OH})_9$ hybrid. Noticeably, a slight negative shift of 2θ angles can also be observed for the original Ni_3Fe alloy, indicating a change in the d -spacing of the plane when the topmost Ni_3Fe alloy has been converted to $\text{Ni}_3\text{Fe}(\text{OH})_9$ film.⁹ This also implies that the formed $\text{Ni}_3\text{Fe}(\text{OH})_9$ shell is tightly attached to the Ni_3Fe alloy nanosheets,

while inducing a certain strain into the crystal structure of the Ni_3Fe alloy nanosheets. From the HRTEM image (Figure 1F) of the region indicated in Figure 1D, lattice fringes with interplanar spacing of 0.25 nm can be observed, which correspond well to the (012) plane of NiFe LDH. A set of cricoid diffraction rings can also be detected in the SAED, corresponding well to the observed lattice fringes (inset of Figure 1F). Moreover, XPS analysis was further performed to probe the changes in chemical valence states of the $\text{Ni}_3\text{Fe}(\text{OH})_9/\text{Ni}_3\text{Fe}$ hybrid. In Figure S6A,B, both Fe^0 and Ni^0 can still be detected, while the relative binding peaks show a significant decrease in peak intensity, revealing the coverage of a thin layer of shell structured $\text{Ni}_3\text{Fe}(\text{OH})_9$. The deconvoluted O 1s spectrum in Figure 1J demonstrates the presence of two kinds of oxygen groups. The peak fitted at 529.4 eV represents the oxygen-metal bonds (O A), while the peak located at 531.2 eV is assigned to the hydroxyl groups (O B).^{35–32} After the anodic oxidation treatment, O B becomes the predominant oxygen species, while the intensity of O A is dramatically lowered, revealing that the outermost surface of the Ni_3Fe alloy has been locally oxidized. (Figure 1J vs Figure S6C).

The electrocatalytic OER performance of the $\text{Ni}_3\text{Fe}(\text{OH})_9/\text{Ni}_3\text{Fe}$ hybrid was first investigated on a glassy-carbon (GC) electrode in alkaline solution (1 M) in a standard three-electrode system. The OER polarization curves were measured

at a scan rate of 5 mV/s, and the data were recorded without iR -correction. To demonstrate the advantages of the thin core-shell structure, recently reported state-of-the-art $\text{Ni}_3\text{Fe}(\text{OH})_9$ nanosheets²⁹ were also synthesized and investigated for comparison. The OER polarization curves obtained from the $\text{Ni}_3\text{Fe}(\text{OH})_9/\text{Ni}_3\text{Fe}$ hybrid, the $\text{Ni}_3\text{Fe}(\text{OH})_9$, and the GC electrodes electrodeposited with Ni (Ni/GC) or Fe (Fe/GC) individually are presented in Figure 2A. The $\text{Ni}_3\text{Fe}(\text{OH})_9/\text{Ni}_3\text{Fe}$ hybrid exhibits remarkable OER activity with an early onset potential of 1.46 V versus RHE, corresponding to an overpotential (η_{onset}) of 230 mV, which is determined by the concomitantly augmented oxygen reduction current obtained from a rotating ring disc electrode (RRDE, Figure 2C). However, both pristine Ni/GC ($\eta_{\text{onset}} = 290$ mV) and Fe/GC ($\eta_{\text{onset}} = 420$ mV) show inferior OER behavior, revealing the outstanding OER catalytic activity of the outer-shell- $\text{Ni}_3\text{Fe}(\text{OH})_9$ film owing to the interaction effect between Ni and Fe in the LDH structure. In comparison, the OER onset of the $\text{Ni}_3\text{Fe}(\text{OH})_9/\text{Ni}_3\text{Fe}$ hybrid is even 50 mV smaller than that of the state-of-the-art $\text{Ni}_3\text{Fe}(\text{OH})_9$ ($\eta = 280$ mV), suggesting its rapid OER response and electrode kinetics. The $\text{Ni}_3\text{Fe}(\text{OH})_9/\text{Ni}_3\text{Fe}$ hybrid also exhibits outstanding charge transfer ability, with a current density of 10 mA cm^{-2} obtained at an overpotential (η_{10}) = 280 mV. This high OER catalytic rate also surpasses those of directly deposited $\text{Ni}_3\text{Fe}(\text{OH})_9$ ($\eta_{10} = 330$ mV) and benchmark catalysts including 20% Ir/C ($\eta_{10} = 380$ mV) and Ru/C ($\eta_{10} = 390$ mV) measured under the same experimental conditions.¹⁹

The high OER rate and fast reaction kinetics of the $\text{Ni}_3\text{Fe}(\text{OH})_9/\text{Ni}_3\text{Fe}$ hybrid can be attributed to its unique thin core/shell structure. The outermost $\text{Ni}_3\text{Fe}(\text{OH})_9$ shell is fabricated by in situ transformation of the as-deposited Ni_3Fe alloy via the anodic polarization process in an alkaline environment. In this case, the formed shell- $\text{Ni}_3\text{Fe}(\text{OH})_9$ is strongly associated with the core- Ni_3Fe alloy nanosheet support and maintains excellent mechanical stability under vigorous gas evolution conditions and electrode integrity for long-term catalytic activity. Moreover, the shell- $\text{Ni}_3\text{Fe}(\text{OH})_9$ allows for a large number of active sites to be electrochemically accessible and has a prominent affinity for OH^- electroadsorption to the exposed OER active sites, which is recognized as the rate-limiting step.²⁸ This can be confirmed by its higher specific current density normalized by catalyst loading (500 mA cm^{-2} g^{-1} at 1.54 V, Figure S7) compared to those of NiFe CNT (1.55 V)¹⁹ and $\text{Ni}_{0.9}\text{Fe}_{0.1}/\text{NC}$ (1.57 V),²⁸ indicating that the excellent OER performance resulted from increased active sites rather than increased catalyst loading. Meanwhile, the interior metallic core- Ni_3Fe remains highly conductive, allowing fast charge transport to the outermost OER active sites. The Tafel plots derived from OER polarization curves were further constructed to analyze the reaction kinetics (Figure 2B). The $\text{Ni}_3\text{Fe}(\text{OH})_9/\text{Ni}_3\text{Fe}$ hybrid exhibits an extremely small Tafel slope of 28 mV/dec, smaller than those of Fe/GC (51 mV/dec), Ni/GC (53 mV/dec), $\text{Ni}_3\text{Fe}(\text{OH})_9$ (50 mV/dec), benchmark Ir/C (50 mV/dec), and even the state-of-the-art NiFe CNTs on a GC electrode (31 mV/dec).²⁸ The three-dimensional $\text{Ni}_3\text{Fe}(\text{OH})_9/\text{Ni}_3\text{Fe}$ hybrid structure is composed of metallic core and extremely thin NiFe LDH and provides a higher number of three-phase boundary reactive sites and facilitates very efficient mass and electron transport. As a result, its advanced OER catalysis process surpasses a majority of the reported high-performance electrocatalysts (Figure 2D and Table S1).^{19,25,27–29,37–41}

The fast electron transfer ability and fast reaction kinetics were further verified with the electrochemical impedance spectra (EIS) measurement (Figure S8). The Nyquist plot (Figure S8A) reveals that the $\text{Ni}_3\text{Fe}(\text{OH})_9/\text{Ni}_3\text{Fe}$ hybrid possessed a smaller electron transfer resistance than that of $\text{Ni}_3\text{Fe}(\text{OH})_9$ during the electrochemical reaction. In the magnified plots in Figure S8B, the intersection at the Z' -axis stands for the equivalent series resistance (ESR). Benefiting from the highly conductive core- Ni_3Fe alloy nanosheets, the ESR of the $\text{Ni}_3\text{Fe}(\text{OH})_9/\text{Ni}_3\text{Fe}$ hybrid ($\sim 2.0 \Omega$) is smaller than that of the $\text{Ni}_3\text{Fe}(\text{OH})_9$ (5.3 Ω), further illustrating its excellent charge transfer capability. Furthermore, the Faradaic efficiency was calculated to be $98.3 \pm 1.1\%$ using the RRDE by comparing the oxygen detected on the Pt ring with the theoretical value based on the total charge consumed on the GC disc, confirming that oxygen is the only anodic product during the water electrolysis process (Figure S9).

In consideration of substantial effects of the catalyst support (conductivity, porosity) on performance, the $\text{Ni}_3\text{Fe}(\text{OH})_9/\text{Ni}_3\text{Fe}$ hybrid was also deposited on nickel foam, which is well-known as an electron collector. To avoid current overflow and curve distortion, iR -compensation was gradually added, and 35% iR -correction is an optimal compensation level to achieve the best curve shape. As shown in Figure 2E, all OER polarization curves at different levels of iR -compensation (0 to 35%) display the same onset potential (around 1.46 V), which is consistent with the above results. With addition of a 35% iR -compensation, $\text{Ni}_3\text{Fe}(\text{OH})_9/\text{Ni}_3\text{Fe}$ /nickel foam exhibits fast reaction kinetics with currents density of 10 mA cm^{-2} or 10 A g^{-1} being achieved with only $\eta_{10}^a = 228$ mV and $\eta_{\text{m}10}^a = 210$ mV, respectively, surpassing the characteristics of state-of-the-art NiFe/CNTs ($\eta_{10}^a = 228$ mV, $\eta_{\text{m}10}^a = 247$ mV, 95% iR -compensation).²⁸ Moreover, the $\text{Ni}_3\text{Fe}(\text{OH})_9/\text{Ni}_3\text{Fe}$ hybrid also shows an outstandingly high OER rate with 500 mA cm^{-2} (793 A g^{-1}) at $\eta_{500}^a = 308$ mV, surpassing that of the previous reported NiFe/ NiCo_2O_4 /nickel foam ($\eta_{500}^a = 320$ mV, 65% iR -compensation).¹⁰ The calculated TOF associated with $\text{Ni}_3\text{Fe}(\text{OH})_9/\text{Ni}_3\text{Fe}$ /nickel foam is 0.083 s^{-1} , which is more than 3-fold higher than that of the benchmark IrO_2 (0.027 s^{-1}). Collectively, the fast reaction kinetics and excellent charge delivery ability makes the $\text{Ni}_3\text{Fe}(\text{OH})_9/\text{Ni}_3\text{Fe}$ /nickel foam electrode suitable for industrial application. Furthermore, long-term catalytic stability was investigated at constant current densities of 10 and 50 mA cm^{-2} , and the potential can be maintained at $\eta = 240$ mV and $\eta = 310$ mV for at least 24 h (Figure 2F).

The development of bifunctional electrode materials possessing catalytic activity for both OER and HER can simplify the manufacturing processes in assembling electrolysis devices, which is critical for economical application. The cathodic HER usually suffers from more sluggish kinetics in alkaline media than under acidic conditions. Importantly, the obtained Ni_3Fe composite electrode also exhibits a high catalytic activity for HER in the same basic electrolyte. As shown in Figure 3A, pristine Ni/GC shows an earlier HER onset ($\eta_{\text{onset}} = 150$ mV), but a larger Tafel slope (172 mV/dec), than those of Fe/GC ($\eta_{\text{onset}} = 310$ mV, 96 mV/dec). With 25% Fe incorporation, the as-deposited Ni_3Fe composites exhibit both smaller onset potential ($\eta_{\text{onset}} = 120$ mV) and Tafel slope (83 mV/dec, Figure 3B) by taking advantage of the synergistic effect between Ni and Fe. Moreover, an overpotential of only 217 mV ($\eta_{10} = 217$ mV) is required to reach a current density of 10 mA cm^{-2} , signifying the favorable kinetics for the HER on

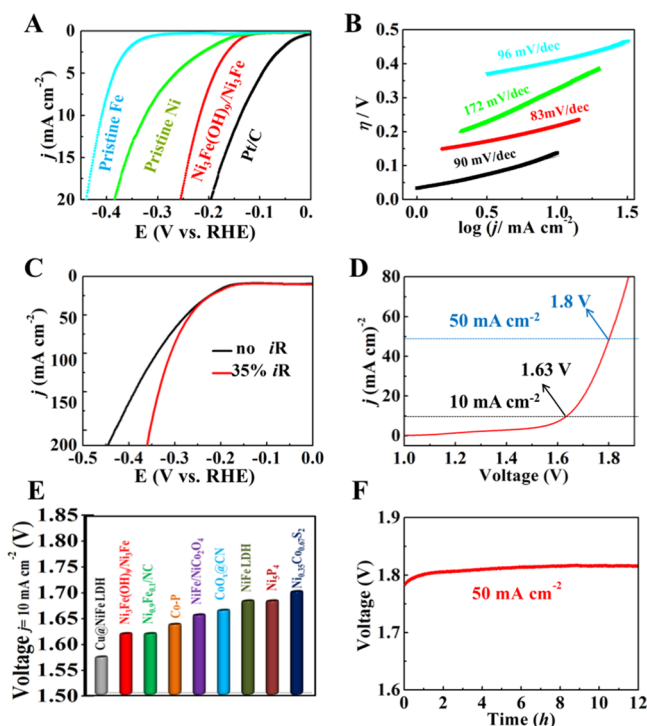


Figure 3. (A) HER polarization curves; (B) corresponding Tafel plots of $\text{Ni}_3\text{Fe}(\text{OH})_9/\text{Ni}_3\text{Fe}/\text{GC}$, Pt/C , Ni/GC , and Fe/GC ; (C) HER polarization curves without and with 35% iR -compensation of $\text{Ni}_3\text{Fe}(\text{OH})_9/\text{Ni}_3\text{Fe}/\text{nickel foam}$; (D) polarization curve for whole cell water electrolysis with $\text{Ni}_3\text{Fe}(\text{OH})_9/\text{Ni}_3\text{Fe}$ hybrid as both anode and cathode; (E) comparison of required cell voltage at $j = 10 \text{ mA cm}^{-2}$ of $\text{Ni}_3\text{Fe}(\text{OH})_9/\text{Ni}_3\text{Fe}$ hybrid with other reported bifunctional catalysts; and (F) chronopotentiometric curves at constant current density of 50 mA cm^{-2} in a symmetric water electrolysis electrolyzer.

the as-deposited Ni_3Fe composites. These excellent HER performances of Ni_3Fe composites in basic electrolyte are better than those of previous reported $\text{Ni}_{0.9}\text{Fe}_{0.1}/\text{NC}$,¹⁹ MnNi/C ,⁴² MoB ,⁴³ and $\text{CoOx}@/\text{CN}$,²⁶ comparable to that of the benchmark Pt/C catalysts (more details are in Table S2). The $\text{Ni}_3\text{Fe}/\text{nickel foam}$ was further used to evaluate the catalytic activity and mechanical stability under high current densities and vigorous gas evolution for practical application (Figure 3C). It is noteworthy that a high HER current density of 200 mA cm^{-2} can be achieved at $\eta_{200} = 355 \text{ mV}$ with 35% iR -compensation. Long-term HER stability was assessed by chronopotentiometric test under constant current densities of 50 mA cm^{-2} for over 12 h of bulk electrolysis (Figure S10), suggesting robustness in the cathodic HER process.

Owing to the outstanding dual functionality, a symmetric alkaline electrolyzer was constructed employing the $\text{Ni}_3\text{Fe}(\text{OH})_9/\text{Ni}_3\text{Fe}$ hybrid and Ni_3Fe composites as anode and cathode, respectively. Figure 3D shows that this electrolyzer only requires a small cell voltage of $\sim 1.5 \text{ V}$ to initiate the water electrolysis and a cell voltage of 1.63 V , corresponding to a combined overpotential of 400 mV , to reach an overall current density of 10 mA cm^{-2} , which surpasses a majority of reported high-performance bifunctional electrocatalysts (Figure 3E, Table S3).^{10,19,26,33,44–48} The calculated electrical-to-fuel efficiency is 75%. This superior performance can rival those of the majority of reported asymmetric and symmetric bifunctional water-splitting electrocatalysts. In addition, the electrolysis current density can remain at 50 mA cm^{-2} at

around 1.8 V during a 12 h vigorous water-splitting test (Figure 3F), and no apparent morphology change can be observed (Figure S11), indicating its outstanding long-term catalytic and mechanical stability.

In conclusion, free-standing Ni_3Fe alloy nanosheets have been fabricated through a facile electroreductive deposition method, and then, the outermost layer has been in situ transformed to $\text{Ni}_3\text{Fe}(\text{OH})_9$ through anodic oxidation in alkaline media, forming a core-shell structured $\text{Ni}_3\text{Fe}(\text{OH})_9/\text{Ni}_3\text{Fe}$ hybrid. The core- Ni_3Fe alloy nanosheets are interconnected and highly conductive, facilitating fast electron transfer to the outer electrode surface. The thin layer of $\text{Ni}_3\text{Fe}(\text{OH})_9$ -shell offers significant enhancement in accessible active sites and fast electroadsorption for overall water splitting. Benefiting from the existing synergistic effects between Ni and Fe, the fabricated core-shell structured $\text{Ni}_3\text{Fe}(\text{OH})_9/\text{Ni}_3\text{Fe}$ hybrid shows excellent catalytic activity and stability toward OER and HER. Finally, an alkaline symmetric electrolyzer has been constructed with this bifunctional electrocatalyst and exhibits efficient whole cell water splitting and long-term stability. These hybrid electrode materials represent a significant step toward the practical application of water splitting.

■ ASSOCIATED CONTENT

Supporting Information

The Supporting Information is available free of charge on the ACS Publications website at DOI: 10.1021/acsaem.8b00172.

Materials and synthesis; XRD details; SEM and TEM images; EDX spectra; XPS measurement; and electrochemical analysis data (PDF)

■ AUTHOR INFORMATION

Corresponding Authors

[Redacted]

ORCID

Changlong Xiao: 0000-0001-5699-9018

Xinyi Zhang: 0000-0003-4695-3731

Shuni Li: 0000-0002-6614-9241

Bryan H. R. Suryanto: 0000-0001-9759-6362

Notes

The authors declare no competing financial interest.

■ ACKNOWLEDGMENTS

The study was supported by the ARC Discovery Grant (DP170102267) and the Australian Laureate Fellowship programs. The authors acknowledge the use of the facilities at the Monash Centre for Electron Microscopy.

■ REFERENCES

- (1) Zhu, Y. P.; Ma, T. Y.; Jaroniec, M.; Qiao, S. Z. Self-Templating Synthesis of Hollow Co_3O_4 Microtube Arrays for Highly Efficient Water Electrolysis. *Angew. Chem., Int. Ed.* **2017**, *56*, 1324–1328.
- (2) Chen, P.; Zhou, T.; Zhang, M.; Tong, Y.; Zhong, C.; Zhang, N.; Zhang, L.; Wu, C.; Xie, Y. 3D Nitrogen-Anion-Decorated Nickel Sulfides for Highly Efficient Overall Water Splitting. *Adv. Mater.* **2017**, *29*, 1701584.
- (3) Turner, J. A. Sustainable Hydrogen Production. *Science* **2004**, *305*, 972–974.

- (4) Montoya, J. H.; Seitz, L. C.; Chakthranont, P.; Vojvodic, A.; Jaramillo, T. F.; Nørskov, J. K. Materials for Solar Fuels and Chemicals. *Nat. Mater.* **2017**, *16*, 70–81.
- (5) Jiao, Y.; Zheng, Y.; Jaroniec, M.; Qiao, S. Z. Design of Electrocatalysts for Oxygen-and hydrogen-involving Energy Conversion Reactions. *Chem. Soc. Rev.* **2015**, *44*, 2060–2086.
- (6) Feng, J. X.; Xu, H.; Ye, S. H.; Ouyang, G.; Tong, Y. X.; Li, G. R. Silica-Polypyrrole Hybrids as High-Performance Metal-Free Electrocatalysts for Hydrogen Evolution Reaction in Neutral Media. *Angew. Chem., Int. Ed.* **2017**, *56*, 8120–8124.
- (7) Kuo, D. Y.; Kawasaki, J. K.; Nelson, J. N.; Kloppenburg, J.; Hautier, G.; Shen, K. M.; Schlom, D. G.; Suntivich, J. Influence of Surface Adsorption on the Oxygen Evolution Reaction on IrO₂ (110). *J. Am. Chem. Soc.* **2017**, *139*, 3473–3479.
- (8) McCrory, C. C.; Jung, S.; Ferrer, I. M.; Chatman, S. M.; Peters, J. C.; Jaramillo, T. F. Benchmarking Hydrogen Evolving Reaction and Oxygen Evolving Reaction Electrocatalysts for Solar Water Splitting Devices. *J. Am. Chem. Soc.* **2015**, *137*, 4347–4357.
- (9) Greeley, J.; Jaramillo, T. F.; Bonde, J.; Chorkendorff, I.; Nørskov, J. K. Computational High-throughput Screening of Electrocatalytic Materials for Hydrogen Evolution. *Nat. Mater.* **2006**, *5*, 909–913.
- (10) Xiao, C.; Li, Y.; Lu, X.; Zhao, C. Bifunctional Porous NiFe/NiCo₂O₄/Ni foam Electrodes with Triple Hierarchy and Double Synergies for Efficient Whole Cell Water Splitting. *Adv. Funct. Mater.* **2016**, *26*, 3515–3523.
- (11) Guan, C.; Liu, X.; Ren, W.; Li, X.; Cheng, C.; Wang, J. Rational Design of Metal-Organic Framework Derived Hollow NiCo₂O₄ Arrays for Flexible Supercapacitor and Electrocatalysis. *Adv. Energy Mater.* **2017**, *7*, 1602391.
- (12) Liu, W.; Du, K.; Liu, L.; Zhang, J.; Zhu, Z.; Shao, Y.; Li, M. One-step Electroreductively Deposited Iron-cobalt Composite Films as Efficient Bifunctional Electrocatalysts for Overall Water Splitting. *Nano Energy* **2017**, *38*, 576–584.
- (13) Wang, L.; Gu, C.; Ge, X.; Zhang, J.; Zhu, H.; Tu, J. Anchoring Ni₂P Sheets on NiCo₂O₄ Nanocone Arrays as Optimized Bifunctional Electrocatalyst for Water Splitting. *Adv. Mater. Interfaces* **2017**, *4*, 1700481.
- (14) Stevens, M. B.; Trang, C. D.; Enman, L. J.; Deng, J.; Boettcher, S. W. Reactive Fe-sites in Ni/Fe(oxy) Hydroxide are Responsible for Exceptional Oxygen Electrocatalysis Activity. *J. Am. Chem. Soc.* **2017**, *139*, 11361–11364.
- (15) Feng, J. X.; Wu, J. Q.; Tong, Y. X.; Li, G. R. Efficient Hydrogen Evolution on Cu Nanodots-Decorated Ni₃S₂ Nanotubes by Optimizing Atomic Hydrogen Adsorption and Desorption. *J. Am. Chem. Soc.* **2018**, *140*, 610–617.
- (16) Trotochaud, L.; Young, S. L.; Ranney, J. K.; Boettcher, S. W. Nickel-iron Oxyhydroxide Oxygen-evolution Electrocatalysts: The Role of Intentional and Incidental Iron Incorporation. *J. Am. Chem. Soc.* **2014**, *136*, 6744–6753.
- (17) Friebel, D.; Louie, M. W.; Bajdich, M.; Sanwald, K. E.; Cai, Y.; Wise, A. M.; Cheng, M. J.; Sokaras, D.; Weng, T. C.; Alonso-Mori, R.; et al. Identification of Highly Active Fe Sites in (Ni, Fe)OOH for Electrocatalytic Water Splitting. *J. Am. Chem. Soc.* **2015**, *137*, 1305–1313.
- (18) Lu, Z.; Xu, W.; Zhu, W.; Yang, Q.; Lei, X.; Liu, J.; Li, Y.; Sun, X.; Duan, X. Three-dimensional NiFe Layered Double Hydroxide Film for High-efficiency Oxygen Evolution Reaction. *Chem. Commun.* **2014**, *50*, 6479–6482.
- (19) Zhang, X.; Xu, H.; Li, X.; Li, Y.; Yang, T.; Liang, Y. Facile Synthesis of Nickel-iron/Nanocarbon Hybrids as Advanced Electrocatalysts for Efficient Water Splitting. *ACS Catal.* **2016**, *6*, 580–588.
- (20) Görlin, M.; Ferreira de Araújo, J.; Schmies, H.; Bernsmeier, D.; Drespr, S. r.; Glich, M.; Jusys, Z.; Chernev, P.; Kraehnert, R.; Dau, H.; Strasser, P. Tracking Catalyst Redox States and Reaction Dynamics in Ni-Fe Oxyhydroxide Oxygen Evolution Reaction Electrocatalysts: The Role of Catalyst Support and Electrolyte pH. *J. Am. Chem. Soc.* **2017**, *139*, 2070–2082.
- (21) Xiao, C.; Li, S.; Zhang, X.; MacFarlane, D. R. MnO₂/MnCo₂O₄/Ni Heterostructure with Quadruple Hierarchy: A Bifunctional Electrode Architecture for Overall Urea Oxidation. *J. Mater. Chem. A* **2017**, *5*, 7825–7832.
- (22) Gong, M.; Zhou, W.; Tsai, M. C.; Zhou, J.; Guan, M.; Lin, M. C.; Zhang, B.; Hu, Y.; Wang, D. Y.; Yang, J.; et al. Nanoscale Nickel Oxide/Nickel Heterostructures for Active Hydrogen Evolution Electrocatalysis. *Nat. Commun.* **2014**, *5*, 4695.
- (23) Xiao, C.; Zhang, X.; Mendes, T.; Knowles, G. P.; Chaffee, A.; MacFarlane, D. R. Highly Ordered Hierarchical Mesoporous MnCo₂O₄ with Cubic *Ia3d* Symmetry for Electrochemical Energy Storage. *J. Phys. Chem. C* **2016**, *120*, 23976–23983.
- (24) Hou, Y.; Lohe, M. R.; Zhang, J.; Liu, S.; Zhuang, X.; Feng, X. Vertically Oriented Cobalt Selenide/NiFe Layered-double-hydroxide Nanosheets Supported on Exfoliated Graphene Foil: An Efficient 3D Electrode for Overall Water Splitting. *Energy Environ. Sci.* **2016**, *9*, 478–483.
- (25) Tang, C.; Wang, H. S.; Wang, H. F.; Zhang, Q.; Tian, G. L.; Nie, J. Q.; Wei, F. Spatially Confined Hybridization of Nanometer-Sized NiFe Hydroxides into Nitrogen-Doped Graphene Frameworks Leading to Superior Oxygen Evolution Reactivity. *Adv. Mater.* **2015**, *27*, 4516–4522.
- (26) Jin, H.; Wang, J.; Su, D.; Wei, Z.; Pang, Z.; Wang, Y. In situ Cobalt-Cobalt Oxide/N-doped Carbon Hybrids as Superior Bifunctional Electrocatalysts for Hydrogen and Oxygen Evolution. *J. Am. Chem. Soc.* **2015**, *137*, 2688–2694.
- (27) Ren, J.; Antonietti, M.; Fellingner, T. P. Efficient Water Splitting Using a Simple Ni/N/C Paper Electrocatalyst. *Adv. Energy Mater.* **2015**, *5*, 1401660.
- (28) Gong, M.; Li, Y.; Wang, H.; Liang, Y.; Wu, J. Z.; Zhou, J.; Wang, J.; Regier, T.; Wei, F.; Dai, H. An advanced Ni-Fe Layered Double Hydroxide Electrocatalyst for Water Oxidation. *J. Am. Chem. Soc.* **2013**, *135*, 8452–8455.
- (29) Lu, X.; Zhao, C. Electrodeposition of Hierarchically Structured Three-dimensional Nickel-iron Electrodes for Efficient Oxygen Evolution at High Current Densities. *Nat. Commun.* **2015**, *6*, 6616.
- (30) Ma, W.; Ma, R.; Wang, C.; Liang, J.; Liu, X.; Zhou, K.; Sasaki, T. A Superlattice of Alternately Stacked Ni-Fe Hydroxide Nanosheets and Graphene for Efficient Splitting of Water. *ACS Nano* **2015**, *9*, 1977–1984.
- (31) Qiu, Y.; Xin, L.; Li, W. Electrocatalytic Oxygen Evolution Over Supported Small Amorphous Ni-Fe Nanoparticles in Alkaline Electrolyte. *Langmuir* **2014**, *30*, 7893–7901.
- (32) Luo, Y.; Zhou, H.; Sun, J.; Qin, F.; Yu, F.; Bao, J.; Yu, Y.; Chen, S.; Ren, Z. Nanowires Shelled with NiFe Layered Double Hydroxide Nanosheets as Bifunctional Electrocatalysts for Overall Water Splitting. *Energy Environ. Sci.* **2017**, *10*, 1820–1827.
- (33) Zhao, S.; Wang, Y.; Dong, J.; He, C. T.; Yin, H.; An, P.; Zhao, K.; Zhang, X.; Gao, C.; Zhang, L.; et al. Ultrathin Metal-organic Framework Nanosheets for Electrocatalytic Oxygen Evolution. *Nat. Energy* **2016**, *1*, 16184.
- (34) Smith, R. D.; Prévot, M. S.; Fagan, R. D.; Zhang, Z.; Sedach, P. A.; Siu, M. K. J.; Trudel, S.; Berlinguette, C. P. Photochemical Route for Accessing Amorphous Metal Oxide Materials for Water Oxidation Catalysis. *Science* **2013**, *340*, 60.
- (35) Liang, J.; Fan, Z.; Chen, S.; Ding, S.; Yang, G. Hierarchical NiCo₂O₄ Nanosheets@Halloysite Nanotubes with Ultrahigh Capacitance and Long Cycle Stability as Electrochemical Pseudocapacitor Materials. *Chem. Mater.* **2014**, *26*, 4354–4360.
- (36) Lee, D. U.; Kim, B. J.; Chen, Z. One-pot Synthesis of A Mesoporous NiCo₂O₄ Nanoplatelet and Graphene Hybrid and Its Oxygen Reduction and Evolution Activities as An Efficient Bifunctional Electrocatalyst. *J. Mater. Chem. A* **2013**, *1*, 4754–4762.
- (37) Yang, Y.; Fei, H.; Ruan, G.; Xiang, C.; Tour, J. M. Efficient Electrocatalytic Oxygen Evolution on Amorphous Nickel-cobalt Binary Oxide Nanoporous Layers. *ACS Nano* **2014**, *8*, 9518–9523.
- (38) Guan, B. Y.; Yu, L.; Lou, X. W. D. General Synthesis of Multishell Mixed-Metal Oxyphosphide Particles with Enhanced Electrocatalytic Activity in the Oxygen Evolution Reaction. *Angew. Chem., Int. Ed.* **2017**, *56*, 2386–2389.

(39) Weng, B.; Xu, F.; Wang, C.; Meng, W.; Grice, C. R.; Yan, Y. A Layered $\text{Na}_{1-x}\text{Ni}_y\text{Fe}_{1-y}\text{O}_2$ Double Oxide Oxygen Evolution Reaction Electrocatalyst for Highly Efficient Water-splitting. *Energy Environ. Sci.* **2017**, *10*, 121–128.

(40) Zhuang, L.; Ge, L.; Yang, Y.; Li, M.; Jia, Y.; Yao, X.; Zhu, Z. Ultrathin Iron-Cobalt Oxide Nanosheets with Abundant Oxygen Vacancies for the Oxygen Evolution Reaction. *Adv. Mater.* **2017**, *29*, 1606793.

(41) Feng, J. X.; Xu, H.; Dong, Y. T.; Ye, S. H.; Tong, Y. X.; Li, G. R. FeOOH/Co/FeOOH Hybrid Nanotube Arrays as High-Performance Electrocatalysts for the Oxygen Evolution Reaction. *Angew. Chem., Int. Ed.* **2016**, *55*, 3694–3698.

(42) Ledendecker, M.; Clavel, G.; Antonietti, M.; Shalom, M. Highly Porous Materials as Tunable Electrocatalysts for The Hydrogen and Oxygen Evolution Reaction. *Adv. Funct. Mater.* **2015**, *25*, 393–399.

(43) Vrubel, H.; Hu, X. Molybdenum Boride and Carbide Catalyze Hydrogen Evolution in Both Acidic and Basic Solutions. *Angew. Chem.* **2012**, *124*, 12875–12878.

(44) Jiang, N.; You, B.; Sheng, M.; Sun, Y. Electrodeposited Cobalt-Phosphorous-Derived Films as Competent Bifunctional Catalysts for Overall Water Splitting. *Angew. Chem.* **2015**, *127*, 6349–6352.

(45) Luo, J.; Im, J. H.; Mayer, M. T.; Schreier, M.; Nazeeruddin, M. K.; Park, N. G.; Tilley, S. D.; Fan, H. J.; Grätzel, M. Water photolysis at 12.3% Efficiency via Perovskite Photovoltaics and Earth-abundant Catalysts. *Science* **2014**, *345*, 1593–1596.

(46) Ledendecker, M.; Krick Calderón, S.; Papp, C.; Steinrück, H. P.; Antonietti, M.; Shalom, M. The Synthesis of Nanostructured Ni_3P_4 Films and their Use as a Non-Noble Bifunctional Electrocatalyst for Full Water Splitting. *Angew. Chem.* **2015**, *127*, 12538–12542.

(47) Peng, Z.; Jia, D.; Al-Enizi, A. M.; Elzatahry, A. A.; Zheng, G. From Water Oxidation to Reduction: Homologous Ni-Co Based Nanowires as Complementary Water Splitting Electrocatalysts. *Adv. Energy Mater.* **2015**, *5*, 1402031.

(48) Yan, X.; Tian, L.; Li, K.; Atkins, S.; Zhao, H.; Murowchick, J.; Liu, L.; Chen, X. $\text{FeNi}_3/\text{NiFeO}_x$ Nanohybrids as Highly Efficient Bifunctional Electrocatalysts for Overall Water Splitting. *Adv. Mater. Interfaces* **2016**, *3*, 1600368.

Experimental Section

Preparation of Ni₃Fe/Ni₃Fe(OH)₉ hybrid electrocatalysts:

Ni₃Fe alloy nanosheets were fabricated onto various substrates including glassy carbon (GC) electrode, nickel foam and carbon fiber paper (CFP) via an electroreductive deposition method. Prior to the electrodeposition, the GC electrode was polished with an aqueous alumina slurry (0.05 μm) on a micro cloth polishing pad, rinsed sequentially with deionized H₂O and acetone, then dried with low-lint tissue. Nickel foam (thickness 1.6 mm, bulk density 0.45 g/cm³) was sonicated sequentially in 0.6 M HCl, deionized H₂O and absolute ethanol for 20 min each to remove the surface NiO_x layer, then dried under a pure N₂ flow at room temperature. CFP was calcined in air at 700 °C for 5 min to generate oxygen-containing functional groups to give a hydrophilic surface. The electroreductive deposition was carried out in a standard three-electrode electrochemical cell containing either pre-treated GC, nickel foam or CFP as the working electrode, a Ag/AgCl (saturated) reference electrode and a Pt wire auxiliary electrode. The electrolyte bath contained equal amounts (5 mM) of FeSO₄ and NiSO₄ in 0.1 M CH₃COONa aqueous solution. The pH of the deposition solution was adjusted to 5 with acetic acid. The electroreductive deposition was performed at -1.2 V vs. Ag/AgCl (saturated) with 80% *i*R compensation for 30 min. After the constant potential deposition, the substrate was withdrawn from the electrolyte, thoroughly rinsed with deionized H₂O and left to dry in air. After electroreductive deposition, an evenly distributed film with metallic luster can be observed, implying the metallic properties of the obtained Ni₃Fe composites. Afterwards, a thin Ni₃Fe(OH)₉ film was obtained by local transformation

of the outermost layer of the Ni₃Fe alloy nanosheet through cycling the potential between 0 V and 0.6 V vs. Ag/AgCl in 1 M KOH.

Materials characterization:

The morphology, composition and structure of the as-prepared Ni₃Fe/Ni₃Fe(OH)₉ hybrid was investigated on a JEOL 7001 scanning electron microscope (SEM) at 5 kV and a FEI Tecnai G2 T20 transmission electron microscope (TEM) at 200 kV. For TEM observation, the Ni₃Fe/Ni₃Fe(OH)₉ hybrid was dispersed in ethanol by sonication and then dropped cast onto a holey carbon copper grid. X-ray diffraction patterns (XRD) were obtained on a Bruker D8 ADVANCE ECO powder X-ray instrument using Cu K α radiation ($\lambda = 0.15418$ nm) in a 2θ range from 30° to 70° with a scanning step size of 0.01°. X-ray photoelectron spectroscopy (XPS) was carried out on a Thermal ESCALA 250i X-ray Photoelectron Spectrometer. All binding energies were calibrated to the C 1s peak (284.6 eV).

Electrochemical characterization:

The electrochemical measurements were conducted on an EC-Lab electrochemical workstation with a standard three-electrode electrochemical cell, employing fabricated Ni₃Fe/Ni₃Fe(OH)₉ hybrid electrode as a working electrode, a Ag/AgCl (saturated) reference electrode, and a Pt wire counter electrode. Unless otherwise noted, the potentials in this study are relative to the reversible hydrogen electrode (RHE, converted using the equation $E_{\text{RHE}} = E_{\text{Ag/AgCl}} + 0.197 + 0.059 \times \text{pH}$, where E_{RHE} is the potential vs. RHE and $E_{\text{Ag/AgCl}}$ is the recorded potential vs. a saturated Ag/AgCl reference electrode). Polarization measurements were measured by linear sweep voltammetry at a scan rate of 5 mV s⁻¹. Electrochemical impedance spectra (EIS) were obtained in a frequency range from 100 kHz to 0.01 kHz at the open circuit potential. The resistance of the electrolyte was measured to be 5.3 Ω using the potentiostat. To minimize the competitive reduction reaction result from hydroxides and/or oxides of Ni and Fe on the surface, a fresh Ni₃Fe composite electrode was directly used for

the HER measurement and compared with pristine Fe and Ni nanosheet electrodes. The overall water electrolysis test was carried out in a two-electrode system using the obtained Ni₃Fe(OH)₉/Ni₃Fe hybrid and Ni₃Fe composites as the anode and cathode, respectively. For comparison purpose, the HER performance of benchmark Pt/C was recorded at the same condition. For the electrode preparation, 1 mg Pt/C was dispersed in 50 μL water, 150 μL isopropanol and 10 μl Nafion solution (wt%) to form a homogeneous ink. 10 μL of the catalyst ink was drop-dried onto the glassy carbon electrode to achieve a catalyst loading of ~ 0.68 mg cm⁻². The OER performance of benchmark IrO₂/C (20 wt% Ir on Vulcan carbon black) are referred to the literature under the same condition (0.2 mg cm⁻²).¹⁹

A rotating Pt ring/GC disc electrode (RRDE purchased from ALS Co., Ltd) was used to monitor the onset potential and efficiency of the oxygen evolution reaction. The Ni₃Fe(OH)₉/Ni₃Fe hybrid was electroreductively deposited onto the GC disc following the procedure identical to the method described in the experimental section. The potential of Ni₃Fe(OH)₉/Ni₃Fe hybrid modified GC disc was swept from 1.2 V to 1.57 V vs. RHE, while the potential of the Pt ring was set at 0.45 V vs. RHE to monitor the electrode-generated oxygen. The Faradaic efficiency of the Ni₃Fe(OH)₉/Ni₃Fe hybrid was validated using stabilized current densities originated from OER and ORR, respectively. A Faradaic efficiency of 98.3 ± 1.1% was determined according to the equation (1):

$$E = j_{ORR} / j_{OER} \times N \times 100\% \quad (1)$$

Where j_{ORR} is the stabilized current density of ORR, N is the collection efficiency (28% according to the manufacturer), and j_{OER} is the stabilized current density of OER.

To elucidate the intrinsic OER catalytic activity, the turnover frequency (TOF) was also calculated at an overpotential of 300 mV, assuming all *deposited* Fe and Ni participates in the OER process. The TOF of the catalyst is calculated according to equation (2):

$$TOF = J \times A / 4 \times F \times m \quad (2)$$

Where J is the current density at an overpotential of 300 mV (A cm^{-2}), A is the surface area of the $\text{Ni}_3\text{Fe}(\text{OH})_9/\text{Ni}_3\text{Fe}$ /nickel electrode (cm^2), F is the Faraday constant (96485 C mol^{-1}) and m is the number of the moles of active materials. In this work, the amount of $\text{Ni}_3\text{Fe}(\text{OH})_9/\text{Ni}_3\text{Fe}$ hybrid on nickel foam is ($0.63 \pm 0.08 \text{ mg cm}^{-2}$) based on the weight increase after the electroreductive deposition, as evaluated using a microbalance. The current density is obtained from $\text{Ni}_3\text{Fe}(\text{OH})_9/\text{Ni}_3\text{Fe}$ /nickel foam with 35% iR compensation.

The electrical-to-fuel efficiency of a full electrolyser set up having the catalyst as both anode and cathode was calculated following the equation (3):

$$\eta_{\text{electrolyzer}} = E_{f, o} / V_{e, i}$$

where $E_{f, o} = 1.23 \text{ V}$; $V_{e, i}$ is the input voltage needed to initiate the water electrolysis at the operating current density of interest. In this study, the electrical-to-fuel efficiency (75%) is obtained at the current density of 10 mA cm^{-2} .

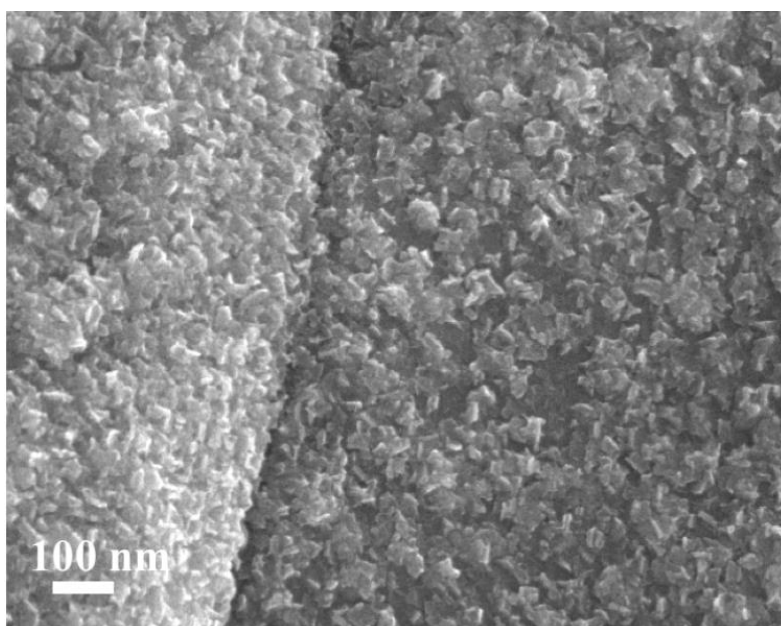


Figure S1. SEM image of electroreductive deposited NiFe alloy nanosheet.

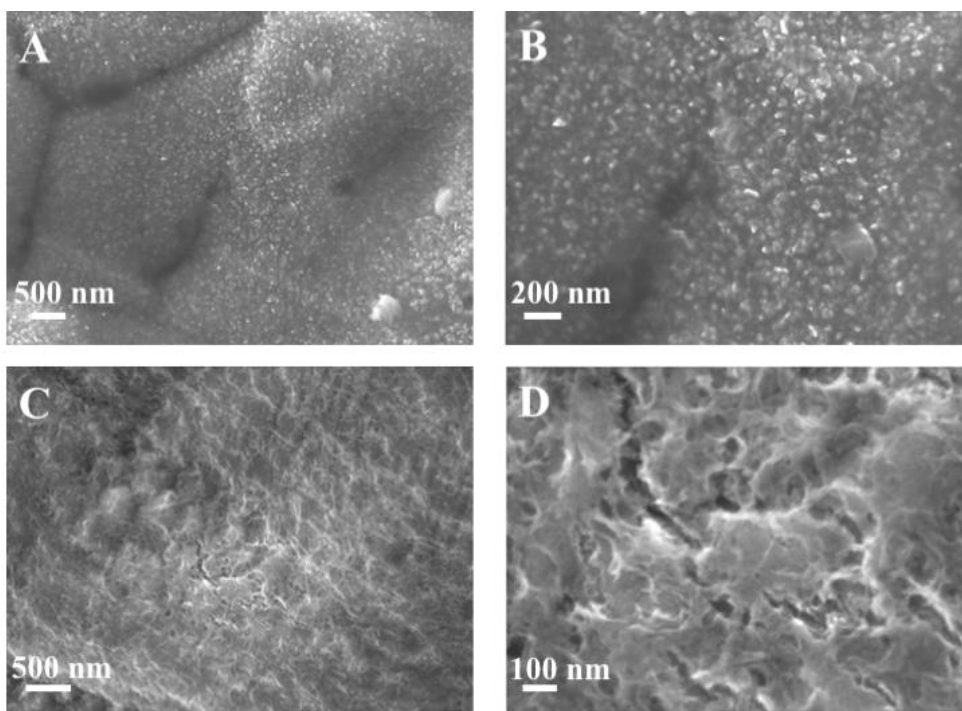


Figure S2. SEM images of (A-B) deposited Fe and (C-D) deposited Ni films.

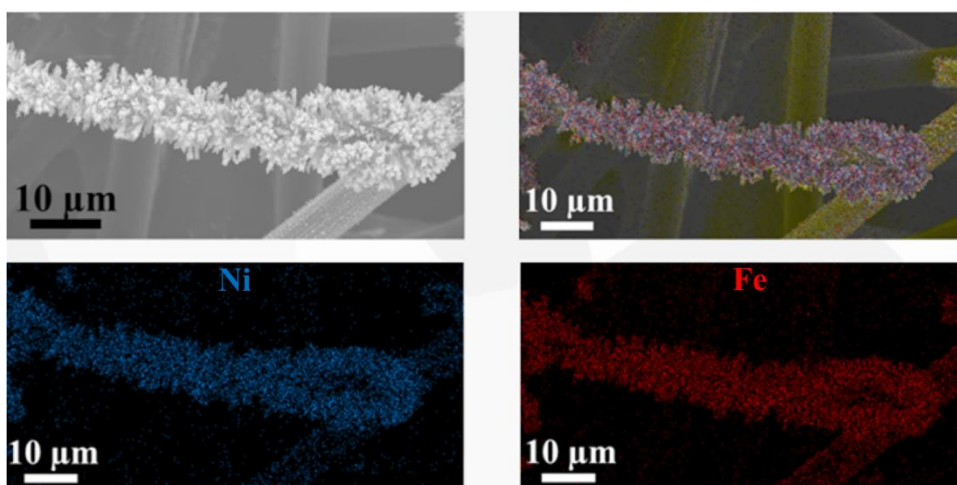


Figure S3. Elemental map of as-deposited Ni_3Fe alloy. The obtained NiFe alloy on CFP exhibit alteration in morphology, which is attributed to different surface composition (metal vs. carbon) and morphology between nickel foam and CFP.

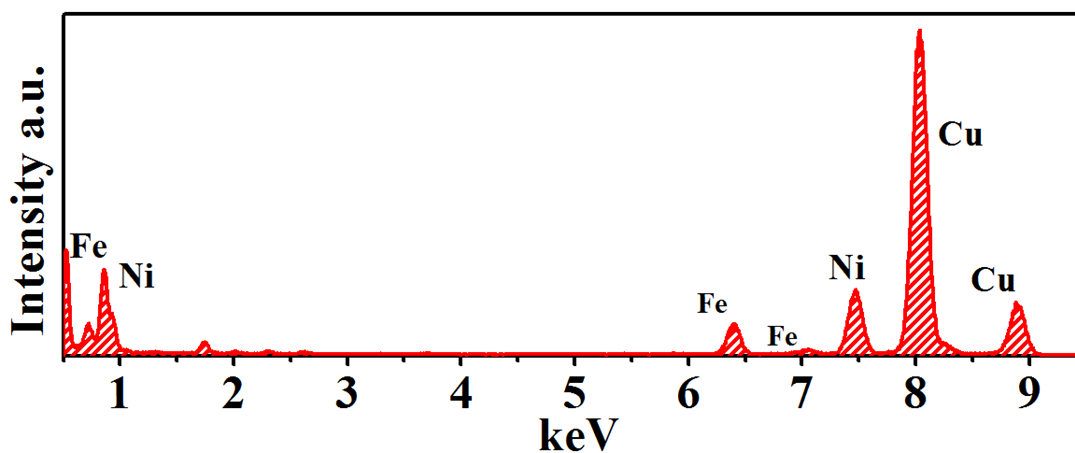


Figure S4. EDX spectrum of as-deposited Ni₃Fe alloy.

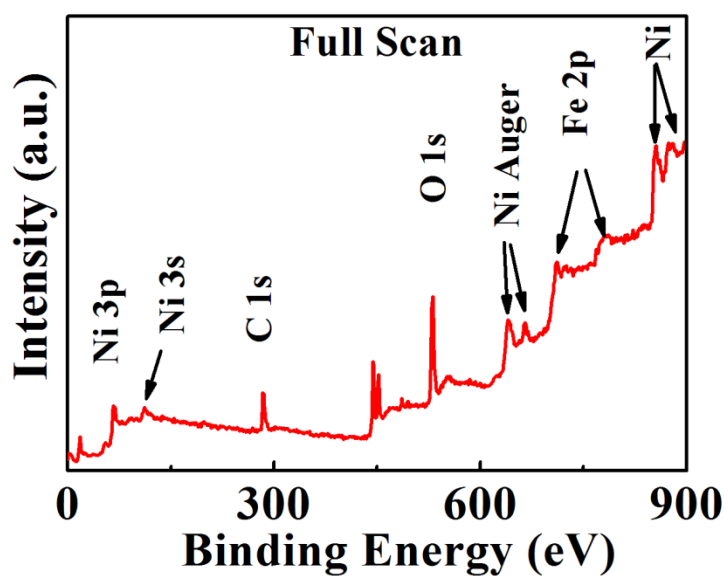


Figure S5. XPS spectrum of Ni₃Fe(OH)₉/Ni₃Fe hybrid.

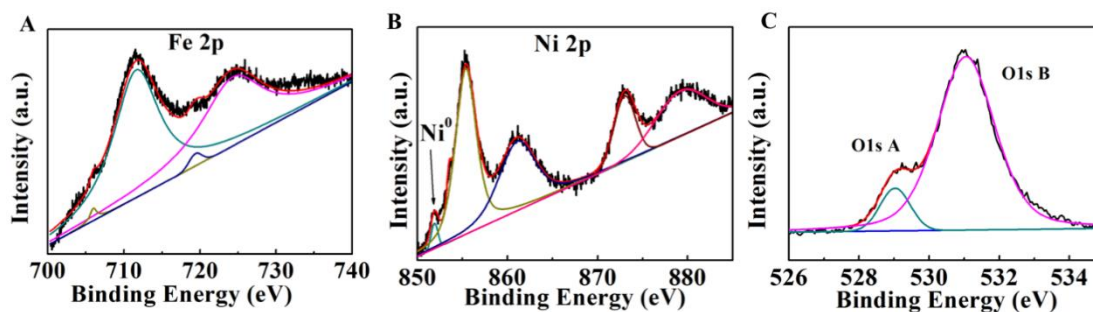


Figure S6. XPS spectra of Ni₃Fe(OH)₉/Ni₃Fe hybrid: (A) High-resolution Fe 2p, (B) High-resolution Ni 2p and (C) O 1s.

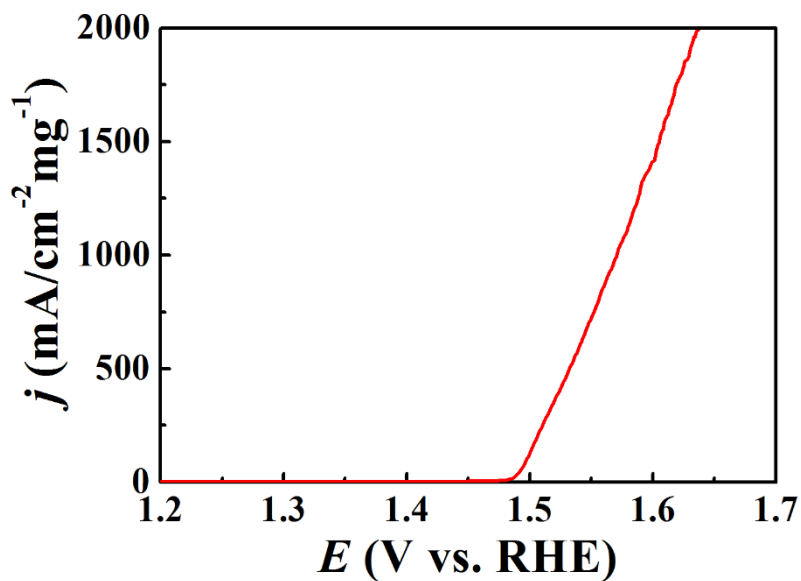


Figure S7. OER mass catalytic activity of $\text{Ni}_3\text{Fe}(\text{OH})_9/\text{Ni}_3\text{Fe}$ hybrid on GC electrode.

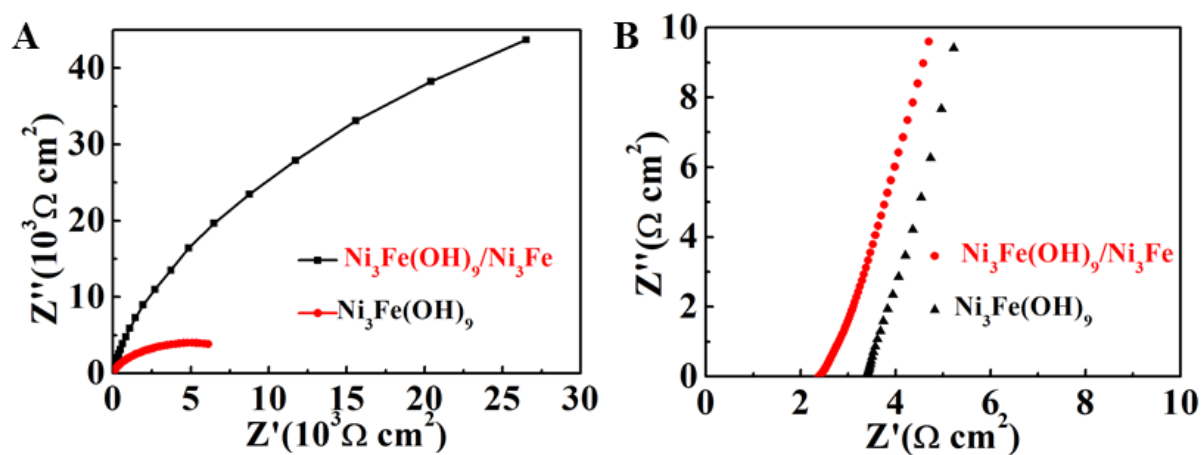


Figure S8. (A) Electrochemical impedance spectra and (B) magnified high frequency region of $\text{Ni}_3\text{Fe}(\text{OH})_9/\text{Ni}_3\text{Fe}$ hybrid (red) and $\text{Ni}_3\text{Fe}(\text{OH})_9$ (black).

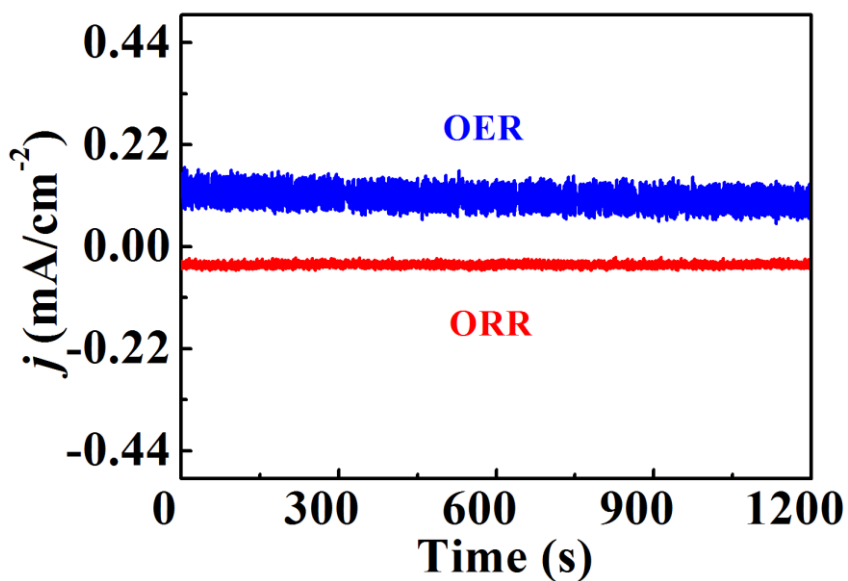


Figure S9. Chronoamperometric curves obtained at the rotating Pt ring GC disc electrode for quantification of oxygen.

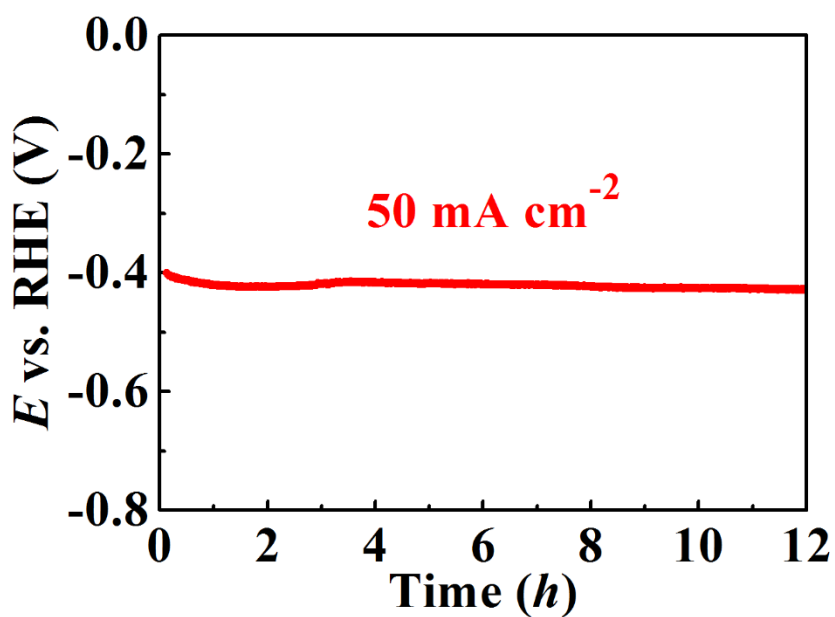


Figure S10. Chronopotentiometric curve at current density of 50 mA cm⁻² for Ni₃Fe(OH)₉/Ni₃Fe/nickel foam.

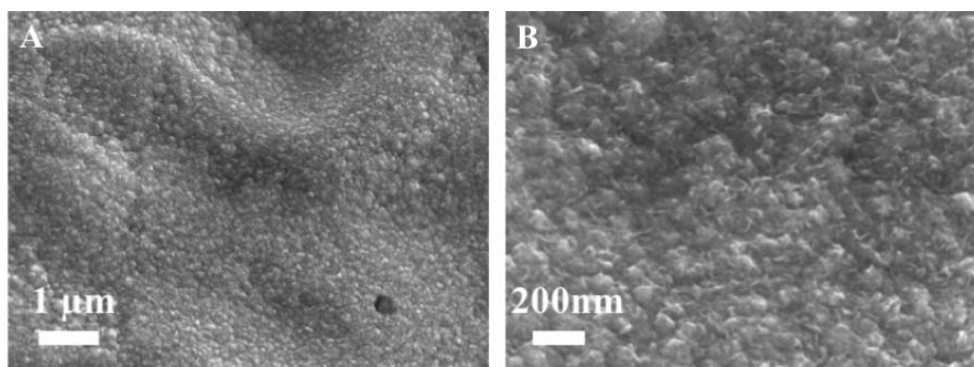


Figure S11. SEM (A) and HRSEM (B) images of $\text{Ni}_3\text{Fe}(\text{OH})_9/\text{Ni}_3\text{Fe}$ after 12h electrolysis test.

Table S1. Comparison of $\text{Ni}_3\text{Fe}(\text{OH})_9/\text{Ni}_3\text{Fe}$ hybrid with benchmark and recently reported non-precious OER electrocatalysts on glassy carbon electrode.

Catalysts	Mass loading mg/cm^{-2}	η_{10} (mV)	Tafel slope (mV/dec)	Reference
$\text{Ni}_3\text{Fe}(\text{OH})_9/\text{Ni}_3\text{Fe}$	~0.63	280	28	This work
$\text{Ni}_3\text{Fe}(\text{OH})_9$	32 μg	330	51	29
$\text{Ni}_{0.9}\text{Fe}_{0.1}/\text{NC}$	2.0	330	45	19
NiFe LDH/CNT	~0.25	250	31	28
Ni/N/C	0.4	390	N/A	27
nNiFe LDH/NGF	0.25	337	45	25
NiCo oxide	N/A	325	39	37
MnCo oxyphosphide	0.4	370	52	38
$\text{Na}_{1-x}\text{Ni}_y\text{Fe}_{1-y}\text{O}_2$	N/A	260	43	39
$\text{Fe}_1\text{Co}_1\text{-ONS}$	0.36	308	36.8	40
FeOOH/Co/FeOOH	N/A	250	32	41

Table S2. Comparison of Ni₃Fe composites with benchmark and recently reported non-precious HER electrocatalysts on glassy carbon electrode.

Catalysts	Mass loading mg/cm ⁻²	η_{10} (mV)	Tafel slope (mV/dec)	Reference
Ni ₃ Fe composites	~0.63	217	83	This work
Ni _{0.9} Fe _{0.1} /NC	2.0	231	111	19
MnNi/C	0.28	360	N/A	42
MoB	2.5	225	59	43
CoO _x @CN	0.12	230	N/A	26

Table S3. Comparison of Ni₃Fe(OH)₉/Ni₃Fe hybrid with recently reported bifunctional electrocatalysts for two-electrode overall water electrolysis in alkaline media.

Catalysts	Catalyst support	Mass loading mg/cm ⁻²	Overall voltage $j=10mA\ cm^{-2}$	Reference
Ni ₃ Fe(OH) ₉ /Ni ₃ Fe	Ni foam	0.63	1.64	This work
Cu@NiFe LDH	Cu foam	2	1.54	32
Ni _{0.9} Fe _{0.1} /NC	Ni foam	2.0	1.58	19
Co-P	Cu foil	Unknown	1.65	44
NiFe/NiCo ₂ O ₄	Ni foam	Unknown	1.67	10
CoO _x @CN	Ni foam	2.0	1.68	26
NiFe LDH	Ni foam	Unknown	1.7	45
Ni ₅ P ₄	Ni foam	3.5	1.7	46
Ni _{0.33} Co _{0.67}	Ti foil	0.3	1.72	47
Ni ₃ Fe/NiFeO _x	Ni foam	N/A	~1.6	48

Chapter 3

MnO₂/MnCo₂O₄/Ni Heterostructure with Quadruple Hierarchy: A Bifunctional Electrode Architecture for Overall Urea Oxidation

3.1 Overview

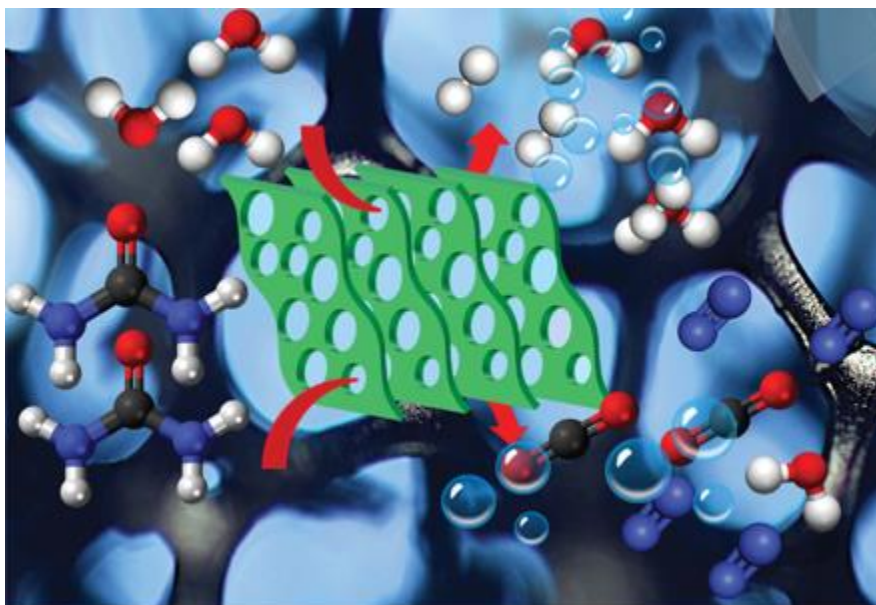
This chapter is a paper titled “MnO₂/MnCo₂O₄/Ni Heterostructure with Quadruple Hierarchy: A Bifunctional Electrode Architecture for Overall Urea Oxidation” that was published in Journal of Materials Chemistry A in 2017.

For hydrogen production, urea oxidation is a more efficient anodic reaction than oxygen evolution, because it has a lower theoretical oxidation potential (0.37 V vs. RHE for urea oxidation, compared to 1.23 V vs. RHE for oxygen evolution). In addition, urea electrolysis techniques are likely to be important developments for urea-containing wastewater treatment. Generally, the urea oxidation reaction involves a 6-electron transfer and complicated gas evolution (N₂ and CO₂) processes. However, the challenge for large-scale application of urea electrolysis is the lack of cost-effective and robust catalysts.¹⁻³

So far, the majority of reported catalyst materials are limited to single- or dual- hierarchical architectures, leading to restricted reaction surface area. Smart catalyst architecture can considerably enlarge the electroactive surface area and active sites. More significantly, it can also enhance mass transport to support long-term, vigorous catalytic reaction, thereby realizing industrial application.

Hence, we fabricated a MnO₂/MnCo₂O₄/Ni core-shell heterostructured electrode with quadruple hierarchy including a macroporous Ni foam scaffold ($\geq 500 \mu\text{m}$), an intermediate vertically-aligned MnCo₂O₄ core-nanoflake array (50-100 nm), ultra-thin MnO₂ nanosheets ($\sim 10 \text{ nm}$) and short-range ordered mesopores ($\sim 5 \text{ nm}$) on the MnO₂ nanosheets. The obtained freestanding and hierarchical electrode shows excellent bifunctional catalytic

activity towards both urea oxidation and hydrogen evolution (The products of the oxidation reaction in this case have yet to be formally identified). Overall, this noble-metal-free quadruple hierarchy $\text{MnO}_2/\text{MnCo}_2\text{O}_4/\text{Ni}$ electrode is promising for the industrial application of urea electrolysis technology and also shows potential as a new platform for multiple applications.



This diagram illustrates an efficient overall urea electrolysis catalysed by a well-designed quadruple hierarchical $\text{MnO}_2/\text{MnCo}_2\text{O}_4/\text{Ni}$ electrode for hydrogen production.

References

1. C. Xiao, S. Li, X. Zhang and D. R. MacFarlane, *J. Mater. Chem. A*, 2017, **5**, 7825.
2. S. Chen, J. Duan, A. Vasileff and S. Z. Qiao, *Angew. Chem. Int. Ed.* 2016, **55**, 3804.
3. D. Wang, W. Yan, S. H. Vijapur and G. G. Botte, *J. Power Sources* 2012, **217**, 498.

CrossMark
click for updatesCite this: *J. Mater. Chem. A*, 2017, 5, 7825

MnO₂/MnCo₂O₄/Ni heterostructure with quadruple hierarchy: a bifunctional electrode architecture for overall urea oxidation†

Changlong Xiao,^a Shuni Li,^b Xinyi Zhang^{*a} and Douglas R. MacFarlane^{*a}

A three-dimensional MnO₂/MnCo₂O₄/Ni core-shell heterostructured electrode has been fabricated through a facile method. This electrode architecture consists of four levels of interconnected hierarchy: a primary macroporous Ni foam scaffold ($\geq 500 \mu\text{m}$), an intermediate vertically-aligned MnCo₂O₄ core-nanoflake array (50–100 nm), topmost ultra-thin MnO₂ nanosheets ($\sim 10 \text{ nm}$) and short-range ordered mesopores ($\sim 5 \text{ nm}$) on the MnO₂ nanosheets. This freestanding, hierarchical porous electrode has advantages in enhancing electroactive surface area, enabling efficient mass transport through the porous structure. The heterostructured electrode exhibits a low onset potential (1.33 V vs. RHE), a high anodic peak current density ($1000 \text{ mA cm}^{-2} \text{ g}^{-1}$ at 1.7 V vs. RHE) and long-term catalytic stability for urea oxidation, which surpasses previous reported electrode materials for urea electrolysis. Remarkably, the MnO₂/MnCo₂O₄/Ni electrode possesses bifunctional catalytic activity for both urea oxidation and hydrogen evolution. A urea electrolytic cell with both anode and cathode using the heterostructured electrodes has been fabricated and a current density of 10 mA cm^{-2} has been achieved at a cell voltage of 1.55 V. This noble metal-free quadruple hierarchy electrode shows potential as a new platform for multi-purpose applications.

Received 31st January 2017

Accepted 1st March 2017

DOI: 10.1039/c7ta00980a

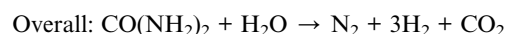
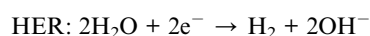
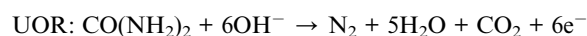
rsc.li/materials-a

Introduction

Urea is an abundant substance that can be derived from global industrial activities and urine-rich sanitary wastewater (2–2.5 wt% urea).^{1–3} The discharged urea can hydrolyze into caustic ammonia and nitrate under natural conditions, which may cause environmental pollution and eutrophication of underground water. On the other hand, urea is also a promising energy carrier owing to its high energy density and easy transport and storage.^{4,5} The gradually increasing energy demand and environmental concerns have triggered the development of alternative clean and sustainable energy resources, such as hydrogen fuel.^{6–9} Hydrogen generation through electrolytic water splitting is a simple and sustainable method, but a large thermodynamic potential is required owing to the sluggish anodic oxygen evolution reaction (OER).^{10–13} In comparison, urea oxidation (UOR) is a more efficient anodic reaction owing to its lower theoretical oxidation potential of 0.37 V vs. RHE compared to OER (1.23 V vs. RHE).^{14,15} Hence, UOR has the potential to replace the sluggish OER for production of hydrogen fuel wherever it is available. In addition

to cheap and efficient hydrogen production, urea electrolysis can also eliminate the potentially harmful urea simultaneously. Therefore, the development of urea electrolysis is significant, not only in new energy applications (*e.g.* hydrogen production), but also for environmental remediation.¹⁶

The urea electrolysis reaction in alkaline media can be expressed as below:^{17,18}



The UOR involves a 6-electron transfer and complicated gas evolution (N₂ and CO₂) processes, which also suffer from intrinsically slow kinetics.^{19,20} Usually, noble metal-based catalysts, such as Pt/C, Rh and Pd, are required to catalyze the UOR to obtain a more appropriate rate.^{4,20,21} Nevertheless, the use of expensive catalysts greatly restricts the commercialization and large-scale application of the UOR technique. Hence, much research effort has been devoted to the development of earth-abundant materials including 2D S-MnO₂,²² Ni-Co composites,¹⁴ LaNiO₃ perovskite² and mesoporous NiO₂ nanosheets.²³ Likewise, Pt based materials^{24,25} are state-of-the-art catalysts to promote the cathodic hydrogen evolution reaction (HER); however most HER catalysts are only efficient in acidic

^aSchool of Chemistry, Australian Centre for Electromaterials Science, Monash University, Victoria, 3800 Australia. E-mail: xinyi.zhang@monash.edu; douglas.macfarlane@monash.edu

^bSchool of Chemistry and Chemical Engineering, Shaanxi Normal University, Xi'an, Shaanxi, 710062, China

† Electronic supplementary information (ESI) available. See DOI: 10.1039/c7ta00980a

media.^{26–28} Therefore, a bifunctional catalyst that is efficient for both UOR and HER in alkaline media is highly desirable in pursuit of efficient whole-cell urea electrolysis. Apart from having superior electroactive activity, sophisticated design of the mesoporous and/or hierarchical architecture is also regarded as crucial for enhancing catalytic performance.^{29–33} So far, the majority of reported materials are limited to single- or dual-hierarchical architecture, leading to restricted reaction surface area. Smart catalyst architecture can considerably enlarge the electroactive surface area, further achieving high active-site density. More significantly, it can also enhance mass transport to support long-term, vigorous catalytic reaction, thereby realizing industrial application. Hence, an electrode material with higher level of hierarchy may be a low cost way to obtain high catalytic activity for efficient urea electrolysis.

In this study, we fabricated a MnO₂/MnCo₂O₄/Ni (abbreviated as MMCN) core-shell heterostructured electrode with quadruple-hierarchy for efficient overall urea electrolysis. As the first level of hierarchy, Ni foam provides large numbers of macroporous channels for the access of electrolyte and dissipation of produced gaseous bubbles. Besides, the evenly distributed open space in the skeleton makes it possible to build more delicate nano-architectures. Thus in a secondary level of hierarchy in this work the MnCo₂O₄ nanoflake array was further hydrothermally deposited onto the Ni foam scaffold, resulting in a significantly enlarged electrode surface area. Both manganese and cobalt oxides are excellent electrochemical catalyst materials, while binary metal oxides usually exhibit higher electrical conductivity than pristine metal oxide materials.^{34–36} Particularly, MnO₂ is a low cost and environmentally benign material. Ultrathin MnO₂ nanocrystals have demonstrated superior electrochemical activity and excellent selectivity towards UOR.²² So a tertiary hierarchy of ultra-thin (~10 nm) MnO₂ nanosheets (NSs) was *in situ* grown on top of the as-fabricated MnCo₂O₄ nanoflakes (NFs). Intriguingly, this topmost layer of MnO₂ NSs possess uniformly distributed mesopores (~5 nm). Thus the resulting MnO₂/MnCo₂O₄/Ni electrode possesses a total of four levels of hierarchy. Overall, a noble metal-free and hierarchical bifunctional electrode has been developed for efficient whole cell urea electrolysis.

Experiment

Materials

Ni foam with a thickness of 1.6 mm and a bulk density of 0.45 g cm⁻³ was used as the substrate. Cobalt nitrate hexahydrate (≥98%), manganese nitrate tetrahydrate (≥98%), potassium hydroxide (≥98%), ammonium fluoride (≥98%) and urea were supplied by Sigma-Aldrich. All the standard electrolyte solutions were prepared using Milli-Q water with a resistance of 18.2 MΩ at 25 °C.

Synthesis of MnCo₂O₄ nanoflake arrays on Ni foam

Ni foam was sonicated in 0.5 M HCl, Milli-Q water and absolute ethanol for 5 min to remove the surface nickel oxide layer. Subsequently, the clean Ni foam was dried under a pure N₂ flow

at room temperature. The MnCo₂O₄ nanoflake arrays were hydrothermally deposited onto the Ni foam. A reaction solution containing 3.3 mM of Co(NO₃)₂, 1.67 mM Mn(NO₃)₂, 10 mM NH₄F and 25 mM CO(NH₂)₂ was prepared and sonicated to ensure homogeneity. Afterwards, 35 mL of the as-prepared solution was transferred into a 45 mL Teflon-lined stainless steel autoclave. Subsequently, Ni foam with the topside covered with polytetrafluoroethylene tape was vertically immersed into the solution. The autoclave was placed in an oven at 120 °C for 5 h. After the hydrothermal reaction, the autoclave was cooled down to room temperature naturally. The Ni foam electrode was rinsed with Milli-Q water and absolute ethanol and dried in air. Finally, the obtained electrode was calcinated at 300 °C in a furnace for 2 h.

Fabrication of MMCN electrodes

The mesoporous MnO₂ nanosheet layer was electrodeposited onto the as-prepared MnCo₂O₄/Ni foam electrode. The electrodeposition was conducted in a standard three-electrode electrochemical cell, using MnCo₂O₄/Ni foam as the working electrode, and Ag/AgCl (saturated) and Pt wire as reference and counter electrodes, respectively. The electrochemical deposition solution containing 3 × 10⁻³ M Mn(NO₃)₂·4H₂O in Milli-Q water (30 mL) was sonicated for 10 min prior to use. The electrodeposition was carried out at a potential of -1.1 V vs. Ag/AgCl (saturated) for 300 s. Finally, the obtained composite electrode was rinsed with Milli-Q water and ethanol and dried in air.

Material characterizations

The scanning electron microscopic (SEM) images were obtained from JEOL 7001 SEM instrument at 3 kV. Transmission electron microscopy (TEM) images were obtained from a FEI Tecnai G2 T20 at 200 kV. Samples were prepared by scraping off directly from Ni foam and drop casting their ethanol solutions onto holey carbon copper grids. X-ray diffraction patterns were obtained on Bruker D8 ADVANCE ECO powder X-ray instrument using Cu Kα radiation (λ = 0.15418 nm) in a 2θ range from 25° to 70° with a scanning step size of 0.01°. Samples were prepared by drop casting of the peeled MnO₂/MnCo₂O₄ and MnCo₂O₄ composites directly onto ITO-glass substrates without using binders. X-ray photoelectron (XPS) characterizations were carried out on a Thermal ESCALA 250i X-ray Photoelectron Spectrometer. All binding energies were calibrated to the C 1s peak (284.6 eV).

Electrochemical analysis

Cyclic voltammetry (CV) measurements were conducted on an EC-Lab electrochemical workstation with a standard three-electrode electrochemical cell, employing fabricated MMCN electrode as working electrode, Ag/AgCl (saturated) reference electrode, and a Pt wire counter electrode. All onset potentials reported in this study have been converted to reversible hydrogen electrode (RHE, using the equation $E_{\text{RHE}} = E_{\text{Ag/AgCl}} + 0.197 + 0.059 \times \text{pH}$, where E_{RHE} is the potential calculated to RHE and $E_{\text{Ag/AgCl}}$ is the recorded potential *versus* Ag/AgCl (saturated) reference electrode). Polarization measurements

were measured by linear sweep voltammetry at a scan rate of 5 mV s^{-1} . Electrochemical impedance spectra (EIS) were obtained in a frequency range from 100 kHz to 0.01 kHz at the open circuit potential.

Results and discussion

Fig. 1A represents the SEM image of MnCo_2O_4 composites on the Ni foam scaffold after hydrothermal deposition and calcination. The entire Ni foam skeleton appears covered with a layer of fluffy MnCo_2O_4 composites, without alteration of the original macro-porosity (Fig. 1A vs. S1†). The highly porous structure of Ni foam with macro-pores $\geq 500 \mu\text{m}$ can maximize the catalyst loading and facilitate the transport of reactant ions to reach the interior active sites. Meanwhile, large amounts of macroscopic channels and open space also enable fast dissipation of gaseous products (such as N_2 , CO_2 and H_2) to avoid blocking of the diffusion channels and electroactive sites. With closer observation (Fig. 1B and C), the deposited MnCo_2O_4 composites are vertically aligned 2-dimensional (2D) nanoflake array with an average length around $1.5 \mu\text{m}$ and thickness between 50 and 100 nm. These uniformly distributed MnCo_2O_4 NFs are mutually interconnected, forming a secondary porous architecture with significantly enlarged electrode surface area. The chemical composition and elemental distribution of the MnCo_2O_4 NFs were characterized by energy-dispersive X-ray spectroscopy (EDX, Fig. S2†), indicating the homogeneity of deposited MnCo_2O_4 composites.

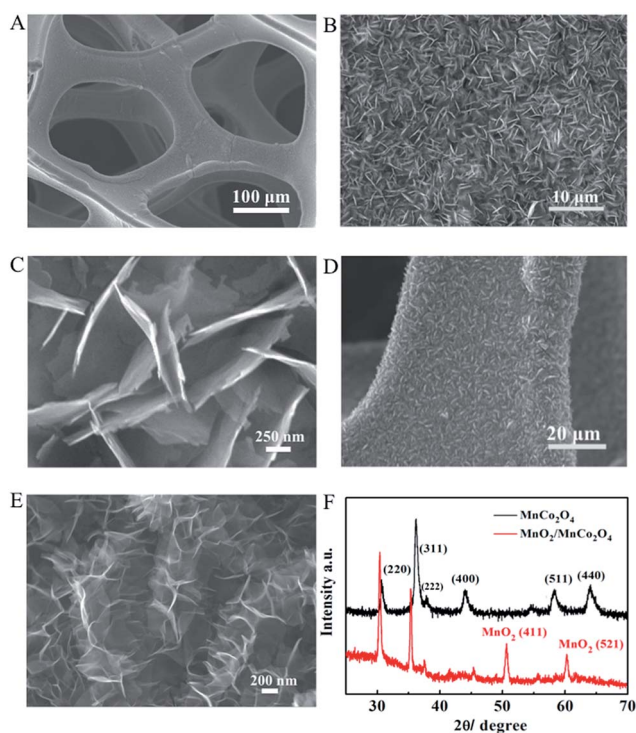


Fig. 1 SEM images of (A)–(C) MnCo_2O_4 NFs/Ni foam composites, (D)–(E) MMCN core-shell heterostructured composites at various magnifications. (F) XRD patterns of MnCo_2O_4 NFs and $\text{MnO}_2/\text{MnCo}_2\text{O}_4$ composites.

In pursuit of higher electroactive surface area, the above-obtained $\text{MnCo}_2\text{O}_4/\text{Ni}$ foam was further used as a platform to electrodeposit a tertiary layer of MnO_2 nanocrystals which have been reported recently as a superior UOR catalyst.^{5,22} As shown in Fig. 1D, a rougher surface can be obtained after the electro-deposition. From the high resolution SEM image shown in Fig. 1E, an ultra-thin layer of MnO_2 shell-NSs each around 300 nm long and less than 10 nm thick were densely attached onto the MnCo_2O_4 NFs. The distance between two adjacent MnO_2 shell-NSs is around 200 nm, which also provides enough space for the diffusion of urea molecules and generated gas bubbles. To verify the chemical composition of the electro-deposited layer, MnO_2 NSs were directly electrodeposited onto the Ni foam to conduct EDX measurements. Only Mn and O species were detected in the EDX spectra (Fig. S3†), confirming that the topmost shell is pure MnO_2 .

In addition, X-ray diffraction (XRD) patterns confirmed the crystallinity of the intermediate MnCo_2O_4 NFs and the topmost MnO_2 nanoshells (Fig. 2F). To minimize the impact from the Ni foam substrate, the MnCo_2O_4 NFs and $\text{MnO}_2/\text{MnCo}_2\text{O}_4$ core-shell composites were scratched off from the Ni foam electrodes and drop-cast on the ITO glass for the XRD analysis. A series of diffraction peaks of MnCo_2O_4 NFs can be detected at $2\theta = 30.8^\circ$,

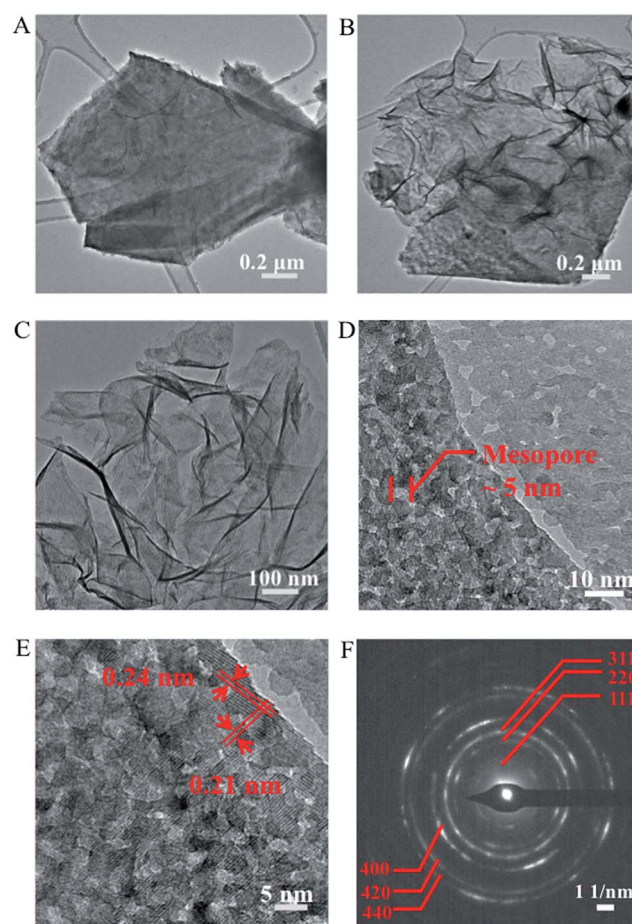


Fig. 2 TEM images of (A) MnCo_2O_4 NFs, (B) $\text{MnO}_2/\text{MnCo}_2\text{O}_4$ core-shell structured composites, (C) MnO_2 NSs, (D)–(E) high-resolution TEM images of MnO_2 NSs and (F) SAED pattern of MnCo_2O_4 NFs.

36.2°, 37.6°, 43.8°, 58.5° and 63.9°, which are assigned to (220), (311), (222), (400), (511) and (440) phase orientations of face-centered-cubic MnCo_2O_4 (space group $Fd\bar{3}m$ (227), JCPDS No. 32-0297). For the XRD pattern of $\text{MnO}_2/\text{MnCo}_2\text{O}_4$ composite, only four obvious diffraction peaks can be detected. The peaks at $2\theta = 30.8^\circ$, 35.3° are indexed as cubic MnCo_2O_4 , while newly observed peaks at $2\theta = 49.7^\circ$ and 60.1° correspond to α -phase MnO_2 . It is noted that some original MnCo_2O_4 diffraction peaks became weak and/or disappeared and the remaining two peaks also shifted slightly to lower angles, suggesting a change in the d -spacing of the plane after the deposition of MnO_2 shell-NSs. It also implies that the deposited MnO_2 shells are tightly bound to the MnCo_2O_4 cores and induce certain strain into the cubic structure of the MnCo_2O_4 , thereby maintaining structural integrity of the entire MMCN electrode. To further confirm the crystal structure of the topmost MnO_2 NSs, MnO_2 was also directly electrodeposited onto ITO glass to carry out the XRD measurement as shown in Fig. S4.† All detected diffraction peaks correspond well to α -phase MnO_2 . The calculated average crystallite sizes of MnCo_2O_4 and $\text{MnO}_2/\text{MnCo}_2\text{O}_4$ are 14.6 nm and 27.4 nm, respectively.

A TEM image of the intermediate MnCo_2O_4 NFs scratched off directly from the electrode (Fig. 2A) reveals that the approximate length is $\sim 1.5 \mu\text{m}$. This result agrees well with the SEM images. After electrodeposition, MnO_2 NSs were grown along the originally flat surface of MnCo_2O_4 NFs, as shown in Fig. 2B. Interestingly, the electrodeposited MnO_2 NSs are ultra-thin and/or transparent with graphene-like morphology (Fig. 2C), which provides more free interspace and electroactive sites. From the high-resolution TEM (HRTEM) image in Fig. 2D, numerous short-range ordered mesopores with average diameter ~ 5 nm are distributed uniformly throughout the MnO_2 NSs. As a result, the mesopores further increase the surface and hence increase the number of edge sites which are expected to be particularly active.^{37,38} Both these changes are likely to increase electrocatalytic activity. Collectively, the fabricated quadruple hierarchical electrode is composed of macroscopic Ni foam, MnCo_2O_4 nanoflake cores and the topmost mesoporous MnO_2 nanosheet shells. The entire hierarchical architecture is well interconnected, thus, the electrons can travel rapidly through the Ni foam scaffold up to the topmost MnO_2 shell-NSs surface to precipitate in catalytic reactions.

Furthermore, selected area diffraction electron (SAED) patterns were obtained to characterize the crystal structure of the intermediate MnCo_2O_4 NFs and topmost MnO_2 NSs. In Fig. 2F, a series of sharp diffraction fringes can be observed in the SAED pattern, which agree well with the (111), (220), (311), (400), (420) and (440) crystal planes of cubic spinel MnCo_2O_4 .³⁹ Moreover, the spot SAED pattern shown in Fig. S5† verifies the single-crystalline feature of the electrodeposited α -phase MnO_2 NSs.⁴⁰ All these results are in agreement with the information obtained from the XRD pattern. From the HRTEM image (Fig. 2E), distinct sets of lattice fringes with inter-planar spacings of 0.24 nm and 0.21 nm can be further observed, which correspond well to the (-112) and (-111) planes of α -phase MnO_2 .⁴¹

More details of the chemical composition and valence states were obtained by X-ray photoelectron spectroscopy (XPS). The

survey XPS spectrum shown in Fig. S6A† indicates that the MnCo_2O_4 composites mainly contain Co, Mn, and O elements. An atomic Mn/Co ratio of approximately 1 : 2 was determined by the XPS analysis, which is in good agreement with the empirical formula. The high-resolution Mn 2p spectrum (Fig. S6B†) shows that the Mn atoms in $2p_{3/2}$ and $2p_{1/2}$ electronic configurations can be observed at 642.9 and 654.1 eV, indicating the coexistence of Mn^{2+} and Mn^{3+} species.³⁹ An XPS measurement was also carried out to analyse the $\text{MnO}_2/\text{MnCo}_2\text{O}_4$ composites. Similarly, the XPS spectrum of core-shell structured $\text{MnO}_2/\text{MnCo}_2\text{O}_4$ composites (Fig. 3A) demonstrates the presence of Co, Mn and O as well. In the high-resolution Mn 2p spectrum in Fig. 3B, the Mn 2p spectrum was best fitted to two prominent peaks at 638.3 (Mn $2p_{3/2}$) and 650.2 eV (Mn $2p_{1/2}$), with a spin energy separation of 11.9 eV, indicating the existence of Mn^{4+} .⁴² The two Mn 2p binding energy peaks can be further deconvoluted into four sub-peaks by Gaussian fitting method. The binding energies at 642.4 and 653.3 eV are ascribed to the presence of Mn^{2+} , while the binding energies at 645 and 654.1 eV are attributed to the Mn^{3+} . Overall, three kinds of Mn species can be detected in the core-shell structured $\text{MnO}_2/\text{MnCo}_2\text{O}_4$ composites. From the high-resolution Co 2p spectra in Fig. S6C† and 3C, the coexistence of Co^{2+} and Co^{3+} species can be confirmed for both MnCo_2O_4 and $\text{MnO}_2/\text{MnCo}_2\text{O}_4$ composites as two dominant energy peaks are located at 781.1 and 796.1 eV, respectively.⁴³

The above results reveal that the core-shell structured $\text{MnO}_2/\text{MnCo}_2\text{O}_4$ composites can provide a surface rich in redox couples ($\text{Mn}^{2+}/\text{Mn}^{3+}/\text{Mn}^{4+}$ and $\text{Co}^{2+}/\text{Co}^{3+}$), contributing to a high-density of electroactive sites.⁴⁴ These synergistic effects between the MnCo_2O_4 nanoflake cores and the MnO_2 nanosheet shells are advantageous in electrochemical catalytic reactions because the multiple valence states of metal cations can provide efficient donor-acceptor chemisorption sites for the reversible desorption of urea molecules.^{45,46} The deconvoluted O 1s spectra in Fig. 3D and S6D† reveal the presence of three different oxygen groups. The fitting peaks at binding energy of 529.8 eV (O 1s A), 530 eV

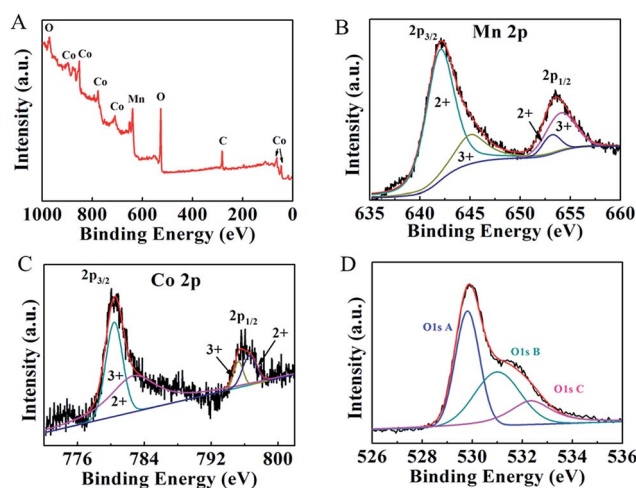


Fig. 3 XPS spectra of $\text{MnO}_2/\text{MnCo}_2\text{O}_4$ core-shell structured composites: (A) full spectrum, high-resolution (B) Mn 2p, (C) Co 2p and (D) O 1s spectra.

(O 1s B) and 532.4 eV (O 1s C) can be assigned to oxygen–metal bonds, hydroxyl groups and surface-adsorbed H₂O molecules, respectively.⁴⁷ A slight decrease in the intensity of O 1s B and O 1s C can be observed after the electrodeposition of MnO₂, indicating the decrease in hydroxyl groups. The loss of surface hydroxyl oxygen and oxygen vacancies may lead to inferior catalytic activity in oxygen evolution and oxygen reduction reactions,⁴⁸ thus enhancing the UOR selectivity of the obtained MnO₂/MnCo₂O₄/Ni electrode.

The catalytic activity of the MMCN electrode toward UOR has been studied by linear sweep voltammetry (LSV) in 1 M KOH in the absence and presence of 0.5 M urea (2.9 wt%). As observed in Fig. 4A, the MMCN electrode shows an excellent UOR performance with a low onset potential of 1.33 V vs. RHE (at a current density of 10 mA cm⁻²), which is comparable to/or lower than recently reported values on S–MnO₂ (1.33 V),²² graphene–Ni(OH)₂ (1.52 V),⁴⁹ NiO nanosheet (1.38 V),²³ Ni(OH)₂ nanocube array (1.55 V)¹⁸ and Pt (1.50 V).⁴ Moreover, a relatively low potential of 1.7 V vs. RHE is required to achieve a high current density of 386 mA cm⁻² (over 1000 mA cm⁻² mg⁻¹, Fig. S7†), which surpasses most, if not all, state-of-the-art electrode materials, as shown in Table S1.† The current density in the absence of urea is only 37 mA cm⁻² at the same potential (1.7 V vs. RHE), which is assigned to the OER. It reveals that the

obtained MMCN electrode favours the UOR rather than OER (~90% current is contributed from UOR), indicating it has excellent catalytic selectivity.

To study the reaction kinetics of the MMCN electrode, the UOR performance of MnO₂/Ni foam, MnCo₂O₄/Ni foam and Ni foam electrodes were also investigated as shown in Fig. 4B. It can be seen that the hydrothermally deposited MnO₂/Ni foam electrode shows similar vertically aligned array as MnCo₂O₄/Ni foam (Fig. 1 and S8†). It can be seen that the core–shell structured MMCN shows lower onset potential of 1.33 V vs. RHE and larger catalytic current density of 384 mA cm⁻² (at 1.7 V vs. RHE) than that of MnO₂/Ni foam (1.38 V, 210 mA cm⁻²), MnCo₂O₄/Ni foam (1.37 V, 240 mA cm⁻²) or bare Ni foam (1.50 V, 50 mA cm⁻²). The exceptional UOR performance obtained with the MMCN electrode can be attributed to the following aspects: first, the highly porous architecture can dramatically increase the accessible surface area, thereby offering larger electrode/electrolyte interfaces.²⁹ This assumption can be verified by its high roughness factor ($R_f = 533$, Fig. S9†),²² 2.7 times and 1.8 times higher than those of MnO₂ ($R_f = 196$, Fig. S10†) and MnCo₂O₄ ($R_f = 284$, Fig. S11†) as listed in Table S2.† Second, the unique 3D and quadruple-hierarchy architecture can provide vast nanochannels to facilitate the transport of electrolyte ions and dissipate produced gases resulting in fast catalytic kinetics. This can be elucidated by the small Tafel slope on the MMCN electrode. Fig. 4C depicts the Tafel plots of MMCN electrode derived from the UOR polarization curves at low scan rate of 0.1 mV s⁻¹ to minimize the impact from the capacitive currents. The MMCN electrode shows a considerably smaller Tafel slope of 72 ± 0.94 mV dec⁻¹ than that of the MnO₂/Ni foam (96 ± 1.04 mV dec⁻¹) or MnCo₂O₄/Ni foam (90 ± 0.57 mV dec⁻¹), and is even slightly smaller than that of the recently reported S–MnO₂ (75 mV dec⁻¹),²² suggesting its favourable reaction kinetics towards UOR. Besides, the enhanced UOR activity of MMCN electrode mainly results from the increased electroactive sites rather than higher catalyst loading, which can be confirmed by the higher specific current densities normalized by mass loading. Fig. S12† shows the absolute UOR polarization curves of MMCN, MnO₂/Ni foam and MnCo₂O₄/Ni foam electrodes by subtracting the current contribution from OER. It can be seen that a high specific current density of ~940 mA cm⁻² g⁻¹ can be obtained from MMCN electrode at 1.7 V vs. RHE, much higher than that of MnO₂/Ni foam (500 mA cm⁻² g⁻¹) or MnCo₂O₄/Ni foam (700 mA cm⁻² g⁻¹) electrodes. Collectively, the 3D and quadruple-hierarchy MMCN electrode design can remarkably increase the effective surface area as well as accessible catalytic active sites to achieve fast UOR reaction kinetics.

In addition to the unique design of electrode architecture, the components for each level of the hierarchy were also well considered. The high conductivity of Ni foam makes it an ideal scaffold as well as a perfect electron collector. For the intermediate layer, MnCo₂O₄ is an excellent electrochemical and capacitive material^{31,50–53} owing to the increased conductivity compared to that of MnO₂, which was further verified by electrochemical impedance spectroscopy (EIS). The EIS spectrum comprises a semicircle at high-frequency and a straight slope at

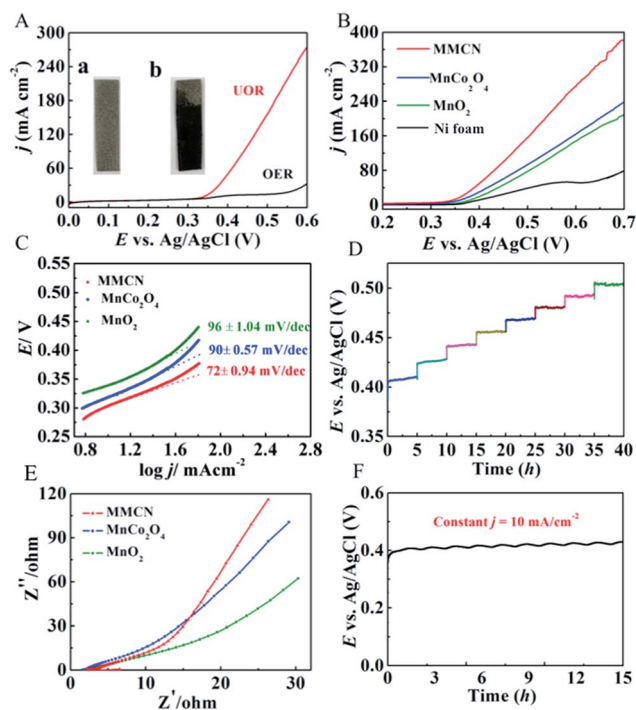


Fig. 4 (A) Linear sweep voltammetry (LSV) curves of MMCN electrode in 1 M KOH in presence (red)/absence (black) of 0.5 M urea at a scan rate of 5 mV s⁻¹. The inset is the optical image of (a) Ni foam (b) MMCN. (B) UOR polarization curves and (C) Tafel plots of MMCN, MnCo₂O₄/Ni foam, MnO₂/Ni foam and Ni foam electrodes. (D) Multi-current process of MMCN, (E) Nyquist plots of MMCN, MnCo₂O₄/Ni foam, MnO₂/Ni foam and Ni foam electrodes and (F) chronopotentiometric curve at a constant current density of 10 mA cm⁻² for MMCN electrode in 0.5 M urea per 1 M KOH.

low-frequency, representing the internal charge transfer resistance and ion diffusion resistance, respectively.⁵⁴ The Nyquist plots recorded in Fig. S13† indicate that the binary MnCo_2O_4 gives a smaller semicircle and higher slope than the pristine MnO_2 , suggesting its small internal resistance and fast charge transport capability. MnO_2 is considered to be a promising electrocatalyst due to its multiple valence states. Moreover, MnO_2 shows better UOR selectivity as 94% current density is contributed from UOR (the rest 6% current density is caused by OER), which is higher than the 84% of MnCo_2O_4 electrode (Fig. S14†). In particular, MnO_2 nanocrystals based materials show excellent UOR performance in recent reports.^{5,22} Therefore, the MnCo_2O_4 NFs and mesoporous ultra-thin MnO_2 NSs are designed as the intermediate cores and topmost shells, respectively, to fully utilize their higher conductivity, catalytic selectivity and activity properties. By diligent design of each level of hierarchy, the electrons can transport efficiently from the Ni foam to spread all over the outermost active sites for robust electrolytic urea conversion.

Fig. 4D shows the multi-step chronopotentiometric analysis of MMCN electrode in 1 M KOH per 0.5 M urea. Specifically, a staircase current is applied to the MMCN electrode from 15 mA cm^{-2} up to 50 mA cm^{-2} with an increment of 5 mA cm^{-2} per 300 s. At the starting current value, the potential immediately levels off and remains constant for the remaining 300 s, especially at higher current. The fast chronopotentiometric response implies excellent mass transport (inwards diffusion of urea molecules and outwards dissipation of N_2 , CO_2 and O_2 bubbles), high conductivity of the mechanically robust core-shell structured MMCN electrode.³⁰ The Nyquist plots of MMCN, MnO_2/Ni foam and $\text{MnCo}_2\text{O}_4/\text{Ni}$ foam electrodes are displayed in Fig. 4E. The MMCN electrode exhibits the highest slope, further confirming the advantages of the core-shell structure for ion diffusion.⁵⁴ Furthermore, the long-term stability under continuous gas evolution is another key consideration for industrial application. The MMCN electrode was tested in a bulk UOR process at a constant current density of 10 mA cm^{-2} , high catalytic stability was maintained over 15 h urea electrolysis (Fig. 4F), which outperforms all reported electrode materials in Table S1.†

During the urea electrolysis, HER is the main cathodic reaction. The catalytic activity of cathode also has a crucial effect on the electrolytic cell for overall urea electrolysis. Intriguingly, the MMCN cathode shows comparable HER activity to Pt in alkaline media, especially at high current densities. As shown in Fig. 5A, the MMCN electrode can produce a current density up to 10 mA cm^{-2} even at a relatively low overpotential (0.2 V and 0.25 V presence/absence urea). At an overpotential of 0.5 V, the MMCN electrode is able to deliver a high current density of 180 mA cm^{-2} , which is comparable to the Pt plate. This performance is mainly contributed by the well-design quadruple-hierarchy electrode architecture. The obtained Tafel slopes (Fig. 5B) in 1 M KOH in presence/absence of urea are 110 mV dec^{-1} and 130 mV dec^{-1} , which are also competitive to those of Pt plate (122 mV dec^{-1} and 96 mV dec^{-1}), suggesting its fast HER kinetics in alkaline media. Fig. 5C displays the full scan CV curves for MMCN and Pt plate in 1 M KOH in the presence/absence of 0.5 M urea,

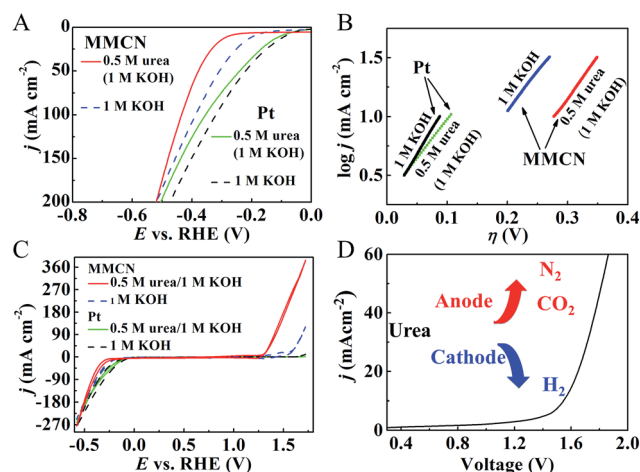


Fig. 5 (A) HER polarization curves, (B) corresponding Tafel plots, (C) full scan CV curves of MMCN electrode and Pt plate in 1 M KOH in the absence and presence of 0.5 M urea, and (D) overall electrolysis in two-electrode configuration in 0.5 M urea per 1 M KOH (inset: corresponding chronopotentiometric response).

demonstrating the obtained MMCN electrode is active for both UOR and HER.

Benefiting from the bifunctional properties of the MMCN electrode, a urea electrolytic cell has been fabricated with both electrodes made from MMCN. As shown in Fig. 5D, the urea electrolyzer delivered a current density of 10 mA cm^{-2} at a voltage of 1.58 V, and high current density of 60 mA cm^{-2} can be achieved at a voltage of 1.85 V. This performance surpasses that of the state-of-art Pt/C- IrO_2 and S- MnO_2 - CoP_x electrode pairs.^{5,25} Furthermore, a stable potential around 1.75 V can be maintained during a 15 h testing period at the current density of 20 mA cm^{-2} , exhibiting its excellent long-term stability as a biocatalyst for both UOR and HER (Fig. S15†). Using earth-abundant metal oxide electrocatalysts which operate in the same electrolyte for both anodic and cathodic reactions, is important for many renewable energy conversion processes, especially for water splitting.^{55–57}

Conclusions

In summary, a freestanding hierarchical MMCN electrode with four levels of hierarchy has been developed through a combination of hydrothermal and electrochemical approaches. This novel electrode architecture leads to ultra-large electroactive surface area and shows extraordinary catalytic activity, selectivity and long-term catalytic stability in electrolytic urea oxidation. Moreover, the multilevel hierarchical design is also favourable for fast electrolysis kinetics, including highly efficient transport of reactant molecules/ions, and rapid dissipation of produced gas bubbles. In addition, the MMCN electrode exhibits excellent selectivity and catalytic activity toward electrolytic UOR and HER in alkaline media. The MMCN electrodes show excellent performance in a complete urea electrolysis cell, which is promising for the industrial application of urea electrolysis technology.

Acknowledgements

The study was supported by the ARC Discovery Grant (DP170102267) and the Australian Laureate Fellowship (DRM) programs. The authors acknowledge the use of the facilities at the Monash Centre for Electron Microscopy.

Notes and references

- 1 A. N. Rollinson, J. Jones, V. Dupont and M. V. Twigg, *Energy Environ. Sci.*, 2011, **4**, 1216.
- 2 R. P. Forslund, J. T. Mefford, W. G. Hardin, C. T. Alexander, K. P. Johnston and K. J. Stevenson, *ACS Catal.*, 2016, **6**, 5044.
- 3 R. Lan, S. Tao and J. T. Irvine, *Energy Environ. Sci.*, 2010, **3**, 438.
- 4 B. K. Boggs, R. L. King and G. G. Botte, *Chem. Commun.*, 2009, **32**, 4859.
- 5 S. Periyasamy, P. Subramanian, E. Levi, D. Aurbach, A. Gedanken and A. Schechter, *ACS Appl. Mater. Interfaces*, 2016, **8**, 12176.
- 6 J. Suntivich, K. J. May, H. A. Gasteiger, J. B. Goodenough and Y. Shao-Horn, *Science*, 2011, **334**, 1383.
- 7 M. W. Kanan and D. G. Nocera, *Science*, 2008, **321**, 1072.
- 8 F. Gao, G. L. Zhao, S. Yang and J. J. Spivey, *J. Am. Chem. Soc.*, 2013, **135**, 3315.
- 9 D. Voiry, H. Yamaguchi, J. Li, R. Silva, D. C. Alves, T. Fujita, M. Chen, T. Asefa, V. B. Shenoy and G. Eda, *Nat. Mater.*, 2013, **12**, 850.
- 10 M. Gong, Y. Li, H. Wang, Y. Liang, J. Z. Wu, J. Zhou, J. Wang, T. Regier, F. Wei and H. Dai, *J. Am. Chem. Soc.*, 2013, **135**, 8452.
- 11 C. Xiao, X. Lu and C. Zhao, *Chem. Commun.*, 2014, **50**, 10122.
- 12 L. C. Seitz, C. F. Dickens, K. Nishio, Y. Hikita, J. Montoya, A. Doyle, C. Kirk, A. Vojvodic, H. Y. Hwang and J. K. Nørskov, *Science*, 2011, **216**, 353.
- 13 R. G. Hadt, D. Hayes, C. N. Brodsky, A. M. Ullman, D. M. Casa, M. H. Upton, D. G. Nocera and L. X. Chen, *J. Am. Chem. Soc.*, 2016, **138**, 11017.
- 14 W. Xu, H. Zhang, G. Li and Z. Wu, *Sci. Rep.*, 2014, **4**, 5863.
- 15 R. L. King and G. G. Botte, *J. Power Sources*, 2011, **196**, 2773.
- 16 W. Xu, Z. Wu and S. Tao, *Energy Technol.*, 2016, **4**, 1329.
- 17 G. Wang, Y. Ling, X. Lu, H. Wang, F. Qian, Y. Tong and Y. Li, *Energy Environ. Sci.*, 2012, **5**, 8215.
- 18 M. S. Wu, R.-Y. Ji and Y. R. Zheng, *Electrochim. Acta*, 2014, **144**, 194.
- 19 R. Ding, L. Qi, M. Jia and H. Wang, *Nanoscale*, 2014, **6**, 1369.
- 20 A. T. Miller, B. L. Hassler and G. G. Botte, *J. Appl. Electrochem.*, 2012, **42**, 925.
- 21 Y. J. Wang, B. Fang, H. Li, X. T. Bi and H. Wang, *Prog. Mater. Sci.*, 2016, **82**, 445.
- 22 S. Chen, J. Duan, A. Vasileff and S. Z. Qiao, *Angew. Chem.*, 2016, **128**, 3868.
- 23 M. S. Wu, G. W. Lin and R. S. Yang, *J. Power Sources*, 2014, **272**, 711.
- 24 E. J. Popczun, C. G. Read, C. W. Roske, N. S. Lewis and R. E. Schaak, *Angew. Chem.*, 2014, **126**, 5531.
- 25 C. Tang, L. Gan, R. Zhang, W. Lu, X. Jiang, A. M. Asiri, X. Sun, J. Wang and L. Chen, *Nano Lett.*, 2016, **16**, 6617.
- 26 E. J. Popczun, J. R. McKone, C. G. Read, A. J. Biacchi, A. M. Wiltrout, N. S. Lewis and R. E. Schaak, *J. Am. Chem. Soc.*, 2013, **135**, 9267.
- 27 H. B. Gray, *Nat. Chem.*, 2009, **1**, 7.
- 28 S. Wang, X. Gao, X. Hang, X. Zhu, H. Han, W. Liao and W. Chen, *J. Am. Chem. Soc.*, 2016, **138**, 16236.
- 29 C. Xiao, Y. Li, X. Lu and C. Zhao, *Adv. Funct. Mater.*, 2016, **26**, 3515.
- 30 X. Lu and C. Zhao, *Nat. Commun.*, 2015, **6**, 6616.
- 31 C. Xiao, X. Zhang, T. C. Mendes, G. P. Knowles, A. L. Chaffee and D. R. MacFarlane, *J. Phys. Chem. C*, 2016, **120**, 23976.
- 32 C. Xu, Z. Li, C. Yang, P. Zou, B. Xie, Z. Lin, Z. Zhang, B. Li, F. Kang and C. P. Wong, *Adv. Mater.*, 2016, **28**, 4105.
- 33 H. D. Lim, H. Song, J. Kim, H. Gwon, Y. Bae, K. Y. Park, J. Hong, H. Kim, T. Kim and Y. H. Kim, *Angew. Chem., Int. Ed.*, 2014, **53**, 3926.
- 34 H. Hu, B. Guan, B. Xia and X. W. Lou, *J. Am. Chem. Soc.*, 2015, **137**, 5590.
- 35 L. Huang, D. Chen, Y. Ding, S. Feng, Z. L. Wang and M. Liu, *Nano Lett.*, 2013, **13**, 3135.
- 36 G. Zhang and X. W. D. Lou, *Adv. Mater.*, 2013, **25**, 976.
- 37 T. F. Jaramillo, K. P. Jørgensen, J. Bonde, J. H. Nielsen, S. Horch and I. Chorkendorff, *Science*, 2007, **317**, 100.
- 38 J. Xie, H. Zhang, S. Li, R. Wang, X. Sun, M. Zhou, J. Zhou, X. W. D. Lou and Y. Xie, *Adv. Mater.*, 2013, **25**, 5807.
- 39 S. Wang, Y. Hou and X. Wang, *ACS Appl. Mater. Interfaces*, 2015, **7**, 4327.
- 40 B. Lee, C. S. Yoon, H. R. Lee, K. Y. Chung, B. W. Cho and S. H. Oh, *Sci. Rep.*, 2014, **4**, 6066.
- 41 M. Asif, A. Aziz, A. Q. Dao, A. Hakeem, H. Wang, S. Dong, G. Zhang, F. Xiao and H. Liu, *Anal. Chim. Acta*, 2015, **898**, 34.
- 42 M. Huang, Y. Zhang, F. Li, Z. Wang, N. Hu, Z. Wen and Q. Liu, *Sci. Rep.*, 2014, **4**, 4518.
- 43 C. Yuan, J. Li, L. Hou, L. Yang, L. Shen and X. Zhang, *J. Mater. Chem.*, 2012, **22**, 16084.
- 44 S. Liu, K. S. Hui and K. N. Hui, *ChemNanoMat*, 2015, **1**, 593.
- 45 R. Li, D. Hu, S. Zhang, G. Zhang, J. Wang and Q. Zhong, *Energy Technol.*, 2015, **3**, 1183.
- 46 T. Y. Ma, Y. Zheng, S. Dai, M. Jaroniec and S. Z. Qiao, *J. Mater. Chem. A*, 2014, **2**, 8676.
- 47 J. Liang, Z. Fan, S. Chen, S. Ding and G. Yang, *Chem. Mater.*, 2014, **26**, 4354.
- 48 H. Y. Su, Y. Gorlin, I. C. Man, F. Calle-Vallejo, J. K. Nørskov, T. F. Jaramillo and J. Rossmeisl, *Phys. Chem. Chem. Phys.*, 2013, **14**, 14010.
- 49 D. Wang, W. Yan, S. H. Vijapur and G. G. Botte, *Electrochim. Acta*, 2013, **89**, 732.
- 50 X. Ge, Y. Liu, F. T. Goh, T. A. Hor, Y. Zong, P. Xiao, Z. Zhang, S. H. Lim, B. Li and X. Wang, *ACS Appl. Mater. Interfaces*, 2014, **6**, 12684.
- 51 F. Song and X. Hu, *J. Am. Chem. Soc.*, 2014, **136**, 16481.
- 52 Y. Liang, H. Wang, J. Zhou, Y. Li, J. Wang, T. Regier and H. Dai, *J. Am. Chem. Soc.*, 2012, **134**, 3523.
- 53 A. K. Mondal, D. Su, S. Chen, A. Ung, H. S. Kim and G. Wang, *Chem.–Eur. J.*, 2015, **21**, 1526.

- 54 X. Xia, J. Tu, Y. Zhang, X. Wang, C. Gu, X. B. Zhao and H. J. Fan, *ACS Nano*, 2012, **6**, 5531.
- 55 J. Luo, J. Im, M. T. mayer, M. Schreier, M. K. Nazeeruddin, N. Park, D. Tilley, H. J. Fan and M. Grätzel, *Science*, 2014, **345**, 1593.
- 56 H. T. Wang, H. Lee, Y. Deng, Z. Y. Lu, P. Hsu, Y. Y. Liu, D. C. Lin and Y. Cui, *Nat. Commun.*, 2015, **6**, 7261.
- 57 Y. Yan, B. Y. Xia, B. Zhao and X. Wang, *J. Mater. Chem A*, 2016, **4**, 17587.

Supporting Information

MnO₂/MnCo₂O₄/Ni Heterostructure with Quadruple Hierarchy: A Bifunctional Electrode Architecture for Overall Urea Oxidation

Changlong Xiao^a, Shuni Li^b, Xinyi Zhang^{a*} and Douglas R. MacFarlane^{a*}

^aSchool of Chemistry, Monash University, Melbourne, Victoria, 3800, Australia

^bSchool of Chemistry and Chemical Engineering, Shaanxi Normal University, Xi'an, Shaanxi, 710062, China

*Email - [REDACTED]

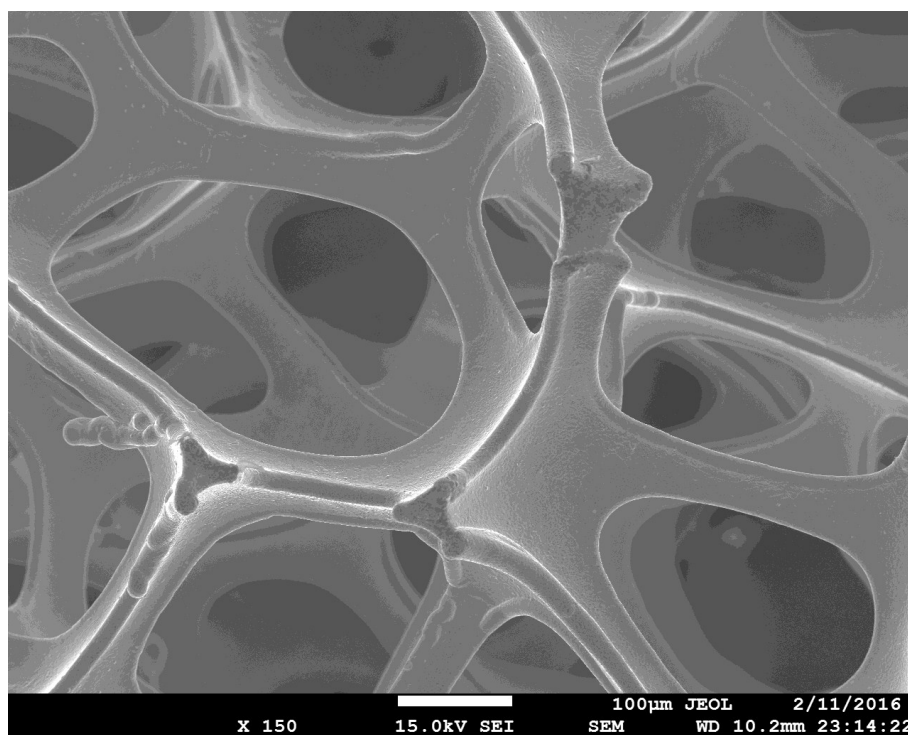


Figure S1. SEM image of bare Ni foam scaffold.

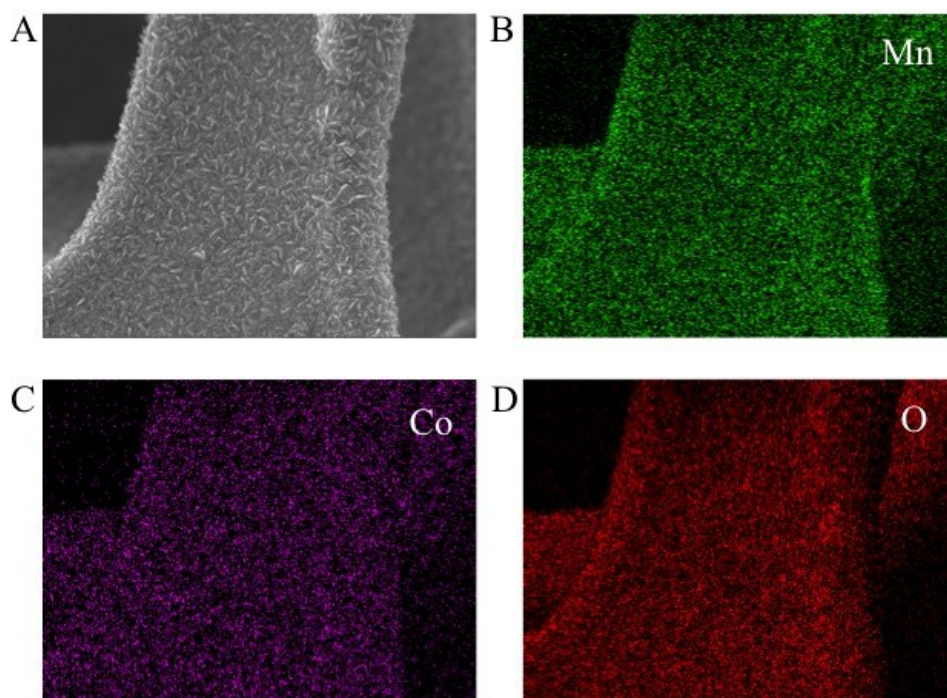


Figure S2. (A) SEM image and (B)-(D) elemental mapping images of $\text{MnCo}_2\text{O}_4/\text{Ni}$ foam composites.

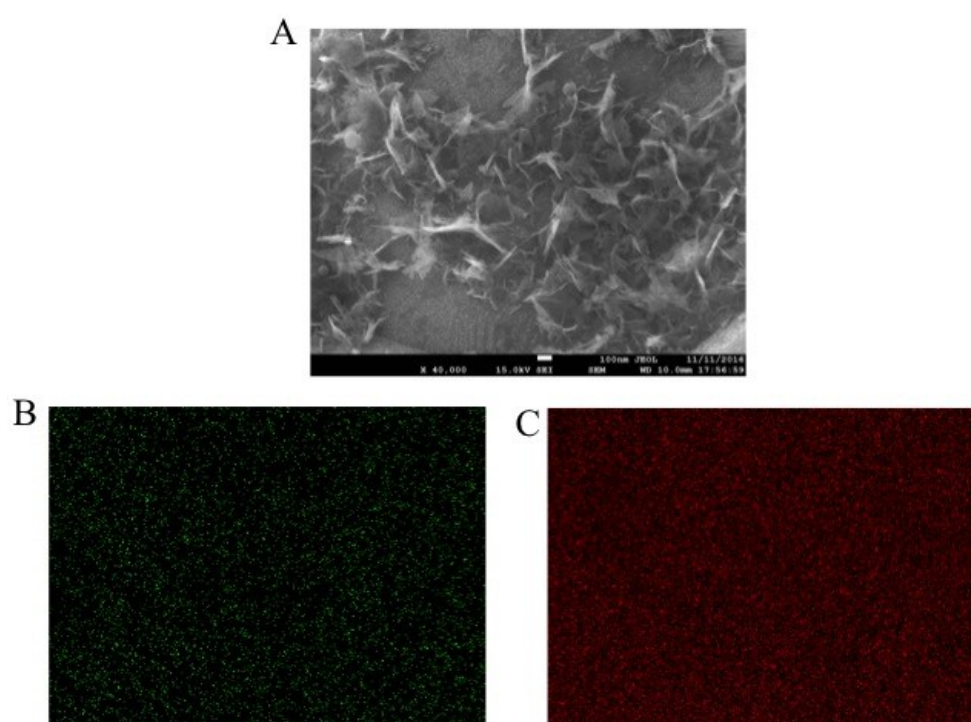


Figure S3. (A) SEM image and (B)-(C) elemental mapping images of MnO_2/Ni foam composites.

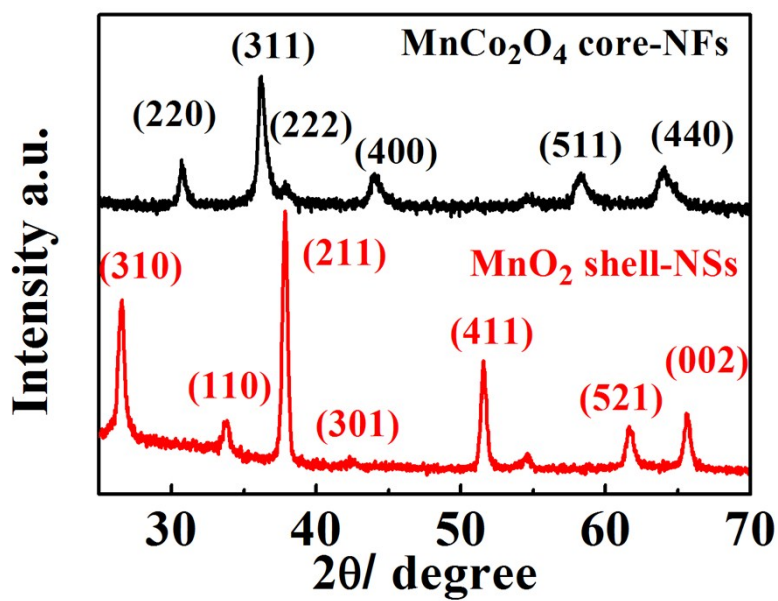


Figure S4. XRD patterns of MnO₂ Shell-NSs electrodeposited on ITO glass (red) and MnCo₂O₄ core-NFs (black) .

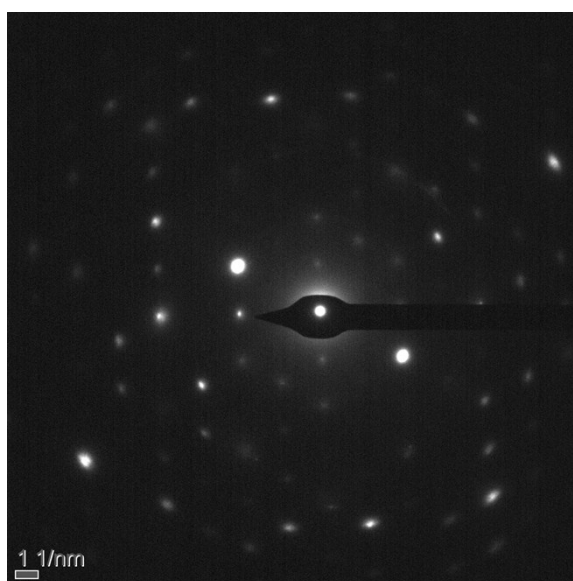


Figure S5. SAED pattern of electrodeposited MnO₂ shell-NSs.

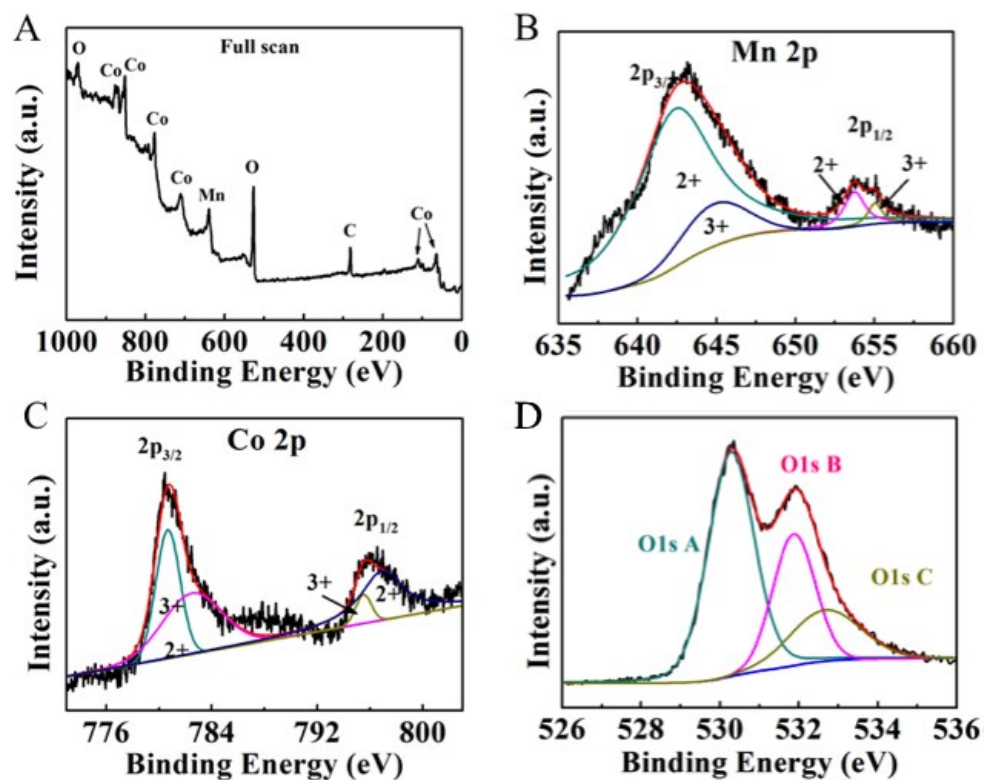


Figure S6. (A) XPS spectrum of MMCN, High-resolution XPS spectrum of (B) Mn 2p, (C) Co 2p and (D) O 1s.

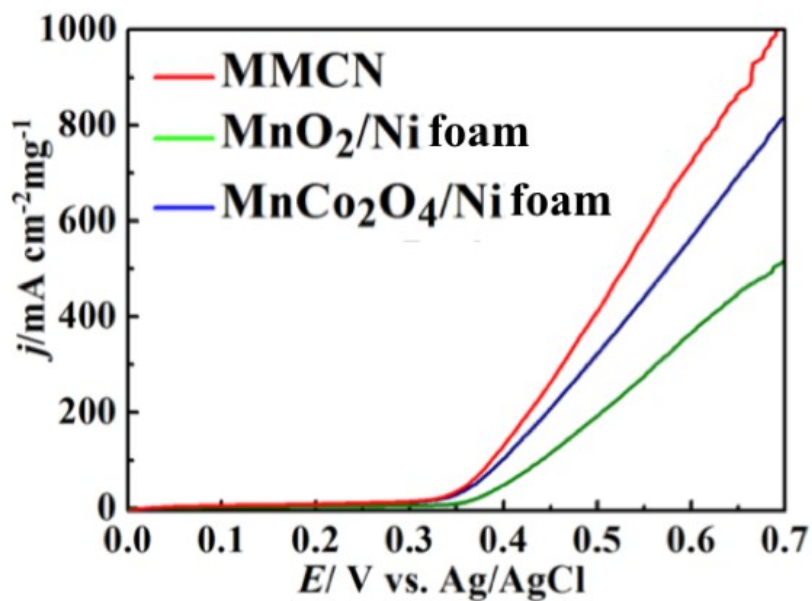


Figure S7. UOR polarization curves of MMCN, $\text{MnCo}_2\text{O}_4/\text{Ni}$ foam and MnO_2/Ni foam electrodes in 0.5 urea/1 M KOH at a scan rate of 5 mV s^{-1} .

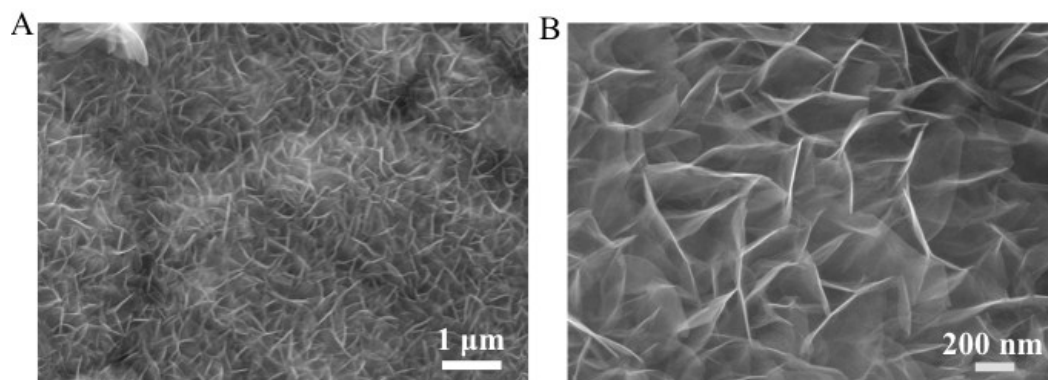


Figure S8. SEM images of MnO₂/Ni foam electrode at different magnifications.

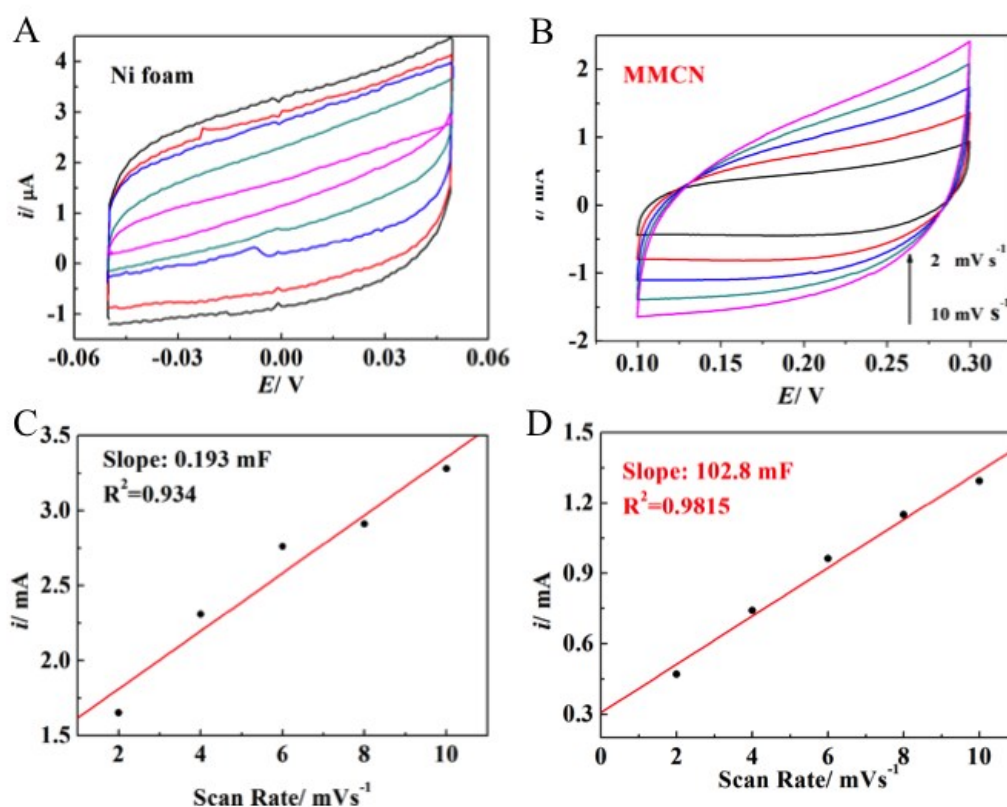


Figure S9. CV curves measured at different scan rates from 2 mV/s to 10 mV/s of (A) Ni foam, (B) MMCN, current densities recorded at 0.2 V plotted vs. scan rates of (C) Ni foam and (D) MMCN.

The calculation of the electrochemical surface area (ECSA) is based on the measured double-layer capacitance of the obtained MMCN, MnO₂/Ni foam, MnCo₂O₄/Ni foam and Ni foam electrodes in 1 M KOH according to previously established methods. The calculated capacitance and corresponding roughness factors for each synthesized electrode are listed in Table S2.

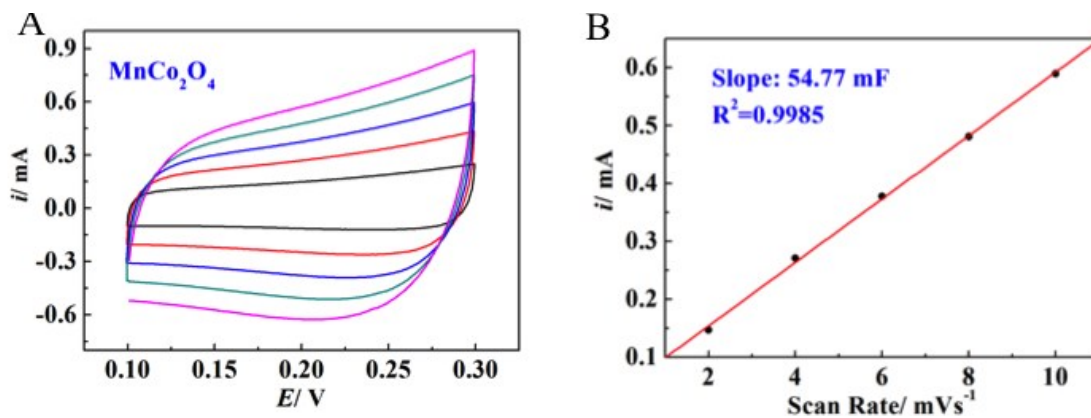


Figure S10. CV curves of $\text{MnCo}_2\text{O}_4/\text{Ni}$ foam electrode measured at different scan rates from 2 mV/s to 10 mV/s and (B) current densities at 0.2 V plotted vs. scan rates.

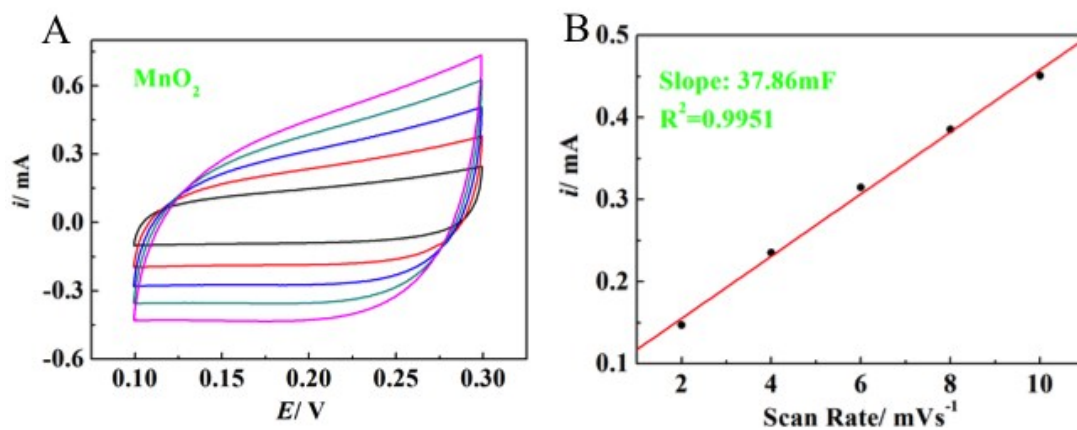


Figure S11. CV curves of MnO_2/Ni foam electrode measured at different scan rates from 2 mV/s to 10 mV/s and (B) current densities at 0.2 V plotted vs. scan rates.

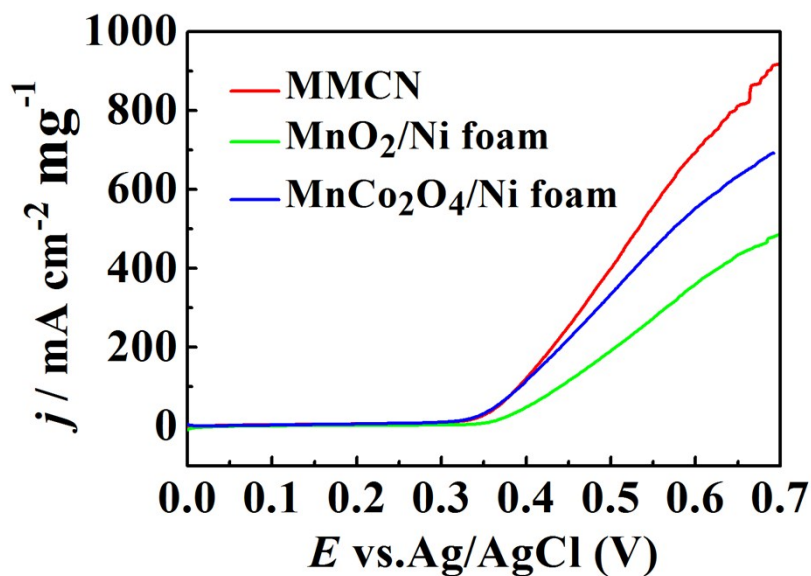


Figure S12. Absolute UOR polarization curves of MMCN, $\text{MnCo}_2\text{O}_4/\text{Ni}$ foam and MnO_2/Ni foam electrodes in 0.5 urea/1 M KOH at a scan rate of 5 mV s^{-1} . The current is normalized by catalyst mass loading and subtracted off the current from OER.

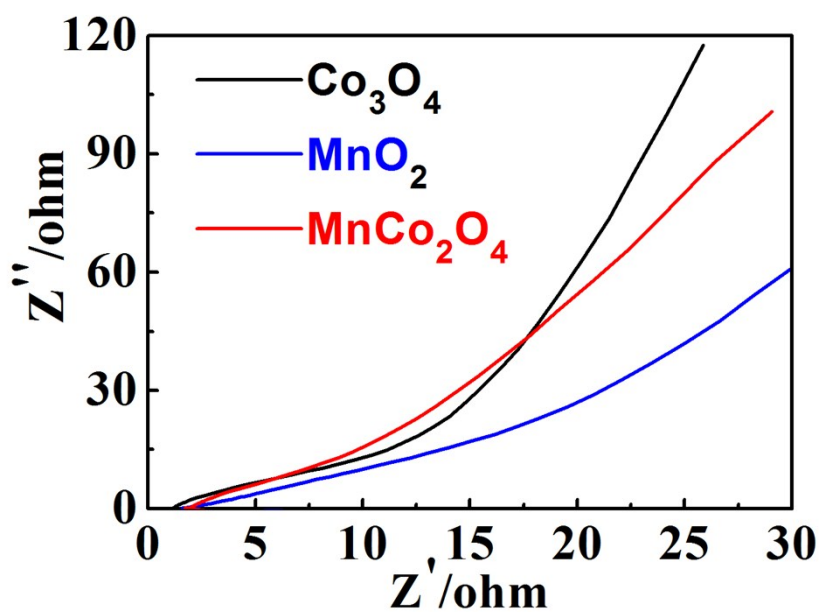


Figure S13. Nyquist plots $\text{Co}_3\text{O}_4/\text{Ni}$ foam, $\text{MnCo}_2\text{O}_4/\text{Ni}$ foam and MMCN electrodes.

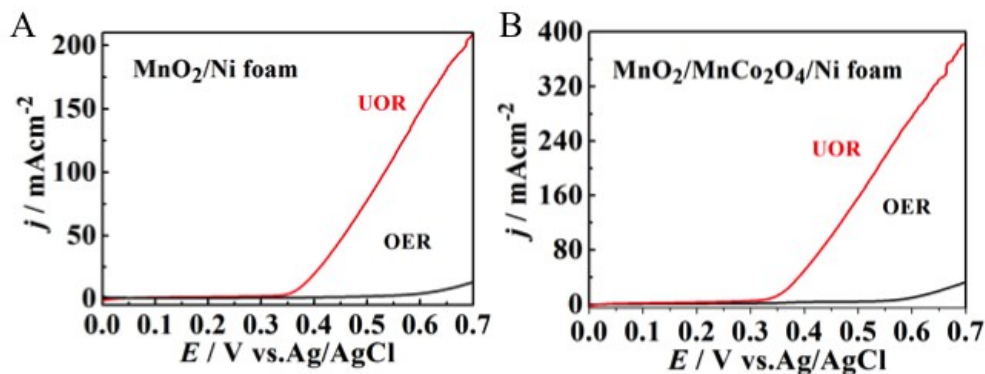


Figure S14. Comparison of UOR and OER polarization curves of (A) MnO_2/Ni foam and (B) MnCo_2O_4 electrodes.

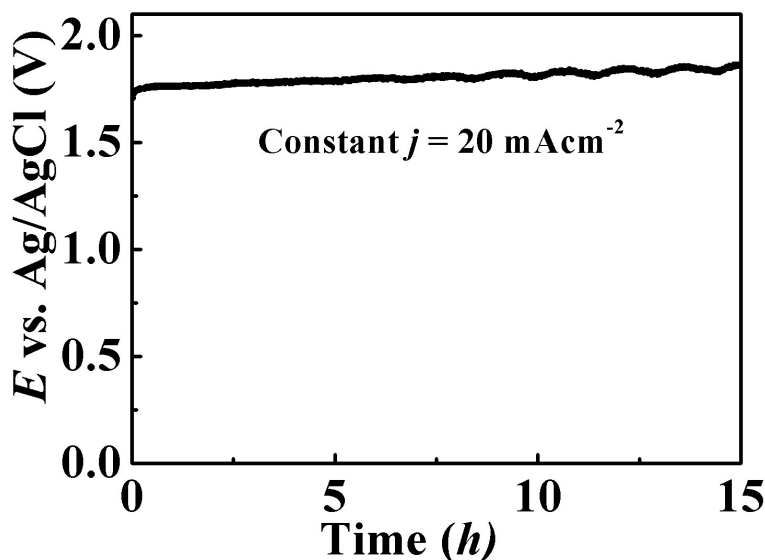


Figure S15. Chronopotentiometric curves at constant current density of 10 mA cm^{-2} for in two-electrode configuration in 0.5 M urea/ 1 M KOH.

The voltage is quite stable during the experiment, suggesting long-term stability of the electrodes.

In order to clarify any possible contribution of metal oxide to the reduction current of the electrode, the quantity of charge consumed by metal oxide reduction during 15 hours has been calculated as follows:

The total charge passed, Q_{total}

$$Q_{\text{total}} = i \cdot t = 0.02 \text{ A cm}^{-2} \cdot 0.3 \text{ cm}^2 \cdot 15 \text{ h} \cdot 3600 = 324 \text{ C}$$

MnO_2 is the main component of the metal oxide. The mass of MnO_2 is $\sim 1.35 \text{ mg}$. The maximum possible charge that could be consumed in reduction of MnO_2 can be calculated as follow:

$$Q_{\text{MnO}_2} = 1.35 \times 10^{-3} \cdot 4 \cdot 96450 / 70.9 = 7.34 \text{ C}$$

$$Q_{\text{MnO}_2 \text{ reduction}} / Q_{\text{total}} \cdot 100\% = 2.25\%$$

The calculation confirms that the cathodic current are substantially from hydrogen generation and the MMCN electrode can act as stable hydrogen catalyst.

Table S1. Comparison of the UOR catalytic activity between recently reported electrode materials .

Catalysts	Onset potential (at 10 mA cm ⁻²)	$j@1.7V$ vs. RHE (mA cm ⁻²)	Mass Activity (1.7 V vs. RHE)	Mass Loading	Reference
MnO ₂ /MnCo ₂ O ₄	1.33	384	1020 mA cm ⁻² mg ⁻¹	1.27	This work
MnCo ₂ O ₄	1.37	240	840	0.97	This work
MnO ₂	1.38	210	550	1.35	This work
S- MnO ₂	1.33	~340	---	1.5	22
Pt	1.50	110	---	2.5	4
Graphene- Ni(OH) ₂	1.52	35	---	0.25	49
Ni(OH) ₂ nanocube array	1.55	---	400	0.3	18
LaNiO ₃	~1.39	---	371	---	2
NiO nanosheet	1.38	---	670	0.27	23

Table S2. Roughness factors of the synthesized electrode materials

Electrode Materials	MnO ₂ /MnCo ₂ O ₄	MnO ₂	MnCo ₂ O ₄	Ni foam
Specific Capacitance	102.8	37.9	54.8	0.193
Roughness Factor	533	196	284	1

Chapter 4

Nanostructured Gold/Bismutite Hybrid Heterocatalysts for Plasmon-Enhanced Photosynthesis of Ammonia

4.1 Overview

This chapter is a paper titled “Nanostructured Gold/Bismutite Hybrid Heterocatalysts for Plasmon-Enhanced Photosynthesis of Ammonia” that was published in ACS Sustainable Chemistry & Engineering in 2017.

Sustainable nitrogen cycle management is one of the major challenges facing engineers and scientists due to its importance for food and energy security. The product of nitrogen reduction, ammonia (in the form of liquid anhydrous ammonia), is also an important hydrogen storage medium owing to its high stored energy density. As an energy carrier, ammonia is zero-carbon emission and plays an important role in the implementation of a hydrogen economy. Recently, a great deal of research interest has been devoted to the development of ammonia synthesis under ambient conditions including electro- and photosynthesis.¹⁻⁴

This work is thus focusing on the synthesis of novel catalysts and their characterization for low temperature NH₃ production, and NH₃ synthesis using new sources of H₂ (H₂O) other than fossil-fuel-derived hydrocarbons, new sources of energy to activate the N–N bond (solar energy), improved reactor design for better reactant/product/heat management, and energy analysis of the overall process. We designed a Au/Bi₂O₂CO₃ hybrid nanostructure which exhibits plasmon-enhanced photocatalytic activity for solar ammonia production at ambient temperature and pressure with a high yield of 38 μmol/h•g.



This figure demonstrates the use of nanostructured Au/Bi₂O₂CO₃ hybrid for photosynthesis of NH₃ from H₂O and N₂ under ambient conditions.

References

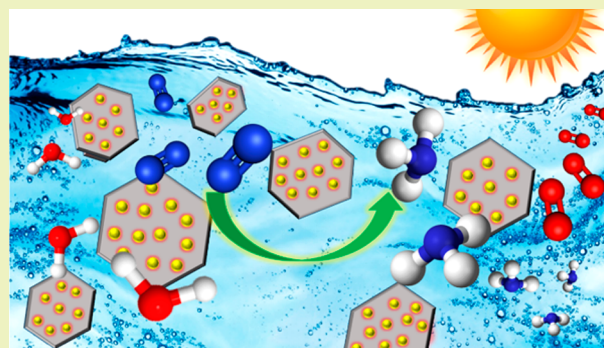
1. M. Ali, F. Zhou, K. Chen, C. Kozur, C. Xiao, L. Bourgeois, X. Zhang and D. R. MacFarlane, *Nat. Commun.* 2016, **7**, 11335.
2. B. H. R. Suryanto, C. S. M. Kang, D. Wang, C. Xiao, F. Zhou, L. M. Azofra, L. Cavallo, X. Zhang and D. R. MacFarlane, *ACS Energy Lett.* 2018, **3**, 1219-1224.
3. F. Zhou, L. M. Azofra, M. Ali, M. Kar, A. N. Simonov, C. McDonnell-Worth, C. Sun, X. Zhang and D. R. MacFarlane, *Energy Environ. Sci.* 2017, **10**, 2516.
4. C. Xiao, H. Hu, X. Zhang and D. R. MacFarlane, *ACS Sustain. Chem. Eng.* 2017, **5**, 10858.

Nanostructured Gold/Bismutite Hybrid Heterocatalysts for Plasmon-Enhanced Photosynthesis of Ammonia

Changlong Xiao,[†] Hong Hu,^{†,‡} Xinyi Zhang,^{*,†} and Douglas R. MacFarlane^{*,†}[†]Australian Centre for Electromaterials Science, School of Chemistry, Monash University, Victoria 3800, Australia[‡]School of Chemistry, Nanjing Institute of Technology, Nanjing 211800, China

Supporting Information

ABSTRACT: Nitrogen (N₂) reduction to produce ammonia (NH₃) is one of the most important chemical processes globally. Nowadays, the Haber–Bosch process is the main industrial procedure for artificial N₂ fixation, which requires extremely harsh synthetic conditions and large energy consumption resulting in massive emission of greenhouse gas. Hence, an alternative photosynthesis of NH₃ under mild condition, which is sustainable and less energy consuming, would be highly desirable. In this study, Au nanoparticles modified (BiO)₂CO₃ nanodisks were fabricated through a facile hydrothermal method followed by chemical bath deposition and investigated for the photocatalytic reduction of N₂ in a pure water system at atmospheric pressure and room temperature. The induction of Au nanoparticles can dramatically enhance the light trapping as well as charge separation in the Au/(BiO)₂CO₃ hybrid, thereby promoting overall energy conversion efficiency. The synergetic effect of the nanostructured gold/bismutite hybrid results in high catalytic activity and exhibits high performance for artificial photosynthesis of ammonia.



KEYWORDS: Plasmonic effect, Nanoparticles, Photosynthesis, Nitrogen fixation, Ammonia

INTRODUCTION

Ammonia is one of the most important chemicals for the industrial production of fertilizers, pharmaceuticals, and many other nitrogenous compounds. Ammonia has also been considered as a potential carbon-free fuel that can be used as an ecofriendly energy storage intermediate.¹ The current industrial scale production of ammonia relies on the classic Haber–Bosch process, which consumes 1–3% of the global annual energy supply^{2,3} and requires extreme conditions (e.g., ~500 °C, 300 bar) to break the strong covalent bonds of nitrogen.⁴ In addition, the process consumes a large amount of the world's natural gas production and emits large quantities of carbon dioxide, aggravating global climate change.^{5–7} To tackle such challenges, many efforts have been made with a focus on the conversion of nitrogen from air into ammonia under mild conditions. Among them, artificial solar-driven photosynthesis of ammonia has attracted great interest due to the inexhaustibility of solar energy and its capacity to reduce carbon emissions.^{8–10}

The development of high-efficiency catalytic systems is the key to photosynthesis of ammonia. Recently, nanostructured bismuth-containing semiconductors, such as Bi₂S₃, Bi₂WO₆, and BiVO₄, fabricated through various methods have been extensively studied for photocatalysis.^{11–14} Among them, Bi₂O₂CO₃ (denoted as BSC) with one-dimensional (1D), two-dimensional (2D), and three-dimensional (3D) nanostructures have drawn particular research interest owing to their

excellent performance in a range of applications, including photocatalysis, supercapacitor, and sensing as well as antibacterial agent.^{15–19} Among them, the Aurivillius-type BSC with alternative (Bi₂O₂)²⁺ and CO₃²⁻ layering^{20–22} exhibits a unique anisotropic crystal structure and internal static electric field effect, which favors photoinduced charge separation and transfer.^{23–25} However, its relatively wide bandgap limits its performance in light harvesting in the visible region. In recent years, plasmonic metallic nanostructures have received much attention for solar energy conversion due to their strong interaction with resonant photons through an excitation of surface plasmon resonance (SPR).²⁶ Solar energy collection can be significantly enhanced by plasmonic nanostructures via photonic or/and plasmonic energy-transfer enhancement.^{27–29} Besides, the charge separation can be enhanced by the transfer of photoexcited electrons from metal nanoparticles to the conduction band of the semiconductor.³⁰ Previously, we have demonstrated plasmon-enhanced nanostructured silicon loaded with gold nanoparticles with excellent light harvesting and charge separation properties for solar-driven nitrogen fixation.³¹ In this work, we have achieved enhanced solar-light-driven conversion of nitrogen to ammonia using a plasmon-enhanced nanostructured BSC

Received: August 13, 2017

Revised: September 15, 2017

Published: September 25, 2017

nanodisks (denoted as NDs) modified with gold nanoparticles (denoted as NPs) as the reduction catalysis sites. This hetero-nanostructure creates an artificial photosynthesis device capable of carrying out solar-driven nitrogen reduction reactions into ammonia.

EXPERIMENTAL SECTION

Materials. Bismuth nitrate, urea, sodium hydroxide, gold chloride, hydrazine hydrate, and sodium sulfite were of analytical grade and supplied by Sigma-Aldrich.

Hydrothermal Preparation of BSC NDs. The $\text{Bi}_2\text{O}_2\text{CO}_3$ (BSC) NDs were prepared through a hydrothermal method. Typically, 4.8252 g of $\text{Bi}(\text{NO}_3)_3$ and 2.5 g of $\text{CO}(\text{NH}_2)_2$ and 0.387 g of $\text{Na}_3\text{C}_6\text{H}_5\text{H}_7$ were dissolved in 30 mL of NaOH (1 M) aqueous solution under magnetic stirring at 600 rpm for 60 min. Subsequently, the as-prepared homogeneous solution was transferred into a 45 mL Teflon-lined stainless steel autoclave. The autoclave was sealed and placed in an oven at 180 °C for 6 h. After the hydrothermal treatment, the autoclave was cooled to room temperature. The precipitate was collected and washed with copious amounts of distilled water and absolute ethanol several times, assisted by sonication treatment to ensure the complete removal of the possible residues. Finally, the obtained sample was dried in a vacuum oven at 80 °C overnight.

Chemical Bath Deposition of Au NPs onto BSC NDs. Au NPs were uniformly loaded on the surface of the as-obtained BSC NDs via chemical bath deposition (CBD). Au NPs with diameters from ~11 to ~36 nm were obtained. Specifically, 40 mg of the above-obtained BSC NDs were first activated in a solution containing 1 g/L PdCl_2 and 5 g/L HCl for 2 h by sonication and dried in a vacuum oven. After the activation treatment, the Pd colloids on the surface of the BSC nanodisks provided the catalytic sites for the electron transfer and nucleation and growth of Au nanoparticles. The deposition solution was prepared by dissolving 48 mg of HAuCl_4 , 640 mg of Na_2SO_3 , 20 mg of EDTA, and 120 mg of KH_2PO_4 in 4 mL of H_2O . The pH of the solution was adjusted to 9.0 with the addition of 1 M NaOH dropwise. Then, 10 mg of activated BSC was dispersed into the as-prepared solution under vigorous stirring. Subsequently, 40 mg of $\text{N}_2\text{H}_4\cdot\text{H}_2\text{O}$ was added into the suspension followed by another 2 h stirring at 60 °C. During the process, the color of the suspension changed from white to gray gradually with the addition of $\text{N}_2\text{H}_4\cdot\text{H}_2\text{O}$. After removing the upper, clear solution, the obtained sample was rinsed with distilled water for 3 times and dried in a vacuum oven at 60 °C overnight.

Characterization. The structures of the as-prepared samples were determined using X-ray diffraction (XRD, D8 ADVANCE) with $\text{Cu K}\alpha$ radiation (25 mA and 40 kV). The materials were investigated by a scanning electron microscope (SEM, Magellan 400 FEGSEM instrument) and energy dispersive spectrometer (EDS) that is attached to the Magellan 400 FEGSEM. A transmission electron microscope (TEM, Philips CM20, 200 kV) and a high-resolution transmission electron microscope (HRTEM, JEOL-2011, 200 kV) were further used to confirm the morphology and crystal phase. The X-ray photoelectron (XPS) analysis was carried out on a Thermal ESCALA 250i X-ray photoelectron spectrometer. All binding energies were calibrated to the C 1s peak at 284.6 eV. UV–vis diffuse reflectance spectra were recorded on a spectrophotometer in the range between 200 and 800 nm (UV–vis, SHIMADZU UV-2600).

Photocatalytic Activity Test. All nitrogen reduction reactions were conducted in a designed photoreduction cell at ambient temperature and pressure. A 300 W Xe lamp was used as an artificial solar light source, while the illumination intensity was 1 sun. The Milli-Q water used in the photocatalytic experiment was bubbled with pure nitrogen for 1 h to remove the dissolved oxygen prior to each test. Typically, 20 mg of photocatalyst was dispersed into 20 mL of Milli-Q water and sonicated for 15 min in darkness to ensure homogeneity. During the photoreduction, the reaction solution was under magnetic stirring and purged with nitrogen with a flow rate of 20 mL/min. A 1 mL aliquot of reaction solution was collected every 30 min, and the photocatalyst was removed by centrifugation. The amount of

produced ammonia was monitored by the indophenol method. Typically, 1 mL of trisodium citrate/NaOH solution, 40 μL of phenol/alcohol, and 40 μL of sodium nitroprusside aqueous solution were added into the obtained 1 mL of reaction solution. The mixed solution was stored in darkness for 3 h prior to UV–vis measurement. The adsorption peak of indophenol at around 630 nm was recorded and used for the ammonia yield calculation. The solar energy conversion efficiency (SEC) is calculated according to the following equation:

$$\text{SEC efficiency/\%} = \frac{\left[\frac{\Delta G \text{ of ammonia generation}}{\text{J/mol}} \right] \left[\frac{\text{produced ammonia}}{\text{mol}} \right]}{\left[\frac{\text{energy input}}{\text{W}} \right] \left[\frac{\text{reaction time}}{\text{s}} \right]} \times 100 \quad (1)$$

The ΔG for NH_3 generation is 339×10^3 J/mol. The calculation is based on a 1 h photoreaction reaction under 1 sun irradiance.

RESULTS AND DISCUSSION

The morphologies of the BSC nanodisks were observed by SEM. As shown in Figure 1a,b, the as-prepared BSCs are

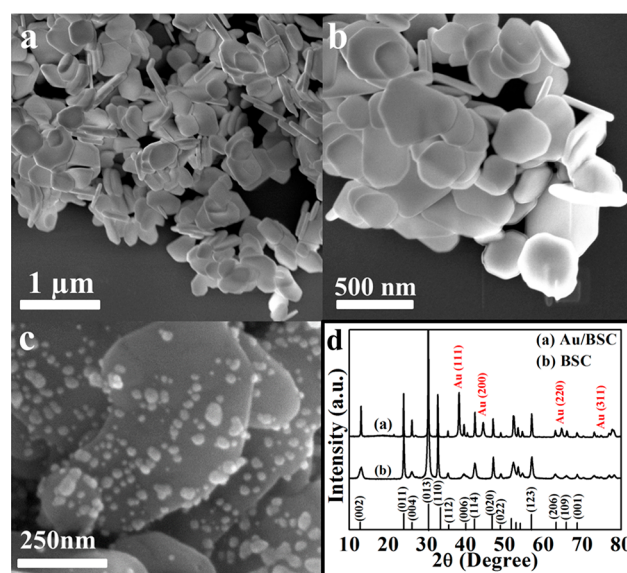


Figure 1. SEM images of as-prepared BSC (a, b) and Au NPs coated BSC (c). XRD pattern of BSC and Au NPs coated BSC (d).

relatively symmetric (NDs) with sizes of 250–400 nm and thicknesses of 30–60 nm. Moreover, the obtained BSC NDs exhibit highly flat facets and sharp edges, indicating the excellent local equilibrium structure. After activation in PdCl_2/HCl , no obvious morphology change can be observed (Supporting Information Figure S1), and the remaining flat NDs are excellent platforms for further deposition of Au nanoparticles.

Au NPs with diameters between ~10 and ~30 nm were deposited onto the surface of activated BSC NDs through the CBD treatment (Figure 1c). Significantly, the deposited Au NPs are tightly attached to the BSC NDs without alternating the original morphology, indicating its excellent mechanical stability. The as-obtained BSC and Au NPs-modified BSC (Au/BSC) samples were further characterized by XRD as shown in Figure 1d. A series of diffraction peaks can be obtained from the as-prepared BSC NDs, which are all indexed to the tetragonal $(\text{BiO})_2\text{CO}_3$ ($a = b = 3.865$ Å; $c = 13.675$ Å; space group, I_4/mmm ; JPCDS Card No. 41-1488). The observed

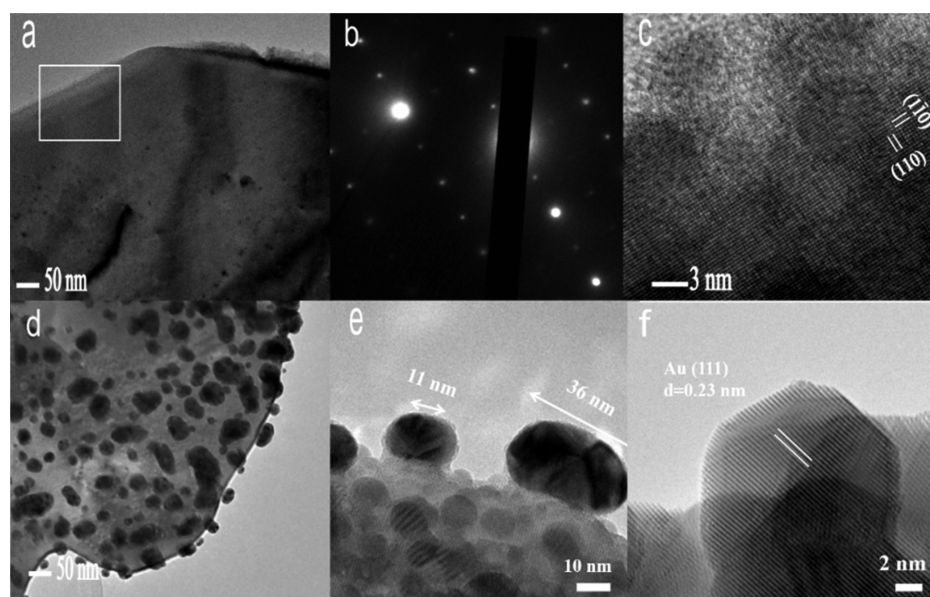


Figure 2. (a–c) TEM image of BSC NDs, SAED pattern, and corresponding HRTEM image. (d, e) TEM images of Au NPs/BSC NDs and (f) corresponding HRTEM image.

BSC diffraction peaks are sharp without appearance of other impurity peaks, suggesting its high crystallinity and purity. After CBD treatment, all the BSC diffraction peaks remained and some new peaks at 38.3° , 44.5° , 54.6° , and 77.5° can be detected, which can be assigned to the (111), (200), (220), and (311) reflections of face-centered metallic Au with cubic structure (JPCDS Card No. 04-0784). The deposited Au NPs can induce a certain strain to the BSC NDs; therefore, some major XRD peaks for BSC slightly shift to lower angles. This implies that the Au NPs are tightly attached onto to the BSC NDs³² and uniformly distributed on the surface of BSC NDs. Interestingly, the intensity ratio between (200) and (111) orientations ($I_{200}/I_{111} = 0.32$) for the as-obtained Au/BSC is smaller than the bulk intensity ratio of 0.53, suggesting the faces of the deposited Au NPs are primarily composed of (111) planes.

Figure 2a shows the TEM image of a BSC ND with a side length of about 300 nm and a thickness of about 50 nm. The corresponding SAED pattern can be indexed as the (001) zone of bulk BSC with the expected (110) and (1 $\bar{1}$ 0) reflections (Figure 2b). The truncated edge of the BSC plate is enclosed by {100} facets, which are the main facets of the octagonal shaped BSC nanodisks that will be discussed further subsequently. The high-resolution TEM image of regions indicated in Figure 2a is displayed in Figure 2c, in which clear (110) and (1 $\bar{1}$ 0) lattice fringes with respective spacings of 2.7 Å are visible. The HRTEM image exhibits a (001) facet with one of the edges parallel to the {110} or {100} facets. As illustrated in a previous study,³³ BSC is a typical “sillén” phase, in which Bi–O layers and CO₃ layers are intergrown with the plane of the CO₃ group orthogonal to the plane of the Bi–O layer.²⁵ The (001) face is the most densely packed face of the crystal, and hence BSC crystals enclosed by dominant {001} faces are commonly observed. When citrate ions are present, they will tend to adsorb onto {100} faces because their surface energy is much higher than that on the {001} and {110} facets. The adsorption of citrate ions then blocks further growth on these facets and leads to the formation of NDs.

The original smooth surface of BSC become much rougher resulting from the homogeneously distributed Au NPs, while no apparent alteration in the shape of BSC NDs can be observed (Figure 2d). Although the Au NPs exhibit nonuniform diameters, these deposited Au NPs are strongly connected with the BSC substrate, which can facilitate the inducing of synergistic effects between Au NPs and BSC NDs during photocatalytic reactions. By a closer observation in Figure 2e, these Au NPs have diameter ranging from ~11 to ~36 nm, which is consistent with the results obtained from the SEM images. Furthermore, SAED pattern and HRTEM images were conducted to reveal the crystallinity of the as-obtained Au/BSC. The SAED pattern of the edge of Au/BSC was presented in Figure S2, showing the polycrystalline nature of the coated Au NPs.³⁴ According to the HRTEM image (Figure 2f), lattice fringe with spacing around 0.23 nm can be detected, which corresponds well to the (111) crystal plane of cubic metallic Au.³⁵

Furthermore, XPS was conducted to confirm the chemical composition and chemical states of the as-obtained Au/BSC. The XPS survey spectrum shown in Figure 3a reveals the existence of Au, Bi, and O in the obtained Au/BSC hybrid, while only Bi and O binding energy peaks can be detected in the XPS survey spectrum of BSC (Figure S3a). From the high-resolution Au 4f spectrum in Figure 3b, two sets of distinct binding energy (BE) peaks including Au 4f_{7/2} located at 82.9 and 85.1 eV and Au 4f_{5/2} positioned at 86.6 and 88.9 eV can be

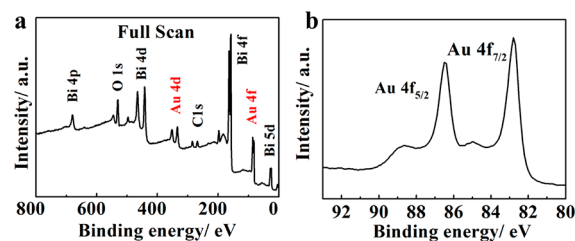


Figure 3. (a) XPS spectra of Au/BSC hybrid. (b) High-resolution Au 4f spectrum.

observed, while no peaks can be detected at the same band position in the high-resolution XPS spectrum of BSC (Figure S3b). The two main BE peaks (82.9 and 86.6 eV) are characteristic of metallic Au, while the two shoulders that appeared at the higher BE region can be ascribed to a small amount of Au³⁺ species.³⁶ The appearance of Au³⁺ species should be caused by minimal residual amounts of HAuCl₄ during the CBD process. Furthermore, the chemical composition and elemental distribution were further investigated by EDS shown in Figure S4. All elements including Au, Bi, O, and C can be detected suggesting the Au NPs are uniformly distributed on the BSC NDs. Collectively, Au NPs (11–36 nm) are strongly attached on the surface of BSC NDs. On the one hand, the Au NPs can induce localized surface plasmon resonance effect, therefore enhancing the absorption of visible light. On the other hand, the Au NPs can act as an electron collector to efficiently separate the photogenerated electrons and relative holes for efficient N₂ reduction reaction.

The optical absorptions of as-obtained BSC and Au/BSC photocatalysts were investigated by UV–vis spectra displayed in Figure 4a. Significantly, Au/BSC exhibits tremendously

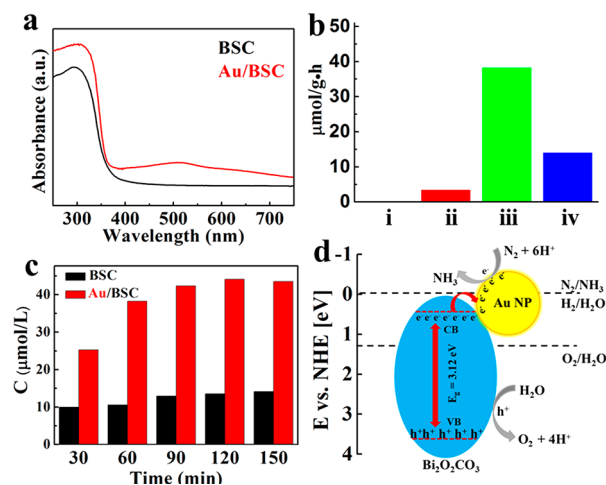


Figure 4. (a) UV–vis spectra of BSC and Au/BSC. (b) Yield of ammonia over 1 h obtained under different conditions: (i) Au/BSC in Ar atmosphere, (ii) Au/BSC in N₂ atmosphere without illumination, (iii) Au/BSC in N₂ atmosphere, and (iv) BSC in N₂ atmosphere. (c) Comparison of ammonia yield between BSC and Au/BSC. (d) Schematic illustration of the charge transfer in Au/BSC hybrids.

enhanced light adsorption ability in both UV and visible regions compared with pure BSC NDs, which can be attributed to the deposited Au NPs. For the pure BSC NDs, the UV adsorption spectrum shows a band edge at the wavelength of 375 nm corresponding to a band gap of 3.12 eV. By coupling with a small amount of Au NPs on the surface, the Au/BSC shows two absorption peaks at 310 and 510 nm, which can be assigned to the BSC NDs and the Au NPs, respectively.³⁷ The slight red shift (~10 nm) of the light absorption edge of BSC arises from the interaction effect between BSC and the Au NPs. As a result, a smaller band gap can be achieved for the BSC by coupling with the Au NPs, which facilitates the excitation of photoelectrons. The second absorption edge can be attributed to the plasmon effect introduced by the surface Au NPs.^{38–41} Consequently, the Au/BSC with enhanced light absorption ability should exhibit better performance in separation and transport of photogenerated charge carriers.

The nitrogen reduction reactions were conducted in a designed photoreduction cell with magnetic stirring under constant N₂ gas bubbling and an artificial solar light 300 W Xe lamp as the illuminant. The illumination intensity at the sample was calibrated using a standard Si–solar cell and the distance adjusted to achieve 1 sun. The reactions occurring during the N₂ photoreduction process are as follows:⁴²

photocathode:



photoanode:



To quantify the ammonia concentration, a calibration curve for standard ammonia solution was established based on the indophenol blue method as shown in Figure S5. First of all, the as-prepared materials were also tested under an argon atmosphere and, in a separate control experiment, without light illumination where only 0 and 3.35 μmol/(g·h) ammonia yield can be detected after 60 min, respectively (Figure 4b). This may be the exposure of the samples to air and/or daylight during the preparation process. The ammonia yields catalyzed by pure BSC and Au/BSC are compared in Figure 4c. Ammonia yield around 10 μmol/(g·h) can be obtained with pure BSC after 30 min illumination with 1 sun and increased to around 14 μmol/(g·h) after 120 min illumination. After coating with Au NPs, the ammonia production increased by 2.5 times in the first 30 min illumination to over 25 μmol/(g·h). Moreover, a total yield of ammonia under the same conditions over 60 min is around 38.2 μmol/(g·h). The corresponding solar-to-chemical energy conversion efficiency is calculated to be 0.006%. The excellent performance of Au/BSC in the first 1 h of N₂ photoreduction reaction surpasses the state-of-the-art TiO₂ with oxygen vacancies and comparable to other previously reported photocatalysts listed in Table 1.^{8,26,31,42,43} The

Table 1. Comparison of Photocatalytic Activity for N₂ Reduction under 1 sun with Previous Reported Photocatalysts

catalyst	R _t /h	yield/[μmol/(mg·h)] or [μmol/(cm ² ·h)]	type ^a	ref
Au/BSC	1	38.23 ^b	D	this work
BiOBr	1	104.2 ^b	D	43
TiO ₂	1	<5 ^b	D	42
Au/bSi	3	0.0411 ^c	I	31
Au/SrTiO ₃	1	<1 × 10 ^{-3c}	I	8
diamond	1	0.25 ^c	I	26

^aD, catalysts are dispersed in reacting solution; I, catalysts are immobilized on substrate. ^bUnit: μmol/(g·h). ^cUnit: μmol/(cm²·h)

working mechanism of Au NPs surface-modified BSC NDs photocatalyst is schematically illustrated as follows: (i) Plasmonic Au NPs can extend the absorption of light from the UV region to the visible light part and improve the electron–hole separation efficiency. (ii) Each Au NP on the surface of BSC NDs can act as an individual photocathode, which generates the hot electrons for the N₂ reduction reaction. (iii) Besides, the loading of Au NPs can collect the photogenerated electron rapidly, thereby preventing the electron–hole recombination as well as enhancing the charge transfer during the nitrogen reduction.

However, the ammonia yields only increased 15% to 44 $\mu\text{mol}/(\text{g}\cdot\text{h})$ in the second 1 h illumination. The trend toward constant yield as time increases in Figure 4c may be the result of the buildup of oxygen in the system, being the product of the oxidation reaction. The reduction of the generated O_2 in the region of the photocathode sites will become a limiting reaction. Finally, we refreshed the solution and carried out another 1 h photoreduction reaction, while only 21% of ammonia yield ($8.3 \mu\text{mol}/(\text{g}\cdot\text{h})$) can be detected compared to the first 1 h reaction. This may be caused by quenching the active sites of BSC NDs during long-term illumination. As a consequence, the interaction between Au NPs and BSC NDs would be reduced, resulting in the decrease of generated photoelectrons. It is hoped that the long-term catalytic stability toward N_2 reduction can be improved by further modification of the material structure.

CONCLUSION

In conclusion, we have successfully synthesized Au NPs' surface-modified $(\text{BiO})_2\text{CO}_3$ NDs as a cost-effective catalyst for solar-driven photosynthesis of ammonia. The plasmonic gold nanoparticles are able to generate hot electrons as well as enhance the separation of charge carriers. The strong synergistic effect between Au NPs and $(\text{BiO})_2\text{CO}_3$ NDs is capable of breaking the strong triple bond of nitrogen to form ammonia. The performance can be further optimized through controlling the composition, structure, and geometry. We hope that this work will stimulate further effort in direct nitrogen photoconversion.

ASSOCIATED CONTENT

Supporting Information

The Supporting Information is available free of charge on the ACS Publications website at DOI: 10.1021/acssuschemeng.7b02788.

SEM, TEM images, SAED pattern, EDX mapping, and UV-vis spectra (PDF)

AUTHOR INFORMATION

Corresponding Authors

(X.Z.).

(D.R.M.).

ORCID

Changlong Xiao: 0000-0001-5699-9018

Xinyi Zhang: 0000-0003-4695-3731

Author Contributions

The manuscript was written through contributions of all authors. All authors have given approval to the final version of the manuscript. C.X. and H.H. contributed equally to this work.

Funding

We are grateful to the Australian Research Council for support through the Australian Centre for Electromaterials Science and under the Discovery Project (Grants DP120104334 and DP170102267) and the Australian Laureate Fellowship program.

Notes

The authors declare no competing financial interest.

ACKNOWLEDGMENTS

We acknowledge the use of facilities at the Monash Centre for Electron Microscopy.

ABBREVIATIONS

NDs nanodisks

NPs nanoparticles

REFERENCES

- (1) Lan, R.; Alkhamzi, K. A.; Amar, I. A.; Tao, S. Synthesis of Ammonia Directly From Wet Air at Intermediate Temperature. *Appl. Catal., B* **2014**, *152-153*, 212–217.
- (2) Jackson, R. B.; Canadell, J. G.; Le Quéré, C.; Andrew, R. M.; Korsbakken, J. I.; Peters, G. P.; Nakicenovic, N. Reaching peak emissions. *Nat. Clim. Change* **2015**, *6*, 7–10.
- (3) Service, R. F. New Recipe Produces Ammonia from Air, Water, and Sunlight. *Science* **2014**, *345* (6197), 610 DOI: 10.1126/science.345.6197.610.
- (4) Smith, B. E. Nitrogenase Reveals Its Inner Secrets. *Science* **2002**, *297*, 1654–1655.
- (5) Rafiqul, I.; Weber, C.; Lehmann, B.; Voss, A. Energy Efficiency Improvements in Ammonia Production—perspectives and Uncertainties. *Energy* **2005**, *30*, 2487–2504.
- (6) Ritter, S. K. Toward Greener Therapeutic Proteins. *Chem. Eng. News* **2008**, *86*, 63–66.
- (7) Smil, V. Review Article: Worrying About the Environment. *Int. Hist. Rev.* **2004**, *26* (4), 796–802.
- (8) Oshikiri, T.; Ueno, K.; Misawa, H. Plasmon-induced Ammonia Synthesis Through Nitrogen Photofixation with Visible Light Irradiation. *Angew. Chem.* **2014**, *126* (37), 9960–9963.
- (9) Fujishima, A.; Honda, K. Electrochemical Photolysis of Water at a Semiconductor Electrode. *Nature* **1972**, *238*, 37–38.
- (10) Schrauzer, G.; Guth, T. Photocatalytic reactions. 1. Photolysis of Water and Photoreduction of Nitrogen on Titanium Dioxide. *J. Am. Chem. Soc.* **1977**, *99*, 7189–7193.
- (11) Tian, J.; Sang, Y.; Yu, G.; Jiang, H.; Mu, X.; Liu, H. A Bi_2WO_6 -based Hybrid Photocatalyst with Broad Spectrum Photocatalytic Properties Under UV, Visible, and Near-Infrared Irradiation. *Adv. Mater.* **2013**, *25*, 5075–5080.
- (12) Han, M.; Chen, X.; Sun, T.; Tan, O. K.; Tse, M. S. Synthesis of Mono-dispersed m-BiVO₄ Octahedral Nano-crystals with Enhanced Visible Light Photocatalytic Properties. *CrystEngComm* **2011**, *13*, 6674–6679.
- (13) Zhang, X.; Ai, Z.; Jia, F.; Zhang, L. Generalized One-pot Synthesis, Characterization, and Photocatalytic Activity of Hierarchical BiOX (X= Cl, Br, I) Nanoplate Microspheres. *J. Phys. Chem. C* **2008**, *112*, 747–753.
- (14) Dong, F.; Ho, W.-K.; Lee, S.; Wu, Z.; Fu, M.; Zou, S.; Huang, Y. Template-free Fabrication and Growth Mechanism of Uniform $(\text{BiO})_2\text{CO}_3$ Hierarchical Hollow Microspheres with Outstanding Photocatalytic Activities Under Both UV and Visible Light Irradiation. *J. Mater. Chem.* **2011**, *21*, 12428–12436.
- (15) Cen, W.; Xiong, T.; Tang, C.; Yuan, S.; Dong, F. Effects of Morphology and Crystallinity on the Photocatalytic Activity of $(\text{BiO})_2\text{CO}_3$ Nano/microStructures. *Ind. Eng. Chem. Res.* **2014**, *53*, 15002–15011.
- (16) Dong, F.; Bian, J.; Sun, Y.; Xiong, T.; Zhang, W. The Rapid Synthesis of Photocatalytic $(\text{BiO})_2\text{CO}_3$ Single-crystal Nanosheets via an Eco-friendly Approach. *CrystEngComm* **2014**, *16*, 3592–3604.
- (17) Dong, F.; Lee, S.; Wu, Z.; Huang, Y.; Fu, M.; Ho, W.-K.; Zou, S.; Wang, B. Rose-like Monodisperse Bismuth Subcarbonate Hierarchical Hollow Microspheres: One-pot Template-free Fabrication and Excellent Visible Light Photocatalytic Activity and Photochemical Stability for NO Removal in Indoor Air. *J. Hazard. Mater.* **2011**, *195*, 346–354.
- (18) Wang, C.; Zhao, Z.; Luo, B.; Fu, M.; Dong, F. Tuning the Morphological Structure and Photocatalytic Activity of Nitrogen-

- doped (BiO)₂CO₃ by the Hydrothermal Temperature. *J. Nanomater.* **2014**, *2014*, 192797.
- (19) Chen, R.; So, M. H.; Yang, J.; Deng, F.; Che, C.-M.; Sun, H. Fabrication of Bismuth Subcarbonate Nanotube Arrays From Bismuth Citrate. *Chem. Commun.* **2006**, *21*, 2265–2267.
- (20) Cheng, H.; Huang, B.; Yang, K.; Wang, Z.; Qin, X.; Zhang, X.; Dai, Y. Facile Template-Free Synthesis of Bi₂O₂CO₃ Hierarchical Microflowers and Their Associated Photocatalytic Activity. *ChemPhysChem* **2010**, *11*, 2167–2173.
- (21) Chen, L.; Yin, S.-F.; Luo, S.-L.; Huang, R.; Zhang, Q.; Hong, T.; Au, P. C. Bi₂O₂CO₃/BiOI Photocatalysts with Heterojunctions Highly Efficient for Visible-light Treatment of Dye-containing Wastewater. *Ind. Eng. Chem. Res.* **2012**, *51*, 6760–6768.
- (22) Wang, W.; Cheng, H.; Huang, B.; Lin, X.; Qin, X.; Zhang, X.; Dai, Y. Synthesis of Bi₂O₂CO₃/Bi₂S₃ Hierarchical Microspheres with Heterojunctions and Their Enhanced Visible Light-driven Photocatalytic Degradation of Dye Pollutants. *J. Colloid Interface Sci.* **2013**, *402*, 34–39.
- (23) Jiang, J.; Zhao, K.; Xiao, X.; Zhang, L. Synthesis and Facet-dependent Photoreactivity of BiOCl Single-crystalline Nanosheets. *J. Am. Chem. Soc.* **2012**, *134*, 4473–4476.
- (24) Sun, Y.; Cheng, H.; Gao, S.; Sun, Z.; Liu, Q.; Liu, Q.; Lei, F.; Yao, T.; He, J.; Wei, S.; Xie, Y. Freestanding tin Disulfide Single-layers Realizing Efficient Visible-light Water Splitting. *Angew. Chem., Int. Ed.* **2012**, *51* (35), 8727–8731.
- (25) Zhao, Z.; Zhou, Y.; Wang, F.; Zhang, K.; Yu, S.; Cao, K. Polyaniline-decorated {001} Facets of Bi₂O₂CO₃ Nanosheets: In Situ Oxygen Vacancy Formation and Enhanced Visible Light Photocatalytic Activity. *ACS Appl. Mater. Interfaces* **2015**, *7* (1), 730–737.
- (26) Linic, S.; Christopher, P.; Ingram, D. B. Plasmonic-metal Nanostructures for Efficient Conversion of Solar to Chemical Energy. *Nat. Mater.* **2011**, *10*, 911.
- (27) Li, H.; Bian, Z.; Zhu, J.; Huo, Y.; Li, H.; Lu, Y. Mesoporous Au/TiO₂ Nanocomposites With Enhanced Photocatalytic Activity. *J. Am. Chem. Soc.* **2007**, *129*, 4538–4539.
- (28) Xiong, Z.; Zhang, L. L.; Ma, J.; Zhao, X. Photocatalytic Degradation of Dyes Over Graphene–gold Nanocomposites Under Visible Light Irradiation. *Chem. Commun.* **2010**, *46*, 6099–6101.
- (29) Murdoch, M.; Waterhouse, G.; Nadeem, M.; Metson, J.; Keane, M.; Howe, R.; Llorca, J.; Idriss, H. The Effect of Gold Loading and Particle Size on Photocatalytic Hydrogen Production From Ethanol Over Au/TiO₂ Nanoparticles. *Nat. Chem.* **2011**, *3*, 489–492.
- (30) Tian, Y.; Tatsuma, T. Mechanisms and Applications of Plasmon-induced Charge Separation at TiO₂ Films Loaded with Gold Nanoparticles. *J. Am. Chem. Soc.* **2005**, *127*, 7632–7637.
- (31) Ali, M.; Zhou, F.; Chen, K.; Kotzur, C.; Xiao, C.; Bourgeois, L.; Zhang, X.; MacFarlane, D. R. Nanostructured Photoelectrochemical Solar Cell for Nitrogen Reduction Using Plasmon-enhanced Black Silicon. *Nat. Commun.* **2016**, *7*, 11335.
- (32) Xiao, C.; Li, S.; Zhang, X.; MacFarlane, D. R. MnO₂/MnCo₂O₄/Ni Heterostructure with Quadruple Hierarchy: A Bifunctional Electrode Architecture for Overall Urea Oxidation. *J. Mater. Chem. A* **2017**, *5*, 7825–7832.
- (33) Zhang, X.; Zheng, Y.; McCulloch, D. G.; Yeo, L. Y.; Friend, J. R.; MacFarlane, D. R. Controlled Morphogenesis and Self-Assembly of Bismutite Nanocrystals into Three-Dimensional Nanostructures and Their Applications. *J. Mater. Chem. A* **2014**, *2*, 2275–2282.
- (34) Gogurla, N.; Sinha, A. K.; Santra, S.; Manna, S.; Ray, S. K. Multifunctional Au-ZnO Plasmonic Nanostructures for Enhanced UV Photodetector and Room Temperature NO Sensing Devices. *Sci. Rep.* **2015**, *4*, 6483.
- (35) Lim, B.; Kobayashi, H.; Yu, T.; Wang, J.; Kim, M. J.; Li, Z.-Y.; Rycenga, M.; Xia, Y. Synthesis of Pd–Au Bimetallic Nanocrystals via Controlled Overgrowth. *J. Am. Chem. Soc.* **2010**, *132*, 2506–2507.
- (36) Wang, L.-C.; Zhong, Y.; Jin, H.; Widmann, D.; Weissmüller, J.; Behm, R. J. Catalytic Activity of Nanostructured Au: Scale Effects Versus Bimetallic/bifunctional Effects in Low-temperature CO Oxidation on Nanoporous Au. *Beilstein J. Nanotechnol.* **2013**, *4*, 111.
- (37) Bajaj, G.; Soni, R. Nanocomposite ZnO/Au Formation by Pulsed Laser Irradiation. *Appl. Surf. Sci.* **2010**, *256*, 6399–6402.
- (38) Neațu, S. t.; Maciá-Agulló, J. A.; Concepción, P.; Garcia, H. Gold–copper Nanoalloys Supported on TiO₂ as Photocatalysts for CO₂ Reduction by Water. *J. Am. Chem. Soc.* **2014**, *136*, 15969–15976.
- (39) Wu, B.; Liu, D.; Mubeen, S.; Chuong, T. T.; Moskovits, M.; Stucky, G. D. Anisotropic Growth of TiO₂ onto Gold Nanorods for Plasmon-enhanced Hydrogen Production from Water Reduction. *J. Am. Chem. Soc.* **2016**, *138*, 1114–1117.
- (40) Han, S.; Hu, L.; Gao, N.; Al-Ghamdi, A. A.; Fang, X. Efficient Self-Assembly Synthesis of Uniform CdS Spherical Nanoparticles-Au Nanoparticles Hybrids with Enhanced Photoactivity. *Adv. Funct. Mater.* **2014**, *24*, 3725–3733.
- (41) Sousa-Castillo, A.; Comesaña-Hermo, M.; Rodríguez-González, B.; Pérez-Lorenzo, M.; Wang, Z.; Kong, X. T.; Govorov, A. O.; Correa-Duarte, M. A. Boosting Hot Electron-Driven Photocatalysis Through Anisotropic Plasmonic Nanoparticles with Hot Spots in Au–TiO₂ Nanoarchitectures. *J. Phys. Chem. C* **2016**, *120*, 11690–11699.
- (42) Hirakawa, H.; Hashimoto, M.; Shiraiishi, Y.; Hirai, T. Photocatalytic Conversion of Nitrogen to Ammonia with Water on Surface Oxygen Vacancies of Titanium Dioxide. *J. Am. Chem. Soc.* **2017**, *139* (31), 10929–10936.
- (43) Li, H.; Shang, J.; Ai, Z.; Zhang, L. Efficient Visible Light Nitrogen Fixation with BiOBr Nanosheets of Oxygen Vacancies on the Exposed {001} Facets. *J. Am. Chem. Soc.* **2015**, *137*, 6393–6399.

Nanostructured Gold/Bismutite Hybrid Heterocatalysts for Plasmon-Enhanced Photosynthesis of Ammonia

Changlong Xiao,^{†,§} Hong Hu,^{†,‡,§} Xinyi Zhang^{*,†} and Douglas R. MacFarlane^{*,†}

[†] Australian Centre for Electromaterials Science, School of Chemistry, Monash University, Victoria, 3800 Australia

[‡] School of Chemistry, Nanjing Institute of Technology, Nanjing, China

Corresponding Authors

*Tel.: [REDACTED] Email: [REDACTED] (X.Z.).

*Tel.: +[REDACTED] Email: [REDACTED] (D.R.M.).

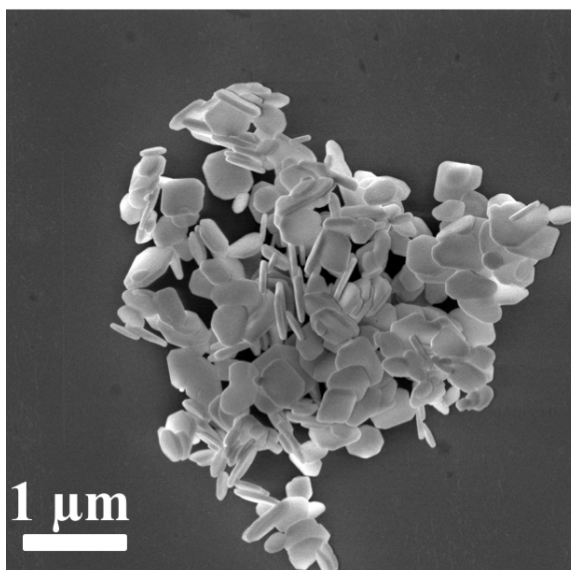


Figure S1. BSC NDs after activation treatment in PdCl₂ solution.

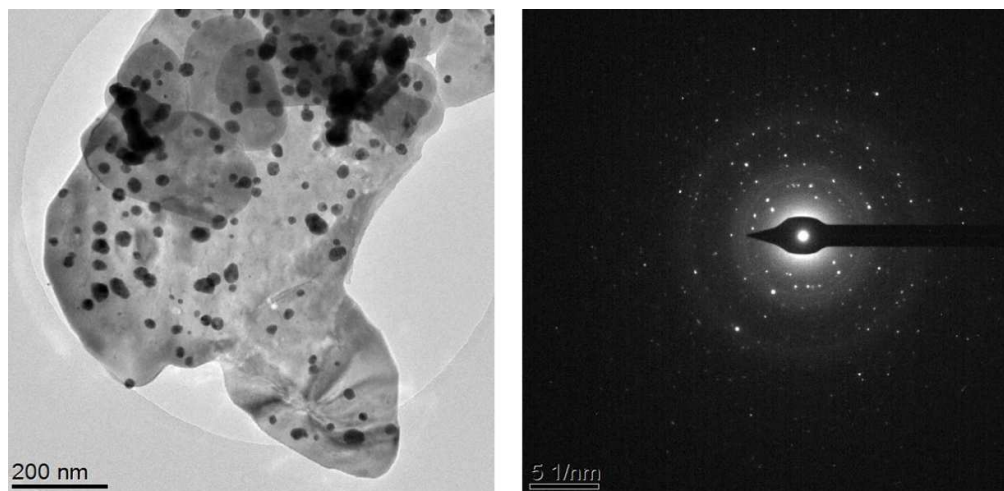


Figure S2. TEM images of Au/BSC and corresponding SAED pattern.

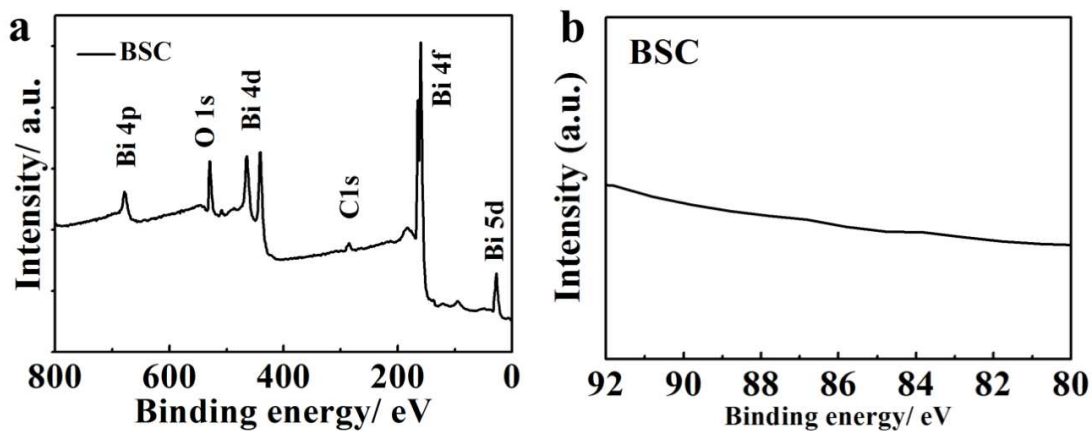


Figure S3. Full curve and high-resolution XPS spectra of BSC NDs.

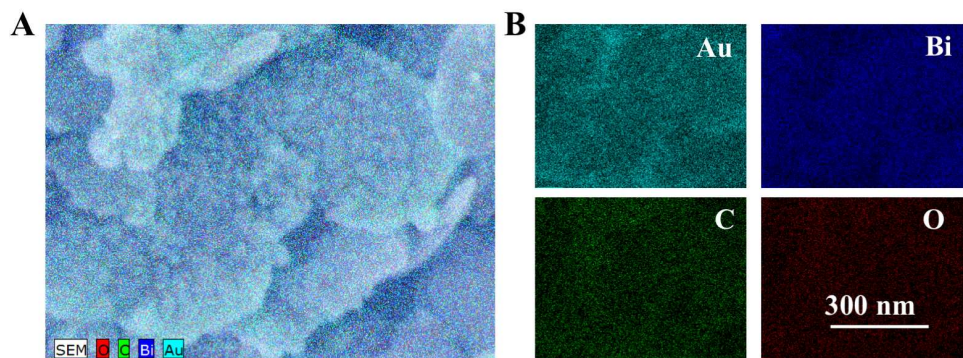


Figure S4. Elemental mapping of Au/BSC illustrating the uniform distribution of Au, Bi and O.

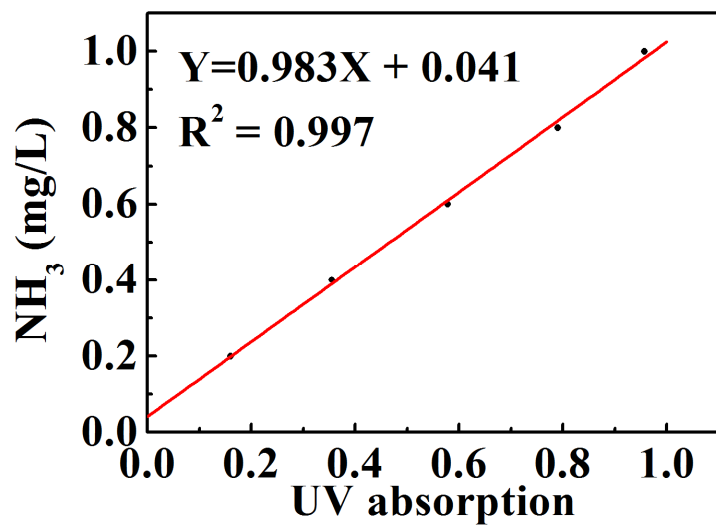


Figure S5. Calibration curve of the NH₃ standard solutions.

Chapter 5

Highly Ordered Hierarchical Mesoporous MnCo₂O₄ for Electrochemical Energy Storage

5.1 Overview

This chapter is a paper titled “Highly ordered hierarchical mesoporous MnCo₂O₄ with cubic *Ia3d* symmetry for electrochemical energy storage” that was published in the Journal of Physical Chemistry C in 2016.

Hybrid supercapacitors have attracted great attention since they combine the advantages of both double-layer capacitors and alkaline battery. The Hybrid capacitors use battery-type electrode materials as the positive side and a capacitor-type electrode as the negative side. The hybrid capacitors have advantages of high power density, minimal maintenance cost, long-life span and fast charge/discharge ability. The outstanding properties of this new type of capacitors make them important power source components for electric vehicles (e.g. buses and trams), forklifts and other high-power portable devices.^{1, 2}

In this chapter, a hierarchically mesoporous MnCo₂O₄ spinel oxide with two levels of hierarchy comprised of large mesopores (~ 17 nm) and small mesopores (~ 5 nm) has been synthesised. The obtained MnCo₂O₄ exhibits enlarged surface area (133 m²/g), pore volume (0.42 cm³/g) and prominent capacity of 199 mAh/g at current density of 1 A/g. It is expected that these tuneable, hierarchical mesoporous architectures can also be applied for other energy-related devices such as batteries, fuel cells and water splitting devices.

References

1. C. Xiao, X. Zhang, T. Mendes, G. P. Knowles, A. Chaffee and D. R. MacFarlane, *J. Phys. Chem. C*, 2016, **120**, 23976.

2. T. C. Mendes, C. Xiao, F. Zhou, H. Li, G. P. Knowles, M. Hilder, A. Somers, P. C. Howlett and D. R. MacFarlane, *ACS Appl. Mater. Interfaces* 2016, **8**, 35243.

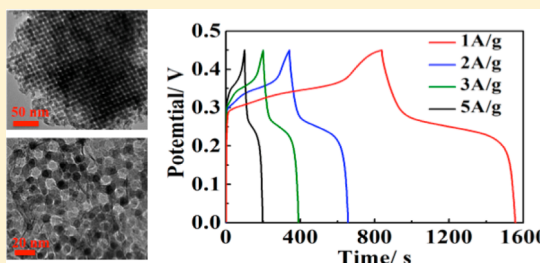
Highly Ordered Hierarchical Mesoporous MnCo_2O_4 with Cubic $Ia\bar{3}d$ Symmetry for Electrochemical Energy Storage

Changlong Xiao, Xinyi Zhang,* Tiago Mendes, Gregory P. Knowles, Alan Chaffee, and Douglas R. MacFarlane*

Australian Centre for Electromaterials Science, School of Chemistry, Monash University, Victoria, 3800 Australia

Supporting Information

ABSTRACT: Highly ordered cubic $Ia\bar{3}d$ mesoporous MnCo_2O_4 with crystalline framework was synthesized through a facile nanocasting method. The obtained mesoporous MnCo_2O_4 possesses hierarchical porosity with pore sizes of about 5 and 17 nm, respectively, and exhibits an enlarged surface area (133 m^2/g) compared to binary mesoporous Co_3O_4 (98.6 m^2/g) and MnO_2 (75.0 m^2/g). Significantly, the hierarchical mesoporous structure of MnCo_2O_4 is beneficial for exposing more electroactive sites, improving the charge transfer and facilitating the ion transport. As a consequence, the mesoporous MnCo_2O_4 shows a high charge storage performance of 199 mAh g^{-1} at a current density of 1 A/g, long cycle stability, and excellent rate capacity. This study demonstrates ordered ternary mesoporous materials with controllable porosity that have great potential for high-energy-density electrochemical energy storage.



INTRODUCTION

The increasingly serious environmental problems associated with fossil fuels have prompted intense research interest into the development of sustainable and reliable energy storage systems. Among a wide variety of innovative technologies, supercapacitors (also known as electrochemical capacitors), as a type of rechargeable energy device, have attracted great attention owing to their high power density, minimal maintenance cost, long lifespan, and fast charge/discharge ability compared to other conventional rechargeable technologies such as the lithium ion battery.^{1–6} The outstanding properties of supercapacitors make them important power source components for electric vehicles (including trams and buses), forklifts, and other high power portable devices. The supercapacitor typically involves two identical electrodes that store charge in the double layer in the electrolyte adjacent to the electrodes. A variation on the supercapacitor is often described as a “hybrid supercapacitor” where one of the electrodes exhibits more battery-like behavior and therefore improves the energy density of the device. There is much interest in such hybrid-type devices made from inexpensive materials using very highly ion conductive KOH as the electrolyte, carbon as a classical double layer capacitive negative electrode, and various transition metal oxide type materials as the positive electrode.^{7–11} There have been many reports of these oxide type materials for this application, most describing these in terms of “pseudocapacity”; however, it has recently been pointed out^{12,13} that this description is incorrect in many cases (with the notable exception of MnO_2 and RuO_2) and that the main charge–discharge behavior of these materials is Faradaic in nature. In other words, the bulk of the charge stored by these materials is electrochemical in nature and the process

takes place over a narrow range of potentials, similar to battery electrodes. Nevertheless, as long as these materials are seen in the appropriate light, and analyzed as such, they remain interesting and important electrochemical materials for charge storage devices, in particular for hybrid-type devices. As is true for all electrochemical storage devices, it is the electrode capacity (in mAh g^{-1}) over the operating potential range that is the important feature of the electrode material. Therefore, it is preferable to interpret the properties of hybrid materials in terms of specific capacity rather than specific capacitance (capacity = capacitance $\times \Delta V$).

Transition metal oxides and their hybrids are well-known electroactive materials owing to their multiple oxidation states. Recently, the development of earth abundant transition metal (Ni, Co, Mn, etc.) oxide and hydroxide materials has attracted enormous research effort owing to their low environmental impact and theoretically high-energy-density capability.^{14–19} Nonetheless, despite recent progress, great challenges still remain for non-noble electrode materials to achieve excellent capacity and stability performance. In pursuit of a high electrochemically active surface area, exploration has been devoted to creating hierarchical and/or three-dimensional porous materials including metal oxide core/shell arrays,²⁰ NiCo_2O_4 nanosheet/halloysite nanotubes,²¹ porous graphene-like network films,²² and mesoporous carbon and carbon nanotubes.²³ Among them, well-ordered mesoporous materials exhibit a unique set of advantages, including great numbers of regular channels, controllable structures, and a multitude of

Received: August 9, 2016

Revised: September 27, 2016

Published: October 5, 2016

composites.^{24–26} Lately, mesoporous first-row transition metal (e.g., Co, Ni, and Fe) oxides have been reported as excellent electrochemical materials in energy conversion and storage, such as water splitting,^{26–30} however, most of them are unimodal mesoporous materials, with pore size less than 5 nm. Such small mesopores limit the access of the electrolyte and ion transport into the inner surface of the mesopores. Therefore, the surface area of the electrodes cannot be efficiently utilized, especially at high rates. In this regard, mesoporous materials with hierarchical porosity are of great current interest because they not only provide large active surface area, but also allow efficient mass transport.^{31,32}

As a typical spinel type of ternary oxide, MnCo_2O_4 is known to have a cubic structure (space group $Fd\bar{3}m$ (227) with lattice constants of $a = b = c = 8.269$ Å). It has wide applications in many fields, such as spintronics, sensors, lithium batteries, and electrochemical energy storage.^{33–37} MnCo_2O_4 nanostructures with different morphologies have been investigated.^{35–41} However, there is no report on the synthesis of ordered hierarchical mesoporous MnCo_2O_4 as yet. In this work, we have synthesized cubic $Ia\bar{3}d$ mesoporous MnCo_2O_4 with crystalline framework. The resultant cubic $Ia\bar{3}d$ mesoporous MnCo_2O_4 has continuous crystalline framework with hierarchical pore sizes (ca. 5.4–17 nm) and high specific surface areas (up to 133 m^2/g). This unique structure of the mesoporous MnCo_2O_4 allows efficient mass and charge transfer. Meanwhile, the combined contributions from both Co and Mn ions in MnCo_2O_4 make its performance superior to the binary counterparts, collectively exhibiting a high capacity, an excellent rate capability, and long-term cycling performance.

EXPERIMENTAL SECTION

Chemicals. Cobalt(II) nitrate hexahydrate, manganese(II) nitrate tetrahydrate, potassium hydroxide, sodium hydroxide, Nafion 117 (5 wt %), Pluronic P-123 ($\text{EO}_{20}\text{PO}_{70}\text{EO}_{20}$), tetraethyl orthosilicate (TEOS), urea, and *n*-butanol were purchased from Sigma-Aldrich. All chemicals used in this study were of analytical grade and used without further purification.

Preparation of Mesoporous Silica Template (KIT-6). Cubic silica template (KIT-6) with ordered channels was synthesized through a hydrolysis approach followed by hydrothermal treatment. Typically, 6 g of Pluronic P-123 was dissolved in acid solution containing 217 g of distilled water and 11.8 g of concentrated hydrochloric acid (35%) by vigorous stirring. Subsequently, 6 g of *n*-butanol was added into the mixture solution with stirring at constant temperature (35 °C) using an oil bath until the formation of homogeneous solution, and then 12.9 g of TEOS was gradually added into the resultant solution. This resultant solution was sealed and vigorously stirred for another 24 h at 35 °C for thorough hydrolysis of the silicone precursor. Afterward, the formed gel-like solution was transferred into an autoclave and placed in an oven for 24 h at 100 °C. After the hydrothermal reaction, the sample was collected by filtration and dried in the oven. The dried sample was soaked in ethanol–HCl solution (20 mL of ethanol/2 mL of concentrated HCl) for another 20 min extraction treatment. Subsequently, the sample was washed with copious water and dried again in an oven. Finally, the obtained powder was annealed in a tube furnace at 550 °C for 6 h to completely remove the residual polymer surfactant.

Preparation of Mesoporous MnCo_2O_4 . Mesoporous MnCo_2O_4 with well-ordered mesopores was synthesized through the hard-template method using the as-prepared

KIT-6 template. Typically, 0.291 g of cobalt(II) nitrate hexahydrate and 0.125 g of manganese(II) nitrate tetrahydrate with a molecular ratio of 2:1 were first dissolved in 10 mL of absolute ethanol by vigorous stirring. Subsequently, 0.2 g of as-prepared KIT-6 was added into the ethanol solution, followed by another 2 h of stirring to form a homogeneous suspension. After that, the resulting solution was heated and maintained at 60 °C using an oil bath to evaporate the ethanol. During the evaporation process, the metal ions were forced to impregnate the channels of the silica template. After the impregnation process, the obtained sample was annealed at 400 and 500 °C, respectively for another 2 h (denoted $\text{MnCo}_2\text{O}_4(400)$ and $\text{MnCo}_2\text{O}_4(500)$, respectively). In order to fully fill the silica template, the impregnation and consolidation process was repeated with 1/3 of the metal precursor. Afterward, the silica template was removed by washing with 2 M NaOH solution three times and distilled water for another three times. Finally, mesoporous $\text{MnCo}_2\text{O}_4(400)$ and $\text{MnCo}_2\text{O}_4(500)$ were collected by centrifugation and dried in an oven at 60 °C overnight.

Preparation of MnCo_2O_4 Nanoparticles. For comparison purposes, MnCo_2O_4 nanoparticles were prepared through a hydrothermal method. Specifically, cobalt(II) nitrate hexahydrate (40 mM), manganese(II) nitrate tetrahydrate (40 mM), and urea (20 mM) were dissolved in a solution containing distilled water and absolute ethanol in a volume ratio of 4:1. Subsequently, the resulting solution was sonicated for 30 min before transferring to a 48 mL autoclave followed by hydrothermal treatment at 150 °C for 6 h. Afterward, the sample was cooled to room temperature and washed with water several times to remove the residual impurities. Finally, the obtained MnCo_2O_4 nanoparticles were calcined at 400 °C for 2 h.

Electrochemical Measurements. The obtained mesoporous $\text{mMnCo}_2\text{O}_4(400)$ and a small amount of carbon black were drop-cast onto a nickel foam electrode (denoted as NF) to achieve the $\text{mMnCo}_2\text{O}_4(400)$ coated NF electrode (denoted as $\text{mMnCo}_2\text{O}_4(400)/\text{NF}$). On the one hand, the $\text{mMnCo}_2\text{O}_4(400)$ is in direct contact with NF, thereby facilitating the electron transport. On the other hand, the macroscopic skeleton of Ni foam and the $\text{mMnCo}_2\text{O}_4(400)$ actually form two levels of hierarchical architecture, which can maximize the electrochemical surface area. Typically, 1 mg of the capacitive materials, 0.1 mg of carbon black, and 10 μL of Nafion solution were added to a 200 μL solution containing water and isopropanol with a volume ratio of 3:1. This suspension was sonicated until the formation of homogeneous black ink. After that, the ink was drop-cast onto a piece of nickel foam and dried, making the material density 1 mg/cm^2 . The electrochemical performance in this study was evaluated in a three-electrode electrochemical cell employing the prepared $\text{MnCo}_2\text{O}_4(400)/\text{NF}$ as the working electrode and Ag/AgCl (saturated) and Pt wire as the reference electrode and counter electrode, respectively. All measurements were conducted in 2 M KOH solution (pH 14) on an EC-Lab electrochemical workstation. Electrochemical impedance spectra (EIS) were measured in a frequency range from 100 to 0.01 kHz at an open circuit potential. The specific capacity was calculated based on the equation

$$C = Q/M = I\Delta t/3600M \quad (1)$$

where C (mAh g^{-1}) is the specific capacity, Q is the quantity of charge, I (mA) is the constant charge current, Δt (s) is the

discharge time, and M (g) represents the mass of the electroactive materials. For comparison purposes, $\text{mMnCo}_2\text{O}_4(500)$ and MnCo_2O_4 nanoparticle nickel foam electrodes were also prepared through the drop-casting method described above.

Material Characterization. The scanning electron microscopy images were conducted on field emission scanning electron microscope (Magellan 400 FEGSEM instrument). Transmission electron microscopic images and energy dispersive spectroscopy were recorded by an FEI Tecnai G2 T20 working at 200 kV. The X-ray diffraction patterns were obtained on a Bruker D8 ADVANCE ECO powder X-ray instrument using $\text{Cu K}\alpha$ radiation ($\lambda = 0.15418$ nm) in the 2θ range from 10 to 90° with a scanning step size of 0.01° . The small-angle X-ray scattering experiment was conducted on an N8 HORIZON small-angle X-ray scattering system. The nitrogen adsorption–desorption isotherms were performed on a Tristar II instrument operating at 77 K. Prior to each measurement, the sample was degassed under vacuum environment for 5 h at 150 °C. The specific surface area and pore size distribution were evaluated by the Brunauer–Emmett–Teller (BET) method.

RESULTS AND DISCUSSION

Figure 1 presents the scanning electron microscopy (SEM) images of $\text{MnCo}_2\text{O}_4(400)$. As shown in Figure 1a, fluffy and

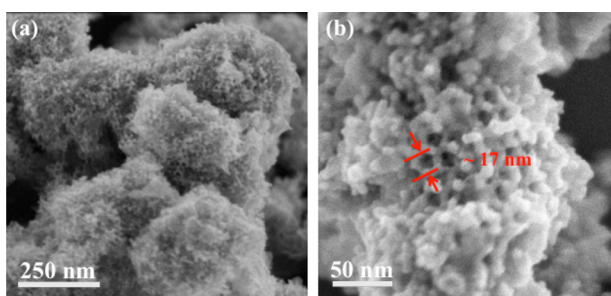


Figure 1. (a) SEM image and (b) high-resolution SEM image of hierarchically mesoporous MnCo_2O_4 .

interconnected nanoparticles with numerous nanocavities and nanopores are obtained via the nanocasting method. By a closer observation in Figure 1b, these fluffy nanoparticles are comprised of well-distributed mesopores with an average diameter around 17 nm. Significantly, these well-distributed mesopores are uniformly embedded among the entire bulk structure of each particle offering enormous open space and accessible channels. Figure 2 displays the transmission electron microscopic (TEM) images of the synthesized $\text{mMnCo}_2\text{O}_4(400)$. It can be clearly observed that slit-like pores are well distributed among the entire $\text{mMnCo}_2\text{O}_4(400)$ nanoparticles with a bulk structure around 200 nm (Figure 2a). Two kinds of primary pores with average diameters of ~ 5 nm (Figure 2a,b) and ~ 17 nm (Figure 2c,d) can be observed, which is in agreement with previously reported Au and Fe induced mesoporous Co_3O_4 .^{28,42} All of these mesopores are well-ordered showing a mesoporous structure with $Ia\bar{3}d$ symmetry, confirming the faithful replication of the cubic structured KIT-6 template.

For comparison, mMnCo_2O_4 calcined at 500 °C, (denoted as $\text{mMnCo}_2\text{O}_4(500)$) and MnCo_2O_4 nanoparticles (denoted as MnCo_2O_4 NPs) were also synthesized (see details in the

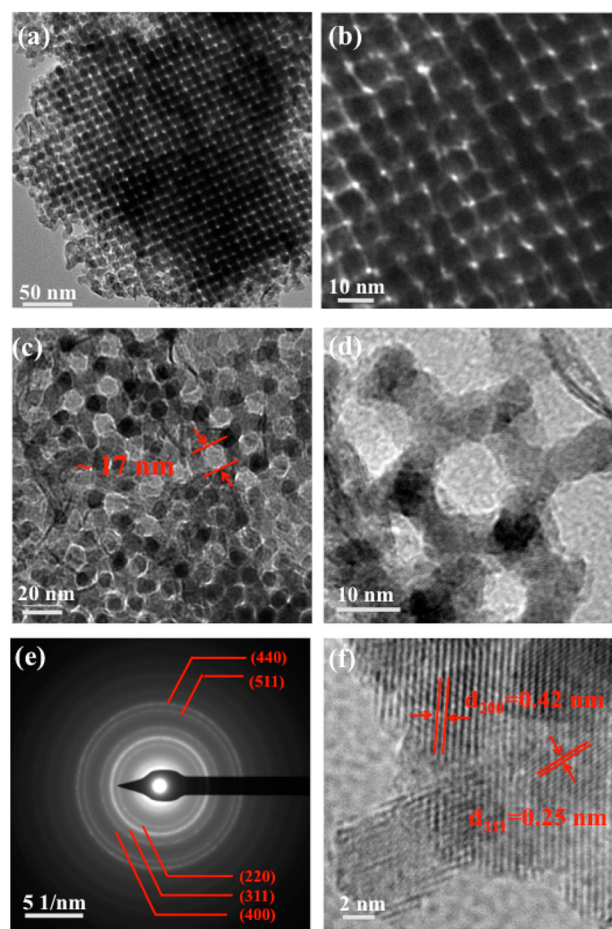


Figure 2. (a–d) TEM images at various magnifications, (e) SAED pattern, and (f) high-resolution TEM image of well-ordered mMnCo_2O_4 .

Experimental Section), as shown in Figure S1. Obviously, $\text{mMnCo}_2\text{O}_4(500)$ shows a porous structure similar to that of $\text{mMnCo}_2\text{O}_4(400)$, while MnCo_2O_4 NPs show irregular size from around 50 to 150 nm, and numerous irregular cavities are randomly distributed on the surface. The mesoporous MnCo_2O_4 with well-ordered mesopores is expected to significantly enlarge the ion-accessible surface area which plays a crucial role in charge storage as the capacity performance is highly dependent on the Faradaic redox reactions occurring on the interface between the electroactive materials and the electrolyte. Furthermore, high-resolution TEM (HRTEM) and selected area diffraction electron (SAED) patterns were also obtained to further investigate the surface structure of the obtained mMnCo_2O_4 . The HRTEM image of $\text{mMnCo}_2\text{O}_4(400)$, shown in Figure 2f, exhibits two kinds of lattice fringes with interplanar distances of 0.42 nm, which correspond to the (200) and (311) atomic planes of cubic MnCo_2O_4 structure.⁴⁰ Meanwhile, the sharp diffraction fringes in the corresponding SAED pattern (Figure 2e) are corresponding to the (220), (311), (400), (440), and (511) crystal planes of the MnCo_2O_4 , indicating the high crystallinity of the mMnCo_2O_4 .³⁵

X-ray diffraction (XRD) measurement was further performed to characterize the crystalline structure of MnCo_2O_4 displayed in Figure 3. Both mMnCo_2O_4 samples (annealed at 400 and 500 °C) and MnCo_2O_4 NPs (Figure S2) show diffraction peaks at $2\theta = 18.6, 32.5, 37.2, 44.9, 56.3, 59.4, 65.1, \text{ and } 75.3^\circ$. All of

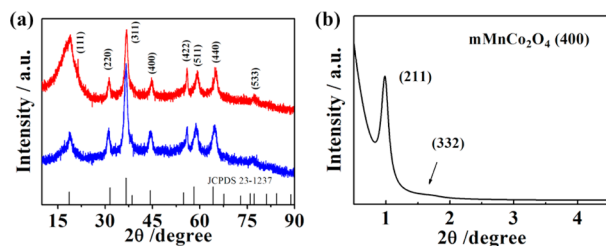


Figure 3. (a) Wide-angle X-ray diffraction patterns of $\text{mMnCo}_2\text{O}_4(400)$ (red) and $\text{mMnCo}_2\text{O}_4(500)$ (blue). (b) Small-angle X-ray diffraction pattern of well-ordered $\text{mMnCo}_2\text{O}_4(400)$.

these observed diffraction peaks can be indexed to the (111), (200), (311), (400), (422), (511), (440), and (533) planes of the cubic MnCo_2O_4 ($a = b = c = 8.269$ Å; space group $Fd\bar{3}m$ (227), JPCDS Card No. 23-1237). The calculated average crystalline size is 11.6 nm by subtracting the diffraction peak from the instrumental broadening component. The low-angle XRD pattern in Figure 3b shows (211) and (332) diffraction peaks, which can further characterize the cubic ($Ia\bar{3}d$) symmetry of the pore system. In addition, the small-angle X-ray scattering (SAXS) pattern in Figure S2 shows that the $\text{mMnCo}_2\text{O}_4(400)$ has three well-resolved scattering peaks. After modeling analysis, this suggests that the $\text{mMnCo}_2\text{O}_4(400)$ contains mesopores with an average diameter of 5.0 nm, which is consistent with the observation of slit-like pores (5.4 nm) in the TEM image, indicating the highly ordered mesoporous architecture. The chemical composition and elemental distribution of the obtained $\text{mMnCo}_2\text{O}_4(400)$ were analyzed by energy dispersive X-ray spectroscopy (EDS) as shown in Figure 4. According to the

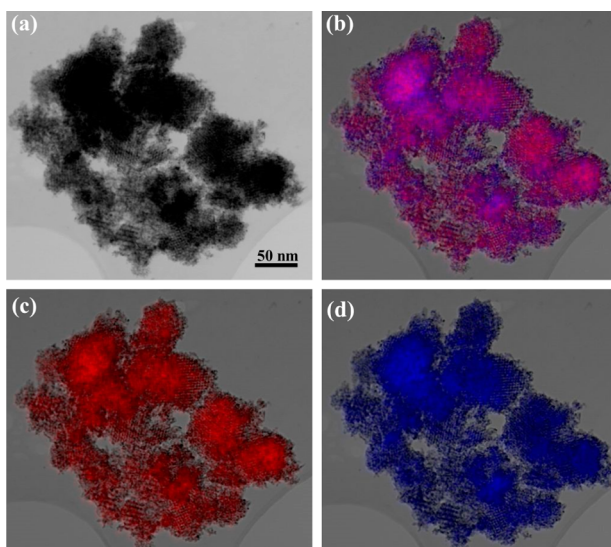


Figure 4. (a) Backscattered TEM image; (b–d) EDS Co (red) and Mn (blue) elemental mapping of mMnCo_2O_4 .

backscattered TEM and elemental mapping images displayed in Figure 4, both Mn and Co ions are uniformly distributed over the entire particle. In addition, an atomic Mn/Co ratio of approximately 1:2 was also determined by the EDS analysis shown in Figure S3, which is in accord with the empirical formula, further confirming the formation of cubic $Ia\bar{3}d$ mesoporous MnCo_2O_4 spinel oxide structure.^{38,43}

Figure 5 presents the N_2 adsorption–desorption isotherms and pore size distributions of $\text{mMnCo}_2\text{O}_4(400)$,

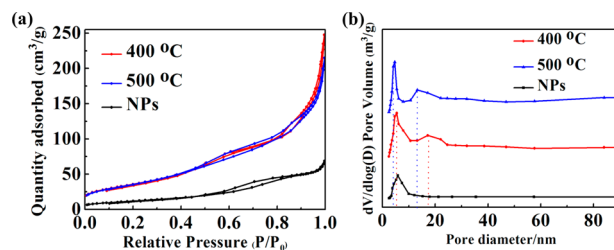


Figure 5. (a) N_2 adsorption–desorption isotherms and (b) pore size distribution plots of $\text{mMnCo}_2\text{O}_4(400$ °C), $\text{mMnCo}_2\text{O}_4(500$ °C), and MnCo_2O_4 NPs.

$\text{mMnCo}_2\text{O}_4(500)$, and MnCo_2O_4 NPs. The isotherms obtained from mMnCo_2O_4 (Figure 5a) exhibit type IV features with H3 hysteresis loops, indicating the mesoporous nature of the mMnCo_2O_4 .^{44,45} According to the calculated Brunauer–Emmett–Teller (BET) surface area data summarized in Table S1, both $\text{mMnCo}_2\text{O}_4(400)$ and $\text{mMnCo}_2\text{O}_4(500)$ have similar surface areas of 133.3 and 132.8 m^2/g , respectively, which are much higher than the value (45.2 m^2/g) for MnCo_2O_4 NPs. Interestingly, $\text{mMnCo}_2\text{O}_4(400)$ has a larger pore volume (0.420 cm^3/g vs 0.369 cm^3/g) than $\text{mMnCo}_2\text{O}_4(500)$. The slight decrease in pore volume may result from the collapse of some large pores at higher annealing temperatures. This hypothesis is confirmed by the pore size distribution plots displayed in Figure 5b. The pore size distribution of $\text{mMnCo}_2\text{O}_4(400)$ exhibits two dominant peaks centered at 5.4 and 17.2 nm, while the dominant peaks of $\text{mMnCo}_2\text{O}_4(500)$ are located at 4.7 and 13.1 nm, respectively. All these results directly evidence the hierarchical characteristic of the $\text{mMnCo}_2\text{O}_4(400)$. It is expected that the high surface area and large pore volume of the hierarchical mesostructure can benefit the penetration of sterically hindered reactants into the internal layer, thereby dramatically enlarging the effective interfaces for electrochemical reactions.

Pristine mesoporous Co_3O_4 (mCo_3O_4) and MnO_2 (mMnO_2) were also prepared under the same conditions as $\text{mMnCo}_2\text{O}_4(400)$ for comparison. As shown in the TEM images (Figure S4), both mCo_3O_4 and mMnO_2 exhibit well-ordered mesoporous structures, revealing a successful replication of KIT-6. However, it can be seen in Figure S5 that mCo_3O_4 exhibits only one dominant pore size centered at ~ 5 nm, while mMnCo_2O_4 shows two dominant peaks at ~ 5 and ~ 17 nm (Figure 5), respectively. According to a previous report, Co species can uniformly impregnate both channels of KIT-6, forming a monomodal pore size distribution. However, the Co species are forced to impregnate one channel in the presence of Fe ions; hence, the replica exhibits bimodal pore size distribution.^{27,28,42} In this study, the obtained mMnCo_2O_4 shows two kinds of pore size distributions, suggesting the Mn can also affect the impregnation of metal precursors inside the KIT-6. It has been reported that Mn ions would grow in only one set of the mesochannels, thus generating two kinds of mesopores after removing the KIT-6 (Figure S5).⁴⁶ However, it is difficult for pristine Mn ions to fully fill the mesochannels of KIT-6 owing to the complex interactions between the silica and the Mn alkali precursor.^{24,47} The outside loaded Mn may accumulate together to form a bulk structure, thereby decreasing the actual surface area (Table S1). Here, we

propose that the Mn can guide the impregnation of the alkali precursors into the targeted KIT-6 mesochannels in the presence of Co precursor. As a result, the generated mMnCo_2O_4 shows excellent homogeneity and a hierarchically mesoporous structure. Significantly, the change in the porous structure leads to a higher surface area and pore volume of MnCo_2O_4 ($133 \text{ m}^2/\text{g}$, $0.42 \text{ cm}^3/\text{g}$) than those of the mCo_3O_4 ($98.6 \text{ m}^2/\text{g}$, $0.17 \text{ cm}^3/\text{g}$) and mMnO_2 ($75.0 \text{ m}^2/\text{g}$, $0.28 \text{ cm}^3/\text{g}$).

The electrochemical performance of the obtained mMnCo_2O_4 samples and MnCo_2O_4 NPs were evaluated in 2 M KOH solution in a standard three-electrode electrochemical cell, employing mMnCo_2O_4 loaded Ni foam working electrodes, a Ag/AgCl (saturated) reference electrode, and a Pt wire counter electrode. Figure 6a depicts the cyclic voltammetry

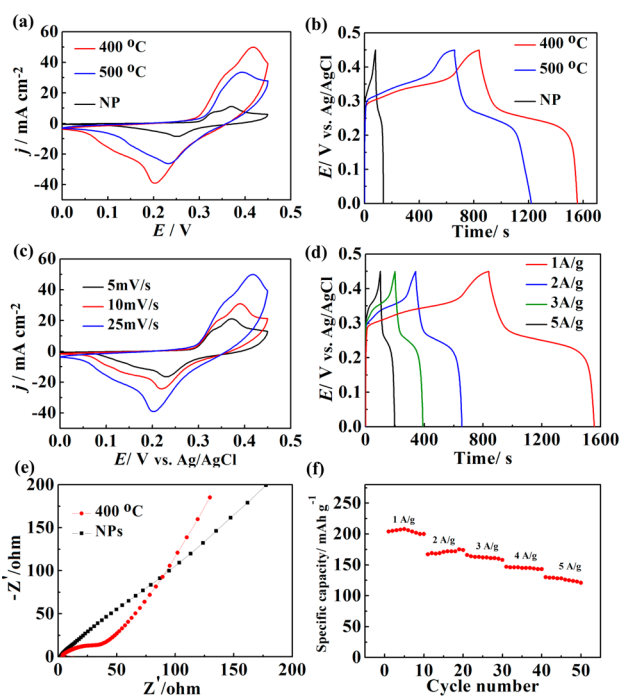
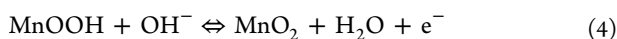
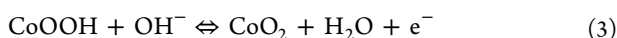
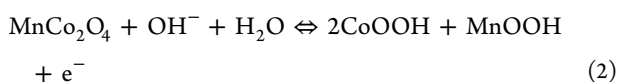


Figure 6. (a) CV curves of $\text{mMnCo}_2\text{O}_4(400)$, $\text{mMnCo}_2\text{O}_4(500)$, and MnCo_2O_4 NPs at a scan rate of 25 mV/s; (b) charge/discharge voltage profiles of $\text{mMnCo}_2\text{O}_4(400)$, $\text{mMnCo}_2\text{O}_4(500)$, and MnCo_2O_4 NPs at 1 A/g; (c) CV curves of $\text{mMnCo}_2\text{O}_4(400)$ with various scan rates from 5 to 25 mV/s; (d) charge/discharge voltage profiles of $\text{mMnCo}_2\text{O}_4(400)$ at various current densities from 1 to 5 A/g; (e) Nyquist plots of $\text{mMnCo}_2\text{O}_4(400)$ and MnCo_2O_4 NPs; and (f) corresponding capacities of $\text{mMnCo}_2\text{O}_4(400)$ at different current densities.

(CV) curves of all prepared MnCo_2O_4 samples at the scan rate of 25 mV/s in 2 M KOH solution. All CV curves exhibit similar shapes with two pairs of Faradaic redox peaks in the potential range from 0 to 0.45 V (vs Ag/AgCl), corresponding to the redox processes as follows:^{47–49}



Apparently, the CV curve obtained from $\text{mMnCo}_2\text{O}_4(400)$ has the largest enclosed area, suggesting the highest capacity.

To quantify their charge storage capability, galvanostatic charge–discharge (GCD) measurements were carried out within the potential window between 0 and 0.45 V vs Ag/AgCl (saturated) at a current density of 1 A/g, as presented in Figure 6b. It can be observed that all MnCo_2O_4 samples exhibit plateau regions in their charge–discharge curves, as expected from the CV behavior. The specific capacities were calculated based on the discharge time of the GCD plots between 0.45 and 0.2 V according to eq 1. The highest capacity is obtained from $\text{mMnCo}_2\text{O}_4(400)$ at the current density of 1 A/g (199 mAh g^{-1}), which is much higher than the values of mMnCo_2O_4 ($500 \text{ }^\circ\text{C}$, 155 mAh g^{-1}) and MnCo_2O_4 NPs (16.1 mAh g^{-1}). These results are consistent with the estimates obtained from the CV curves in Figure 6a. The theoretical capacity of the MnCo_2O_4 compound was calculated to be 452 mAh g^{-1} (see calculation details in the Supporting Information). The high specific capacity of $\text{mMnCo}_2\text{O}_4(400)$ outperforms many recent reported nonprecious electroactive materials in terms of charge storage capability, such as mesoporous $\text{Co}_3\text{O}_4/\text{CeO}_2$ hybrid nanowires (130 mAh g^{-1}),⁵⁰ Ni–Co–S composites (167 mAh g^{-1}),⁵¹ and flake-like MnCo_2O_4 (165 mAh g^{-1}),⁵² urchin-like NiCo_2S_4 (175 mAh g^{-1}),⁵³ and hierarchical Co_3O_4 twin spheres (76 mAh g^{-1}),⁵⁴ as shown in Table S2.

Figure 6c shows the CV curves obtained from $\text{mMnCo}_2\text{O}_4(400)$ at various scan rates from 5 to 25 mV/s. Despite a slight shift in peak positions, the shapes of all CV curves basically remain unchanged, revealing a high electrochemical reversibility and excellent rate capacity. In addition, bare Ni foam was also characterized by CV and GCD techniques, as shown in Figure S6. It can be observed that bare Ni foam shows a pair of redox peaks with low current densities (Figure S6a). This redox process is assigned to the reversible reaction of Ni(II)/Ni(III) occurring on the Ni foam surface. However, bare Ni foam exhibited negligible capacity compared with the $\text{mMnCo}_2\text{O}_4/\text{NF}$ electrode shown in the GCD curve (Figure S6b). Figure S7a depicts the initial and fifth cycle discharge curves of $\text{mMnCo}_2\text{O}_4(400)/\text{NF}$ electrode at a current density of 5 A/g. This reveals that the initial discharge capacity is around 125 mAh g^{-1} , while the capacity increases to 150 mAh g^{-1} after five cycles. This phenomenon is attributed to the gradual kinetic activation of mMnCo_2O_4 upon the ion transportation and redox process on the electrochemical interphase. Additionally, the CV profile (Figure S7b) also exhibits an activation process in the first seven cycles (Figure S7), which is in agreement with the discharge data.

The GCD curves of $\text{mMnCo}_2\text{O}_4(400)$ obtained at various current densities from 1 to 5 A/g are depicted in Figure 6d. It can be observed that specific capacities of 199, 172, 158, 145, and 137 mAh g^{-1} can be obtained at current densities of 1, 2, 3, 4, and 5 A/g (Figure 6f), respectively. As a result, about 70% capacity is retained when the charge–discharge rate increases from 1 to 5 A/g. These results are comparable to, or even better than, those in previous reports (Table S2).^{50–54} Moreover, the $\text{mMnCo}_2\text{O}_4(400)$ also exhibits higher capacity (199 mAh g^{-1}) than that of the corresponding monometallic oxides mCo_3O_4 (75 mAh g^{-1}) and mMnO_2 (56 mAh g^{-1}) (Figure S8), suggesting the combined contribution from both Co and Mn ions produces enhanced charge storage capability. To check the material loading effect, we further investigated the charge storage performance of a $\text{mMnCo}_2\text{O}_4(400)/\text{NF}$ electrode with a mass loading of $2 \text{ mg}/\text{cm}^2$. However, the capacity is lower than the $1 \text{ mg}/\text{cm}^2$ electrode (Figure S9). Higher mass loading may hinder the ion transport into the

inner surface of mesoporous materials, and decrease the availability of the internal structure of the electrode.

The mMnCo_2O_4 was further investigated by electrochemical impedance spectroscopy (EIS). The recorded Nyquist plots shown in Figure 6e were obtained after 50 charge–discharge cycles, and the measurement was carried out in open circuit condition. The semicircle in the high-frequency region is related to the charge transfer resistance within the capacitive materials (R_{ct}), and the straight slope in the low-frequency region reveals the ion diffusion on the electrode/electrolyte interface.^{21,54} It can be seen that the MnCo_2O_4 NP displays no obvious semicircle in the high-frequency region, but a lowered slope in the low-frequency region, suggesting its inferior ion diffusion process. In comparison, the mMnCo_2O_4 exhibits a smaller semicircle and a high slope, indicating a small internal resistance ($R_{\text{ct}} = 11.6 \Omega$), fast charge transfer, and low ion diffusion resistance, which is even better than the reported flake-like MnCo_2O_4 .⁵² The high capacity and good rate capability can be summarized as follows. First, the $\text{mMnCo}_2\text{O}_4(400)$ with highly ordered hierarchical mesopores and continuous crystalline framework can facilitate the transport of electrolyte ions, reducing the diffusion resistance. Second, the mesoporous MnCo_2O_4 has higher exposed surface area and offers more stable and efficient electroactive sites in comparison to its nanoparticle counterparts, resulting in the high capacitive performance. Third, the porous structure of Ni foam allows rapid electron transfer and ion diffusion between MnCo_2O_4 and electrolyte on the entire electrode.

The stability and Coulombic efficiency of the $\text{mMnCo}_2\text{O}_4(400)$ were tested with continuous charge–discharge cycling at a high current density of 10 A/g, as shown in Figure 7. In the first cycle, the $\text{mMnCo}_2\text{O}_4(400)/\text{NF}$

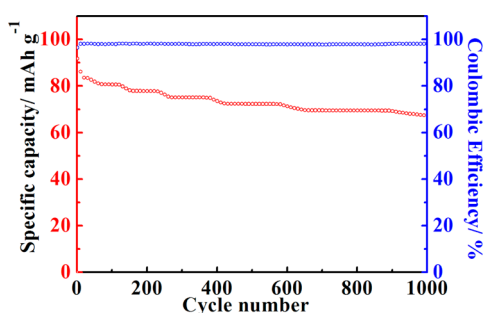


Figure 7. Cycling performance and Coulombic efficiency of $\text{mMnCo}_2\text{O}_4(400)/\text{NF}$ electrode in 2 M KOH at a discharge current density of 10 A/g.

electrode can deliver a capacity of 93 mAh g^{-1} . After 1000 charge–discharge cycles, around 76% of the capacity is retained compared to the first cycle. Moreover, the Coulombic efficiencies at the first and last cycles are 96.5 and 98.1%, respectively, probably as a result of a small amount of oxygen production in the high potential region. As shown in Figure S10, the mesoporous structure is still maintained after 1000 cycles, suggesting the excellent stability of the mMnCo_2O_4 . The slow decrease in the capacity with cycling process is mainly caused by the detachment of mMnCo_2O_4 from the Ni foam substrate. It is expected that the cycling stability can be further improved by using a more effective binder and optimized design of the electrode.

CONCLUSION

In summary, hierarchical mesoporous MnCo_2O_4 spinel oxide with two levels of hierarchy comprised by large mesopores ($\sim 17 \text{ nm}$) and small mesopores ($\sim 5 \text{ nm}$) has been synthesized. A MnCo_2O_4 electrode has been developed by using Ni foam as the electron collector. The $\text{MnCo}_2\text{O}_4/\text{NF}$ hierarchical electrode material has high charge storage capability as well as excellent long-term cyclic stability, making it a promising candidate for high-performance electrochemical energy storage devices. It is expected that this tunable, hierarchical mesoporous architecture can also be applied for other applications, such as batteries, fuel cells, and water-splitting devices.

ASSOCIATED CONTENT

Supporting Information

The Supporting Information is available free of charge on the ACS Publications website at DOI: 10.1021/acs.jpcc.6b08021.

TEM images of $\text{mMnCo}_2\text{O}_4(400)$, $\text{mMnCo}_2\text{O}_4(500)$, mCo_3O_4 , mMnO_2 , and MnCo_2O_4 NPs; XRD diffraction pattern; EDS spectrum; N_2 adsorption–desorption isotherms; electrochemical characterization of bare Ni foam, $\text{mMnCo}_2\text{O}_4(400)$, mCo_3O_4 , and mMnO_2 (PDF)

AUTHOR INFORMATION

Corresponding Authors

*Tel: [REDACTED] E-mail: [REDACTED] (X.Z.).

*Tel: [REDACTED] E-mail: [REDACTED] (D.R.M.).

Notes

The authors declare no competing financial interest.

ACKNOWLEDGMENTS

The authors are grateful to the Australian Research Council for support through the Australian Centre for Electromaterials Science and under the Discovery Projects (DP: 120104334) and the Australian Laureate Fellowship programs. The authors acknowledge the use of facilities at the Monash Centre for Electron Microscopy.

REFERENCES

- (1) Miller, J. R.; Simon, P. Electrochemical Capacitors for Energy Management. *Science* **2008**, *321*, 651–652.
- (2) Han, J.; Xu, G.; Dou, H.; MacFarlane, D. R. Porous Nitrogen-Doped Carbon Microspheres Derived from Microporous Polymeric Organic Frameworks for High Performance Electric Double-Layer Capacitors. *Chem. - Eur. J.* **2015**, *21*, 2310–2314.
- (3) Chmiola, J.; Largeot, C.; Taberna, P. L.; Simon, P.; Gogotsi, Y. Monolithic Carbide-Derived Carbon Films for Micro-Supercapacitors. *Science* **2010**, *328*, 480–483.
- (4) El-Kady, M. F.; Strong, V.; Dubin, S.; Kaner, R. B. Laser Scribing of High-Performance and Flexible Graphene-Based Electrochemical Capacitors. *Science* **2012**, *335*, 1326–1330.
- (5) Simon, P.; Gogotsi, Y. Materials for Electrochemical Capacitors. *Nat. Mater.* **2008**, *7*, 845–854.
- (6) MacFarlane, D. R.; Forsyth, M.; Howlett, P. C.; Kar, M.; Passerini, S.; Pringle, J. M.; Ohno, H.; Watanabe, M.; Yan, F.; Zheng, W.; et al. Ionic Liquids and Their Solid-State Analogues as Materials for Energy Generation and Storage. *Nat. Rev. Mater.* **2016**, *1*, 15005.
- (7) Kurra, N.; Alhebshi, N. A.; Alshareef, H. N. Microfabricated Pseudocapacitors Using $\text{Ni}(\text{OH})_2$ Electrodes Exhibit Remarkable

Volumetric Capacitance and Energy Density. *Adv. Energy Mater.* **2015**, *5*, 1401303.

(8) Li, R.; Wang, Y.; Zhou, C.; Wang, C.; Ba, X.; Li, Y.; Huang, X.; Liu, J. Carbon-Stabilized High-Capacity Ferroferric Oxide Nanorod Array for Flexible Solid-State Alkaline Battery-Supercapacitor Hybrid Device with High Environmental Suitability. *Adv. Funct. Mater.* **2015**, *25*, 5384–5394.

(9) Dong, S.; Shen, L.; Li, H.; Pang, G.; Dou, H.; Zhang, X. Flexible Sodium-Ion Pseudocapacitors Based on 3D $\text{Na}_2\text{Ti}_3\text{O}_7$ Nanosheet Arrays/Carbon Textiles Anodes. *Adv. Funct. Mater.* **2016**, *26*, 3703–3710.

(10) Li, W.; Xin, L.; Xu, X.; Liu, Q.; Zhang, M.; Ding, S.; Zhao, M.; Lou, X. Facile Synthesis of Three-Dimensional Structured Carbon Fiber- NiCo_2O_4 - $\text{Ni}(\text{OH})_2$ High-Performance Electrode for Pseudocapacitors. *Sci. Rep.* **2015**, *5*, 9277.

(11) Zhao, Y.; Hu, L.; Zhao, S.; Wu, L. Preparation of MnCo_2O_4 @ $\text{Ni}(\text{OH})_2$ Core-Shell Flowers for Asymmetric Supercapacitor Materials with Ultrahigh Specific Capacitance. *Adv. Funct. Mater.* **2016**, *26*, 4085–4093.

(12) Brousse, T.; Bélanger, D.; Long, J. W. To Be or Not to Be Pseudocapacitive? *J. Electrochem. Soc.* **2015**, *162*, A5185–A5189.

(13) Stoller, M. D.; Ruoff, R. S. Best Practice Methods for Determining an Electrode Material's Performance for Ultracapacitors. *Energy Environ. Sci.* **2010**, *3*, 1294–1301.

(14) Li, H. B.; Yu, M. H.; Wang, F. X.; Liu, P.; Liang, Y.; Xiao, J.; Wang, C. X.; Tong, Y. X.; Yang, G. W. Amorphous Nickel Hydroxide Nanospheres with Ultrahigh Capacitance and Energy Density as Electrochemical Pseudocapacitor Materials. *Nat. Commun.* **2013**, *4*, 1894.

(15) Xia, X.; Tu, J.; Mai, Y.; Chen, R.; Wang, X.; Gu, C.; Zhao, X. Graphene Sheet/Porous NiO Hybrid Film for Supercapacitor Applications. *Chem. - Eur. J.* **2011**, *17*, 10898–10905.

(16) Gao, Z.; Yang, W.; Wang, J.; Song, N.; Li, X. Flexible All-Solid-State Hierarchical NiCo_2O_4 /Porous Graphene Paper Asymmetric Supercapacitors with an Exceptional Combination of Electrochemical Properties. *Nano Energy* **2015**, *13*, 306–317.

(17) Guo, D.; Luo, Y.; Yu, X.; Li, Q.; Wang, T. High Performance NiMoO_4 Nanowires Supported on Carbon Cloth as Advanced Electrodes for Symmetric Supercapacitors. *Nano Energy* **2014**, *8*, 174–182.

(18) An, C.; Wang, Y.; Huang, Y.; Xu, Y.; Jiao, L.; Yuan, H. Porous NiCo_2O_4 Nanostructures for High Performance Supercapacitors via a Microemulsion Technique. *Nano Energy* **2014**, *10*, 125–134.

(19) Hong, W. T.; Welsch, R. E.; Shao-Horn, Y. Descriptors of Oxygen-Evolution Activity for Oxides: A Statistical Evaluation. *J. Phys. Chem. C* **2016**, *120*, 78–86.

(20) Xia, X.; Tu, J.; Zhang, Y.; Wang, X.; Gu, C.; Zhao, X. B.; Fan, H. J. High-Quality Metal Oxide Core/Shell Nanowire Arrays on Conductive Substrates for Electrochemical Energy Storage. *ACS Nano* **2012**, *6*, 5531–5538.

(21) Liang, J.; Fan, Z.; Chen, S.; Ding, S.; Yang, G. Hierarchical NiCo_2O_4 Nanosheets@Haloalloy Nanotubes with Ultrahigh Capacitance and Long Cycle Stability as Electrochemical Pseudocapacitor Materials. *Chem. Mater.* **2014**, *26*, 4354–4360.

(22) Zhang, L. L.; Zhao, X.; Stoller, M. D.; Zhu, Y.; Ji, H.; Murali, S.; Wu, Y.; Perales, S.; Clevenger, B.; Ruoff, R. S. Highly Conductive and Porous Activated Reduced Graphene Oxide Films for High-Power Supercapacitors. *Nano Lett.* **2012**, *12*, 1806–1812.

(23) Frackowiak, E.; Metenier, K.; Bertagna, V.; Beguin, F. Supercapacitor Electrodes from Multiwalled Carbon Nanotubes. *Appl. Phys. Lett.* **2000**, *77*, 2421–2423.

(24) Ren, Y.; Ma, Z.; Bruce, P. G. Ordered Mesoporous Metal Oxides: Synthesis and Applications. *Chem. Soc. Rev.* **2012**, *41*, 4909–4927.

(25) Lu, X.; Ng, Y. H.; Zhao, C. Gold Nanoparticles Embedded within Mesoporous Cobalt Oxide Enhance Electrochemical Oxygen Evolution. *ChemSusChem* **2014**, *7*, 82–86.

(26) Xiao, C.; Lu, X.; Zhao, C. Unusual Synergistic Effects Upon Incorporation of Fe and/or Ni Into Mesoporous Co_3O_4 for Enhanced Oxygen Evolution. *Chem. Commun.* **2014**, *50*, 10122–10125.

(27) Tüysüz, H.; Hwang, Y. J.; Khan, S. B.; Asiri, A. M.; Yang, P. Mesoporous Co_3O_4 as an Electrocatalyst for Water Oxidation. *Nano Res.* **2013**, *6*, 47–54.

(28) Grewe, T.; Deng, X.; Tüysüz, H. Influence of Fe Doping on Structure and Water Oxidation Activity of Nanocast Co_3O_4 . *Chem. Mater.* **2014**, *26*, 3162–3168.

(29) Liu, S.; Hu, L.; Xu, X.; Al-Ghamdi, A. A.; Fang, X. Nickel Cobaltite Nanostructures for Photoelectric and Catalytic Applications. *Small* **2015**, *11*, 4267–4283.

(30) Sun, S.; Zhao, X.; Yang, M.; Wu, L.; Wen, Z.; Shen, X. Hierarchically Ordered Mesoporous Co_3O_4 Materials for High Performance Li-ion Batteries. *Sci. Rep.* **2016**, *6*, 19564.

(31) Yuan, C.; Yang, L.; Hou, L.; Shen, L.; Zhang, X.; Lou, X. W. D. Growth of Ultrathin Mesoporous Co_3O_4 Nanosheet Arrays on Ni Foam for High-Performance Electrochemical Capacitors. *Energy Environ. Sci.* **2012**, *5*, 7883–7887.

(32) Yuan, C.; Li, J.; Hou, L.; Yang, L.; Shen, L.; Zhang, X. Facile Template-Free Synthesis of Ultralayered Mesoporous Nickel Cobaltite Nanowires Towards High-Performance Electrochemical Capacitors. *J. Mater. Chem.* **2012**, *22*, 16084–16090.

(33) Meena, P. L.; Pal, S.; Sreenivas, K.; Kumar, R. Structural and Magnetic Properties of MnCo_2O_4 Spinel Multiferroic. *Adv. Sci. Lett.* **2015**, *21*, 2760–2763.

(34) Zhang, Y.; Luo, L.; Zhang, Z.; Ding, Y.; Liu, S.; Deng, D.; Zhao, H.; Chen, Y. Synthesis of MnCo_2O_4 Nanofibers by Electrospinning and Calcination: Application for a Highly Sensitive Non-Enzymatic Glucose Sensor. *J. Mater. Chem. B* **2014**, *2*, 529–535.

(35) Ma, T. Y.; Zheng, Y.; Dai, S.; Jaroniec, M.; Qiao, S. Z. Mesoporous MnCo_2O_4 with Abundant Oxygen Vacancy Defects as High-Performance Oxygen Reduction Catalysts. *J. Mater. Chem. A* **2014**, *2*, 8676–8682.

(36) Fu, C.; Li, G.; Luo, D.; Huang, X.; Zheng, J.; Li, L. One-Step Calcination-Free Synthesis of Multicomponent Spinel Assembled Microspheres for High-Performance Anodes of Li-Ion Batteries: A Case Study of MnCo_2O_4 . *ACS Appl. Mater. Interfaces* **2014**, *6*, 2439–2449.

(37) Li, L.; Zhang, Y. Q.; Liu, X. Y.; Shi, S. J.; Zhao, X. Y.; Zhang, H.; Ge, X.; Cai, G. F.; Gu, C. D.; Wang, X. L.; et al. One-Dimension MnCo_2O_4 Nanowire Arrays for Electrochemical Energy Storage. *Electrochim. Acta* **2014**, *116*, 467–474.

(38) Cao, X.; Wu, J.; Jin, C.; Tian, J.; Strasser, P.; Yang, R. MnCo_2O_4 Anchored on P-Doped Hierarchical Porous Carbon as an Electrocatalyst for High-Performance Rechargeable Li- O_2 Batteries. *ACS Catal.* **2015**, *5*, 4890–4896.

(39) Liu, S.; San Hui, K.; Hui, K. N.; Yun, J. M.; Kim, K. H. Vertically Stacked Bilayer CuCo_2O_4 / MnCo_2O_4 Heterostructures on Functionalized Graphite Paper for High-Performance Electrochemical Capacitors. *J. Mater. Chem. A* **2016**, *4*, 8061–8071.

(40) Wang, S.; Hou, Y.; Wang, X. Development of a Stable MnCo_2O_4 Cocatalyst for Photocatalytic CO_2 Reduction with Visible Light. *ACS Appl. Mater. Interfaces* **2015**, *7*, 4327–4335.

(41) Qiu, M.; Zhan, S.; Yu, H.; Zhu, D.; Wang, S. Facile Preparation of Ordered Mesoporous MnCo_2O_4 for Low-Temperature Selective Catalytic Reduction of NO with NH_3 . *Nanoscale* **2015**, *7*, 2568–2577.

(42) Ma, C. Y.; Mu, Z.; Li, J. J.; Jin, Y. G.; Cheng, J.; Lu, G. Q.; Hao, Z. P.; Qiao, S. Z. Mesoporous Co_3O_4 and $\text{Au/Co}_3\text{O}_4$ Catalysts for Low-Temperature Oxidation of Trace Ethylene. *J. Am. Chem. Soc.* **2010**, *132*, 2608–2613.

(43) Ge, X.; Liu, Y.; Goh, F. T.; Hor, T. A.; Zong, Y.; Xiao, P.; Zhang, Z.; Lim, S. H.; Li, B.; Wang, X.; et al. Dual-Phase Spinel MnCo_2O_4 and Spinel MnCo_2O_4 /Nanocarbon Hybrids for Electrocatalytic Oxygen Reduction and Evolution. *ACS Appl. Mater. Interfaces* **2014**, *6*, 12684–12691.

(44) Sing, K. S. Reporting Physisorption Data for Gas/Solid Systems with Special Reference to the Determination of Surface Area and Aorosity. *Pure Appl. Chem.* **1985**, *57*, 603–619.

- (45) Ravikovitch, P. I.; Neimark, A. V. Characterization of Nanoporous Materials from Adsorption and Desorption Isotherms. *Colloids Surf., A* **2001**, *187–188*, 11–21.
- (46) Ren, Y.; Ma, Z.; Morris, R. E.; Liu, Z.; Jiao, F.; Dai, S.; Bruce, P. G. A Solid with a Hierarchical Tetramodal Micro-Meso-Macro Pore Size Distribution. *Nat. Commun.* **2013**, *4*, 2015.
- (47) Li, L.; Zhang, Y.; Shi, F.; Zhang, Y.; Zhang, J.; Gu, C.; Wang, X.; Tu, J. Spinel Manganese-Nickel-Cobalt Ternary Oxide Nanowire Array for High-Performance Electrochemical Capacitor Applications. *ACS Appl. Mater. Interfaces* **2014**, *6*, 18040–18047.
- (48) Kong, D.; Luo, J.; Wang, Y.; Ren, W.; Yu, T.; Luo, Y.; Yang, Y.; Cheng, C. Three-Dimensional $\text{Co}_3\text{O}_4@\text{MnO}_2$ Hierarchical Nanoneedle Arrays: Morphology Control and Electrochemical Energy Storage. *Adv. Funct. Mater.* **2014**, *24*, 3815–3826.
- (49) Krishnan, S. G.; Reddy, M. V.; Harilal, M.; Vidyadharan, B.; Misnon, I. I.; Ab Rahim, M. H.; Ismail, J.; Jose, R. Characterization of MgCo_2O_4 as an Electrode for High Performance Supercapacitors. *Electrochim. Acta* **2015**, *161*, 312–321.
- (50) Cui, J.; Zhang, X.; Tong, L.; Luo, J.; Wang, Y.; Zhang, Y.; Xie, K.; Wu, Y. A Facile Synthesis of Mesoporous $\text{Co}_3\text{O}_4/\text{CeO}_2$ Hybrid Nanowire Arrays for High Performance Supercapacitors. *J. Mater. Chem. A* **2015**, *3*, 10425–10431.
- (51) Chen, H. C.; Jiang, J. J.; Zhao, Y. D.; Zhang, L.; Guo, D. Q.; Xia, D. D. One-Pot Synthesis of Porous Nickel Cobalt Sulphides: Tuning the Composition for Superior Pseudocapacitance. *J. Mater. Chem. A* **2015**, *3*, 428–437.
- (52) Mondal, A. K.; Su, D.; Chen, S.; Ung, A.; Kim, H. S.; Wang, G. Mesoporous MnCo_2O_4 with a Flake-Like Structure as Advanced Electrode Materials for Lithium-Ion Batteries and Supercapacitors. *Chem. - Eur. J.* **2015**, *21*, 1526–1532.
- (53) Chen, H.; Jiang, J.; Zhang, L.; Wan, H.; Qi, T.; Xia, D. Highly Conductive NiCo_2S_4 Urchin-Like Nanostructures for High-Rate Pseudocapacitors. *Nanoscale* **2013**, *5*, 8879–8883.
- (54) Xiao, Y.; Liu, S.; Li, F.; Zhang, A.; Zhao, J.; Fang, S.; Jia, D. 3D Hierarchical Co_3O_4 Twin-Spheres with an Urchin-Like Structure: Large-Scale Synthesis, Multistep-Splitting Growth, and Electrochemical Pseudocapacitors. *Adv. Funct. Mater.* **2012**, *22*, 4052–4059.

**Synthesis of Highly Ordered Hierarchically Mesoporous MnCo₂O₄
with Cubic *Ia3d* Symmetry for Electrochemical Energy Storage**

Changlong Xiao, Xinyi Zhang^{*}, Tiago Mendes, Gregory P. Knowles, Alan Chaffee
and Douglas R. MacFarlane^{*}

The redox reactions and theoretical capacity calculation for MnCo₂O₄:



Calculation of theoretical capacity:

$$C_{\text{cap}} = \frac{n \times e}{M / N_A} \quad \text{Eq. (S4)}$$

, where C_{cap} is the theoretical capacity, n (4) is the transferred electrons during the electrochemical reaction, e ($-1.602176565 \times 10^{-19}$ C) is the electric charge of a electron, M (~ 237 g/mol) is the molecular weight of MnCo₂O₄ and N_A is the avogadro's constant ($6.022140857 \times 10^{23}$). Substituting the values in equation S4: $C_{\text{cap}} = \sim 452$ mAh g⁻¹.

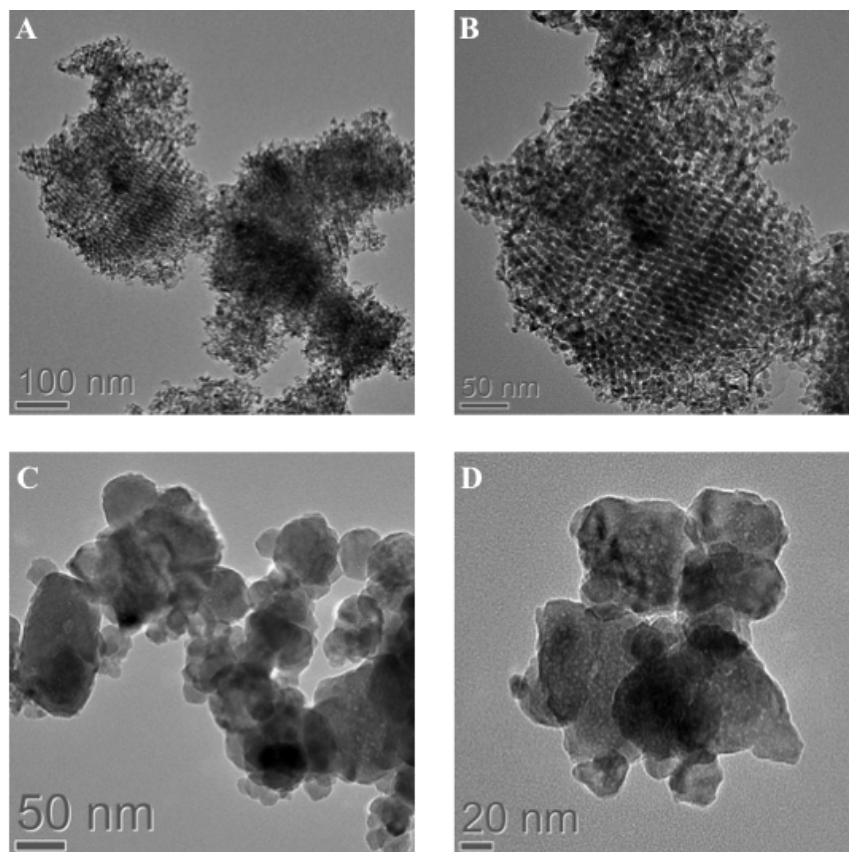


Figure S1. (a)-(b)TEM images of $m\text{MnCo}_2\text{O}_4$ (500) and (c)-(d) TEM images of MnCo_2O_4 NPs.

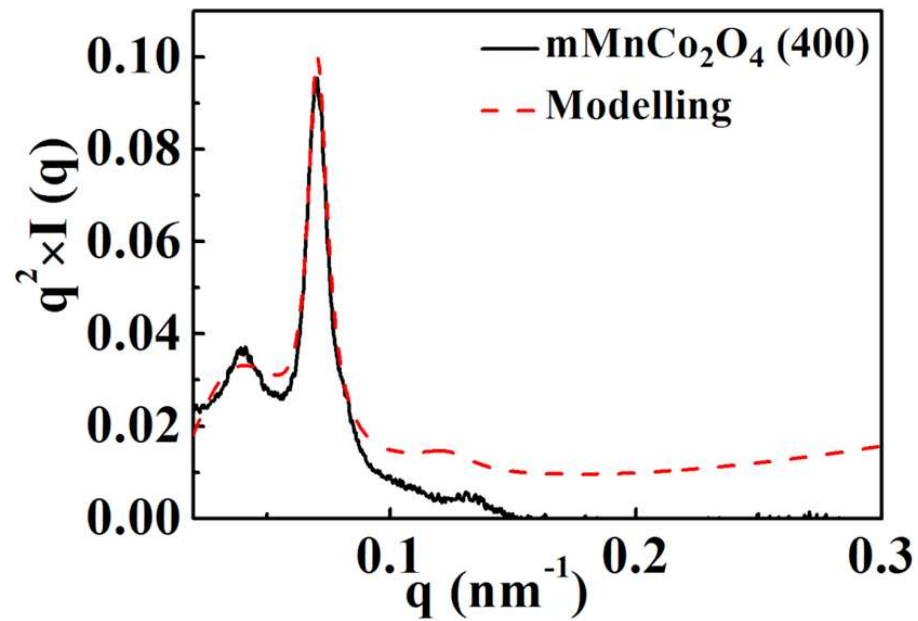


Figure S2. Small-angle X-ray scattering pattern of well-ordered mMnCo_2O_4 (400).

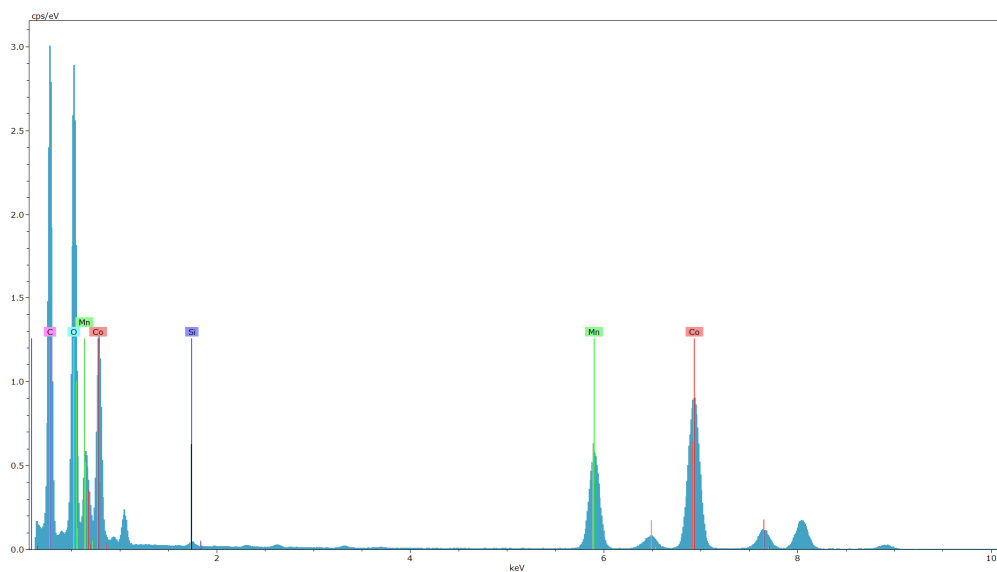


Figure S3. Energy dispersive X-ray spectrum of mesoporous MnCo_2O_4 (400). The energy peak at 1.73 keV represents Si (~ 0.37 wt.%), which is residual from the silica template.

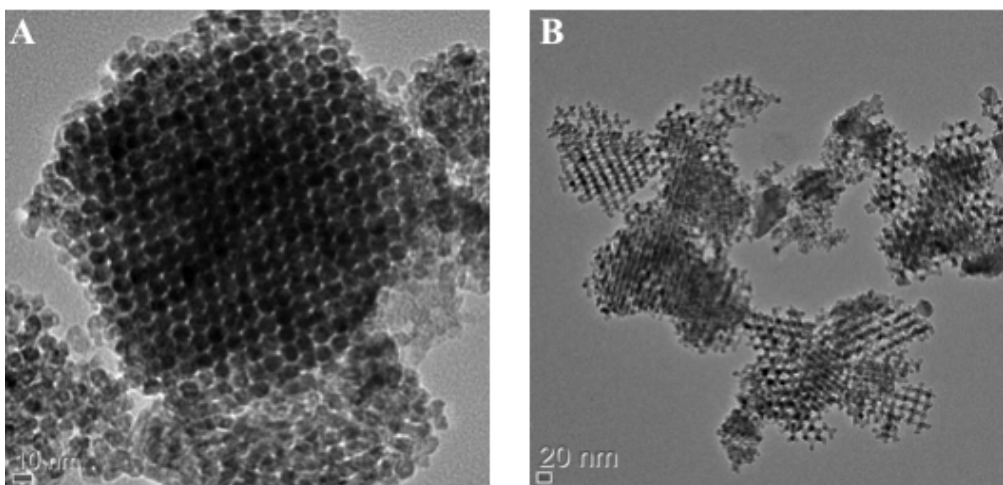


Figure S4. TEM images of (a) mesoporous Co_3O_4 and (b) mesoporous MnO_2 .

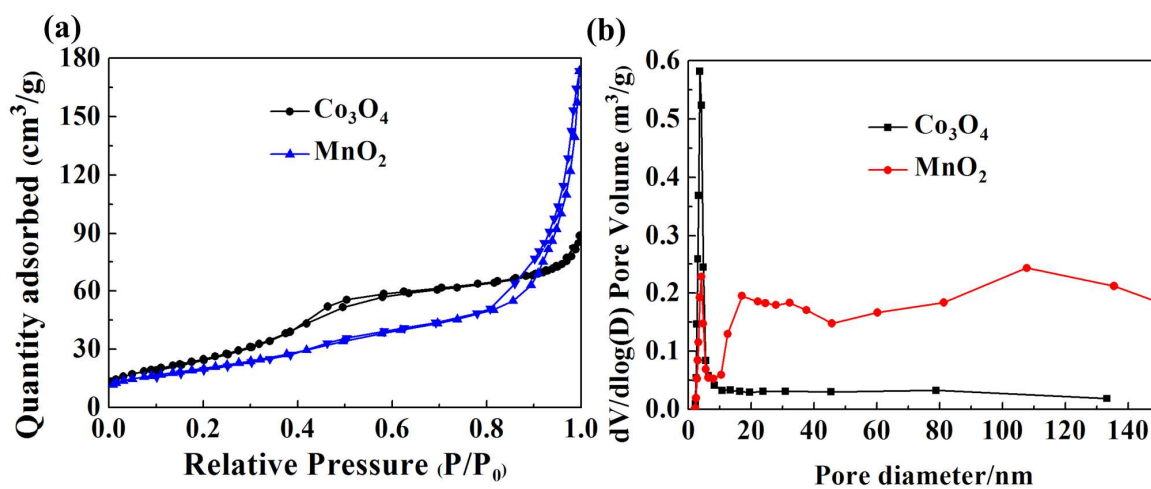


Figure S5. (a) N₂ adsorption-desorption isotherms and (b) pore size distribution plots of mCo_3O_4 and mMnO_2 .

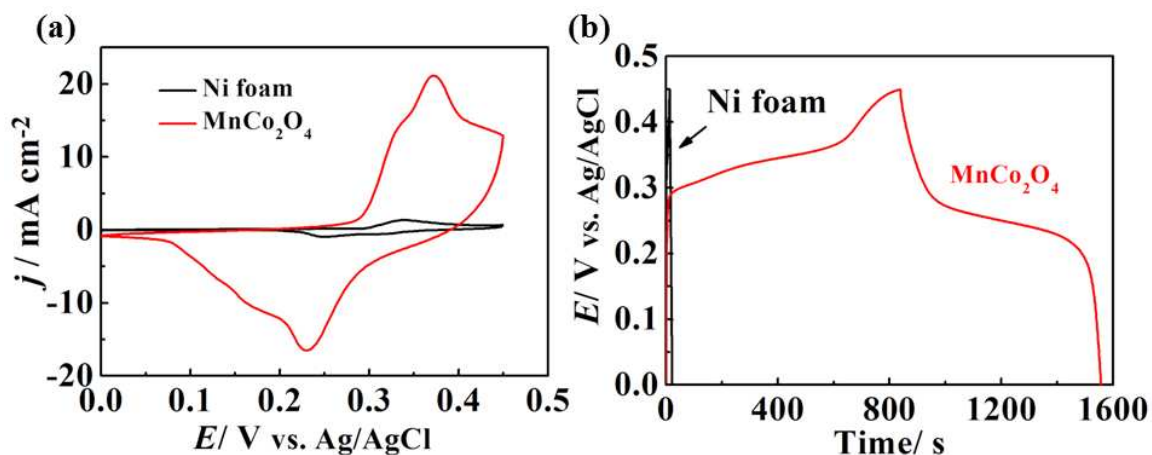


Figure S6. (a) CV curves of mMnCo_2O_4 (400) and Ni foam at the scan rate of 5mV/s , (b) charge/discharge voltage profiles of mMnCo_2O_4 (400) and Ni foam at current density of 1 A/g .

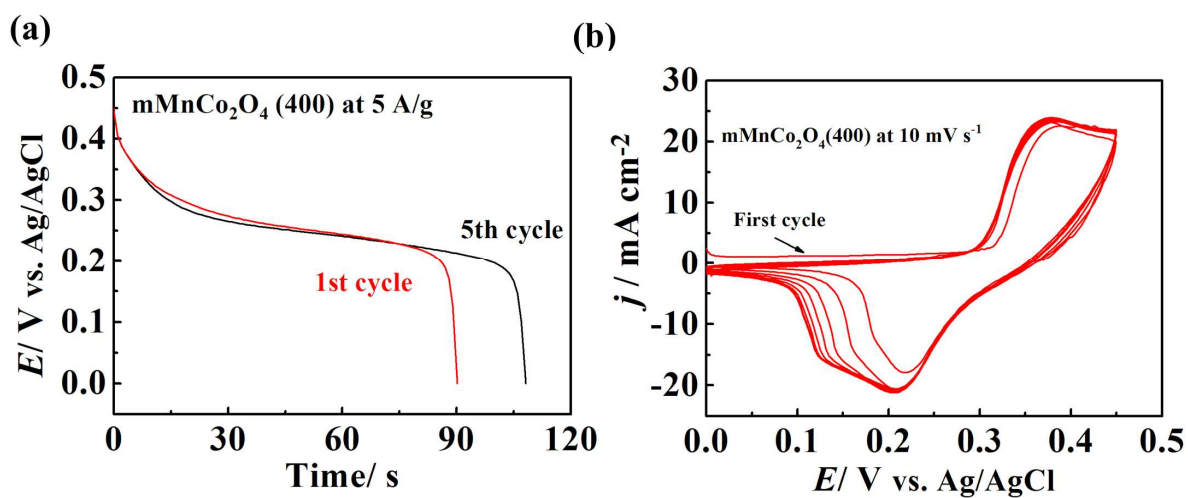


Figure S7. (a) Discharge curves at first and fifth cycle with current density of 5 A/g . and (b) CV curves of curves of mMnCo_2O_4 (400) at scan rate of 10 mV/s showing action process.

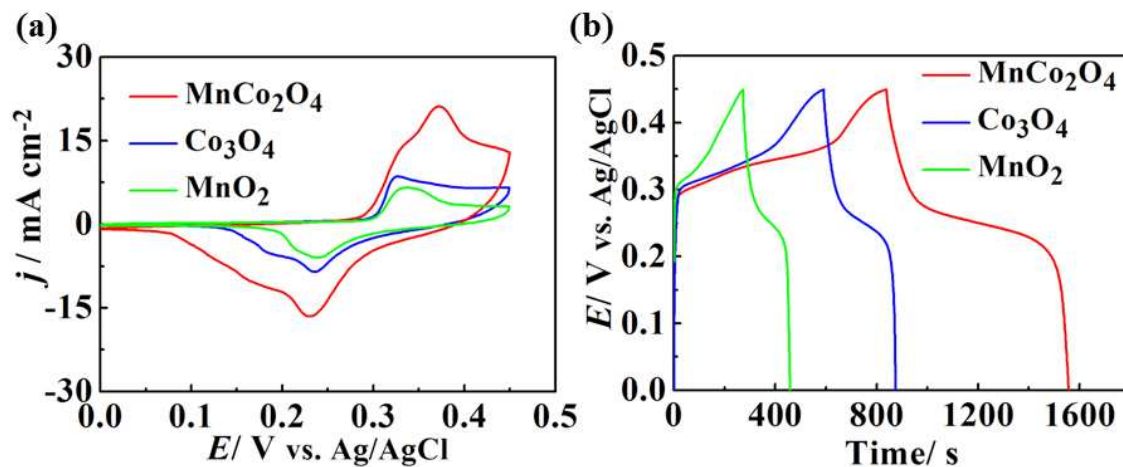


Figure S8. (A) CV curves of mMnCo_2O_4 (400), mCo_3O_4 and mMnO_2 at the scan rate of 5mV/s , (B) charge/discharge voltage profiles of mMnCo_2O_4 (400), mCo_3O_4 and mMnO_2 .

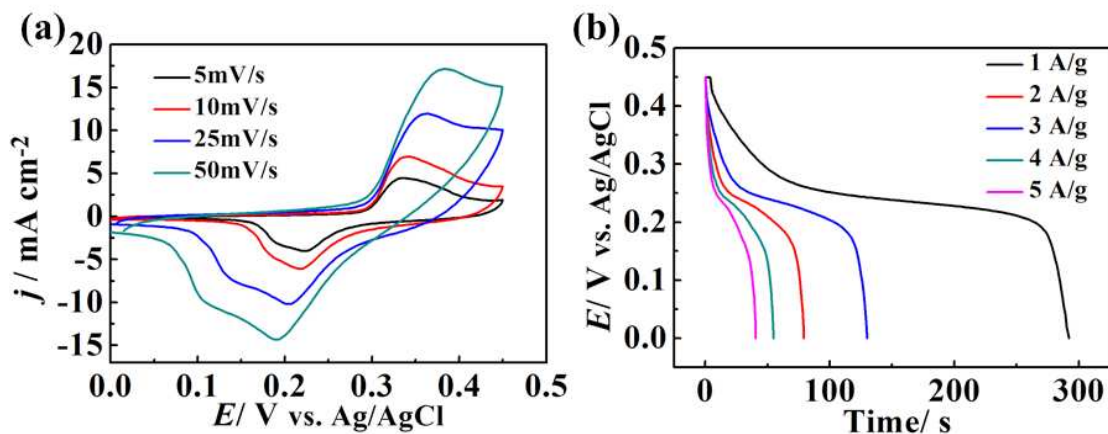


Figure S9. CV and discharge curves at various current densities of mMnCo_2O_4 (400) electrode with 2 mg/cm^2 materials loading.

The CV curves of $\text{mMnCo}_2\text{O}_4(400)/\text{NF}$ electrode with mass loading of 2 mg/cm^2 also shows two pairs of redox process associated with $\text{Co}^{3+}/\text{Co}^{4+}$ and $\text{Mn}^{3+}/\text{Mn}^{4+}$. No apparent alternation of the shape can be observed indicating the high rate capability. Capacities of 82 mAh g^{-1} , 73 mAh g^{-1} , 67 mAh g^{-1} , 62 mAh g^{-1} and 57 mAh g^{-1} can be obtained at various

current densities from 1 A/g up to 5 A/g. The decreased capacity compared to the mass loading of 1 mg/cm² is mainly caused by the block of the original macropores of NF, which hinder the transport of the ions into the inner layer of the active materials.

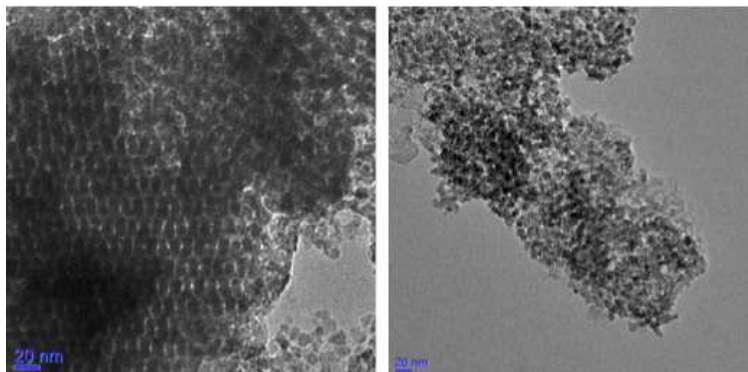


Figure S10. TEM image of mMnCo₂O₄ (400) after 1000 charge-discharge

Table S1. BET surface area, BJH pore volume and average diameter of MnCo₂O₄ samples.

Sample	S _{BET} [m ² /g]	V _p [cm ³ /g]	D _p [nm]
mMnCo ₂ O ₄ (400 °C)	133 ± 0.72	0.420	9.7
mMnCo ₂ O ₄ (500 °C)	133 ± 0.96	0.369	8.5
MnCo ₂ O ₄ NP	45.2 ± 0.35	0.125	---
mCo ₃ O ₄	98.6 ± 1.9	0.17	4.7
mMnO ₂	75.0 ± 0.53	0.28	12.7

Table S2 Comparison of specific capacitance of various capacitive materials [values have been calculated from the original papers from the equation below: Specific capacity (mAh g⁻¹) = Specific capacitance (F/g) × ΔV/3.6]

Samples	Capacities at (1A/g)	Capacities at (5A/g)	Electrolyte	Mass loading	Ref.
mMnCo ₂ O ₄ (400 °C)	199 mAh g ⁻¹ (1593 F/g)	137 mAh g ⁻¹ (1100 F/g)	2 M KOH	1 mg/cm ²	This work
mMnCo ₂ O ₄ (500 °C)	155 mAh g ⁻¹ (1246 F/g)		2 M KOH	1 mg/cm ²	This work
MnCo ₂ O ₄ NPs	16.1 mAh g ⁻¹ (128.9 F/g)		2 M KOH	1 mg/cm ²	This work
Co ₃ O ₄ /CeO ₂ hybrid nanowire	130 ^a mAh g ⁻¹ (1037 F/g)	~ 123 mAh g ⁻¹ (~980 F/g)	2 M KOH	1 mg/cm ²	50
Ni-Co-S	167 mAh g ⁻¹ (1093 F/g)	~ 152 mAh g ⁻¹ (~1000 F/g)	6 M KOH	1.7-2.6 mg/cm ²	51
Flake-like MnCo ₂ O ₄	1165 mAh g ⁻¹ (1487 F/g)	129 mAh g ⁻¹ (1162 F/g)	2 M KOH	1 mg/cm ²	52
Urchin-like NiCo ₂ S ₄	175 mAh g ⁻¹ (1149 F/g)	61 mAh g ⁻¹ (1056 F/g)	6 M KOH	1.7-2.6 mg/cm ²	53
Hierarchical Co ₃ O ₄ twin-spheres	76 mAh g ⁻¹ (781 F/g)	65 ^b mAh g ⁻¹ (670 F/g)	6 M KOH	----	54

^a value obtained at 1A/g, ^b value obtained at 4 A/g.

Chapter 6

Dual-MnCo₂O₄/Ni Electrode with Three-level Hierarchy for High-performance Electrochemical Energy Storage

6.1 Overview

This chapter is a paper titled “Dual-MnCo₂O₄/Ni Electrode with Three-level Hierarchy for High-performance Electrochemical Energy Storage” that was published in *Electrochimica Acta* in 2018.

In pursuit of reliable energy storage technologies, high-performance supercapacitors need to be developed to replace batteries when high power density is required. Despite recent progress, a great challenge still remains in the development of cost-effective capacitive materials to achieve high capacitance and stability comparable to those of noble-metal based capacitors. Mesoporous oxide materials have shown great potential for electrochemical energy storage; however, the majority of reported mesoporous materials in capacitors are limited to a single level of structural hierarchy with pore sizes less than 10 nanometers, which hampers their capacitive performance.¹ In this manuscript, we report a well-designed MnCo₂O₄/Ni electrode with multilevel hierarchy containing a mesoporous MnCo₂O₄ nanosheet layer and vertically aligned MnCo₂O₄ nanoflake layer on a macroporous Ni foam support (~ 500 μm). The dual-MnCo₂O₄ layers are well connected with each other and grown directly on the Ni foam support. As a result, the obtained dual-MnCo₂O₄/Ni electrode delivers an excellent specific capacity up to 283 mAh g⁻¹ and long-term performance stability over 2000 cycles.

Reference

1. C. Xiao, X. Zhang and D. R. MacFarlane, *Electrochim. Acta* 2018, **280**, 55.



Dual-MnCo₂O₄/Ni electrode with three-level hierarchy for high-performance electrochemical energy storage

Changlong Xiao^a, Xinyi Zhang^{a, b, *}, Douglas R. MacFarlane^{a, **}

^a ARC Centre of Excellence for Electromaterials Science, Monash University, Victoria 3800, Australia

^b Guangxi Innovation Centre for Renewable Energy Materials; Laboratory for Electrochemical Energy Materials, Guangxi University, Nanning 530004, China

ARTICLE INFO

Article history:

Received 16 December 2017

Received in revised form

16 May 2018

Accepted 16 May 2018

Available online 18 May 2018

Keywords:

Supercapacitor

Hierarchical

Mesoporous

Energy storage

ABSTRACT

The design of micro/nanostructures with high porosity is very important to achieve reliable and high-performance capacitive materials for electrochemical energy storage. The complexity of this strategy is limited by the lack of a facile method to synthesize multi-hierarchical architectures with both high electroactive surface area and fast ion diffusion ability. Here, we report a designed MnCo₂O₄/Ni electrode with multilevel hierarchy containing mesoporous MnCo₂O₄ nanosheet layers and vertically aligned MnCo₂O₄ nanoflake layers on a macroporous Ni foam support (~500 μm). The dual-MnCo₂O₄ layers are well connected with each other and grown directly on the Ni foam support. As a result, the obtained dual-MnCo₂O₄/Ni electrode delivers an excellent specific capacity up to 283 mAh g⁻¹ and long-term performance stability over 2000 cycles.

© 2018 Elsevier Ltd. All rights reserved.

1. Introduction

The worldwide environmental issues surrounding CO₂ emissions and the rising demand for energy have triggered rapid development in reliable and high-performance electrical energy storage technologies. As portable and rechargeable electronic devices, supercapacitors offer numerous advantages including high-rate charge/discharge, long lifespan and high power density [1–6]. Unlike battery behaviour, the charge/discharge phenomena in a supercapacitor system is attributed to the ion transfer across the liquid-solid interfaces between the electrode materials and electrolyte [7–10]. However, the working mechanism of supercapacitors leads to a lower energy density property, which restricts their large-scale application in high power devices such as electric vehicles. As a new type of electrochemical energy storage device, battery-supercapacitor hybrid systems have attracted great research interest, employing battery-type materials as the positive electrode and nanostructured carbon materials as the negative electrode [11–14]. This combined hybrid-type device can benefit from both the high energy density of batteries and the high-power

density of supercapacitors. So far, many transition metal oxide/hydroxides have been studied for this application owing to their high capacities, low cost and environmental compatibility [15–19]. However, technological progress in terms of power density, manufacturing cost and cycling performance is still elusive.

Controllable synthesis of electrode materials with well-designed architecture has significant impact on achieving outstanding performance in electrochemical energy storage [20,21]. For example, flexible one-dimension (1D) NiO/Ni nanowires [22], ultrathin two-dimensional (2D) VOPO₄ nanosheets [23] and three-dimensional (3D) MnO₂/NiO nanoflakes [24] have been reported to exhibit excellent capacitance benefiting from their high electroactive surface area. In this regard, core-shell structured, multi-hierarchical and/or porous capacitive materials such as Co₃O₄ nanowire@NiO nanosheet core-shell arrays [25] and hierarchical mesoporous ZnCo₂O₄ nanoparticles [26] were designed in pursuit of maximization of the effective surface area. With their high surface area, tuneable pore structure and high specific capacity, mesoporous MnCo₂O₄ nanostructures have been investigated as electrode materials for batteries and supercapacitors. Usually, insulating polymeric binder materials such as Nafion or PVDF are used in the preparation of electrode, which significantly deteriorate the charge transfer and energy storage capacity [11].

In this work, we have synthesized a freestanding and dual-hierarchical MnCo₂O₄/Ni electrode (D-MnCo₂O₄/Ni) constructed with 3D macroporous Ni foam, vertically aligned 2D MnCo₂O₄

* Corresponding author. ARC Centre of Excellence for Electromaterials Science, Monash University, Victoria 3800, Australia.

** Corresponding author.

E-mail addresses: [redacted] (X. Zhang), [redacted] (D.R. MacFarlane).

nanoflakes and mesoporous MnCo_2O_4 nanosheets. The porous Ni foam acts as a robust support for high effective surface area, and supplies reliable electrical connection to the outer superstructures. The in-between vertically aligned MnCo_2O_4 nanoflakes form a secondary macro porosity. The tertiary, very thin, MnCo_2O_4 nanosheets are embedded with numerous mesopores, which can also provide channels for the transport of OH^- ions to the interior active sites. All of these three nanostructures are mutually connected, forming a highly hierarchical porous system as a whole. Moreover, integrated diffusion channels are also established from the bottom macropores ($\sim 500 \mu\text{m}$ and $200 \mu\text{m}$) up to the top mesopores ($\sim 5 \text{ nm}$). The obtained D- $\text{MnCo}_2\text{O}_4/\text{Ni}$ electrode shows a dramatically increased capacity of up to 283 mAh g^{-1} at 2 mA cm^{-2} (1.67 A g^{-1}) and excellent long-term cycling stability over 2000 cycles.

2. Experimental

2.1. Materials

Ni foam with a thickness of 1.6 mm and a bulk density of 0.45 g cm^{-2} was used as the electrode support. Cobalt nitrate hexahydrate ($\text{Co}(\text{NO}_3)_2 \cdot 6\text{H}_2\text{O}$, $\geq 98\%$), Manganese nitrate tetrahydrate ($\text{Mn}(\text{NO}_3)_2 \cdot 4\text{H}_2\text{O}$, $\geq 98\%$), potassium hydroxide (KOH , $\geq 98\%$), ammonium fluoride (NH_4F , $\geq 98\%$) and urea ($\text{CO}(\text{NH}_2)_2$, $\geq 98\%$) were supplied by Sigma-Aldrich. All chemicals were used directly without further purification.

2.2. Hydrothermal deposition of MnCo_2O_4 nanoflake on Ni foam

Ni foam was sonicated in HCl (0.5 M) for 15 min to remove the NiO layer on the surface, rinsed with DI water and absolute ethanol, then dried under a pure N_2 flow at room temperature (25°C). The reaction solution containing 3.3 mM $\text{Co}(\text{NO}_3)_2$, 1.67 mM $\text{Mn}(\text{NO}_3)_2$, 10 mM NH_4F and 25 mM $\text{CO}(\text{NH}_2)_2$ was sonicated for 15 min to ensure the homogeneity. Subsequently, 35 mL of the resultant solution was transferred to a 50 mL Teflon-lined stainless-steel autoclave. A piece of Ni foam with the top side covered with polytetrafluoroethylene tape was vertically soaked into the solution. The autoclave was then sealed and placed in an oven at 120°C for 5 h. After the hydrothermal synthesis, the autoclave was cooled down to room temperature and the Ni foam was rinsed with water and absolute ethanol, and dried in air. Finally, the obtained sample was calcinated at 350°C in a furnace for 2 h.

2.3. Synthesis of core-shell structured D- $\text{MnCo}_2\text{O}_4/\text{Ni}$ electrode

Another thin layer of MnCo_2O_4 nanosheets were electro-deposited onto the as-obtained $\text{MnCo}_2\text{O}_4/\text{Ni}$ foam. The electrodeposition process was carried out in a standard three-electrode system, using $\text{MnCo}_2\text{O}_4/\text{Ni}$ foam as the working electrode, Pt wires and Ag/AgCl (saturated) as counter and reference electrodes, respectively. The electrodeposition was conducted in an aqueous solution containing 1.67 mM $\text{Mn}(\text{NO}_3)_2$ and 3.3 mM $\text{Co}(\text{NO}_3)_3$ under a constant potential of -1.1 V vs. Ag/AgCl (saturated) for 5 min. Subsequently, the obtained Dual-hierarchy $\text{MnCo}_2\text{O}_4/\text{Ni}$ foam (D- $\text{MnCo}_2\text{O}_4/\text{Ni}$) electrode was rinsed with deionized water, dried in air, and calcinated at 350°C in a furnace for another 2 h.

2.4. Materials characterization

The scanning electron microscopic (SEM) images were performed on JEOL 7001 SEM instrument at 3 kV and the transmission electron microscopic (TEM) images were obtained from a FEI Tecnai G2 T20 at 200 kV. X-ray diffraction patterns were conducted on

Bruker D8 ADVANCE ECO powder X-ray instrument using Cu $K\alpha$ radiation ($\lambda = 0.15418 \text{ nm}$) in a 2θ range from 20° to 80° with a scanning step size of 0.01° . X-ray photoelectron (XPS) characterizations were carried out on a Thermal ESCALA 250i X-ray Photoelectron Spectrometer. All binding energies were calibrated to the C 1s peak (284.6 eV).

2.5. Electrochemical analysis

All electrochemical measurements were conducted on an EC-Lab electrochemical workstation with a standard three-electrode electrochemical cell, employing fabricated D- $\text{MnCo}_2\text{O}_4/\text{Ni}$ electrode as working electrode, Ag/AgCl (saturated) reference electrode, and a Pt wire counter electrode. The cyclic voltammetry (CV) was conducted with a voltage window of $0-0.5 \text{ V}$ (vs. Ag/AgCl) at various scan rates from 5 to 20 mV s^{-1} , while the galvanostatic charge/discharge experiments were performed within a potential window ($0-0.45 \text{ V}$ vs. Ag/AgCl) under different current densities (2, 5, 10 and 20 mA cm^{-2}). Electrochemical impedance spectra (EIS) were obtained in a frequency range from 100 kHz to 0.01 kHz at the open circuit potential. The specific capacity was calculated based on equation (1):

$$C = Q/M = I\Delta t/M \quad (1)$$

where C (mAh g^{-1}) is the specific capacity, Q is the quantity of charge, I (mA) is the applied constant discharge current, Δt (h) is the discharge time, and M (g) is the total mass of the capacitive materials.

3. Results and discussion

Fig. 1A shows the morphology and structure properties of the hydrothermally deposited freestanding MnCo_2O_4 composites on Ni foam. The basic building block is vertically aligned 2-dimensional (2D) nanoflakes (NFs) with lengths of $1-3 \mu\text{m}$. Each of these NFs are interconnected with adjacent units forming large amounts of secondary macroscopic channels ($2-3 \mu\text{m}$). These newly formed secondary macropores ($2-3 \mu\text{m}$) are well linked with the macropores ($500 \mu\text{m}$) of the Ni foam, creating easily accessible open spaces for fast transport of OH^- ions. According to our previous study, the obtained MnCo_2O_4 NFs can also act as excellent platform for the loading of a tertiary layer of active materials, thereby increasing the actual surface area [27]. Herein, another thin layer of MnCo_2O_4 nanosheets (NSs) were deposited on the as-obtained MnCo_2O_4 NFs through a facile electrodeposition method followed by calcination treatment. As shown in Fig. 1B, the MnCo_2O_4 NSs are very thin and strongly combined with the MnCo_2O_4 NFs, forming a core-shell structured dual-hierarchy $\text{MnCo}_2\text{O}_4/\text{Ni}$ foam (D- $\text{MnCo}_2\text{O}_4/\text{Ni}$) electrode with greatly increased surface area. From a closer observation, the original smooth surface of the MnCo_2O_4 NFs has adopted a crumpled appearance, while retaining the macro-channels separated by the MnCo_2O_4 nanoflake-network (Fig. 1C). Furthermore, the elemental distribution was analysed by energy dispersive X-ray spectroscopy (EDX, Fig. 1D), confirming the homogeneity of both Mn and Co in the deposited MnCo_2O_4 composites.

The nanostructure of the as-obtained D- MnCo_2O_4 was further characterized by TEM images. Fig. 2A shows a single D- MnCo_2O_4 unit with crumpled surface, revealing that a thin layer of MnCo_2O_4 NS was uniformly grown onto the MnCo_2O_4 NF. From the high-resolution TEM (HRTEM) image in Fig. 2B, nanocavities and mesopores with average diameter around 5 nm are densely embedded throughout the MnCo_2O_4 NSs, forming a tertiary porosity architecture. These mesopore walls are composed of crystalline

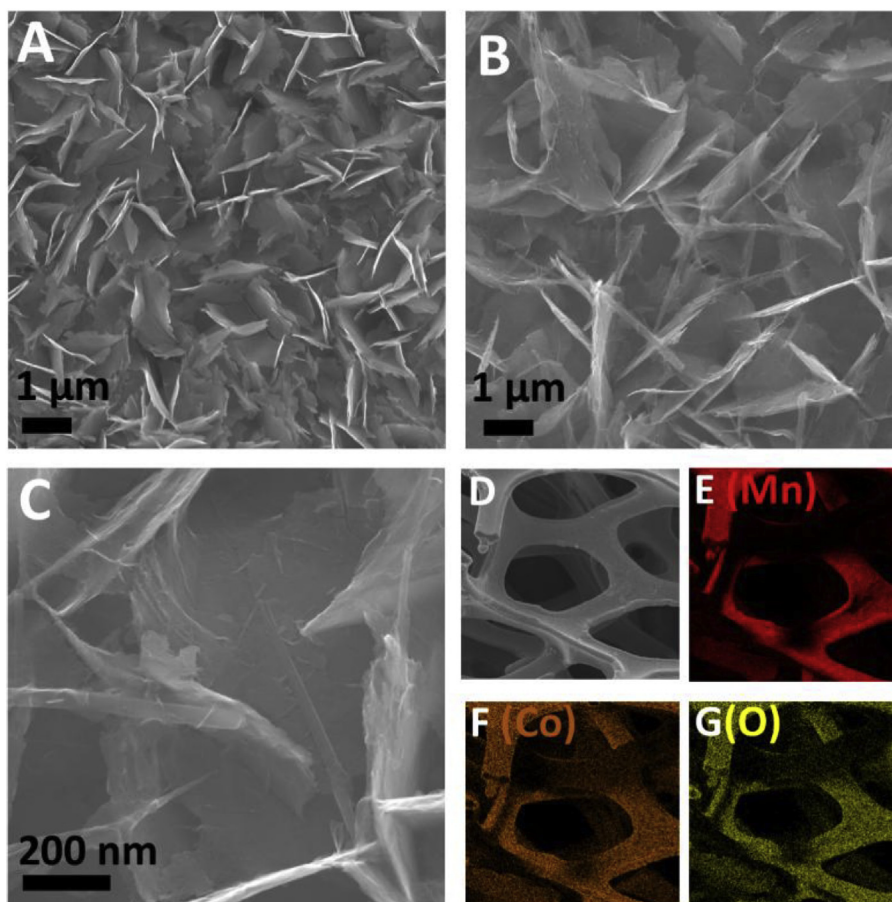


Fig. 1. SEM images of MnCo_2O_4 NFs (A), dual-hierarchy MnCo_2O_4 (B–C) and corresponding elemental mapping images (D–F).

MnCo_2O_4 nanoparticles as verified by the selected area electron diffraction (SAED) pattern, in which several cricoid diffraction spots can be observed corresponding well to the (111), (220), (311), (400) and (420) crystal phases of cubic spinel MnCo_2O_4 (Fig. 2D) [28]. Moreover, distinct sets of lattice fringes with inter-planar spacing of 0.25 nm and 0.42 nm can be detected in the HTEM image in Fig. 2C, which are in good agreement with the (311) and (200) orientation phases of the cubic MnCo_2O_4 structure.

The phase evolution of the D- MnCo_2O_4 were further verified by the X-ray diffraction (XRD) patterns shown in Fig. 3A. A series of Bragg reflections can be detected at $2\theta = 30.8^\circ$, 36.2° , 37.6° , 43.8° , 58.5° and 63.9° , which matches well with (220), (311), (222), (400), (511) and (440) phase orientations of face-centered-cubic MnCo_2O_4 (space group Fd-3m (227), JCPDS No. 32-0297). These results are consistent with the observation obtained from SAED pattern, confirming the high crystallinity for both the MnCo_2O_4 core-nanoflake and the MnCo_2O_4 shell-nanosheet. The survey XPS spectrum in Fig. 3B reveals the presence of Co, Mn and O elements in the as-obtained D- MnCo_2O_4 composites. Besides, an atomic Mn/Co ratio of approximately 1:2 was determined by the XPS measurement, which matches well with the empirical formula. In the high-resolution Mn 2p spectrum (Fig. 3C), the Mn atoms in $2\text{P}_{3/2}$ and $2\text{P}_{1/2}$ electronic configurations appear at 642.9 and 654.1 eV, respectively. The high-resolution Co 2p spectrum (Fig. 3D) shows the Co atoms in $2\text{P}_{3/2}$ and $2\text{P}_{1/2}$ electronic configurations locate at 779.9 and 795.3 eV, respectively. The XPS analysis further confirmed the formation of cubic MnCo_2O_4 .

The electrochemical behaviours were evaluated in 2 M KOH solution in a standard three-electrode electrochemical cell,

employing D- $\text{MnCo}_2\text{O}_4/\text{Ni}$ as working electrode, a Ag/AgCl (saturated) reference electrode and Pt wire counter electrode. For comparison purposes, single layered MnCo_2O_4 (S- $\text{MnCo}_2\text{O}_4/\text{Ni}$), MnO_2 (S- MnO_2/Ni) and Co_3O_4 (S- $\text{Co}_3\text{O}_4/\text{Ni}$) electrodes were also prepared and evaluated. It can be seen that both the hydrothermally deposited MnO_2 and Co_3O_4 exhibit similar, roughly vertically aligned nanoflakes to the binary MnCo_2O_4 NFs (Fig. S1). As displayed in Fig. S2A, the obtained CV curve from binary S- $\text{MnCo}_2\text{O}_4/\text{Ni}$ electrode has the largest enclosed area, indicating its higher capacity than pristine S- $\text{Co}_3\text{O}_4/\text{Ni}$ and S- MnO_2/Ni electrodes. Furthermore, galvanostatic charge/discharge measurement was carried out to quantify the charge storage capability within the potential window between 0 and 0.45 V vs. Ag/AgCl (saturated) as shown in Fig. S2B. Noticeably, all samples exhibit plateau regions during the charge/discharge process, which is consistent with their individual CV behaviours. Specific capacities were calculated based on the discharge time between 0.45 V and 0.2 V at the current density of 2 mA cm^{-2} according to equation (1). The S- $\text{MnCo}_2\text{O}_4/\text{Ni}$ electrode exhibits higher capacity (229 mAh g^{-1}) than those of MnO_2 (115 mAh g^{-1}) and Co_3O_4 (164 mAh g^{-1}). This result is consistent with our previous study and reveals the existence of synergistic effects between Co and Mn ions, which can enhance the charge storage capability [11]. Furthermore, electrochemical impedance spectroscopy (EIS) was employed to investigate the frequency response of pristine MnO_2 and binary MnCo_2O_4 in open circuit conditions. Typically, the semicircle in the high frequency region represents the internal charge transfer resistance (R_{ct}) and the straight slope in the low-frequency region indicates the ion diffusion resistance on the electrode/electrolyte interfaces. The

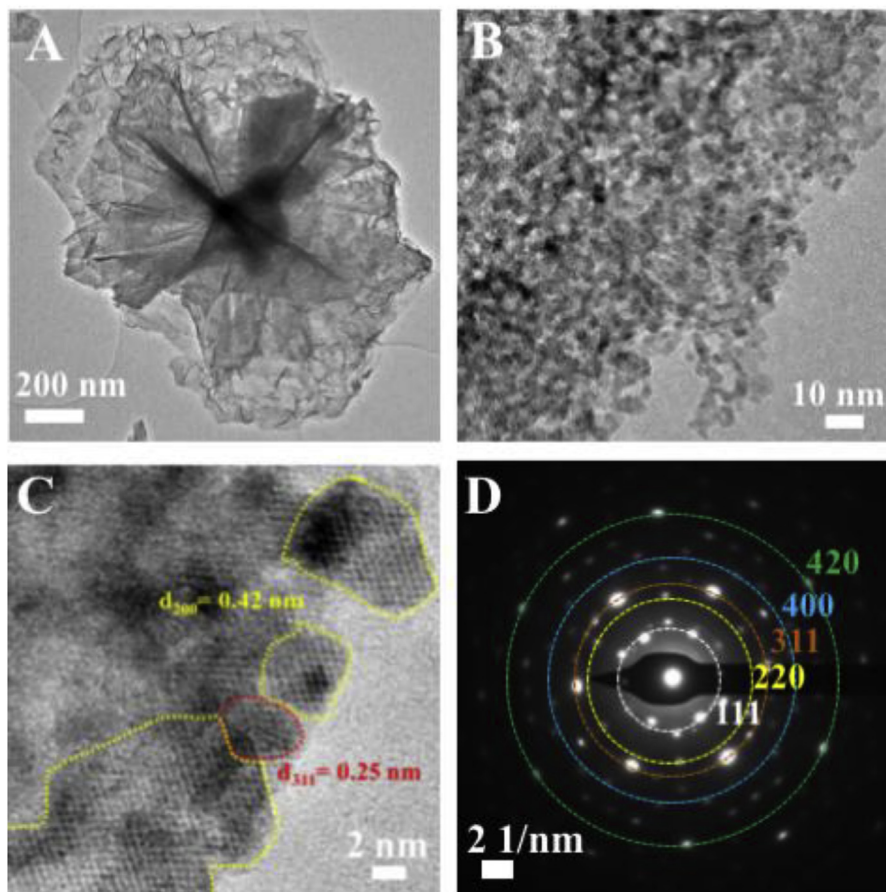


Fig. 2. (A–C) TEM and HRTEM images of D-MnCo₂O₄/Ni electrode and (D) corresponding SAED pattern.

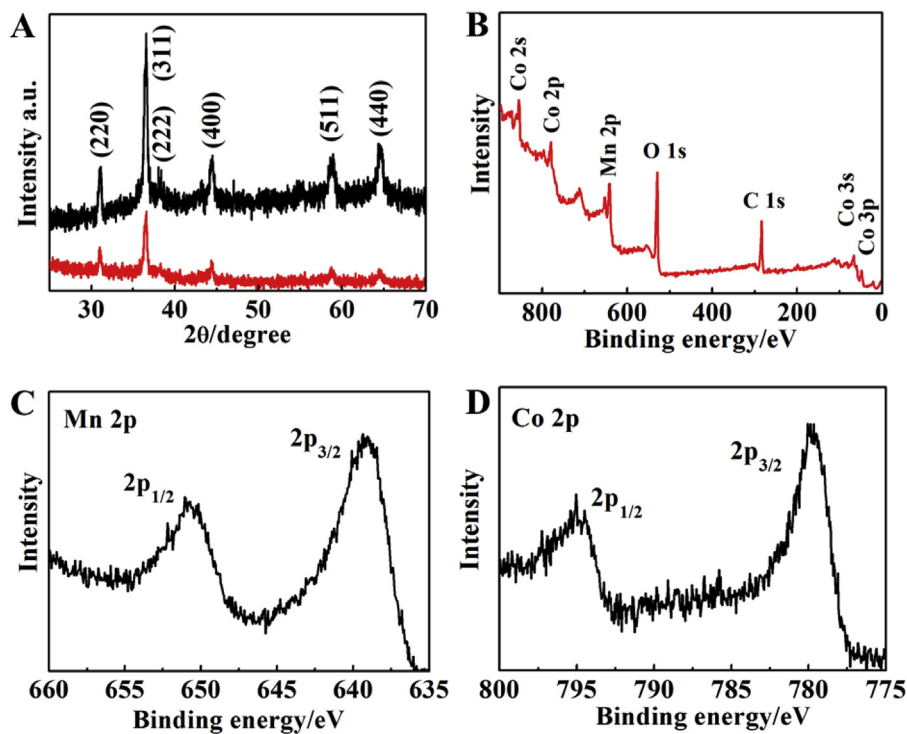


Fig. 3. (A) XRD patterns of MnCo₂O₄ NFs (black) and D-MnCo₂O₄ composites (red), (B) XPS survey spectrum of D-MnCo₂O₄ composites and (C–D) high resolution XPS spectra of Mn 2p and Co 2p. (For interpretation of the references to colour in this figure legend, the reader is referred to the Web version of this article.)

Nyquist plots displayed in Fig. S2D reveals that the binary MnCo_2O_4 exhibits a smaller semicircle and higher slope than pristine MnO_2 , suggesting its small internal resistance and fast ion diffusion process.

Fig. 4A compares the charge/discharge behaviours of the D- $\text{MnCo}_2\text{O}_4/\text{Ni}$ electrode with the S- $\text{MnCo}_2\text{O}_4/\text{Ni}$ electrode at a constant discharge current density of 2 mA cm^{-2} . The D- $\text{MnCo}_2\text{O}_4/\text{Ni}$ electrode shows much higher capacity of 283 mAh g^{-2} than that of the S- $\text{MnCo}_2\text{O}_4/\text{Ni}$ electrode (229 mAh g^{-1}). This reveals the design of dual-hierarchy of MnCo_2O_4 can dramatically increase the effective surface area rather than simply increase the material loading. This can be verified by the higher roughness factor (837 mF) of D- $\text{MnCo}_2\text{O}_4/\text{Ni}$ electrode, which is over 15 times higher than that of S- $\text{MnCo}_2\text{O}_4/\text{Ni}$ electrode (52.9 mF), as shown in Fig. S3. Fig. 4B depicts the CV curves of the D- $\text{MnCo}_2\text{O}_4/\text{Ni}$ electrode at various scan rates

from 5 to 20 mV s^{-1} . Although a slight shift in the peak position can be observed, the shapes of all CV curves basically remained unchanged, indicating its high electrochemical reversibility and excellent rate capability. In addition, the galvanostatic charge/discharge curves of the D- $\text{MnCo}_2\text{O}_4/\text{Ni}$ electrode recorded at three different current densities of 2 mA cm^{-2} (1.7 A g^{-1}), 5 mA cm^{-2} (4.2 A g^{-1}) and 10 mA cm^{-2} (8.3 A g^{-1}), reveal high capacities of 283 , 256 and 194 mAh g^{-1} , corresponding to capacitance of 2265 , 2050 and 1550 F/g , respectively (Fig. 4C and D). As a result, around 70% capacity can be retained when the discharge current increases from 2 up to 10 mA cm^{-2} . These results are comparable to, or even better than, previous reported high-performance supercapacitor materials (Table S1) [29–35].

Collectively, the high charge storage performance and long cycle stability can be ascribed to the following several advances achieved

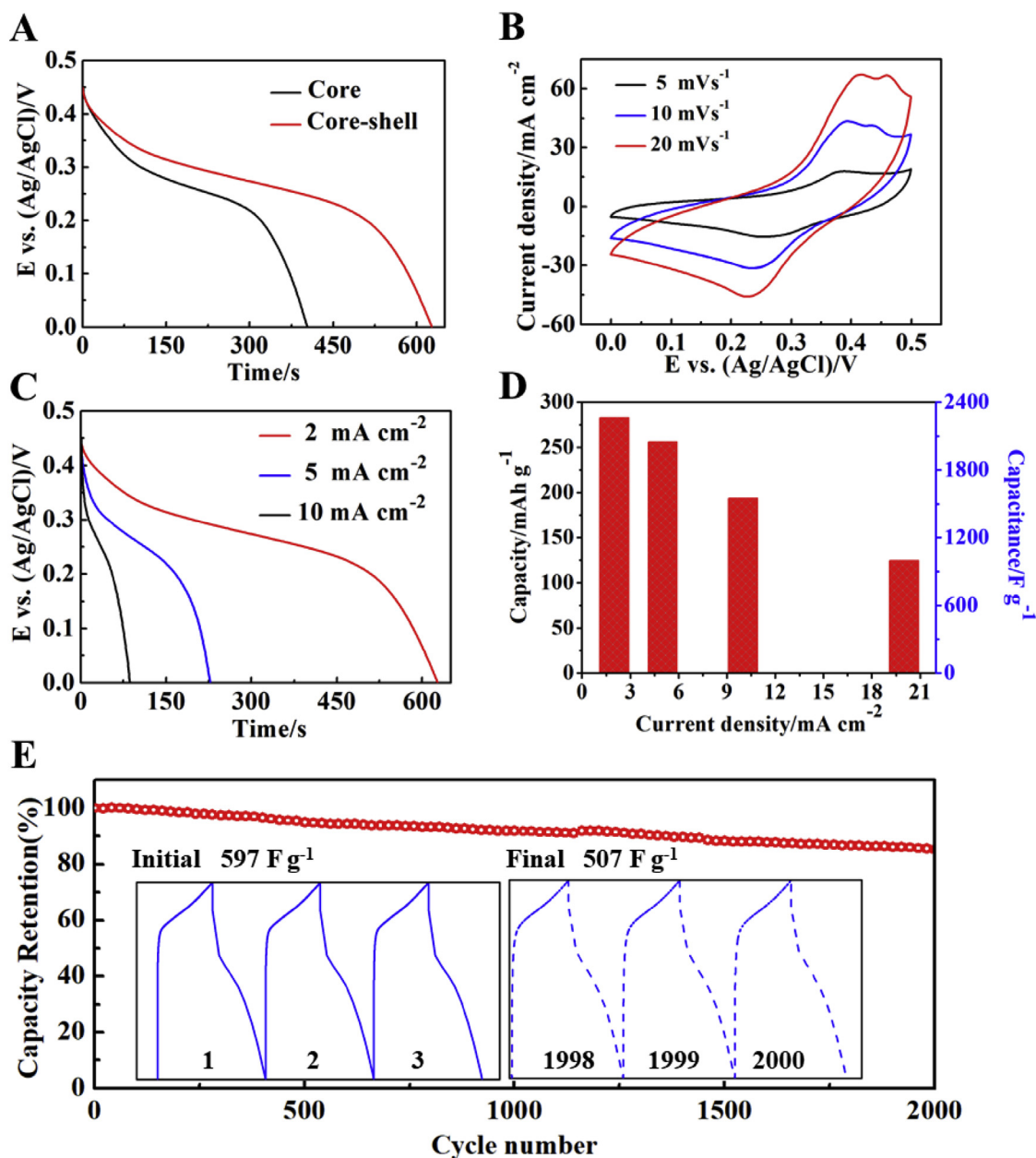


Fig. 4. (A) Galvanostatic charge/discharge curves of $\text{MnCo}_2\text{O}_4/\text{Ni}$ and D- $\text{MnCo}_2\text{O}_4/\text{Ni}$ electrodes, (B) CV curves at various scan rates, (C) charge/discharge curves at various current densities of D- $\text{MnCo}_2\text{O}_4/\text{Ni}$ electrode and (D) corresponding specific capacities and (E) cycling performance at a current density of 40 mA cm^{-2} over 2000 cycles.

in the D-MnCo₂O₄/Ni electrode: *i*) the highly porous and conductive Ni foam is an excellent electrode support for electron collection and building of a hierarchical architecture. *ii*) MnO₂ is considered to be an excellent pseudocapacitive electrode material. With incorporation of Co ions, the binary MnCo₂O₄ shows synergistic effects between Mn and Co ions resulting in prominent electrochemical activity and capacitive behaviour. Meanwhile, the MnCo₂O₄ also shows increased conductivity compared to pristine MnO₂, which facilitates fast charge transfer to the surface-active sites. *iii*) the unique design of multi-level hierarchical electrode architecture. Two levels of macroporous channels generated from the Ni foam and the MnCo₂O₄ nanoflakes allow fast OH⁻ ions transport resulting in fast electrode responses. The mesoporous MnCo₂O₄ shell-nanosheets can further increase the electrode surface area. Significantly, these mesochannels can enhance the electrochemical accessibility, thereby allowing the diffusion of OH⁻ into the interior layers. In addition, all three levels of hierarchy are tightly connected with each other and this freestanding D-MnCo₂O₄/Ni electrode also exhibits excellent long cycle stability at high current density of 40 mA cm⁻². As shown in the GCD curves, around 85% of the capacity is retained after continuous cycling for 2000 cycles (Fig. 4E), indicating its good cycling stability.

4. Conclusions

In conclusion, we have demonstrated a freestanding multi-level hierarchical D-MnCo₂O₄/Ni electrode through a facile hydrothermal and electrodeposition approach. The obtained D-MnCo₂O₄/Ni electrode contains three levels of hierarchy including macroporous Ni foam scaffold, macroporous MnCo₂O₄ nanoflakes and mesoporous MnCo₂O₄ nanosheets. All these nanostructures are interconnected forming a continuous transport channel from the bottom Ni foam up to the exterior Mn³⁺/Co³⁺ active sites. As a result, the D-MnCo₂O₄/Ni electrode exhibits excellent charge storage capability (283 mAh g⁻¹ at 2 mA cm⁻²) and over 2000 cycles stability. We believe this highly porous and hierarchical electrode design can be extended for a wide variety of materials for electrocatalysis and energy storage.

Acknowledgements

This work was funded by the Australian Research Council (ARC) through the Australian Centre for Electromaterials Science. DRM acknowledges the support from the ARC through his Australian Laureate Fellowship.

Appendix A. Supplementary data

Supplementary data related to this article can be found at <https://doi.org/10.1016/j.electacta.2018.05.112>.

References

- [1] J.S. Chen, Y. Gui, D.J. Blackwood, A versatile ionic liquid-assisted approach to synthesize hierarchical structures of β-Ni(OH)₂ nanosheets for high performance pseudocapacitor, *Electrochim. Acta* 188 (2016) 863–870.
- [2] L. Liu, Y. Luo, W. Tan, F. Liu, S.L. Suib, Y. Zhang, G. Qiu, Zinc removal from aqueous solution using a deionization pseudocapacitor with a high-performance nanostructured birnessite electrode, *Environ. Sci. Nano.* 4 (2017) 811–823.
- [3] H. Wang, H.S. Casalongue, Y. Liang, H. Dai, Ni(OH)₂ nanoplates grown on graphene as advanced electrochemical pseudocapacitor materials, *J. Am. Chem. Soc.* 132 (2010) 7472–7477.
- [4] Y. Yuan, X. Xia, J. Wu, J. Yang, Y. Chen, S. Guo, Nickel foam-supported porous Ni(OH)₂/NiOOH composite film as advanced pseudocapacitor material, *Electrochim. Acta* 56 (2011) 2627–2632.
- [5] D. Du, R. Lan, W. Xu, R. Beanland, H. Wang, S. Tao, Preparation of a hybrid Cu₂O/CuMoO₄ nanosheet electrode for high-performance asymmetric

- supercapacitors, *J. Mater. Chem. A* 4 (2016) 17749–17756.
- [6] D. Du, R. Lan, J. Humphreys, W. Xu, K. Xie, H. Wang, S. Tao, Synthesis of NiMoS₄ for high-performance hybrid supercapacitors, *J. Electrochem. Soc.* 164 (2017) A2881–A2888.
- [7] H. Sun, L. Mei, J. Liang, Z. Zhao, C. Lee, H. Fei, M. Ding, J. Lau, M. Li, C. Wang, Three-dimensional hole-graphene/nitria composite architectures for ultrahigh-rate energy storage, *Science* 356 (2017) 599–604.
- [8] K.A. Owusu, L. Qu, J. Li, Z. Wang, K. Zhao, C. Yang, K.M. Hercule, C. Lin, C. Shi, Q. Wei, Low-crystalline iron oxide hydroxide nanoparticle anode for high-performance supercapacitors, *Nat. Commun.* 8 (2017) 14264.
- [9] Y. Liu, N. Fu, G. Zhang, M. Xu, W. Lu, L. Zhou, H. Huang, Design of hierarchical Ni-Co@ Ni-Co layered double hydroxide core-shell structured nanotube array for high-performance flexible all-solid-state battery-type supercapacitors, *Adv. Funct. Mater.* 27 (2017), 1605307.
- [10] S. Yu, N. Yang, H. Zhuang, S. Mandal, O.A. Williams, B. Yang, N. Huang, X. Jiang, Battery-like supercapacitors from diamond networks and water-soluble redox electrolytes, *J. Mater. Chem. A* 5 (2017) 1778–1785.
- [11] C. Xiao, X. Zhang, T. Mendes, G.P. Knowles, A. Chaffee, D.R. MacFarlane, Highly ordered hierarchical mesoporous MnCo₂O₄ with cubic *1a3d* symmetry for electrochemical energy storage, *J. Phys. Chem. C* 120 (2016) 23976–23983.
- [12] R. Li, Y. Wang, C. Zhou, C. Wang, X. Ba, Y. Li, X. Huang, J. Liu, Carbon-stabilized high-capacity ferrocene oxide nanorod array for flexible solid-state alkaline battery-supercapacitor hybrid device with high environmental suitability, *Adv. Funct. Mater.* 25 (2015) 5384.
- [13] Y. Jiao, J. Pei, C. Yan, D. Chen, Y. Hu, G. Chen, Layered nickel metal-organic framework for high performance alkaline battery-supercapacitor hybrid devices, *J. Mater. Chem. A* 4 (2016) 13344–13351.
- [14] B.E. Conway, Transition from “supercapacitor” to “battery” behavior in electrochemical energy storage, *J. Electrochem. Soc.* 138 (1991) 1539–1548.
- [15] P. Wu, S. Cheng, M. Yao, L. Yang, Y. Zhu, P. Liu, O. Xing, J. Zhou, M. Wang, H. Luo, A Low-Cost, Self-standing NiCo₂O₄@CNT/CNT multilayer electrode for flexible asymmetric solid-state supercapacitors, *Adv. Funct. Mater.* 27 (2017) 1702160.
- [16] D. Nathiya, P. Muthukumar, J. Wilson, K. Gurunathan, Stable and robust nanobiocomposite preparation using aminated guar gum (mimic activity of graphene) with electron beam irradiated polypyrrole and Ce-Ni bimetal: effective role in simultaneous sensing of environmental pollutants and pseudocapacitor applications, *Electrochim. Acta* 246 (2017) 484–496.
- [17] X. Zhong, L. Zhang, J. Tang, J. Chai, J. Xu, L. Cao, M. Yang, M. Wang, W. Kong, S. Wang, Efficient coupling of a hierarchical V₂O₅@Ni₃S₂ hybrid nanowire array for pseudocapacitors and hydrogen production, *J. Mater. Chem. A* 5 (2017) 17954–17962.
- [18] Y. Zhang, Z. Shi, L. Liu, Y. Gao, J. Liu, High conductive architecture: bimetal oxide with metallic Properties@Bimetal hydroxide for high-performance pseudocapacitor, *Electrochim. Acta* 231 (2017) 487–494.
- [19] J.M. Whiteley, S. Hafner, S.S. Han, S.C. Kim, V.D. Le, C. Ban, Y.H. Kim, K.H. Oh, S.H. Lee, All Solid-state disordered LiTiS₂ pseudocapacitor, *J. Mater. Chem. A* 5 (2017) 15661–15668.
- [20] C. Xiao, X. Zhang, S. Li, B.H. Suryanto, D.R. MacFarlane, In situ synthesis of core-shell-Ni₃Fe(OH)₉/Ni₃Fe hybrid nanostructures as highly active and stable bifunctional catalysts for water electrolysis, *ACS Appl. Energy Mater.* 1 (2018) 986–992.
- [21] C. Xiao, H. Hu, X. Zhang, D.R. MacFarlane, Nanostructured gold/bismutite hybrid heterocatalysts for plasmon-enhanced photosynthesis of ammonia, *ACS Sustain. Chem. Eng.* 5 (2017) 10858–10863.
- [22] M. Hasan, M. Jamal, K.M. Razeeb, Coaxial NiO/Ni nanowire arrays for high performance pseudocapacitor applications, *Electrochim. Acta* 60 (2012) 193–200.
- [23] C. Wu, X. Lu, L. Peng, K. Xu, X. Peng, J. Huang, G. Yu, Y. Xie, Two-dimensional vanadyl phosphate ultrathin nanosheets for high energy density and flexible pseudocapacitors, *Nat. Commun.* 4 (2013) 2431.
- [24] J. Liu, J. Jiang, M. Bosman, H.J. Fan, Three-dimensional tubular arrays of MnO₂-NiO nanoflakes with high areal pseudocapacitance, *J. Mater. Chem.* 22 (2012) 2419–2426.
- [25] D. Han, X. Jing, J. Wang, Y. Ding, Z. Cheng, H. Dang, P. Xu, Three-dimensional Co₃O₄ Nanowire@NiO nanosheet core-shell construction arrays as electrodes for low charge transfer resistance, *Electrochim. Acta* 241 (2017) 220–228.
- [26] G.M. Tomboc, H.S. Jadhav, H. Kim, PVP assisted morphology-controlled synthesis of hierarchical mesoporous ZnCo₂O₄ nanoparticles for high-performance pseudocapacitor, *Chem. Eng. J.* 308 (2017) 202–213.
- [27] C. Xiao, S. Li, X. Zhang, D.R. MacFarlane, MnO₂/MnCo₂O₄/Ni heterostructure with quadruple hierarchy: a bifunctional electrode architecture for overall urea oxidation, *J. Mater. Chem. A* 5 (2017) 7825–7832.
- [28] T.Y. Ma, Y. Zheng, S. Dai, M. Jaroniec, S.Z. Qiao, Mesoporous MnCo₂O₄ with abundant oxygen vacancy defects as high-performance oxygen reduction catalysts, *J. Mater. Chem. A* 2 (2014) 8676–8682.
- [29] B.Y. Guan, A. Kushima, L. Yu, S. Li, J. Li, X.W.D. Lou, Coordination polymers derived general synthesis of multishelled mixed metal-oxide particles for hybrid supercapacitors, *Adv. Mater.* 29 (2017), 1605902.
- [30] J. Cui, X. Zhang, L. Tong, J. Luo, Y. Wang, Y. Zhang, K. Xie, Y. Wu, A facile synthesis of mesoporous Co₃O₄/CeO₂ hybrid nanowire arrays for high performance supercapacitors, *J. Mater. Chem. A* 3 (2015) 10425–10431.
- [31] Y. Xi, B. Dong, Y. Dong, N. Mao, L. Ding, L. Shi, R. Gao, W. Liu, G. Su, L. Cao, Well-defined, nanostructured, amorphous metal phosphate as electrochemical pseudocapacitor materials with high capacitance, *Chem. Mater.* 28

- (2016) 1355–1362.
- [32] M. Amiri, S.K. Konda, W. Keeler, A. Chen, Superb pseudocapacitance based on three-dimensional porous nickel oxide modified with iridium oxide, *J. Phys. Chem. C* 121 (2017) 27274–27284.
- [33] H. Chen, J. Jiang, Y. Zhao, L. Zhang, D. Guo, D. Xia, One-pot synthesis of porous nickel cobalt sulphides: tuning the composition for superior pseudocapacitance, *J. Mater. Chem. A* 3 (2015) 428–437.
- [34] A.K. Mondal, D. Su, S. Chen, A. Ung, H.S. Kim, G. Wang, Mesoporous MnCo_2O_4 with a flake-like structure as advanced electrode materials for lithium-ion batteries and supercapacitors, *Chem. Eur. J.* 21 (2015) 1526–1532.
- [35] H. Li, M. Yu, F. Wang, P. Liu, Y. Liang, J. Xiao, C. Wang, Y. Tong, G. Yang, Amorphous nickel hydroxide nanospheres with ultrahigh capacitance and energy density as electrochemical pseudocapacitor materials, *Nat. Commun.* 4 (2013) 1894.

Supporting Information

Dual-MnCo₂O₄/Ni Electrode with Three-level Hierarchy for High-performance Electrochemical Energy Storage

Changlong Xiao^a, Xinyi Zhang^{a,b*} and Douglas R. MacFarlane^{a*}

^aARC Centre of Excellence for Electromaterials Science, Monash University, Victoria 3800, Australia

^bGuangxi Innovation Centre for Renewable Materials; Laboratory for Electrochemical Energy Materials, Guangxi University, Nanning 530004, China.

***Corresponding Author**

[Redacted]

E-mail address: [Redacted]

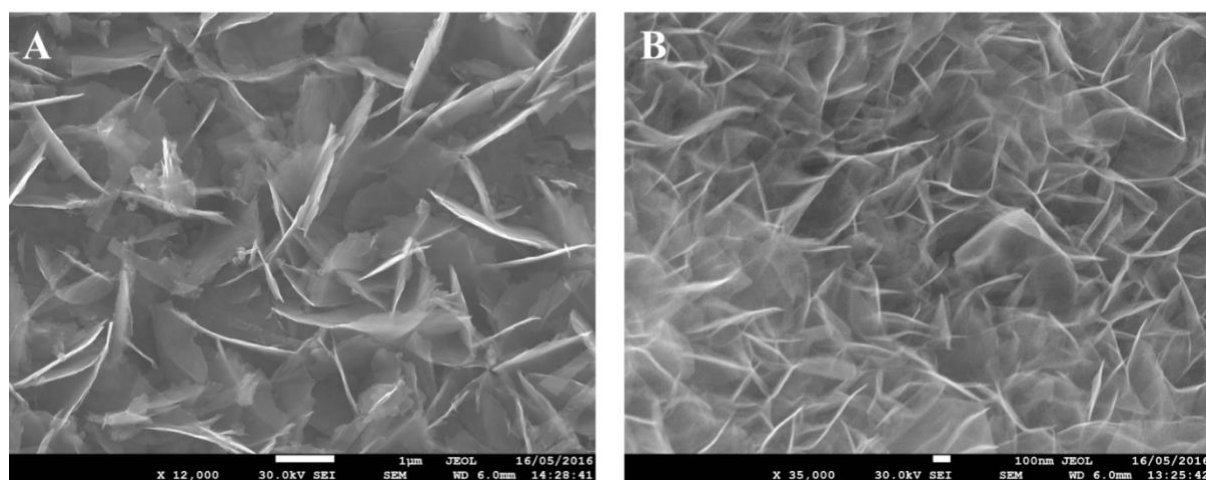


Figure S1. SEM images of hydrothermally (A) Co₃O₄ and (B) MnO₂ on nickel foams.

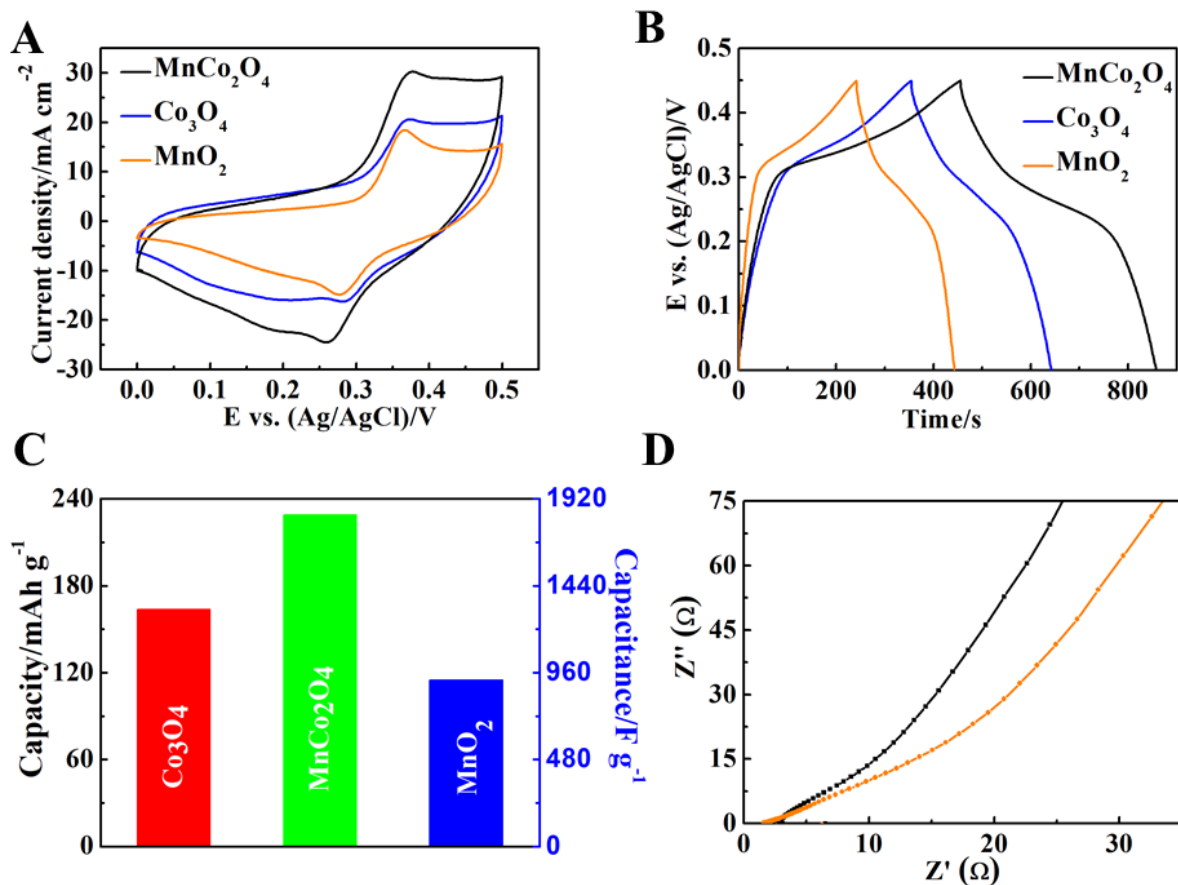


Figure S2. (A) CV curves at scan rate of 10 mV s^{-1} , (B) galvanostatic charge/discharge curves and (C) corresponding specific capacities of MnCo_2O_4 , MnO_2 and Co_3O_4 nanoflakes and (D) Nyquist plots of MnCo_2O_4 and MnO_2 .

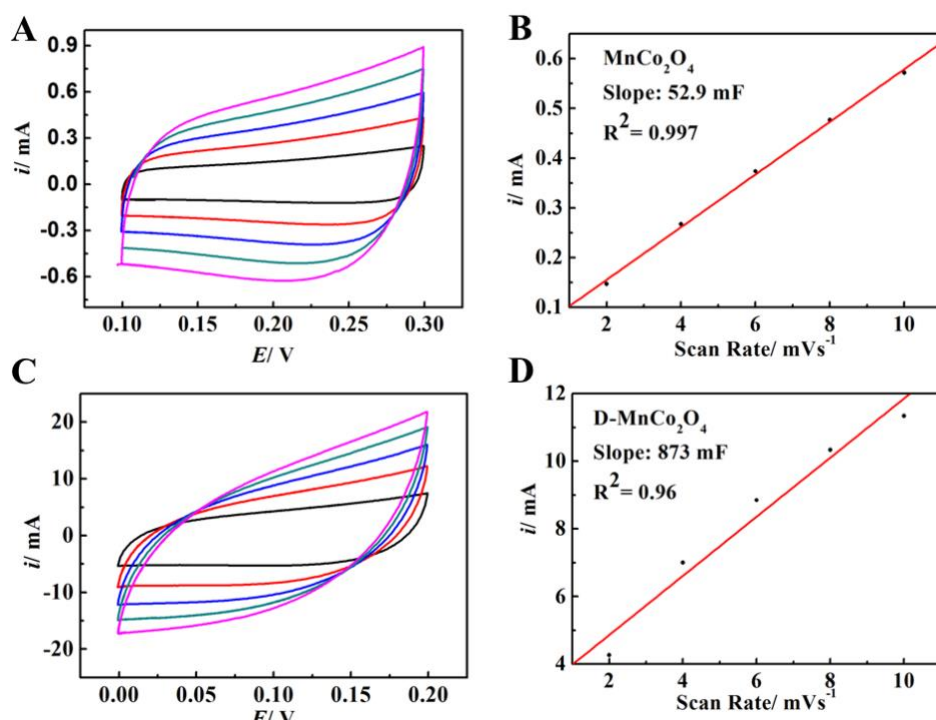


Figure S3. CV curves measured at various scan rates (2 to 10 mV/s) and corresponding current densities plotted versus scan rates of MnCo₂O₄/Ni foam and D-MnCo₂O₄/Ni foam.

Table S1. Comparison of specific capacities (and specific capacitance) of D-MnCo₂O₄/Ni electrode with previous reported high-performance capacitive electrode materials. [Values have been calculated from the original papers based the equation below: Specific capacity (mAh g⁻¹) = Specific capacitance (F/g) × ΔV/3.6]

Materials	Capacities 1 A g ⁻¹	Capacities 5 A g ⁻¹	Electrolyte	Mass loading (mg cm ⁻²)	Ref.
D-MnCo ₂ O ₄ /Ni	283 mAh g ⁻¹ (2265 F g ⁻¹)	256 mAh g ⁻¹ (2050 F g ⁻¹)	2 M KOH	1.2 ± 0.15	This work
S-MnCo ₂ O ₄ /Ni	229 mAh g ⁻¹ (1830 F g ⁻¹)	---	2 M KOH	1.0 0.10	This work
mMnCo ₂ O ₄	199 mAh g ⁻¹ (1593 F g ⁻¹)	137 mAh g ⁻¹ (1100 F g ⁻¹)	2 M KOH	1.0	10
Amorphous Co ₃ (PO ₄) ₂	^a 130 mAh g ⁻¹ (1174 F g ⁻¹)	105 mAh g ⁻¹ (944 F g ⁻¹)	3 M KOH	0.864	31
NiIr(10%)	^b 228 mAh g ⁻¹ (1643 F g ⁻¹)	^c 208 mAh g ⁻¹ (1497 F g ⁻¹)	1 M KOH		32

Multishelled Ni-Co	^a 239 mAh g ⁻¹ (1908 F g ⁻¹)	213 mAh g ⁻¹ (1707 F g ⁻¹)	6 M KOH	1.52	29
Ni-Co-S	167 mAh g ⁻¹ (1093 F g ⁻¹)	~152 mAh g ⁻¹ (~1000 F g ⁻¹)	6 M KOH	1.7-2.6	33
Flake-like MnCo ₂ O ₄	1165 mAh g ⁻¹ (1487 F g ⁻¹)	129 mAh g ⁻¹ (1162 F g ⁻¹)	2 M KOH	1.0	34
Co ₃ O ₄ /CeO ₂	~130 mAh g ⁻¹ (1037 F g ⁻¹)	~123 mAh g ⁻¹ (980 F g ⁻¹)	2 M KOH	1.0	30
Amorphous Ni(OH) ₂	303 mAh g ⁻¹ (2188 F g ⁻¹)	232 mAh g ⁻¹ (1667 F g ⁻¹)	1 M KOH	0.1 μg	35

^a value obtained at 2 A g⁻¹, ^b value obtained at 1.9 A g⁻¹ value obtained at 3.8 A g⁻¹.

Chapter 7

Conclusions and future work

7.1 Conclusions

Solar energy is the most important renewable energy resource due to its massive scope. The application of solar energy in practical devices rests on the conversion of the energy from sunlight into electricity (solar electricity) and energy-rich molecules (solar fuel) via photo- and electrocatalytic processes which suffer from sluggish kinetics. To this end, highly active catalysts are required to improve the energy conversion efficiency. The scope of this thesis involves the synthesis of hierarchical and/or nanoporous materials and their applications in hydrogen production, ammonia synthesis and electrochemical energy storage.

The intense interest in nickel-iron LDH for electrolytic water splitting within the literature has been summarised in chapter 2. A key issue is its poor electrical conductivity for fast charge transfer.¹ To address this, a material comprising nickel-iron alloy nanosheets wrapped in nickel-iron LDH was studied in chapter 2. By taking advantage of the high conductivity of nickel-iron alloys, the core-shell structured nickel-iron alloy/nickel-iron LDH exhibit excellent performance in whole cell water splitting.

The electrooxidation of urea has been studied much less than the OER, and its reaction mechanism remains unclear. However, the UOR is a more efficient anodic reaction than the OER in terms of its low half-reaction potential (0.37 V vs. RHE).² In chapter 3, a quadruple hierarchical electrode was functionalized with an ultrathin MnO₂ nanosheets, and examined as a bifunctional electrode in urea-containing alkaline media. Benefiting from the advanced electrode structure and high catalytic selectivity, the fabricated MnO₂/MnCo₂O₄/Ni electrode exhibits outstanding performance in whole cell urea electrolysis.

In addition to hydrogen fuel, ammonia is also an important hydrogen-storage medium, and the relevant nitrogen cycle is another important energy-related cycle. Nitrogen accounts for almost 78% of the atmosphere composition, while the challenge in utilization of nitrogen is the requirement to break its strong covalent bond. In chapter 4, gold-nanoparticle modified bismutite hybrid (Au/BSC) was fabricated and investigated for nitrogen reduction under ambient conditions. The fabricated Au/BSC shows enhanced light adsorption attributed to the plasmon effect, which improves photoinduced charge separation and transport.

Controllable synthesis of materials with high surface area and delicate architecture is crucial in achieving high-performance electromaterials. Furthermore, synergistic effects between each component and the hierarchy of the electrode material are also significant aspects to be considered. Binary Mn-Co oxide has been verified as a redox-active material in previous studies.³ In this research, a hard-template method and a chemical bath deposition method have been investigated to fabricate MnCo_2O_4 with a hierarchically mesoporous structure (chapter 5) and a dual-level hierarchy (chapter 6), respectively. The well-designed electrode structures show significant enhancement in electrochemical energy storage.

7.2 Suggested future work

Iron is one of the most earth-abundant metals, and iron-based composites such as iron oxide/hydroxide, iron phosphite, and iron sulfite have been intensively studied in energy conversion and storage.⁴ Therefore, several prospects for well-designed iron oxides and iron phosphite are:

1| Electrolytic water splitting for hydrogen production has been extensively studied. Nevertheless, conventional commercial water electrolysis is conducted in strongly alkaline media, which can cause serious corrosion and environmental pollution. In addition, 70% of the earth is covered by sea water with pH around 8–8.5. Therefore, the development of catalysts for hydrogen generation in nearly neutral media has already attracted significant

research interest. In this project, a porous flower-like FeP was fabricated (Figure 7.1 c), and shown to be a promising catalyst for HER in a neutral electrolyser.

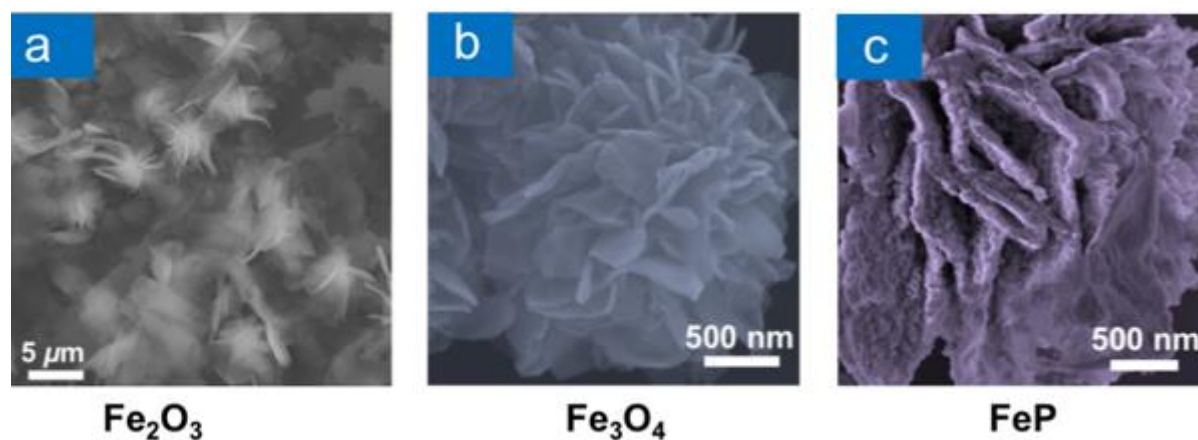


Figure 7.1 SEM images of nanoporous (a) Fe₂O₃, (b) Fe₃O₄ and (c) FeP.

2| The Ni-Fe battery is a traditional aqueous battery, which has been studied for over a hundred years. Owing to its low cost and high capacity, many efforts have been made to develop functionalized FeO_x anode materials. In this research, nanostructured Fe₃O₄ (Figure 7.1 a and b) has been synthesized through a chemical bath deposition method. Further research on optimizing the synthetic conditions and assembling batteries should be explored.

References

1. Y. Hou, M. R. Lohe, J. Zhang, S. Liu, X. Zhuang, X. Feng, *Energy Environ. Sci.* 2016, **9**, 478.
2. X. Zhu, X. Dou, J. Dai, X. An, Y. Guo, L. Zhang, S. Tao, J. Zhao, W. Chu, X. C. Zeng, C. Wu, *Angew. Chem. Int. Ed.* 2016, **55**, 12465.
3. Y. Xu, X. Wang, C. An, Y. Wang, L. Jiao, H. Yuan, *J. Mater. Chem. A*, 2014, **2**, 16480.
4. H. Jin, G. Guo, X. Liu, J. Liu, A. Vasileff, Y. Jiao, Y. Zheng, S. Z. Qiao, *Chem. Rev.* 2018, **118**, 6337-6408.